Catalyst design for clean and efficient fuels

Šaric, Manuel

Publication date:
2016

Document Version
Publisher's PDF, also known as Version of record

Catalyst design for clean and efficient fuels

Manuel Šarić

Ph.D. Thesis

Center for Atomic-scale Materials Design - CAMD

Technical University of Denmark
Department of Physics

Fysikvej, bygning 307
DK-2800 Kongens Lyngby

www.fysik.dtu.dk

DTU
Manuel Šarić
Catalyst design for clean and efficient fuels

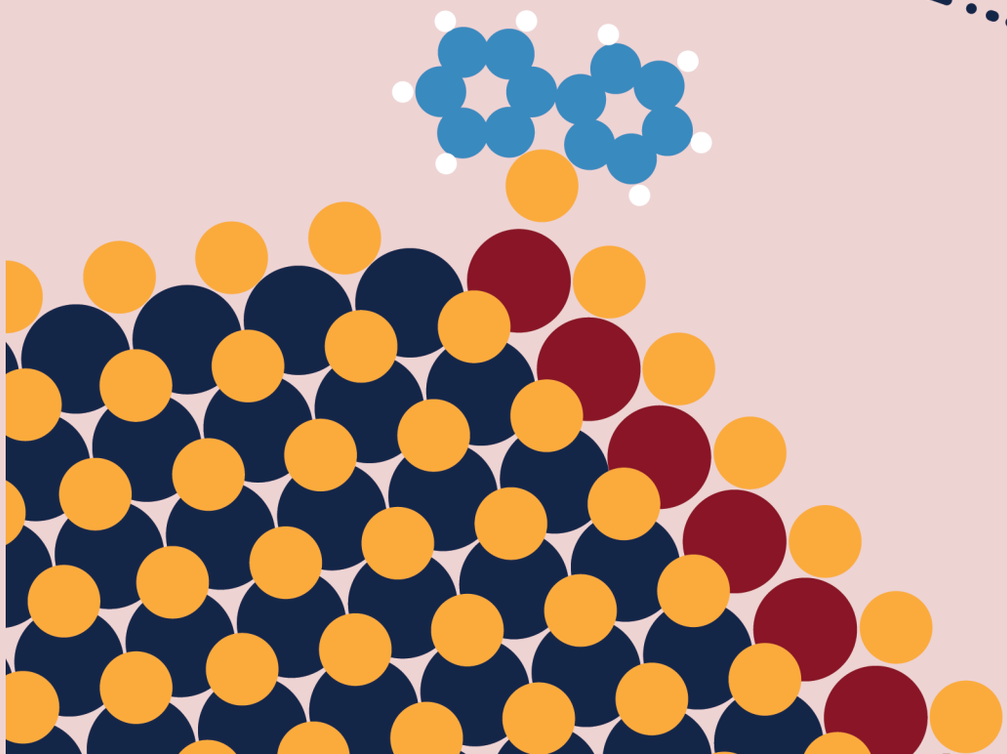

PH.D. THESIS

Catalyst design for clean and efficient fuels

Manuel Šarić

December 2016

Catalyst design for clean and efficient fuels
Ph.D. Thesis
December 30, 2016

Manuel Šarić
msaric@fysik.dtu.dk

Supervisors
Jan Rossmeisl
Poul Georg Moses
Karsten Wedel Jacobsen

Center for Atomic-scale Materials Design
Department of Physics
Technical University of Denmark

Preface

This thesis is submitted in candidacy for the Ph.D. degree in applied physics from the Technical University of Denmark. The work was carried out at the Center for Atomic-scale Materials Design (CAMd) of the Department of Physics at the Technical University of Denmark, the Theoretical Catalysis group of the Department of Chemistry at the University of Copenhagen and at Haldor Topsøe A/S, under the supervision of Jan Rossmeisl, Poul Georg Moses and Karsten Wedel Jacobsen. The Ph.D. project, namely HYDECAT (Enabling Ultra Deep Hydrodesulfurization by Nanoengineering of New Catalysts), was funded by the Danish Council for Independent Research and the Innovation Fund Denmark.

There are many people that made this work possible and I wish to thank them through the following words. I would like to thank my supervisors for all the help and motivation during the last three years. You really helped me to grow as a person. Thanks to all my co-workers at DTU, KU and Haldor Topsøe for a great working environment. Thanks to Marianne for making all the administrative tasks effortless. Thanks to Ole, Marcin and Jens Jørgen for helping with the computers and the code. Thanks to Alexander, Thomas, Ivano and Bethan for proofreading and Alexander and Thomas for translating the abstract. Thanks to my friends back in Istria for making every vacation day memorable and for never letting me feel alone during the long winters in Denmark. Thanks to Signe, Bethan and Christian for the work that we've done together, it was difficult but we made it. Thanks to my family for all the love and support, I will never be able to thank you enough. Last but not least, thank you Katarina for the awesome cover and for being there for me, all the laughs, tears and all the good food.

Vodnjan, December 30, 2016
Manuel Šarić

Abstract

This thesis contains a theoretical approach to specific problems in catalysis and is based upon fundamental concepts from thermodynamics and density functional theory calculations. It investigates the already existing and well established process of hydrodesulfurization and a novel process of synthesizing dimethyl carbonate electrochemically.

Hydrodesulfurization is an industrial refining process in which sulfur is removed from oil in order to reduce SO_2 emissions. The study on hydrodesulfurization involves determining the active sites and their atomic scale structure for the industrially used cobalt promoted MoS_2 catalyst. Reactivity of a series of model molecules, found in oil prior to desulfurization, is studied on cobalt promoted MoS_2. Such an approach has the potential to explain the underlying processes involved in the removal of sulfur at each specific site of the catalyst. The goal is to identify which sites are active towards specific molecules and in getting insight to what the ideal catalyst should look like in terms of morphology.

Dimethyl carbonate is an environmentally benign compound that can be used as a solvent and precursor in chemical synthesis or as a fuel and fuel additive. It can replace different toxic compounds that are nowadays used as precursors for various reactions. An electrocatalytic process for synthesizing dimethyl carbonate is studied as part of this thesis. Producing dimethyl carbonate electrochemically makes it possible to avoid using hazardous chemical processes currently used. It is found that noble metals can be used as electrocatalysts for the synthesis of dimethyl carbonate, significantly lowering the potential when using copper instead of gold. Besides being active, copper was found to be selective towards dimethyl carbonate. A non-selective catalyst will yield unwanted coproducts, causing the need for additional separation techniques to extract pure dimethyl carbonate after synthesis. This in return increases the production cost of dimethyl carbonate.

This thesis is another step in the collective effort to make today's fuels and chemicals environmentally friendlier and creating new, efficient and clean technologies for chemical and fuel production.

Resumé

Denne afhandling indeholder en teoretisk tilgang til specifikke problemer indenfor katalyse og er baseret på fundamentale koncepter fra termodynamikken og tæthedsfunktionalteori beregninger. Afhandlingen behandler den velkendte afsvovlingskatalytiske process og en hidtil ukendt elektrokemisk fremstillingsmetode af dimethylkarbonat.

Afsvovling er en industriel raffineringsproces hvori svovl bliver fjernet fra olie, således at SO_2 emission minimeres. Studiet i afsvovlingskatalyse er udført for at finde og forstå de aktive katalytiske sites og dermed den atomare stuktur for den industrielle koboltaktiverede MoS_2 katalysator. Reaktiviteten for en rkke modelmolekyler, der findes i olien inden svovlen fjernes, undersøges på den koboltaktiverede MoS_2 katalysator. Den fundamentale fremgangsmetode anvendt her, har potentiale til at bestemme de underliggende processer, som fører til svovlfjernelsen ved hvert enkelt specifikt katalytisk site. Målet er herved at identificere hvilke katalytiske sites der er aktive for hvert af de enkelte molekyler og derved få indsigt i hvorledes den ideelle katalysator bør se ud i forhold til morfologien.

Dimetylkarbonat er et miljøvenligt kemikalie der kan bruges som opløsnings-middel og til at danne udgangspunkt for anvendelser, både indenfor kemiske synteser, men også som brændstof eller som tilsætningsstof i brændstoffer. Indefor kemisk syntese kan dimethylkarbonat afløse giftige kemikalier som nutildags bruges som reaktanter i forskellige processer. I denne afhandling undersøges en elektrokemisk fremstillingsmetode af dimethylkarbonat. Hvis dimethylkarbonat bliver produceret elektrokemisk kan man undgå at bruge farlige kemiske processer, som i dag anvendes til at producere dimethylkarbonat. Det bliver vist at ædelmetaller kan bruges som elektrokatalysatore til at produce dimethylkarbonat, og yderligere viser det sig at anvendes kobber frem for guld bliver potentialet til at drive reaktionen kraftigt reduceret. Ud over at kobber er mere aktiv overfor dimethylkarbonat processen er den også mere selektiv. En ikke-selektiv katalysator vil danne uønskede biprodukter, hvilket gør at man skal separere produkterne for at få ren dimethylkarbonat. Dette vil i sidste ende øge prisen for den elektrokemiske fremstilling af dimethylkarbonat.

Denne afhandling er endnu et skridt i en fælles indsats for at kunne fremstille brændstof og kemikalier på en mere miljøvenlig måde og er derved et skridt imod en grøn omstilling af teknologierne til fremstilling af kemikalier og brændstof.

Outline

The following is a brief description of the main chapters of the thesis.

Chapter 1 gives a short motivation regarding the importance of making fuels and chemical processes used nowadays cleaner and more efficient. It also introduces the non-chemist readers to the concept of green chemistry, catalysis, electrocatalysis, hydrodesulfurization, hydrogen evolution and the chemistry of dimethyl carbonate.

Chapter 2 explains the theory behind the computer simulations used in this thesis. It enables the reader, who is not familiar with density functional theory or other computational chemistry methods, to grasp the concepts on a higher level of abstraction.

Chapter 3 explains the process of converting the calculated energies into values that can be used to describe catalytic processes. It describes fundamental concepts from thermodynamics such as internal energy, enthalpy, entropy and Gibbs free energy. Advanced concepts that make it possible to analyze complex catalytic processes in terms of a few simple parameters are also introduced.

Chapter 4 is a summary of the research papers that I have written or contributed to as co-author during my Ph.D. study. The goal of this chapter is to give a qualitative and descriptive overview of the individual studies contained in each paper and linking them together in a full picture. This should make it easier to understand the articles which the reader is encouraged to read in chapter 5.

Chapter 5 includes the research papers written as part of the Ph.D. study.

Chapter 6 contains additional studies in progress.

Contents

Chapter 1

Introduction

Very different stories are presented when asking people belonging to my parents' and grandparents' generation about their daily lives when they were children. As a reference, the reader should know that I was born in 1990. While the oldest among them did not have access to electricity, today's generations could not imagine a day passing by without using some sort of electronic device. This drastic change in daily life is surely attributed to the exponential increase of technological prowess of our civilization. Such progress was made possible by exploiting fossil fuels (coal, gas, oil) for over 100 years. Although leading to great things such as electricity, more food, cars, computers, the Internet and video games, exploiting this energy rich source also led to clear consequences for our planet. The atmospheric levels of CO_2, a greenhouse gas, are now larger than ever in recorded history [1–3]. Greenhouse gases are essential for keeping Earth at mild and comfortable temperatures as they trap part of the infra-red radiation (heat), coming from the Sun. Add more of these gases in the atmosphere and more heat is trapped, leading to global warming [4]. Increasing the temperature of the planet also disturbs the sensitive carbon cycle, especially for oceans in which a large quantity of CO_2 is dissolved [5, 6]. Increasing the temperature of the ocean makes it less capable of dissolving gases such as CO_2. This means that warmer oceans lead to more CO_2 in the atmosphere and more CO_2 in the atmosphere leads to warmer oceans. Increasing the temperature of earth also leads to thawing of permafrost which releases methane, a much stronger greenhouse gas than CO_2 [7–10], as well as the melting of polar icecaps that leads to higher sea levels, thus, endangering coastal cities and entire countries [11–13]. All things considered, it seems that there is a vicious cycle in which increasing the concentration of greenhouse gases in the atmosphere increases the rate at which their concentration in the atmosphere increases. Besides CO_2, large quantities of SO_2 and NO_x gases are released by the combustion of fossil fuels [14–16]. These gases pose a threat to both the flora and fauna of our ecosystems by creating acid rain and decreasing the quality of air [17, 18].

Using renewable energy sources [19, 20] such as solar [21–25] or wind [26, 27] for the production of electricity could be a way to avoid using fossil fuels. Unfortunately, using renewable energy sources to satisfy the entire energy need of our civilization is presently not feasible. By switching to renewable energies we would need to store energy

in batteries or in fuels for use when the Sun is not shining or winds are not blowing. Lithium-ion batteries have proven to be quite reliable for electronic devices and vehicles that traverse short ranges (up to a couple of hundreds kilometers) [28–32]. For aviation and heavy duty machinery some sort of high energy density fuel is required [19]. One popular ideology is the hydrogen society [33–35] where hydrogen gas can be used as fuel in fuel cells [36–39], yielding water as product. This eliminates CO_2 and other unwanted gases as long as the hydrogen gas was initially made from a clean energy source such as solar or wind. The hydrogen fuel itself can be made by water electrolysis [40–43], in other words, by splitting water into hydrogen and oxygen by using electricity in an electrolyser. One issue with hydrogen is that electrolysers and fuel cells require expensive and very rare elements as electrodes, making the hydrogen society presently unfeasible [44]. Another idea is a closed carbon cycle in which there would be a controlled amount of carbon cycling in our atmosphere as CO_2. Carbon could be collected from air as CO_2 which could then be transformed into fuels electrochemically [45–48]. The use of these fuels would lead to waste CO_2, thus, closing the cycle. Harvesting CO_2 as well as reducing it electrochemically to fuels is at present not technologically feasible.

It was believed in previous decades that the exploitation of nuclear energy from fission processes (cleaving a large atomic nucleus into smaller nuclei) could satisfy global energy needs without CO_2 emissions, although there is still the issue of nuclear waste. There are ample resources of uranium and other nuclear fuels on earth as well as novel methods that allow a wider range of isotopes to be used. This in principle makes nuclear energy, if not a renewable energy source, an energy source that can last for very long time scales [19]. Due to various nuclear disasters and meltdowns in the past decades various countries have been moving away from nuclear power. Although it seems like fission will not be satisfying global energy needs, the fusion process could. In fusion, two smaller nuclei are merged into a larger one [19]. The same process powers stars throughout the universe by fusing hydrogen atoms into helium. Merging two nuclei into one requires tremendous amounts of energy to begin with, requiring very high temperatures. This in return makes it very hard to design such a reactor, find materials for it and keep it running [49]. Because of that, nuclear energy from fusion reactors is nowadays still in its infancy. The next big project for nuclear fusion is the International Thermonuclear Experimental Reactor (ITER), a fusion reactor being built in France [50].

It is clear that we will still heavily depend on fossil fuels in the years to come, thus, damaging our planet even more. Such a situation calls for the development of technologies that decrease the impact of using fossil fuels on the environment, in other words, an effort of making fossil fuels more environmentally friendly. The catalytic process of hydrodesulfurization is an example of such an effort. Performed in refineries, it reduces the concentration of sulfur in fuels which in return decreases SO_2 emissions [51, 52]. The elementary chemistry of hydrodesulfurization is discussed further in this thesis.

A slightly different story from fuel production and fuel refining is the production of chemicals. Today, a large number of chemicals are produced in hazardous processes from various toxic precursors. It is often the case that the amount of desired products is several orders of magnitude lower than the amount of reactants due to the formation of

co-products [53]. These large amounts of unwanted co-products, caused by poor selectivity of the process, have to be separated from the desired products. In cases where there is no practical application of such co-products they are discarded as waste, thus, potentially harming the environment. Due to this, there is an effort towards developing novel atom-efficient processes that involve harmless reagents, in other words, non-hazardous processes selective towards wanted products. This concept is called green chemistry [53–57]. The processes following the principles of green chemistry are often called green processes or green reactions and reagents that are used in such processes are similarly called green reagents [55]. The concept of green chemistry and the ideas associated to it are described in the next section. A green process of electrocatalytically producing dimethyl carbonate, a green reagent, was studied and is presented in this thesis.

1.1 Green chemistry

In the beginning of 1990s the concept of green chemistry was formulated as the design of chemical processes to reduce or eliminate the use of hazardous substances and avoid the formation of unwanted or undesirable waste products [54–57]. Green chemistry can also be defined as the development of processes that lead to economic profit while at the same time being benign towards the flora and fauna of our planet. Design is the most important aspect of green chemistry as it leads to novelty, efficiency and sustainability. The twelve principles of green chemistry were introduced in the 1990s as design guidelines for new chemical processes. These twelve principles were formulated as follows [56]:

1. **Prevention**. It is better to prevent waste than to treat or clean up waste after it has been created.

2. **Atom Economy**. Synthetic methods should be designed to maximize the incorporation of all materials used in the process into the final product.

3. **Less Hazardous Chemical Syntheses**. Wherever practicable, synthetic methods should be designed to use and generate substances that possess little or no toxicity to human health and the environment.

4. **Designing safer chemicals**. Chemical products should be designed to affect their desired function while minimizing their toxicity.

5. **Safer Solvents and Auxiliaries**. The use of auxiliary substances (e.g., solvents, separation agents, etc.) should be made unnecessary wherever possible and innocuous when used.

6. **Design for Energy Efficiency**. Energy requirements of chemical processes should be recognized for their environmental and economic impacts and should be minimized. If possible, synthetic methods should be conducted at ambient temperature and pressure.

7. **Use of Renewable Feedstocks**. A raw material or feedstock should be renewable rather than depleting whenever technically and economically practicable.

8. **Reduce Derivatives**. Unnecessary derivatization (use of blocking groups, protection/deprotection, temporary modification of physical/chemical processes) should be minimized or avoided if possible, because such steps require additional reagents and can generate waste.

9. **Catalysis**. Catalytic reagents (as selective as possible) are superior to stoichiometric reagents.

10. **Design for Degradation**. Chemical products should be designed so that at the end of their function they break down into innocuous degradation products and do not persist in the environment.

11. **Real-time analysis for Pollution Prevention**. Analytical methodologies need to be further developed to allow for real-time, in-process monitoring and control prior to the formation of hazardous substances.

12. **Inherently Safer Chemistry for Accident Prevention**. Substances and the form of a substance used in a chemical process should be chosen to minimize the potential for chemical accidents, including releases, explosions, and fires.

1.2 Catalysis

Catalysis is the phenomenon of increasing reaction rates by adding materials, called catalysts, into the reactor where the reaction occurs [53, 58–60]. A catalyst increases the rate of a reaction without being consumed by it. Besides giving high reaction rates, a good catalyst also avoids unwanted products by being selective towards desired products. Catalysts speed up reactions by bringing the reactants in a configuration from which it is favorable for them to react. During a chemical reaction reactants have to pass through a transition state before being converted to products. The transition state can be thought of as an activated complex with the amount of energy needed for product formation. Using a catalyst decreases the energy required to form the activated complex. A simple scheme explaining this concept is shown in figure 1.1.

If the activated complex is to decompose to products, an amount of energy called the activation energy, E_a, is required. In case the reactants collide and form an activated complex with an energy lower than the activation energy, the complex will shortly after break up into the initial reactants. On the other hand, if the activated complex has an energy value equal or greater than the activation energy, the activated complex will shortly after turn into the products. Using a catalyst leads to a decrease in the activation energy which in return increases the rate of the reaction. In other words, a lower activation energy of a given reaction makes it easier for the reactants to react and form products. One can think of this as trying to throw tennis balls over two different walls. The first wall is very tall

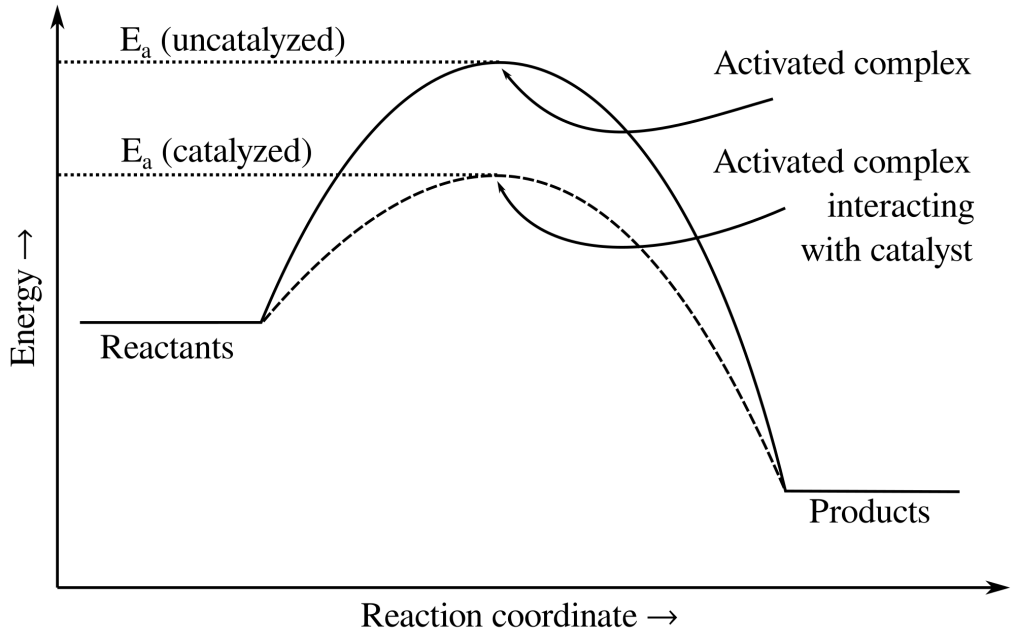

Figure 1.1: Scheme showing that the use of a catalyst lowers the activation energy of a reaction. Adapted from Pauling's general chemistry [60].

and represents the situation with no catalyst, while the second wall is shorter and represents the situation when using a catalyst. It is obviously easier to throw the tennis ball over the short wall than the tall wall. This also means that when throwing balls over each wall for the same period of time with the same effort, one will throw more balls over the short wall than the tall wall. In such an analogy the height of each wall represents the activation energy of the uncatalyzed (tall wall) and catalyzed (short wall) reaction. The effort with which the ball is thrown represents the temperature at which the reaction is preformed as well as the attempt frequency (number of collisions of the reactants), while the number of balls that were successfully thrown over the wall represents the rate or turnover frequency of the reaction (number of successful conversions from reactant to product in a given period of time on a given catalyst surface area).

In order to describe catalysis further let us introduce the mathematical expression for the reaction rate constant of an elementary step of a reaction:

$$k = Ae^{-E_a/(k_B T)} \tag{1.1}$$

This is known as the Arrhenius expression [53, 58–60]. A is the attempt frequency and it indicates how many collisions or attempts of the reactants reacting into products there are in a given period of time, E_a is the activation energy, k_B is the Boltzmann constant and T is the temperature at which the reaction is occurring. The rate of the reaction or the turnover frequency is proportional to the reaction rate constant. It can be seen from equation 1.1 that larger activation energies lead to smaller reaction rate constants which in return leads to a low reaction rate or turnover frequency. As the reaction rate constant changes

exponentially with the activation energy, even small changes of the activation energies lead to significant changes in the reaction rate constant and reaction rate. One can think of the exponential part, $e^{-E_a/(k_B T)}$, in equation 1.1 as a weight parameter which defines how many of the reactant collisions or reaction attempts result in a successful reaction. According to this, higher activation energies lead to a higher weight on unsuccessful collisions. Suppose the activation energy of a given reaction was 0. In that case the exponential part of equation 1.1 becomes 1. This means that all the collisions of reactants or attempts at reacting lead to a successful conversion of reactants to products. From this mathematical analysis one can clearly see the idea behind catalysis. By using a catalyst that will minimize the activation energy of a given reaction it is possible to significantly increase the rate of a reaction, thus, it is not surprising that the chemical industry is largely based on catalytic processes. About 85-90 % of all chemical products are made in catalytic processes such as cracking and hydrotreating of oil, various polymerization processes, steam reforming, methanation, ammonia synthesis and oxidation of various gases in car exhausts [53].

Catalysis occurs in a very wide length scale [53]. As such, catalysis is studied by a wide community of engineers and scientist from various fields such as chemistry, physics and material science. On a macroscopic scale, catalysis occurs in reactors that make up an operating process plant or a lab setup. At this scale engineers design reactors and control process parameters in order to optimize the yield of the process. At the millimeter scale, catalysis occurs on catalyst pellets for which it is important to optimize the shape, porosity and strength so that they can cope with the conditions inside the reactor. On the micrometer scale, in the pores of a support material, the catalytically active particles are found. On this scale the parameters of interest are the shape, structure and size of the active particle and their relation to catalytic activity. The smallest and fundamental length scale of catalysis is the atomic scale (angstroms). Here, the focus is on understanding reactions in terms of breaking and forming bonds with the goal of finding the underlying physical and chemical rules of catalysis and later using this knowledge to design future catalysts. This is the length scale of catalysis studied in this thesis.

Catalysis can be divided into various sub-disciplines depending on the nature of the catalyst itself [53, 58–60]. The most common distinction is between homogeneous, heterogeneous and biocatalysis. In homogeneous catalysis, both the catalyst and reactants are in the same phase. Most commonly the catalyst and reactants are in liquid phase. In biocatalysis, catalysts are called enzymes. These are large proteins with very specific shapes which allow selectivity towards specific reactions as this is very important in biological systems. In heterogeneous catalysis the catalyst is solid while the reactants are in gas or liquid phase. The solid catalyst serves as a surface for the reactants to adsorb onto and react further, in that way decreasing activation energies.

As an example, heterogeneous catalysis on the atomic scale can be described using the following hypothetical reaction:

$$A_2 + 2B \leftrightarrow 2AB \tag{1.2}$$

A molecule in gas phase, A_2, reacts with two atoms in gas phase, B, to give two molecules

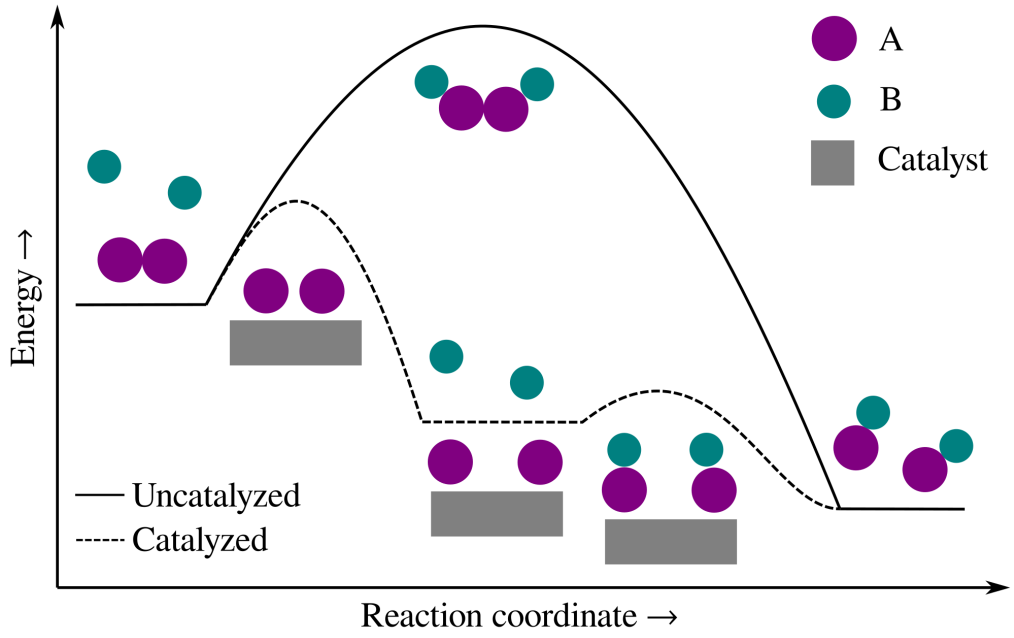

Figure 1.2: Diagram of a hypothetical reaction catalyzed by a solid catalyst.

in gas phase, AB. Let us write a series of elementary steps that add up to the considered reaction. Elementary steps can be thought of as reactions that cannot be simplified further by dividing them into multiple steps. The first step of the hypothetical reaction will be the dissociation of an A_2 molecule on the surface of a solid catalyst into two A atoms. This type of elementary surface reaction mechanism is called the Langmuir-Hinshelwood mechanism. In the second step, one B atom will adsorb directly on one of the A atoms formed in the previous step, in that way forming AB. This type of elementary surface reaction mechanism is called the Eley-Rideal mechanism. This step happens twice to give two AB molecules. The two elementary steps can be written as follows:

$$A_2 + 2* \leftrightarrow 2A^* \tag{1.3}$$

$$B + A^* \leftrightarrow AB + * \tag{1.4}$$

Here, $*$ represents a site on the surface of the catalyst. If $*$ is in the superscript of a given species it means that it is adsorbed. For example, A^* is an A species adsorbed on the surface. A hypothetical diagram for the process is given in figure 1.2. It can be seen from this example how the use of a catalyst enables a different reaction path to be taken, a path that facilitates the conversion from reactants to products.

As can be seen from figure 1.2, in order to describe a given catalytic process we are dealing with energies of various configurations of atoms and molecules. Chapter 2 explains how these energies can be calculated by using supercomputers and software implementation [61, 62] (computer code) of various theoretical concepts, more precisely, herein, density functional theory is used.

Chapter 3 explains how the calculated energies can be used in order to qualify different catalysts in terms of activity as well as quantifying rates of reactions. It introduces concepts related to catalysis such as adsorption energies, surface equilibrium, surface coverage, adsorption isotherms, kinetics and scaling relations.

1.3 Electrocatalysis

Electrocatalysis is very similar to heterogeneous catalysis in terms of how the surface of the solid catalyst enables an alternative reaction path to be taken. The difference is that, in electrocatalysis, energies of various elementary steps can be controlled by applying a potential difference on the electrodes (electrocatalysts) [53, 58]. This is possible if the reaction mechanism consists of elementary steps that are redox reactions. In redox reactions, reactants get reduced or oxidized and there is an exchange of ions and electrons. Therefore, electrocatalysis is closely related to electrochemistry. Not all of the elementary steps in an electrocatalytic process have to be potential dependent steps (electrochemical steps). Some steps may be potential independent (chemical steps) as well.

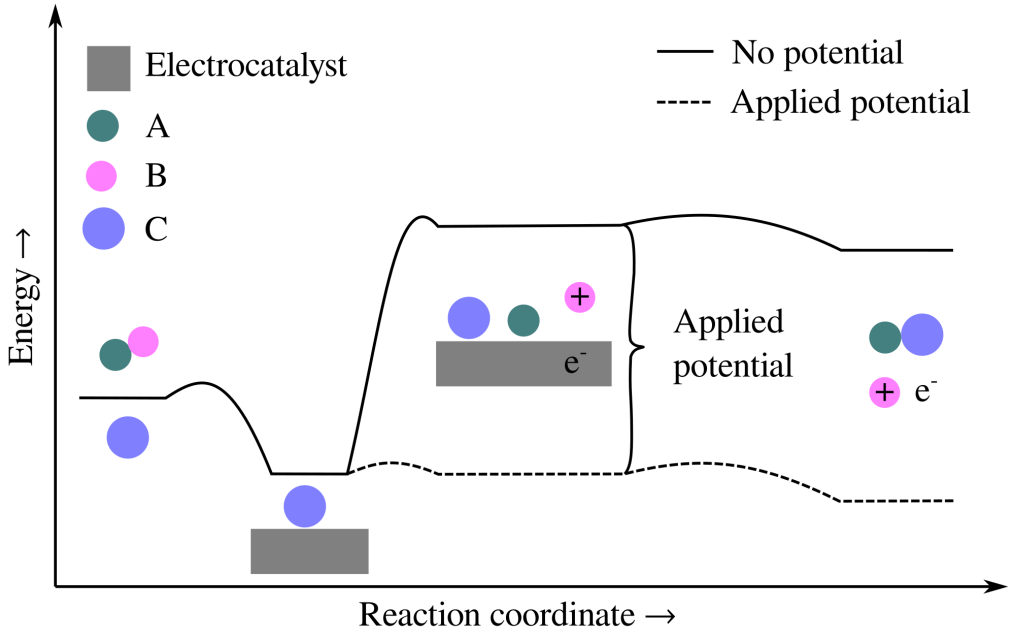

Figure 1.3: Diagram of a hypothetical electrocatalytic process at no potential (solid) and with an applied potential needed to drive the reaction (dash).

To get a better idea on how electrocatalysis differs from standard heterogeneous catalysis, consider the following reaction:

$$AB + C \leftrightarrow AC + (B^{+} + e^{-}) \tag{1.5}$$

One can see that an ion and electron pair have been formed as part of this process. This makes it a potential dependent, or electrochemical, reaction. Let us assume the following elementary steps:

$$C + * \leftrightarrow C^* \tag{1.6}$$
$$AB + * \leftrightarrow A^* + (B^+ + e^-) \tag{1.7}$$
$$A^* + C^* \leftrightarrow AC + 2* \tag{1.8}$$

The first elementary step is a simple chemical adsorption step. In the second elementary step a molecule, AB, is oxidized and A is adsorbed on the surface while B becomes a cation. In the third elementary step A and C adsorbed on the surface combine to form AC. Figure 1.3 shows a diagram for such a process. By applying a potential it is possible to affect the chemical potential of the ion-electron pair in the second elementary step. This in return lowers the energy difference for the electrochemical step as seen in figure 1.3. One can also notice that applying potential does not change the energy of the first elementary step since it is not an electrochemical step. When no potential is applied the electrochemical step is uphill, which means that it is unfavorable for it to occur. Since it is not favorable for the electrochemical step to occur, no product will be formed. By applying potential, the position of the electrochemial step on the diagram is tuned. Therefore, a potential that is sufficient enough to make the electrochemical step, and in return the entire process, energetically favorable (downhill in energy) needs to be applied. From this picture one can see the true power of electrocatalysis as it is possible to perform reactions that were energetically unfavorable to begin with.

In chapter 3 it is explained how to take potential into account when studying electrocatalytic processes computationally, which is important when studying the electrochemical synthesis of compounds such as dimethyl carbonate.

1.4 Chemistry of dimethyl carbonate

Dimethyl carbonate (DMC) is an organic compound which is, at standard conditions, a flammable and colorless liquid with appearance similar to methanol [63–65]. It is used as a precursor and solvent in chemical synthesis but it can also be used as an electrolyte, fuel and fuel additive [63, 64, 66, 67]. The structure of DMC is shown in figure 1.4.

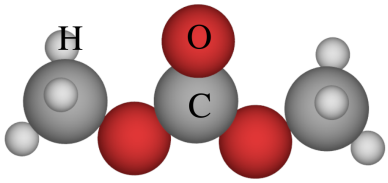

Figure 1.4: Structure of DMC.

DMC is considered a green reagent with the potential to replace toxic compounds which are nowadays used in various chemical processes, for example, it is possible to replace phosgene, dimethyl sulfate and methyl iodide which are used for carbonylation and

methylation reactions with alternative reactions using DMC [63–65, 68]. Using DMC results in a much cleaner, atom efficient and less hazardous process, complying with the principles of green chemistry. The following are examples of processes using dimethyl sulfate ($(CH_3)_2SO_4$), methyl iodide (CH_3I) and phosgene ($COCl_2$):

$$\begin{aligned} PhOH + (CH_3)_2SO_4 + NaOH &\leftrightarrow PhOCH_3 + NaCH_3SO_4 + H_2O && (1.9)\\ PhOH + CH_3I + NaOH &\leftrightarrow PhOCH_3 + NaI + H_2O && (1.10)\\ 2ROH + COCl_2 + 2NaOH &\leftrightarrow ROCOOR + 2NaCl + 2H_2O && (1.11) \end{aligned}$$

The following are examples of DMC ($CH_3OCOOCH_3$) substituting the toxic compounds:

$$\begin{aligned} PhOH + CH_3OCOOCH_3 &\leftrightarrow PhOCH_3 + CO_2 + CH_3OH && (1.12)\\ ROH + CH_3OCOOCH_3 &\leftrightarrow ROCOOCH_3 + CH_3OH && (1.13) \end{aligned}$$

Here, Ph denotes a phenyl group and R denotes a hydrocarbon chain.

Besides the methylation and carbonylation reactions shown above, DMC can also be used as precursor for the synthesis of aromatic polycarbonates [69–71]. DMC can be also used as an oxygenating agent in fuels, reducing vehicle emissions that are associated to environmental and health risks [72]. This is possible due to the high oxygen content in DMC as well as its good blending properties.

The method of producing DMC has changed throughout the years. The most notable process until the 1980s was phosgenation of methanol:

$$\begin{aligned} COCl_2 + CH_3OH &\leftrightarrow ClCOOCH_3 + HCl && (1.14)\\ ClCOOCH_3 + CH_3OH &\leftrightarrow CH_3OCOOCH_3 + HCl && (1.15) \end{aligned}$$

where the first reaction is fast and the second is slow. Producing DMC by phosgenation is a hazardous process, thus, an alternative method of producing DMC is required. A newer chemical method of producing DMC by avoiding the use of phosgene was developed by the Italian company Enichem[1]. This method involves a catalytic reaction of methanol with carbon monoxide and oxygen:

$$2CH_3OH + CO + \frac{1}{2}O_2 \leftrightarrow CH_3OCOOCH_3 + H_2O \quad (1.16)$$

Another chemical method used nowadays, developed by the Japanese Ube Industries, includes carbonylation of methyl nitrite using a palladium based catalyst:

$$\begin{aligned} 2NO + \frac{1}{2}O_2 &\leftrightarrow N_2O_3 && (1.17)\\ 2CH_3OH + N_2O_3 &\leftrightarrow 2CH_3ONO + H_2O && (1.18)\\ 2CH_3ONO + CO &\leftrightarrow CH_3OCOOCH_3 + 2NO && (1.19) \end{aligned}$$

[1] Nowadays called Syndial.

Other methods of producing DMC include transesterification of ethylene carbonate or urea, direct synthesis from methanol and carbon dioxide and alkylation of metal carbonates with organic halides [63–65, 68, 72].

Chemical methods of synthesizing DMC often include toxic precursors, waste products and explosive mixtures of carbon monoxide and oxygen, thus, failing at being classified as green processes. This calls for the development of a novel process of producing DMC that can avoid the use of hazardous chemicals or mixtures. Although usually requiring expensive electrocatalysts and an applied potential to operate, electrochemical methods avoid hazardous reaction conditions and satisfy the principles of green chemistry if the electricity comes from a renewable energy source like solar or wind.

It was shown that DMC can be made electrochemically using gold as the electrocatalyst material and applying a high potential [73, 74]:

$$2CH_3OH + CO \leftrightarrow CH_3OCOOCH_3 + H_2 \tag{1.20}$$

Additional methods for producing DMC involving more complex catalysts or reactor designs were also reported [75–82]. As part of this thesis, density functional theory simulations and experiments were performed in order to understand this electrocatalytic synthesis of DMC at the atomic scale, with the goal of finding a selective and efficient electrocatalyst.

1.5 Hydrodesulfurization catalysis

Hydrodesulfurization (HDS) is a catalytic process used to remove sulfur from oil [51, 52, 83]. The purpose of removing sulfur is to reduce SO_2 emissions that result from the combustion of sulfur containing fuels.

We can describe hydrodesulfurization with the following reaction:

$$RSH + H_2 \leftrightarrow RH + H_2S \tag{1.21}$$

Here, R is the main body of an organic molecule. We can see that, in HDS, an organic molecule containing sulfur reacts with hydrogen. The product of the reaction is an organic molecule with no sulfur and hydrogen disulfide. The process is performed at high temperatures (500-700 K) and high pressures (30-130 atm) with a high ratio of partial pressure of hydrogen to hydrogen disulfide. Reaction 1.21 seems very simple, but the complete mechanism of HDS is very complicated and its complexity increases with the complexity of the molecule that is being desulfurized [84–86].

Two reaction pathways have been proposed for HDS in the literature [84–86]. Let us define these reaction pathways and further illustrate them using the HDS of ethenethiol as example.

Direct desulfurization (DDS). In this pathway, the least amount of hydrogen required for removing sulfur from the sulfur containing organic molecule is used. The example for ethenethiol goes as follows:

$$CH_2CHSH + H_2 \leftrightarrow CH_2CH_2 + H_2S \tag{1.22}$$

It can be seen that the carbon-sulfur (C-S) bond of ethenethiol is cleaved by using only one molecule of hydrogen. In other words, the C-S bond of ethenethiol is cleaved after an initial hydrogenation step in which a hydrogen atom is transfered (from the catalyst's surface) to ethenethiol.

Hydrogenation (HYD). In this pathway, multiple hydrogenation steps are performed prior to the cleavage of the C-S bond. Using ethenethiol as example:

$$CH_2CHSH + H_2 \leftrightarrow CH_3CH_2SH \quad (1.23)$$

$$CH_3CH_2SH + H_2 \leftrightarrow CH_3CH_3 + H_2S \quad (1.24)$$

One can see that ethenethiol is initially turned into ethanethiol by hydrogenation. After that, ethanethiol is desulfurized directly. It is hypothesized that hydrogenation enables the molecule to interact with the catalyst in a way that facilitates the cleavage of the C-S bond with respect to the non-hydrogenated molecule.

HDS is performed by using MoS_2 particles promoted by cobalt (CoMoS) or nickel (NiMoS) as catalyst [87–101]. MoS_2 particles have a triangular shape[2], exposing the $10\bar{1}0$ edge, also called the M-edge. Promoting MoS_2 particles with nickel or cobalt truncates the triangular particles along the $\bar{1}010$ edge, also called the S-edge. This leads to hexagonal CoMoS or NiMoS particles as shown in fiugre 1.5.

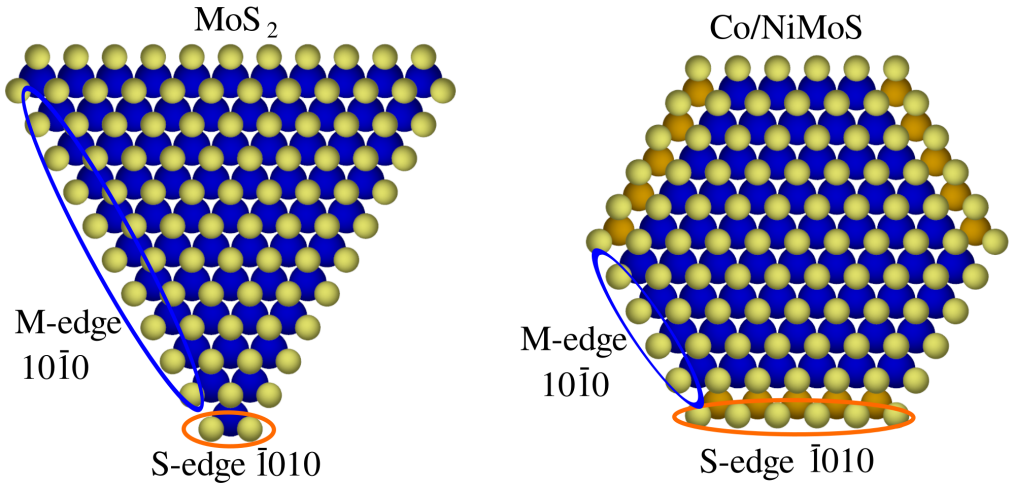

Figure 1.5: Model of unpromoted (left) and cobalt or nickel promoted (right) MoS_2 particles. Blue and yellow spheres represent molybdenum and sulfur atoms respectively, while orange spheres represent cobalt or nickel.

It was shown that the edges of MoS_2 and promoted MoS_2 particles have edges with metallic character [102, 103]. These edges appear is bright brims around the MoS_2 plane when studied with scanning tunneling microscopy [87, 90–92, 99, 101]. Various theoretical and experimental studies suggest that it is the edges of such particles that are active

[2]Hexagnoal MoS_2 particles have also been reported [101].

towards desulfurization while the basal plane is believed to be inert [85–89, 93, 94, 98–101, 104–106]. Although there are strong indications that HDS occurs on the edges, the exact mechanism of HDS is still not thoroughly understood. It is not completely clear whether sulfur vacancies at the edges are needed to perform desulfurization or if it is possible for molecules to get desulfurized simply by interacting with the brim. Furthermore, the role of corner sites has been largely overlooked until recent. These are some of the topics addressed in this thesis.

1.6 Hydrogen evolution

The hydrogen evolution reaction (HER), also known as hydrogen reduction reaction is an electrochemical half reaction in which protons are reduced into hydrogen [42, 107–109]. The HER is performed in acidic media by using platinum as catalyst material or in alkaline media by using less noble metals such as nickel. The HER most commonly occurs as the cathodic reaction during water electrolysis but it can occur as the cathodic reaction of other electrochemical processes, for example, during oxidation of sulfur dioxide to sulfuric acid [110]. Using water electrolysis in acidic media as an example, both half reactions can be written as follows:

$$\mathrm{C}: \quad 4(\mathrm{H^+} + \mathrm{e^-}) \leftrightarrow 2\mathrm{H_2} \tag{1.25}$$

$$\mathrm{A}: \quad 2\mathrm{H_2O} \leftrightarrow \mathrm{O_2} + 4(\mathrm{H^+} + \mathrm{e^-}) \tag{1.26}$$

$$\mathrm{C+A}: \quad 2\mathrm{H_2O} \leftrightarrow 2\mathrm{H_2} + \mathrm{O_2} \tag{1.27}$$

In hydrogen evolution, as in all electrochemical processes, the reduction reaction occurs on an electrode called cathode (C) while the oxidation reaction occurs on an electrode called anode (A). The two half reactions together result in the water splitting reaction (C+A).

The catalytic mechanism of the HER has been discussed in various studies and the following elementary reactions were determined as part of the HER mechanism:

$$\text{Volmer}: \quad (\mathrm{H^+} + \mathrm{e^-}) + * \leftrightarrow \mathrm{H^*} \tag{1.28}$$

$$\text{Tafel}: \quad 2\mathrm{H^*} \leftrightarrow \mathrm{H_2} + 2* \tag{1.29}$$

$$\text{Heyrovsky}: \quad \mathrm{H^*} + (\mathrm{H^+} + \mathrm{e^-}) \leftrightarrow \mathrm{H_2} + * \tag{1.30}$$

Here, * represents a site on the surface of the catalysts [108]. The first step in the HER is the so called Volmer step in which a proton-electron pair forms a hydrogen on the surface. In the second step of the HER, hydrogen is formed. This occurs through either the Tafel or the Heyrovsky reaction or perhaps through both. In the Tafel reaction, two adsorbed hydrogen atoms diffuse on the catalytst's surface and they form a hydrogen molecule upon meeting. This mechanism of evolving hydrogen is the electrochemical version of the already mentioned Langmuir-Hinshelwood mechanism in heterogeneous catalysis. In the Heyrovsky reaction, a proton from the electrolyte adsorbs directly onto a hydrogen atom already adsorbed on the surface of the catalyst and gets reduced to

hydrogen gas. This mechanism of evolving hydrogen is the electrochemical version of the already metnioned Eley-Rideal mechanism in heterogeneous catalysis.

It can be seen from these mechanisms that adsorbed hydrogen (H^*) is the only surface intermediate in the entire process. Based on the qualitative rule of Sabatier, an optimal catalyst for a given process should not interact with the reactants too strongly or too weakly. The interaction should be an intermediate one. It was established that, in the context of the HER, the Sabatier principle means that the optimal catalyst for the HER should neither bind hydrogen too strongly nor too weakly. Thus, the adsorption free energy of hydrogen under the conditions of the HER (298 K and 1 bar) should be 0 eV [107, 111]. This makes it possible to computationally search for good HER catalysts as the adsorption energy of hydrogen is the only value that needs to be calculated.

Due to the recent computational and experimental efforts it was found that MoS_2 and similar sulfides can be used as HER catalysts [111–117]. This holds great promise for the HER as such catalysts, that are often also used for HDS, are a potential replacement for platinum as electrocatalyst, one that is much cheaper and more abundant.

Chapter 2

Density functional theory

Density functional theory (DFT) is a method for calculating the ground state energy of an interacting system by mapping it to a simpler non-interacting system. But what does this mean and how does it look in practice? Imagine a black box that can take input from a user and, after some time, produce a result. The user does not have to know anything about what goes on inside the black box, except that it is performing some complex calculations. In DFT, the user sets up a system of atoms by defining the element associated to each atom (atomic number) as well as the position of each atom. This, along with some parameters that can be thought of as defining the precision and speed of the calculation, is the input for the black box. After the black box performs the calculation, the user is given a number. This number is the ground state energy of the system.

2.1 Schrödinger equation

At the atomic scale, the world is built out of negatively charged electrons and various types of positively charged nuclei. These basic particles interact by Coulomb (electrostatic) interactions. As illustrated in figure 2.1, using a hydrogen molecule as example, the electrons repel other electrons, nuclei repel other nuclei while nuclei and electrons attract each other.

The fundamental postulate of quantum mechanics is that a wavefunction, Ψ, exists for any system. Appropriate operators, $\hat{\upsilon}$ acting on the wavefunction return observable properties, e, of the system [118]:

$$\hat{\upsilon}\Psi = e\Psi \tag{2.1}$$

The operator that returns the energy of a system, E, is called the Hamiltonian operator, $\hat{H}$ [118–120]:

$$\hat{H}\Psi = E\Psi \tag{2.2}$$

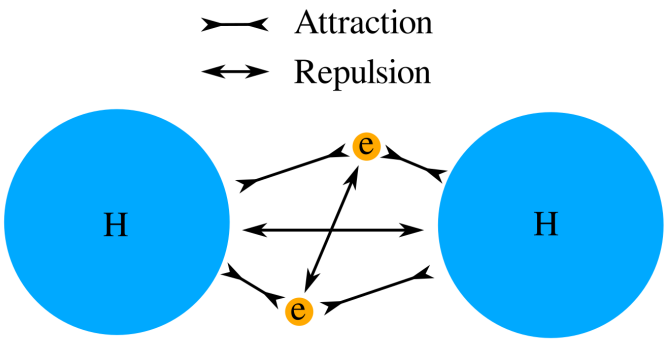

Figure 2.1: Interactions in a system of nuclei and electrons.

This is the Schrödinger equation[1]. The Hamiltonian operator:

$$\begin{aligned}\hat{H} = &-\sum_i \frac{\hbar}{2m}\nabla_i^2 - \sum_I \frac{\hbar}{2M_I}\nabla_I^2 - e^2 \sum_I \sum_i \frac{Z_I}{|r_i - R_I|} \\ &+ \frac{e^2}{2}\sum_I \sum_{J\neq I} \frac{Z_I Z_J}{|R_I - R_J|} + \frac{e^2}{2}\sum_i \sum_{j\neq i} \frac{1}{|r_i - r_j|}\end{aligned} \tag{2.3}$$

includes, in order of appearance, a kinetic energy term for the electrons, a kinetic energy term for the nuclei, a nuclei-electron attraction potential energy term, a nuclei-nuclei repulsion potential energy term and an electron-electron repulsion potential energy term. Here, i and j run over all the electrons, I and J run over all the nuclei, $\{r_i\}$ is a set of electron coordinates, $\{R_I\}$ is a set of nuclear coordinates, m is the mass of an electron, M_I is the mass of a nucleus I, e is the charge of an electron, Z_I is the atomic number of a nucleus I, and $\hbar$ is the reduced Planck constant.

Atomic nuclei are much heavier than individual electrons[2], thus, the electrons respond to changes in their surroundings faster than nuclei. This makes it possible to approach the equations governing quantum systems by separately solving the electronic part and finding the lowest energy state (ground state) for fixed positions of the atomic nuclei [118–120]. Such separate treatment of the electrons and nuclei is called the Born-Oppenheimer approximation. After the Born-Oppenheimer approximation and by using some shorthand notation the electronic Hamiltonian can be written as:

$$\hat{H} = -\frac{\hbar}{2m}\sum_i \nabla_i^2 + \sum_i V_i + \sum_i \sum_{i\neq j} U_{i,j} \tag{2.4}$$

where the first term is the kinetic energy of the electrons, the second term is the electron-nuclei interaction and the last term is the electron-electron repulsion.

Thinking about the electron-electron repulsion term, one can realize that each electron in the system depends on all the other electrons of the system and the electrons

[1]Time independent form.

[2]Protons and neutrons are ≈1800 times the mass of an electron.

cannot be treated individually[3] [118–120]. The wavefunction depends on $3N$ electron coordinates, 3 coordinates for each of the N electrons. A single water molecule contains 10 electrons and the wavefunction is a 30-dimensional function. This is the reason why the Schrödinger equation is very complex and difficult to solve and the wavefunction difficult to work with for any system with more than one electron. In catalysis one works with complex molecules and surfaces as well as molecules adsorbed on surfaces in systems containing even hundreds of atoms. Solving the Schrödinger equation and working with the wavefunction in this context is seemingly impossible.

The wavefunction is interpreted in terms of probability by squaring it, $|\Psi|^2 = \Psi^*\Psi$, where Ψ^* is the complex-conjugate of Ψ. This quantity, referred to as probability density or simply density, represents the probability that a set of N electrons has a given set of coordinates, $\{r_i\}$ [118–121]. Integrating the density over a region of space, τ, gives the probability, P_τ, of finding the system inside of τ:

$$P_\tau = \int_\tau |\Psi|^2 d\tau \tag{2.5}$$

In terms of individual electron wave functions, ψ_i, the density can be expressed as:

$$n = 2\sum_i \psi_i^* \psi_i \tag{2.6}$$

Here, n is the density, i goes over all the individual electron wave functions occupied by electrons. The term inside the summation represents the probability that an electron in an individual wave function is located at a given position, r. The factor of two appears because two electrons[4] occupy each orbital. The electron density, n, is a function of three coordinates regardless the number of electrons and it contains a great amount of information contained in the the full wave function [118–121]. The electron density is the central object in DFT.

2.2 Hohenberg-Kohn theorems

The Hohenberg-Kohn theorems describe how it is possible to use the electron density as the central object for solving the Schrödinger equation [118–120, 122].

Theorem I: the ground state energy is a unique functional of the electron density[5].

Theorem II: the electron density that minimizes the energy of the functional is the ground state electron density.

[3] A simple approximation to the full wavefunction is to express it as the product of single electron wavefunctions, $\Psi = \psi_1\psi_2\ldots\psi_N$, this is known as the Hartree product.

[4] Of opposite spin according to the Pauli exclusion principle.

[5] A functional is similar to a function, it takes a function as input and returns a number.

The first theorem means that there is a single ground state electron density corresponding to a ground state wave function. The ground state electron density uniquely determines the properties of a quantum system, including the energy. The importance of this theorem is that it shows that it is possible to find the ground state energy by working with the electron density (function of 3 variables) instead of the full wavefunction (function of $3N$ variables). Therefore, to find the ground state energy of a water molecule the problem is reduced from 30 dimensions to 3 dimensions. Although it shows that a functional of the electron density can be used to get the ground state energy, the theorem does not say what the functional form is.

The second theorem prescribes a way of finding the ground state energy if the functional form is known. This can be achieved by varying the electron density until the energy from the functional is minimized.

The functional described by the Hohenberg-Kohn theorems can be written in terms of single electron wavefunctions:

$$E[\{\psi_i\}] = E_{\text{known}}[\{\psi_i\}] + E_{XC}[\{\psi_i\}] \tag{2.7}$$

where $\{\psi_i\}$ is a set of single electron wavefunctions. The functional form was split into a term that is known, $E_{\text{known}}[\{\psi_i\}]$, and the rest of the unknown contributions, $E_{XC}[\{\psi_i\}]$, called exchange-correlation functional. The known part can be written as:

$$\begin{aligned} E_{\text{known}}[\{\psi_i\}] = &-\frac{\hbar}{m}\sum_i \int \psi_i^* \nabla^2 \psi_i d^3r + \int V n d^3r \\ &+ \frac{e^2}{2}\int\int \frac{nn'}{|r-r'|} d^3r d^3r' + E_{\text{ion}} \end{aligned} \tag{2.8}$$

with the terms, appearing in order, being the electron kinetic energies, the Coulomb interactions between the electrons and the nuclei, the Coulomb interactions between pairs of electrons, and the Coulomb interactions between pairs of nuclei.

2.3 Kohn-Sham equations

Kohn and Sham showed that the ground state electron density can be found by solving a set of equations in which each equation only involves a single electron [118–120, 123][6]:

$$\left[-\frac{\hbar^2}{2m}\nabla^2 + V + V_H + V_{XC}\right]\psi_i = \varepsilon_i \psi_i \tag{2.9}$$

where V is the interaction between an electron and the atomic nuclei, V_H is the Hartree potential and V_{XC} is the exchange-correlation contribution to the single electron equations. The Hartree potential is defined as:

$$V_H = e^2 \int \frac{n'}{|r-r'|} d^3r' \tag{2.10}$$

[6]The solution of the Kohn-Sham equations are single electron wave functions depending on 3 spatial variables.

and it describes the Coulomb repulsion between the electron in one of the Kohn-Sham wavefunctions and the total electron density. This also means that the Hartree potential includes a self-interaction contribution since the electron in one of the Kohn-Sham wavefunctions is also contained in the total electron density. In other words, V_H includes interaction between the electron and itself. Correction to this self interaction is included in V_{XC}. V_{XC} is obtained as a functional derivative of the exchange-correlation energy, E_{XC}:

$$V_{XC} = \frac{\delta E_{XC}}{\delta n} \tag{2.11}$$

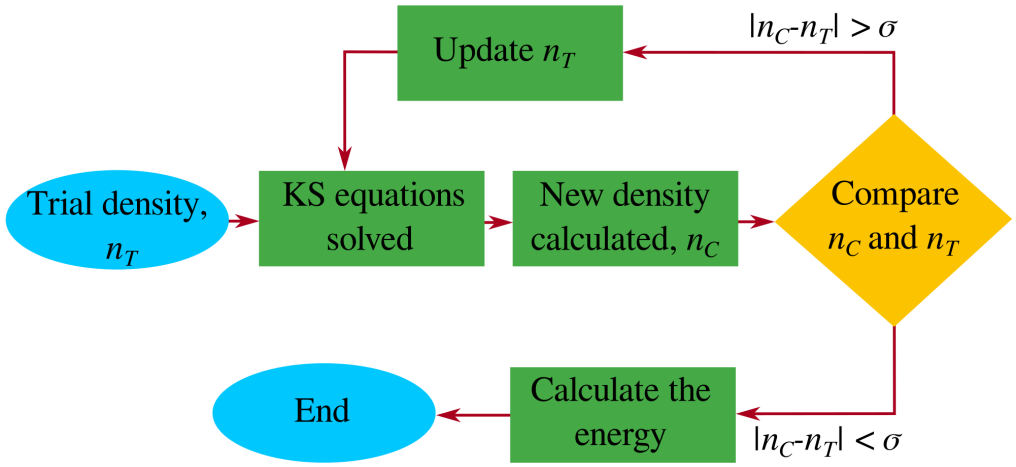

Figure 2.2: Diagram illustrating the iterative process of solving the Kohn-Sham equations self-consistently. n_T is the trial density, n_C is the calculated density, σ defines the deviation or accuracy when comparing n_T and n_C.

To solve the Kohn-Sham equations, the Hartree potential is required. To obtain the Hartree potential, the electron density is required. To get the electron density, single electron wavefunctions are needed. To obtain single electron wavefunctions the Kohn-Sham equations have to be solved. This circular problem is solved using the following iterative algorithm, further illustrated in figure 2.2:

1. An initial trial density is defined.
2. The Kohn-Sham equations are solved using the trial density and the single electron wavefunctions are found.
3. The electron density is calculated from the single electron wavefunctions.
4. The calculated density is compared to the initial density. If they are the same, within some deviation σ, self-consistency is reached and the density corresponds to the ground state electron density which can be used to compute the ground state energy. Otherwise, the initial electron density is updated and the iterative process starts again from step 2.

2.4 Exchange-correlation functional

In order to solve the Kohn-Sham equations, the exchange-correlation functional must be specified. The exchange-correlation functional is unknown, but it can be derived for a homogeneous electron gas. The homogeneous electron gas can be thought of as a cloud of electrons that has constant electron density for all points in space [119, 120]. Real systems have variations in the electron density so the homogeneous electron gas might appear to be of limited value. Still, the homogeneous electron gas provides a simple way to solve the Kohn-Sham equations. At each point in a system of interest, the exchange-correlation potential is set to be the known exchange-correlation potential of the homogeneous electron gas using the electron density of the system of interest:

$$V_{XC} = V_{XC}^{el.\ gas}[n] \tag{2.12}$$

Such an approximation uses the local density to define the exchange-correlation functional, thus, it is called the local density approximation (LDA). The LDA makes it possible to define and solve the Kohn-Sham equations but the result from these equations does not exactly correspond to the solution of the Schrödinger equation since the true exchange-correlation functional was not used.

The LDA is not the only functional used for DFT calculations. The most common set of functionals, particularly popular in computational catalysis, use information about the local electron density as well as the local gradient in the electron density. The approach of using the local gradient of the electron density is called generalized gradient approximation (GGA). There are many ways to include information for the gradient of the electron density, thus, there is a large number of GGA functionals [119, 120]. Different functionals give different results and some are better at describing particular properties than others. Therefore, the exchange correlation functional used in DFT calculations is often picked based on the problem being solved. Results contained in this thesis were obtained using the RPBE functional which is particularly good at describing chemisorption energies [124] and the BEEF-vdW [125] which can also capture long range vdW interactions [126–128].

A hierarchy of functionals that gradually include more and more physical information exists and GGA is only a step towards chemical accuracy[7]. Naturally, including more information leads to greater accuracy but also to longer computation times.

[7]Describing all these methods is not the topic of this thesis as the main focus is on catalysis. The reader interested in these methods can find more information from various sources [118–120].

Chapter 3

Computational approach to catalysis

This chapter describes how to use energies calculated from DFT simulations to obtain values used for describing catalytic properties. Additional concepts from catalysis as well as frameworks that make it possible to qualify and quantify catalytic properties in terms of simple parameters are presented.

3.1 Reaction energies

In order to describe how to calculate simple reaction energies from DFT, consider the following hypothetical reaction:

$$\mathrm{AB} + \mathrm{CD} \leftrightarrow \mathrm{AC} + \mathrm{BD} \tag{3.1}$$

Here, two molecules react to give two different molecules. In order to calculate the reaction energy, in other words, the change in energy when the reactants are converted to products, one first needs to perform four DFT calculations. These four DFT calculations consist of calculating the energy of each individual molecule in the reaction. Once these energies have been calculated it is possible to calculate the reaction energy by subtracting the sum of the reactant energies form the sum of the product energies as follows:

$$\Delta E = E_{AC} + E_{BD} - (E_{CD} + E_{AB}) \tag{3.2}$$

Here, E_x is the energy of a molecule x calculated from DFT [58, 119]. The calculated reaction energy, ΔE, describes the energy gained ($\Delta E < 0$) or energy required ($\Delta E > 0$) when going from reactants to products at zero kelvin[1].

Similarly, it is also possible to calculate reaction energies for adsorption reactions, in other words, adsorption energies of various species [58, 119]. This is essential for heterogeneous catalysis and electrocatalysis as these phenomenons occur on surfaces. Consider the following adsorption reaction:

$$\mathrm{A} + * \leftrightarrow \mathrm{A}^* \tag{3.3}$$

[1] Without taking in account the zero point energy.

where $*$ represents a site on the catalyst surface. The adsorption energy is calculated as:

$$\Delta E_{ads} = E_{A^*} - E_A - E_* \tag{3.4}$$

In general, the adsorption energy of any molecule can be calculated as:

$$\Delta E_{ads} = E_{mol+surf} - E_{mol} - E_{surf} \tag{3.5}$$

Here, $E_{mol+surf}$ is the calculated energy for a molecule adsorbed on a surface, E_{mol} is the calculated energy of a molecule and E_{surf} is the calculated energy of the catalyst's surface without a molecule adsorbed on it. Therefore, to calculate adsorption energies, one needs to set up three systems and perform three calculations, a surface, a molecule and a combination of the two (molecule adsorbed on the surface).

3.2 Potential energy diagram

When studying a number of reactions, for example, a series of elementary steps, it is useful to construct a potential energy diagram (PED). Let us assume that reaction 3.1 is a catalytic reaction occurring on the surface of a solid catalyst. Additionally, let us assume the following mechanism:

$$\mathrm{AB} + 2* \leftrightarrow \mathrm{A}^* + \mathrm{B}^* \tag{3.6}$$
$$\mathrm{CD} + 2* \leftrightarrow \mathrm{C}^* + \mathrm{D}^* \tag{3.7}$$
$$\mathrm{A}^* + \mathrm{C}^* \leftrightarrow \mathrm{AC} + 2* \tag{3.8}$$
$$\mathrm{B}^* + \mathrm{D}^* \leftrightarrow \mathrm{BD} + 2* \tag{3.9}$$

Using DFT, it is possible to calculate a reaction energy, ΔE, for each elementary reaction as described earlier. By plotting the energies one obtains a PED. A hypothetical PED for the process above is shown in figure 3.1. Adding all the elementary steps together results in equation 3.1, therefore, according to Hess's law [59][2], summing the reaction energies of all the elementary steps results with the same reaction energy as calculated with equation 3.2. This also means that the difference between the first and last line on the PED corresponds to the energy calculated from equation 3.2.

From the PED one can already roughly see whether the catalysis will work on a simulated surface. The first line in the example shown in figure 3.1 is the energy level of the reactants. The reactants are usually chosen as chemical reference and are consequently set to zero. One can see that all the steps are downhill in energy. Such a picture indicates that the conversion from AB and CD to AC and BD will be energetically favorable on the simulated surface. This is true as long as there is not a single energy level significantly uphill in energy so that it cannot be overcome by thermal energy ($k_B T$) at the operating conditions [53, 58].

[2]The energy change during the complete course of a chemical reaction is the same whether the reaction is made in one step or in several steps.

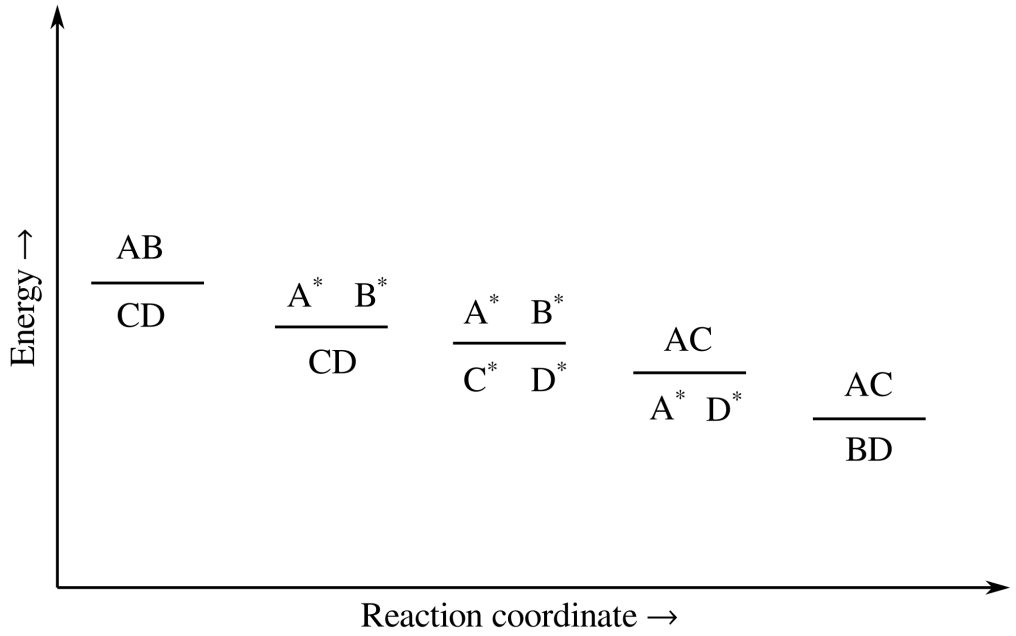

Figure 3.1: An example of a potential energy diagram for a hypothetical process.

It is important to mention that a PED as the one shown in figure 3.1 contains only thermodynamic data. This means that one can only see whether the process is thermodynamically favorable. Even if the process is thermodynamically favorable it is still possible for the process to be limited by kinetics [53, 58–60]. Between any two energy levels on the PED there is a energetic barrier associated to the activation energy required to pass through the transition state (form an activated complex with sufficient energy). If this barrier is sufficiently high, the process will be limited by unfavorable kinetics even though the thermodynamics might be favorable. It is possible to update the PED with these barriers by calculating the transition state energies between each level [58, 119]. Although calculating transition state energies gives a complete picture of the catalysis, doing so is sometimes not very practical since calculating transition state energies is often quite difficult and computationally demanding [58, 119, 129–131].

Energies calculated from DFT as well as the reaction energies obtained from them correspond to zero kelvin[3]. No catalytic process is performed at zero temperature. Furthermore, besides elevated temperatures, catalytic processes are often performed at elevated pressures with different partial pressures of the involved species. To construct energy diagrams that better describe real catalytic processes the electronic energies calculated from DFT have to be corrected with zero point energy, enthalpy and entropy contributions [53, 58, 119]. This in return gives free energies and the energy diagram constructed using free energies is called a free energy diagram. The following section explains how to obtain free energies from the electronic energies calculated in DFT.

[3]Without zero point energy corrections.

Regardless of not giving the full picture, simple PEDs are a good staring point for learning whether a catalyst could be useful for a given process. Looking at differences between two or more PEDs or between two or more simple reaction energies is often enough to determine energy trends for a series of catalysts. This is true because the contributions to the free energy do not change significantly by changing the catalyst. If a complete picture is required, energies are turned to free energies and further calculations of transitions state energies are performed [58, 119, 129–131].

3.3 From energy to free energy

In order to transform zero kelvin energies calculated with DFT into free energies that match a given set of temperatures and pressures relevant for the process that is being modeled, a series of contributions have to be added to the calculated zero kelvin energy.

The first correction is due to the Heisenberg uncertainty principle [58, 59, 119, 121]. It states that it is not possible to simultaneously predict the position and momentum of a quantum particle with arbitrary accuracy. In other words, the uncertainty in position, Δx, is related to the uncertainty in momentum, Δp:

$$\Delta x \Delta p \geq \frac{\hbar}{2} \tag{3.10}$$

where $\hbar$ is the reduced Planck constant. Lower uncertainty in the position of the particle leads to higher uncertainty in the momentum of the particle and vice versa. As a result, a quantum particle is prevented from being perfectly still at a specified position. This also causes some energy fluctuations around the local potential energy minimum. Such fluctuations are often accurately represented as harmonic vibrations, thus, allowing for simple corrections to the potential energy minimum to get an estimate of the ground state energy of a quantum system [58, 119]. Using DFT it is possible to calculate the vibrational frequencies of all the vibrational modes in the simulated system [118]. The correction to the potential energy minimum, called zero point energy (ZPE) correction, is given by:

$$ZPE = \sum_i \frac{1}{2} h \nu_i \tag{3.11}$$

where i is a specific vibrational mode, ν_i is the vibrational frequency of mode i and h is the Planck constant [58, 119]. The zero point energy corrected ground state energy is the sum of the DFT calculated energy and the ZPE correction:

$$E_0 = E_{DFT} + ZPE \tag{3.12}$$

At zero temperature, only the ground state is occupied, thus, the energy of the system is E_0. Increasing the temperature leads to the occupation of higher quantum states with a higher weight on low-energy states according to the Boltzmann distribution:

$$\frac{P(E_i)}{P(E_j)} = e^{-\frac{(E_i - E_j)}{k_B T}} \tag{3.13}$$

where E_i and E_j are energies of state i and j respectively, $\frac{P(E_i)}{P(E_j)}$ is the probability of finding energy state E_i occupied relative to E_j, k_B is the Boltzmann constant and T is the temperature. This means that at temperatures higher than 0 K the potential energy is not E_0 but is instead averaged over different quantum states [53, 58, 59, 118, 119]. The probability of the system being in a given quantum state i is:

$$P_i = \frac{e^{-\frac{E_i}{k_B T}}}{Z} \tag{3.14}$$

Here, Z is the canonical[4] partition function:

$$Z = \sum_i e^{-\frac{E_i}{k_B T}} \tag{3.15}$$

From a quantum-statistical mechanics perspective, internal energy can be defined as the thermally averaged energy of various occupied states:

$$U = \langle E \rangle = \sum_i P_i E_i = \frac{\sum_i E_i e^{-\frac{E_i}{k_B T}}}{Z} \tag{3.16}$$

Classically, the amount of heat that needs to be supplied to a system at constant volume in order to change its temperature by one degree is given by the constant volume heat capacity, C_v. The internal energy of the system can be expressed as the sum of the zero point energy corrected ground state energy and the thermal energy of the system:

$$U = E_0 + \int_0^T C_v dT \tag{3.17}$$

For systems that can change volume when heat is transferred, such as an ideal gas, enthalpy is used instead of internal energy as part of the thermal energy is lost as work:

$$H = E_0 + \int_0^T C_p dT \tag{3.18}$$

where C_p is the heat capacity at constant pressure [58, 59].

The change in enthalpy for a given process, ΔH, indicates whether the process gives out heat or consumes heat [59]. If $\Delta H < 0$ the reaction is exothermic, on the other hand, if $\Delta H > 0$ the reaction is endothermic. Exothermic reactions give out heat while endothermic reactions consume heat from the environment. Normally, one would expect that exothermic reactions occur spontaneously while endothermic reactions need to be supplied with energy (heat) in order to occur. Although this is true when the reaction

[4] A canonical system is a system in thermal contact with a heat reservoir.

is very exothermic, $\Delta H << 0$ or very endothermic, $\Delta H >> 0$, it is not necessarily true when the absolute value of ΔH is close to zero. Entropy is the second term that has an impact on whether it is favorable for a process to occur. Before discussing entropy, let us first discuss Gibbs free energy.

The key value in chemical thermodynamics is the Gibbs free energy [53, 58, 59]. The change in Gibbs free energy of a reaction indicates whether it is favorable for the reaction to occur:

$$\Delta G = \Delta H - T\Delta S \tag{3.19}$$

where ΔG is the change in Gibbs free energy, ΔH is the change in enthalpy, T is the temperature and ΔS is the change in entropy. If $\Delta G < 0$ then the process is thermodynamically favorable and it is expected that products will spontaneously form from reactants[5]. On the other hand, if $\Delta G > 0$ then the process is thermodynamically unfavorable and the products will not form. From equation 3.19 it can be seen that if $T\Delta S >> 0$ even endothermic reactions can occur spontaneously. By the same logic, if $T\Delta S << 0$ even exothermic reactions can be thermodynamically unfavorable.

The entropy, S, can be thought of as a measure of order or disorder:

$$S = k_B log\sigma \tag{3.20}$$

where k_B is the Boltzmann constant and σ is the number of microstates, in other words, the number of ways in which the building blocks of a system can be arranged [53, 58, 59]. A value close to zero is associated to very ordered systems (zero being the most ordered system achievable with only 1 microstate) while high entropy values are associated to disordered systems. A positive change in entropy of a system, $\Delta S > 0$, means that the system increased in disorder after the change. Similarly, a negative change in entropy of a system, $\Delta S < 0$, means that the system decreased in disorder after the change. The universe works in a way that all spontaneous processes are associated to an increase in entropy. Non-isolated systems are allowed to lose entropy as long as the entropy of the environment (universe) increases by at least the same amount. A popular example of explaining entropy is sandcastles. Sandcastles always crumble down to piles of sand with time. The opposite, piles of sand forming sandcastles on their own, never occurs[6]. There are many more microstates in a pile of sand than in a sandcastle (the grains of sand can be arranged in many more ways when in a pile of sand compared to a sandcastle). The same analogy holds true for chemical reactions where the reactants and products have different entropies. The change in entropy for a reaction is the difference between the entropy of the products and the entropy of the reactants. Reactions with $\Delta S >> 0$ are thus more likely to be spontaneous.

Finally, after introducing the relevant thermodynamic values, let us describe how one can calculate the adsorption free energy of a simple adsorption step in practice by using equation 3.3 as example. Assuming that A is an ideal gas, the free energy of A can be

[5] Assuming the process is not limited by kinetics.

[6] Time flows in the direction of increasing entropy.

expressed as:

$$G_A = E_A + ZPE_A + \Delta H_A^{0,T} - TS_A^T + k_B T ln\frac{p_A}{p^\circ} \tag{3.21}$$

where E_A is the DFT calculated energy of A, ZPE_A is the zero point energy correction of A, $\Delta H_A^{0,T}$ is the change in enthalpy of A when going from zero temperature to a temperature T, S_A^T is the entropy of A at a specific temperature T, k_B is the Boltzmann constant, p_A is the partial pressure of A and p° is the standard pressure (1 bar). E_A can be calculated using DFT. ZPE_A can be calculated by calculating vibrational frequencies with DFT and employing the harmonic approximation as described earlier. $\Delta H_A^{0,T}$ and S_A^T can usually be found in various thermochemical tables [59, 132, 133]. Alternatively they can be calculated from the calculated vibrational frequencies using the ideal gas approximation [118, 132] which is implemented as computer code [134]. The free energy of the adsorbate, A*, is calculated as:

$$G_{A^*} = E_{A^*} + ZPE_{A^*} + \Delta U_{A^*}^{0,T} - TS_{A^*}^T \tag{3.22}$$

Since we assume that adsorbates do not change in volume, the enthalpy term turns to internal energy[7]. $\Delta U_{A^*}^{0,T}$ and $S_{A^*}^T$ can be calculated from the vibrational frequencies of the adsorbate and using the harmonic approximation [134, 135] which is implemented as computer code [134]. For the surface, $*$, the zero temperature energy is normally used instead of the free energy:

$$G_* = E_* \tag{3.23}$$

Based on this, the adsorption free energy of A can be calculated as:

$$\Delta G_A = G_{A^*} - (E_* + G_A) \tag{3.24}$$

3.4 Scaling relations in catalysis

Suppose that a given catalytic process involves two surface species, A and B. In order to look for a suitable catalyst for the given process one might consider calculating the adsorption energies of A and B on a range of different surfaces. Let us assume that the adsorption energies of A and B have been calculated for five different surfaces, denoted as S_1, S_2, S_3, S_4 and S_5. By plotting the relation between the calculated adsorption energies on the considered surfaces one can find whether a linear scaling relation exists [58]. A graph giving an example of a hypothetical linear scaling relation between adsorption energies of A and B is shown in figure 3.2.

The scaling relation means that if surface S_2 binds adsorbate A weaker than surface S_1, it will at the same time bind adsorbate B weaker than surface S_1. Scaling relations usually occur between species that bind to a surface in a similar way. For example, adsorption energies of CH_3, CH_2, CH and C all scale with each other since they all bind on the surface through a carbon atom. The same logic applies to NH_2, NH and N or O and OH or S and SH etc [136, 137].

[7] Turning this into Helmholtz free energy; $A = U - TS$.

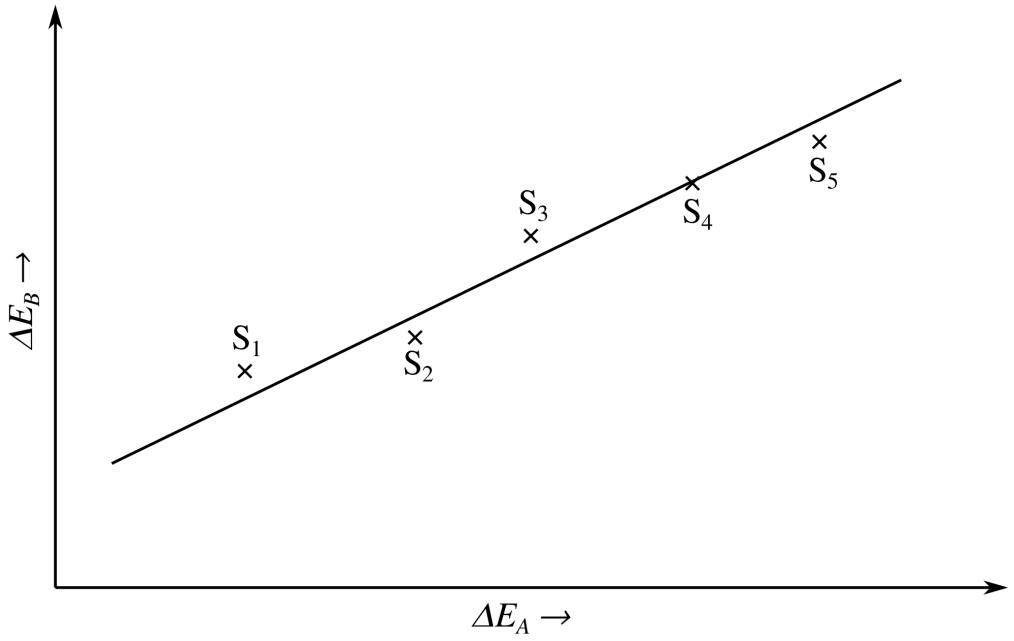

Figure 3.2: Example of a linear scaling relation between two hypothetical adsorbates (A and B) on a series of surfaces (S_1, S_2, S_3, S_4 and S_5).

The benefit of scaling relations is that it is possible to reduce the complexity of modeling various catalytic processes by decreasing the number of parameters one has to work with [58]. From the previous example it can be seen that, since there is a linear scaling relation between A and B, it is possible to express the adsorption energy of A in terms of the adsorption energy of B and vice versa. For example, it is possible to express the adsorption energy of B as:

$$\Delta E_B = a\Delta E_A + b \tag{3.25}$$

where a is the slope of the linear scaling relation and b is the intercept on the y-axis. In the case of ammonia synthesis, where one in principle needs to consider adsorption energies of multiple surface species (NH_3, NH_2, NH, N, H), it is possible to reduce the complexity to a single parameter (adsorption energy of nitrogen) because of scaling relations [138].

Scaling relations also pose some fundamental issues when trying to optimize catalytic reactions. Assume that surface S_2 is optimal for a given process in terms of how strongly it binds adsorbate A. Also assume that it possible to further improve the process by decreasing the adsorption energy of B (towards more negative values). Changing to a catalyst that binds B stronger (S_1), in order to decrease the adsorption energy of adsorbate B, also causes the adsorption energy of A to decrease, thus, moving it away from the previously established optimum value for the adsorption energy of A. Therefore, it is not straightforward to independently optimize adsorption energies of two surface species that follow a linear scaling relation [139, 140]

Similarly to scaling relations for adsorbed surface species there are also scaling relations between reaction energies and activation energies (scaling relations between ad-

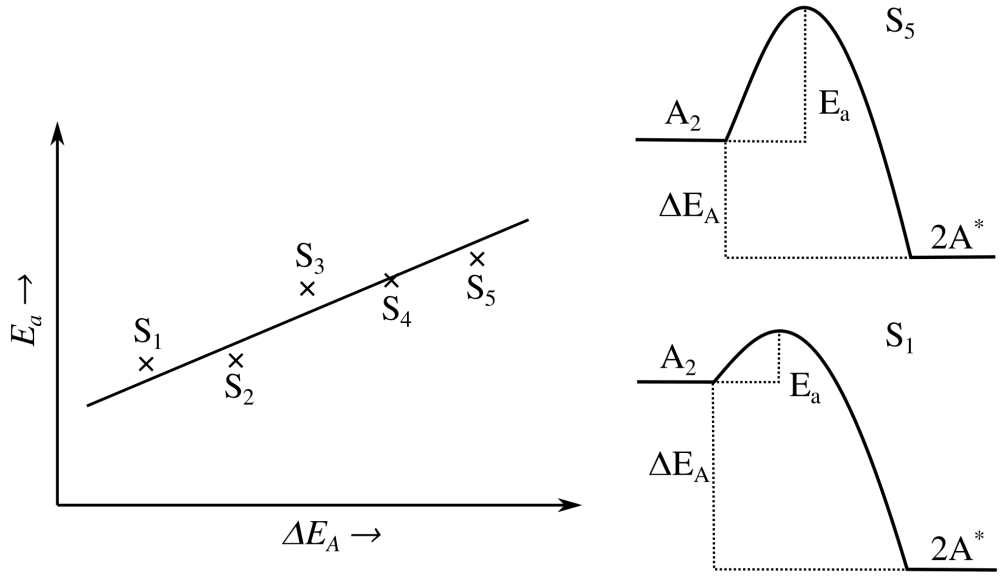

Figure 3.3: Example of a BEP scaling relation between activation energy (transition state energy) and reaction energy (adsorption energy).

sorption energies and transition state energies). Such scaling relations are named BEP relations in honor of Brønsted, Evans and Polanyi [53, 58, 141]. Consider the dissociation of a molecule, A_2, on a surface:

$$A_2 + 2* \leftrightarrow 2A^* \tag{3.26}$$

If such a process follows a BEP relation so that:

$$E_a = a\Delta E_A + b \tag{3.27}$$

then going to a surface that has a more negative adsorption energy, ΔE_A, the activation energy (transition state energy) will decrease as well. This is illustrated by the graphs in figure 3.3, where the activation energy on the more reactive surface S_1 has a lower activation energy due to the greater driving force (more negative ΔE_A) compared to a less reactive surface, such as S_5.

3.5 Equilibrium, reaction rates and kinetics

A reaction reaches equilibrium when the amount of products formed and amount of products reverted back to reactants is equal for a given period of time [53, 58–60]. In other words, the forward reaction rate and backward reaction rate are equal. In terms of Gibbs free energy, equilibrium is reached when ΔG of a reaction is 0.

$$\Delta G = G_{\text{products}} - G_{\text{reactants}} = 0 \tag{3.28}$$

Based on this requirement it is possible to determine the equilibrium concentrations, pressures or surface coverage of species for a given reaction. For example, consider the following gas phase reaction:

$$\alpha \mathrm{A} \leftrightarrow \beta \mathrm{B} \tag{3.29}$$

where α and β are stoichiometric coefficients. The change in free energy at equilibrium is given as:

$$\Delta G = \Delta G^{\circ} + k_B T ln\left(\frac{p_B^{\beta}}{p_A^{\alpha}}\right) = 0 \tag{3.30}$$

where ΔG° is the change in free energy at 1 bar. Therefore, it follows that:

$$\left.\frac{p_B^{\beta}}{p_A^{\alpha}}\right|_{eq} = e^{\frac{-\Delta G^{\circ}}{k_B T}} = K_{eq} \tag{3.31}$$

where K_{eq} is the equilibrium constant of the reaction. For low equilibrium constants, the reaction is shifted towards the reactants (very little or no products present) and at large equilibrium constants it is shifted towards products. Changing the conditions (temperature, pressure or concentration) affects the equilibrium constant and in return determines whether the reaction is shifted towards products or reactants[8].

For a surface reaction it is possible to obtain the surface coverage of each species in a similar way. Let us once again consider adsorption of A on a surface, as shown in equation 3.3. There is an additional contribution to the adsorption entropy that was not shown in equation 3.22[9]. This term is associated to the different ways in which N_A adsorbates can fill N surface sites. Such a configurational entropy depends on the coverage, $\theta_A = \frac{N_A}{N}$, and it is given by the following relation:

$$S^{conf} = -k_B ln\left(\frac{\theta_A}{\theta_*}\right) \tag{3.32}$$

where θ_A is the coverage of the surface with A and θ_* is the coverage of the surface with empty (free) sites [58]. From the requirement that $\Delta G = 0$ at equilibrium and that the

[8] This is known as the Le Chatelier's principle [59].

[9] Equation 3.22 assumes that the surface is covered by half a monolayer of A so that the configurational entropy is 0.

summed coverage of all species has to be unity, $\sum_i \theta_i = 1$, it follows that:

$$\Delta G = \Delta G^\circ + k_B T ln\left(\frac{\theta_A}{\theta_*}\right) - k_B T ln\left(\frac{p_A}{p^\circ}\right) = 0 \tag{3.33}$$

$$\left(\frac{\theta_A}{\theta_*}\right)\left(\frac{p_A}{p^\circ}\right)^{-1} = e^{-\frac{\Delta G^\circ}{k_B T}} = K_A \tag{3.34}$$

$$\theta_A + \theta_* = 1 \tag{3.35}$$

$$\theta_* = \frac{1}{1 + K_A \frac{p_A}{p^\circ}} \tag{3.36}$$

$$\theta_A = \frac{K_A \frac{p_A}{p^\circ}}{1 + K_A \frac{p_A}{p^\circ}} \tag{3.37}$$

Such an expression, giving the equilibrium coverage of a surface intermediate as a function of pressure and the standard Gibbs free energy, ΔG°, is called a Langmuir isotherm [53, 58, 59]. Similarly, Langmuir isotherms for multiple surface species competing for free sites can be derived.

As the fundamental goal in catalysis is to speed up the reaction rate where the reactants and products are not in equilibrium, it is sometimes necessary to go beyond energy diagrams and equilibrium to study reaction rates and model the kinetics of a given process. So far an Arrhenius expression for the reaction rate constant was given in terms of a prefactor and the activation energy. From harmonic transition state theory[10] an expression for the prefactor can be obtained:

$$A = \frac{k_B T}{h} e^{\frac{\Delta S^\circ_{TS}}{k_B}} \tag{3.38}$$

where ΔS°_{TS} is the change in entropy for going from an initial state to a transition state. Therefore, the Arrhenius expression can be written as:

$$k = \frac{k_B T}{h} e^{\frac{-\Delta G^\circ_{TS}}{k_B T}} \tag{3.39}$$

where ΔG°_{TS} is the change in Gibbs free energy for going from an initial state to a transition state [53, 58].

Let us show how the kinetics of a process consisting of a series of elementary steps can be modeled [53, 58][11]. Consider the following elementary steps:

$$\mathrm{A} + * \quad \leftrightarrow \quad \mathrm{A}^* \tag{3.40}$$

$$2\mathrm{A}^* \quad \leftrightarrow \quad \mathrm{A}_2 + 2* \tag{3.41}$$

[10] The topics of transition state theory and harmonic transition state theory will not be discussed herein. The reader further interested in this topic can find it in various sources [53, 58, 119].

[11] This approach is called microkinetic modeling.

leading to the full reaction:

$$2\mathrm{A} \leftrightarrow \mathrm{A}_2 \tag{3.42}$$

Two gas species, A, adsorb on a surface, *, and recombine into a dimer, A_2. The rates of the elementary steps are:

$$R_1 = r_1 - r_{-1} = k_1 p_A \theta_* - k_{-1}\theta_A \tag{3.43}$$
$$R_2 = r_2 - r_{-2} = k_2 \theta_A^2 - k_{-2} p_{A_2} \theta_*^2 \tag{3.44}$$

where r_i and r_{-i} are rates in the forward and backward direction of reaction i. Both elementary steps influence the coverage of A which means that they have to be solved simultaneously to obtain the total rate [53, 58]. In terms of the time dependence of the coverage of A, a differential equation can be written[12]:

$$\frac{\delta \theta_A}{\delta_t} = R_1 - 2R_2 \tag{3.45}$$

Solving this differential equation leads to the coverage of A but also to the coverage of free sites since the coverage must add up to unity. In real reactors the pressure and temperature is not constant throughout the reactor but when modeling the kinetics it is very useful to assume steady reaction conditions. This means that a part of the reactor where the pressure and temperature are constant is being described. Due to this assumption, the differential equation is simplified as the rate constants and partial pressures are not time dependent [53, 58].

Further simplification of the differential equation can be introduced by assuming steady state. It assumes that there is no change in coverage for all surface species [53, 58].

$$\frac{\delta \theta_i}{\delta t} = 0 \tag{3.46}$$

This turns the differential equation into a time independent problem simpler to solve. In the present example, assuming steady state gives:

$$R_1 - 2R_2 = k_1 p_A \theta_* - k_{-1}\theta_A - 2k_2 \theta_A^2 + 2k_{-2} p_{A_2} \theta_*^2 = 0 \tag{3.47}$$

leading to a steady state coverage of A.

For many catalytic reactions the overall rate is limited by one elementary step which is hard to carry out (energetically unfavorable step or high activation energy). For such an elementary step reaching equilibrium is more difficult than for the rest of the elementary steps [53, 58]. This elementary step is referred to as the rate determining or rate limiting step. It is now useful to introduce the concept of reversibility for an elementary step, γ_i. Reversibility is the rate of the backward reaction divided by the rate of the forward reaction and it indicates whether the flow of the reaction is in the forward direction ($\gamma_i < 1$), backward direction ($\gamma_i > 1$) or if the reaction reached equilibrium ($\gamma_i = 1$). Assuming

[12] Reaction 1 creates one A^* and reaction 2 removes two A^*.

a rate determining step, j, means that all the other steps reach equilibrium, $\gamma_{i\neq j} = 1$. This assumption along with steady state and constant reaction conditions leads to an equation that can be solved analytically regardless of the initial complexity [53, 58]. The reversibilities in the present example are:

$$\gamma_1 = \frac{\theta_A}{\theta_* p_A} K_1^{-1} \tag{3.48}$$

$$\gamma_2 = \frac{\theta_*^2 p_{A_2}}{\theta_A^2} K_2^{-1} \tag{3.49}$$

Let us assume that the second elementary step in which two surface species A recombine into a dimer A_2 (Langmuir-Hinshelwood mechanism, or Tafel in electrochemistry) is rate determining. The first step reaches equilibrium and it follows that:

$$\gamma_1 = \frac{\theta_A}{p_A \theta_*} K_1^{-1} = 1 \tag{3.50}$$

From this and the requirement that the sum of the coverages is unity, the coverage of A and of free sites is obtained:

$$\theta_A = \frac{K_1 p_A}{1 + K_1 p_A} \tag{3.51}$$

$$\theta_* = \frac{1}{1 + K_1 p_A} \tag{3.52}$$

Finally, the rate of reaction is obtained from the rate of the rate-determining step and by using the reversibility of the overall reaction:

$$R = k_2 \theta_A^2 (1 - \gamma) = k_2 \left(\frac{K_1 p_A}{1 + K_1 p_A} \right)^2 \left(1 - \frac{p_{A_2}}{p_A^2} K_1^{-2} K_2^{-1} \right) \tag{3.53}$$

where γ is the reversibility of the overall reaction:

$$\gamma = \frac{p_{A_2}}{p_A^2} K^{-1} \tag{3.54}$$

Here, K is the equilibrium constant of the overall reaction expressed as a product of the equilibrium constants of each elementary step to the power of the number of times an elementary step needs to be carried out[13]:

$$K = K_1^2 K_2 \tag{3.55}$$

3.6 Sabatier principle and volcanos

The Sabatier principle[14] states that the interactions between the catalyst and surface species should not be too strong or too weak but just right [53, 58, 59]. There is thus

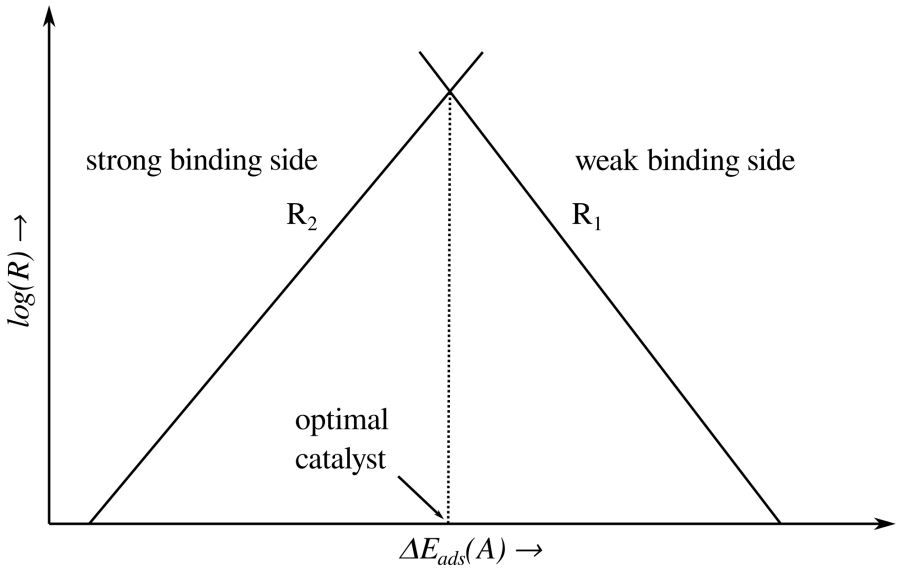

Figure 3.4: Sabatier volcano plot for a hypothetical reaction $2A \leftrightarrow A_2$.

an optimal adsorption energy of one or more surface species for any given process [107, 111, 139, 142, 143].

Let us use the same example as for the microkinetic modeling to describe the Sabatier principle but without assuming a rate limiting step. The reversibility of the overall reaction can be expressed in terms of the reversibilities of each elementary step:

$$\gamma = \gamma_1^2 \gamma_2 \tag{3.56}$$

where the exponent of two on γ_1 is because the first elementary step has to occur twice to satisfy the stoichiometry of the overall reaction. Assume that there are two types of surfaces, one binds the surface species A too strongly and the other one binds it too weakly. In between these two categories lies the optimal catalyst. On a surface that binds A too strongly the coverage of A will be high, $\theta_A \approx 1$. Because of that the desorption of A_2 will be the limiting step. Therefore, the first step in which A gets adsorbed will reach equilibrium. This means that:

$$\gamma_1 \approx 1 \tag{3.57}$$

$$\gamma_2 \approx \gamma \tag{3.58}$$

$$R = R_2 = k_2 \theta_A^2 (1 - \gamma) \tag{3.59}$$

On a noble surface that binds A very weakly the number of free sites will be high, $\theta_* \approx 1$. Therefore, the adsorption of A will be the rate limiting step and the second elementary

[13]The first elementary step has to be carried out twice.

[14]Named after the french chemist Paul Sabatier.

step will reach equilibrium.

$$\gamma_2 \approx 1 \tag{3.60}$$

$$\gamma_1 \approx \sqrt{\gamma} \tag{3.61}$$

$$R = R_1 = k_1 p_A \theta_* (1 - \sqrt{\gamma}) \tag{3.62}$$

The overall rate is therefore limited by the slowest elementary reaction:

$$R = min\Big\{R_1, R_2\Big\} = min\Big\{k_1 p_A \theta_* (1 - \sqrt{\gamma}), k_2 \theta_A^2 (1 - \gamma)\Big\} \tag{3.63}$$

The graphical result of such analysis is shown in figure 3.4. Such diagrams are often referred to as volcano plots due to their distinct shape. It can be seen that there is a weak and a strong binding side of the volcano on which the process is limited by the catalyst being too reactive or too noble. The top of the volcano corresponds to an optimal adsorption energy (of species A in this case). With this simple but powerful analysis it is possible to find new catalysts computationally by looking through a large number of surfaces that have an adsorption energy of A close to the top of the volcano.

3.7 Computational hydrogen electrode

Equilibrium between proton-electron pairs with gas phase hydrogen defines a potential. This potential is 0 relative to the standard hydrogen electrode (SHE) when the proton-electron pairs are in equilibrium with gas phase hydrogen at 1 bar, 298.15 K and a pH value of 0:

$$(\mathrm{H^+ + e^-}) \leftrightarrow \frac{1}{2}\mathrm{H_2} \tag{3.64}$$

The reversible hydrogen electrode (RHE) defines this potential to be 0 at any given pH. Therefore, the difference between the SHE and RHE scales corresponds to the free energy difference of going from pH zero to a different pH [58, 59]. By using the RHE it is possible to account for the effect of applied potential on the energy change of reactions that involve exchanging proton-electron pairs. This concept is called the computational hydrogen electrode (CHE) [58, 144] and can be illustrated with the following example. Assume the following reaction:

$$\mathrm{R^* + (H^+ + e^-) \leftrightarrow RH + *} \tag{3.65}$$

This is a potential dependent reaction since it involves a proton-electron pair. At standard conditions and a potential of 0 V vs RHE, the proton electron-pair on the left side of the equation is in equilibrium with gas phase hydrogen, thus, the reaction can be written as:

$$\mathrm{R^* + \frac{1}{2}H_2 \leftrightarrow R^* + (H^+ + e^-) \leftrightarrow RH + *} \tag{3.66}$$

From this it is straightforward to calculate the change in free energy at 0 V vs RHE since the chemical potential of the proton-electron pair can be replaced with the free energy of

hydrogen gas. To account for an applied potential a simple term is added to the change in free energy at 0 V vs RHE:

$$\Delta G_{U_{RHE}} = \Delta G^{\circ} + eU_{RHE} \tag{3.67}$$

where $\Delta G_{U_{RHE}}$ is the change in free energy at a given potential, U_{RHE} vs RHE, and ΔG° is the change in free energy without an applied potential at standard conditions. For the example given in equation 3.65 the change in free energy at a given potential can be written as:

$$\Delta G = G_{RH} + E_{*} - \frac{1}{2}G_{H_2} - G_{R^{*}} + eU_{RHE} \tag{3.68}$$

This concept can be used for any reaction involving transfer of protons and electrons.

Chapter 4

Summary of results

This chapter gives an overview of the scientific articles that were published, accepted or submitted for publication during and as a part of my studies. The results are presented in a descriptive and qualitative way which should allow the reader to get an idea about the key concepts and results from each article and how they relate to each other. This should allow for easier reading and understanding of the full articles included in chapter 5.

4.1 Paper I: Electrosynthesis of dimethyl carbonate

The chemical industry today is not sustainable as it is largely based on exploiting fossil fuels. Furthermore, hazardous precursors or reaction conditions are often employed in order to provide enough driving force for performing specific reactions. The chemical industry of tomorrow has to move away from such hazardous precursors and reaction conditions, turning towards renewable energy sources and environment friendly reagents, leading to a sustainable future. In electrocatalysis a potential difference provides the driving force needed to drive a reaction, thus, not requiring the use of hazardous agents and/or reaction conditions. Therefore, electrocatalysis holds great promise for the future of fuel and chemical production. The synthesis of DMC, which is normally performed in hazardous thermal processes with toxic precursors (phosgene) or explosive mixtures (carbon monoxide and oxygen), is one example of a chemical that can be made using an alternative electrocatalytic process (directly from methanol and carbon monoxide) [63–65].

It was shown that DMC can be produced electrochemically by using a gold electrode as electrocatalyst, also yielding dimethyl oxalate (DMO) as co-product [73, 74]. Although it was shown that the electrosynthesis is possible on gold, understanding of the underlying criteria defining the efficiency and selectivity of the process are lacking. What defines the potential required to produce DMC? What determines the selectivity between various co-products, most notably between DMC and DMO? Is it possible to use a different electrocatalyst in order to improve the efficiency and selectivity towards DMC?

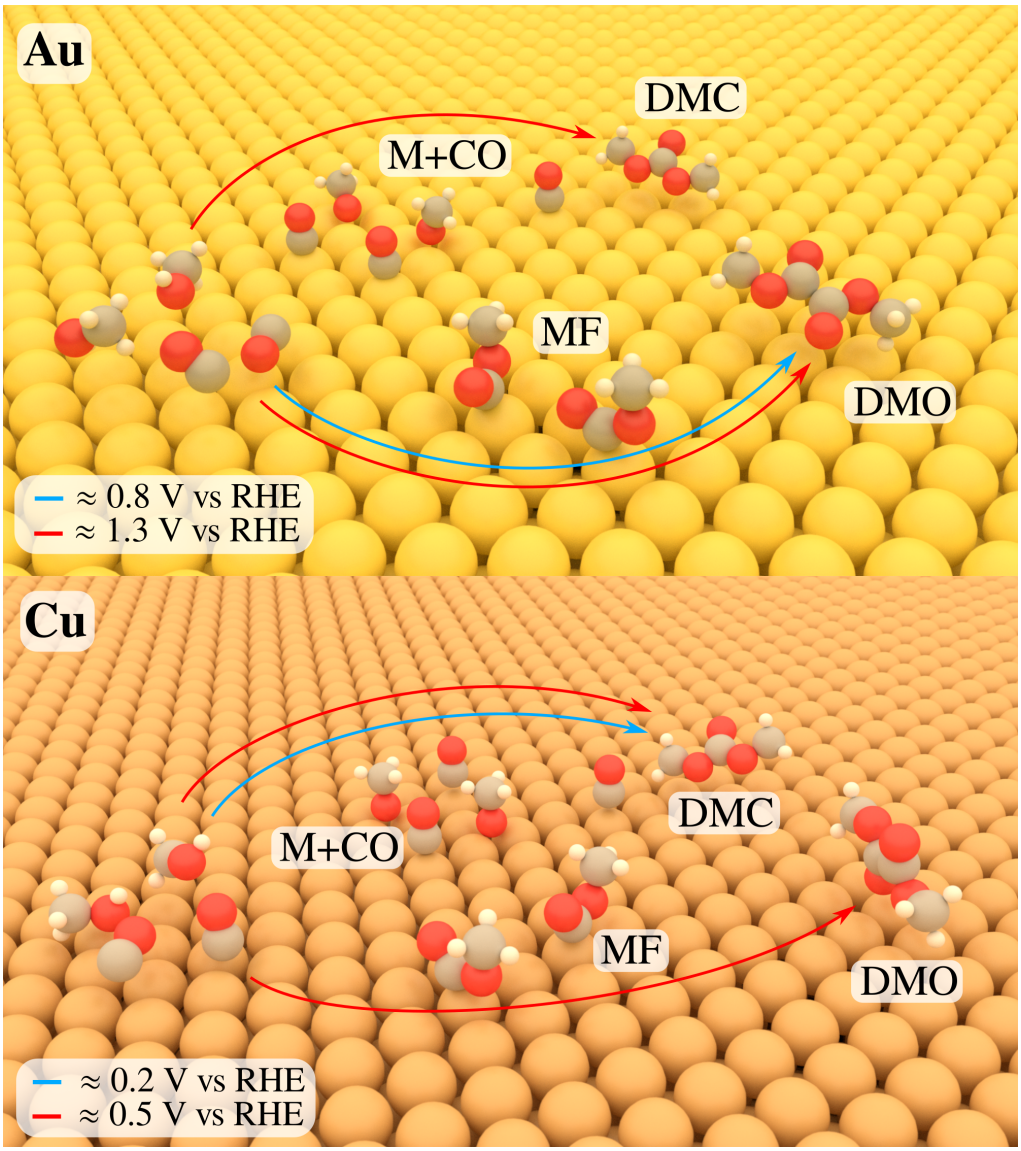

Figure 4.1: Illustration showing the steps and potentials involved in the synthesis of dimethyl carbonate on a gold electrode and copper electrode. On gold, DMO is made initially as methyl formate adsorption becomes favorable at lower potentials than methoxy; increasing the potential further leads to the adsorption of methoxy and formation of DMC as consequence. On copper, DMC is made at lower potentials as it is more favorable to adsorb methoxy compared to methyl formate. The yellow, brown, red, gray and white spheres represent gold, copper, oxygen, carbon and hydrogen atoms respectively.

We employed a combination of DFT simulations and experiments (cyclic voltammetry and potential hold tests) in order to get insight in the factors determining the electrochemical synthesis of DMC, thus, enabling the identification of suitable electrocatalysts for the process. The analysis is based on reaction free energies of various possible prod-

ucts as well as adsorption free energies of various surface species on transition metal surfaces (methoxy, carbon monoxide, hydroxy methyl, methyl formate, glycol aldehyde) which are possible intermediates during the synthesis. Furthermore, we find scaling relations between adsorbates that bind through carbon (carbon monoxide, hydroxy methyl, methyl formate, glycol aldehyde) which enables us to reduce the number of descriptors from five (five different surface species) to two, namely the adsorption free energy of methoxy and carbon monoxide [145, 146].

We find the the potential needed to synthesize DMC corresponds to the potential required to adsorb methoxy. Thus, when using copper instead of gold as electrocatalyst the potential can be reduced by ≈ 1 V as can be seen from the legend in figure 4.1. Regarding the selectivity between DMC and DMO we find that it is defined by the adsorption energies of methoxy and methyl formate. If a surface binds methyl formate rather than methoxy it will first start being filled by methyl formate species and by increasing the potential further, methoxy can be adsorbed as well. If there are only methyl formate species on a surface DMO will be made selectively. On the other hand, if it is more favorable to bind methoxy than methyl formate, the surface starts getting filled by methoxy. By increasing the potential further, methyl formate can adsorb as well. In the situation where the surface is covered by methoxy (and carbon monoxide) DMC is made selectively. On gold it is more favorable to adsorb methyl formate which means that gold is selective towards DMO at lower potentials (≈ 0.8 V vs RHE). Increasing the potential further (to ≈ 1.3 V vs RHE) makes it possible for methoxy to adsorb and for DMC to be produced. On the other hand, copper rather binds methoxy than methyl formate and DMC is made selectively at lower potentials (≈ 0.2 V vs RHE). Increasing the potential further (to ≈ 0.5 V vs RHE) should also lead to the production of DMO. These observations are illustrated in figure 4.1.

We have shown that the efficiency of the process is defined by the adsorption free energies of methoxy and carbon monoxide. More positive adsorption free energies (weaker binding) of methoxy and more negative adsorption free energies of carbon monoxide (stronger binding) lead to higher required potentials. The selectivity between DMC and DMO was explained through the tendency for adsorbing methoxy and methyl formate. If methoxy is preferred, DMC is made at lower potential and if methyl formate is preferred DMO is made at lower potentials. Copper stands out among the studied transition metal surfaces as a promising material for the electrosynthesis of DMC by operating at ≈ 1 V lower than gold and at the same time being selective towards DMC over DMO. The conclusions drawn from the DFT simulations were all confirmed by the performed experimental work and vice versa.

4.2 Paper II: Relation between HER and HDS

In order to produce hydrogen fuel by electrolysis, expensive noble metal electrodes are required (platinum) [42]. The same problem is present in fuel cells where hydrogen and oxygen are used as fuel. In order to make the hydrogen society feasible, novel materials

that can replace platinum need to be discovered.

It was observed in various studies that catalysts similar to those used for HDS often work well for the acidic HER [42, 111–115]. Sulfide based catalysts used for HDS are much more abundant and cheaper compared to platinum. The observation that HDS catalysts are often good candidates as catalysts for the HER can be used when looking for alternatives to platinum. But what is the reason behind this relation between HDS and HER and what does it mean for HDS?

For the HER, hydrogen adsorption free energy can be used as descriptor. Similarly, it was shown that the adsorption energy of sulfhydryl (SH) can be used as descirptor for HDS [142]. This indicates that the rate determining step of HDS is usually determined by breaking carbon-sulfur (C-S) bonds or by generating active sites on the sulfide catalyst. We analyze a set of hydrogen and SH adsorption energies and calculate zero point energy and thermal contributions to obtain the adsorption free energies of hydrogen at HER and HDS conditions. We find that the sulfides which are usually considered for HDS satisfy the criteria of having an adsorption free energy of hydrogen close to 0 eV at HER conditions. This means that the sulfides normally considered for HDS all satisfy hydrogen adsorption criteria for the HER. Such an observation indicates that both HDS and HER have similar requirements for binding hydrogen.

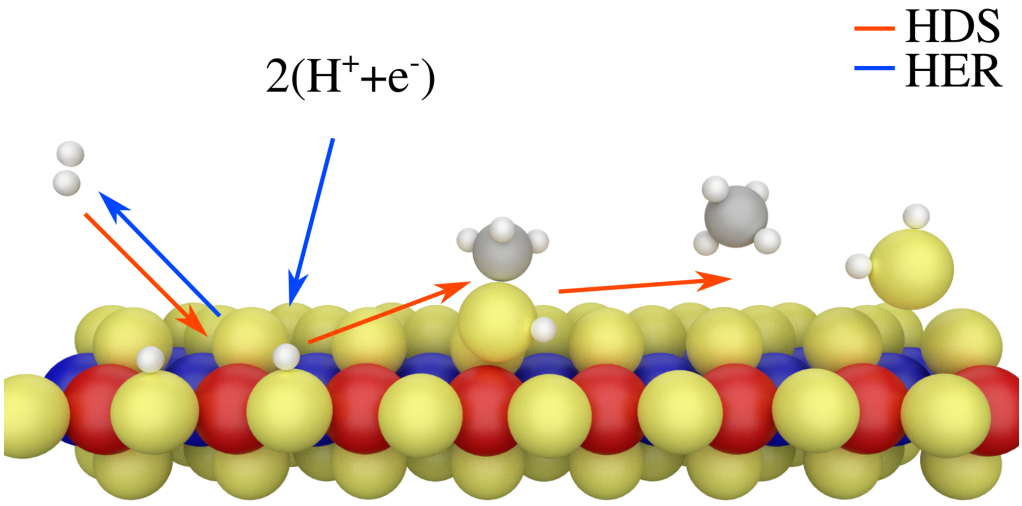

Figure 4.2: Illustration showing the relation between the hydrogen chemistry of HER and HDS. A similar trade-off between strong and weak hydrogen adsorption is required for both HER and HDS. HDS has further requirements for adsorbing SH with the right energy. HDS catalysts are good candidates for HER while HER catalysts do not necessarily satisfy the right sulfur chemistry for HDS. The red, blue, yellow, gray and white spheres represent cobalt, molybdenum, sulfur, carbon and hydrogen atoms respectively.

As shown in figure 4.2, both the HER and HDS have a common surface species, namely adsorbed hydrogen. Furthermore, there is a similar requirement in both the HER

and HDS for having an intermediate adsorption of hydrogen. If the adsorption energy is too positive (weak adsorption) additional potential has to be applied under HER, thus losing efficiency, while under HDS, there is not enough driving force for the dissociation of hydrogen which yields hydrogen atoms necessary for hydrogenation. If the adsorption energy is too negative (strong adsorption) the rate of the HER starts being limited by desorbing hydrogen, while under HDS, transferring hydrogen from the surface to sulfur containing molecules (hydrogenation) becomes difficult. This means that HDS catalysts, besides having the right SH adsorption energy, need to bind hydrogen in the right window of energies, not too strongly and not too weakly. In other words, the adsorption energy of hydrogen should also be considered as a descriptor when looking for suitable HDS catalysts.

We have shown that, although seemingly unrelated processes operating at different conditions, the HER and HDS are related by similar requirements for the adsorption of hydrogen (right trade-off between strong and weak adsorption). HDS catalysts are often good candidates for HER since they need to satisfy similar hydrogen chemistry, while HER catalysts are not necessarily good candidates for HDS as they do not have to satisfy any sulfur chemistry.

4.3 Paper III: Sterical effects in adsorbing 4,6-DMDBT on CoMoS

The last fraction of sulfur that needs to be removed from oil in order to achieve deep HDS [83] is contained in difficult to desulfurize molecules such as 4,6-dimethyldibenzothiophene (4,6-DMDBT). In order to achieve ultra-deep HDS, insight in the way 4,6-DMDBT interacts with the CoMoS catalysts is needed.

By using a combination of scanning tunneling microscopy (STM) and DFT simulations we study the adsorption of 4,6-DMDBT on CoMoS particles. As shown in figure 4.3 we find that 4,6-DMDBT adsorbs in two different modes called π-mode and σ-mode. The π-mode is associated to 4,6-DMDBT physisorbing on the S-edge brim. The name π-mode comes from the physisorption nature of the configuration in which the π-system (delocalized electrons) of the molecule interact with the catalyst. From STM the molecule appears as a bright protrusion over the entire length of the S-edge. This was interpreted as 4,6-DMDBT diffusing along the S-edge and is supported by the low calculated activation energy (lower than 0.1 eV) for diffusion. The σ-mode is associated to 4,6-DMDBT chemisorbing at vacancies formed at corner sites. The name σ-mode comes from the chemisorption nature of the configuration in which the sulfur atom interacts directly with the catalyst. The binding of 4,6-DMDBT is stronger in σ-mode as it is associated to 4,6-DMDBT chemisorbing at vacancies. On the other hand, the π-mode is observed more often since the σ-mode requires the formation of corner vacancies. An additional observation from STM is a dynamic switching between the σ-mode and π-mode. Such a dynamic process shows that it is possible for 4,6-DMDBT to change between the two modes which indicates that different stages of desulfurization might occur on dif-

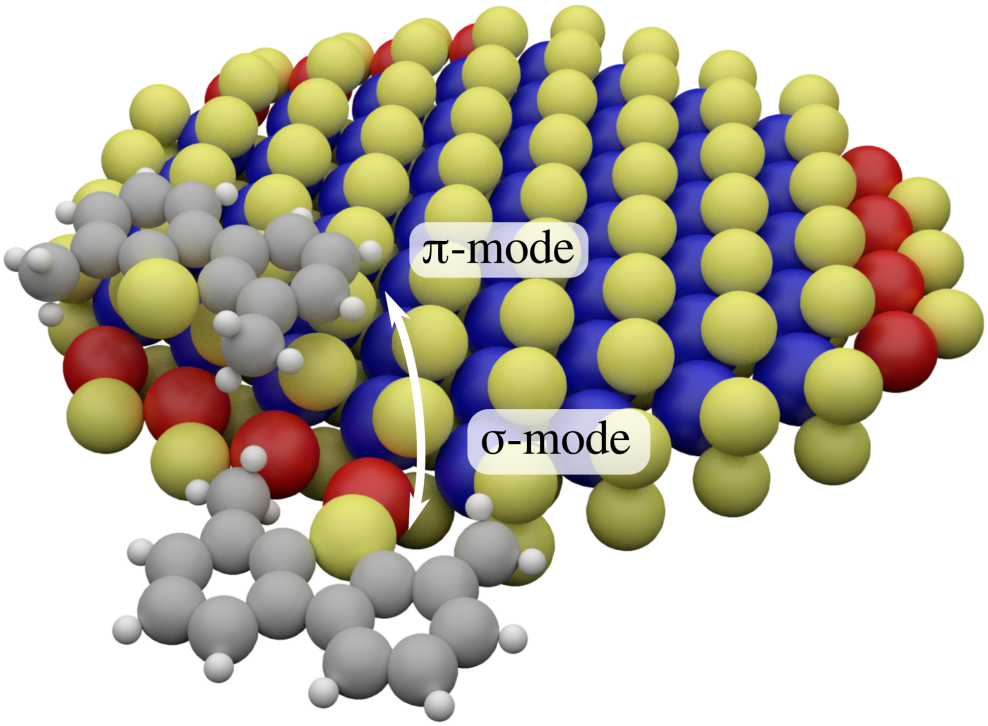

Figure 4.3: Illustration showing the two dominant adsorption modes of 4,6-DMDBT on CoMoS. The π-mode consists of 4,6-DMDBT physisorbed and diffusing along the S-edge. The σ-mode consists of 4,6-DMDBT chemisorbed at a corner vacancy. The arrow between the π-mode and σ-mode indicates that it is possible for the molecule to switch from one mode to the other. The red, blue, yellow, gray and white spheres represent cobalt, molybdenum, sulfur, carbon and hydrogen atoms respectively.

ferent sites, in different adsorption modes. We hypothesize that 4,6-DMDBT adsorbs in π-mode and diffuses along the S-edge which allows it to get hydrogenated by hydrogen atoms adsorbed on the S-edge. Once a vacancy is made at the corner, 4,6-DMDBT can switch to σ-mode in which the binding is stronger, thus facilitating the process of removing sulfur from the molecule. In other words, we hypothesize that 4,6-DMDBT gets hydrogenated in π-mode and the removal of sulfur occurs in σ-mode.

4.4 Paper IV: Modeling the active sites of CoMoS

Although the HDS process on the CoMoS catalyst has been studied for decades [84–88, 90, 96–99, 102], the exact atomic scale structure of the active sites and the underlying properties that make each of the sites active are still not completely clear. What makes the edges active? What is the role of corners? Why is the basal plane inert? These are some of the questions that need an answer in order to better understand the activity of CoMoS. Furthermore, the same questions are related to the activity towards the HER as

CoMoS can catalyze both HDS and the HER.

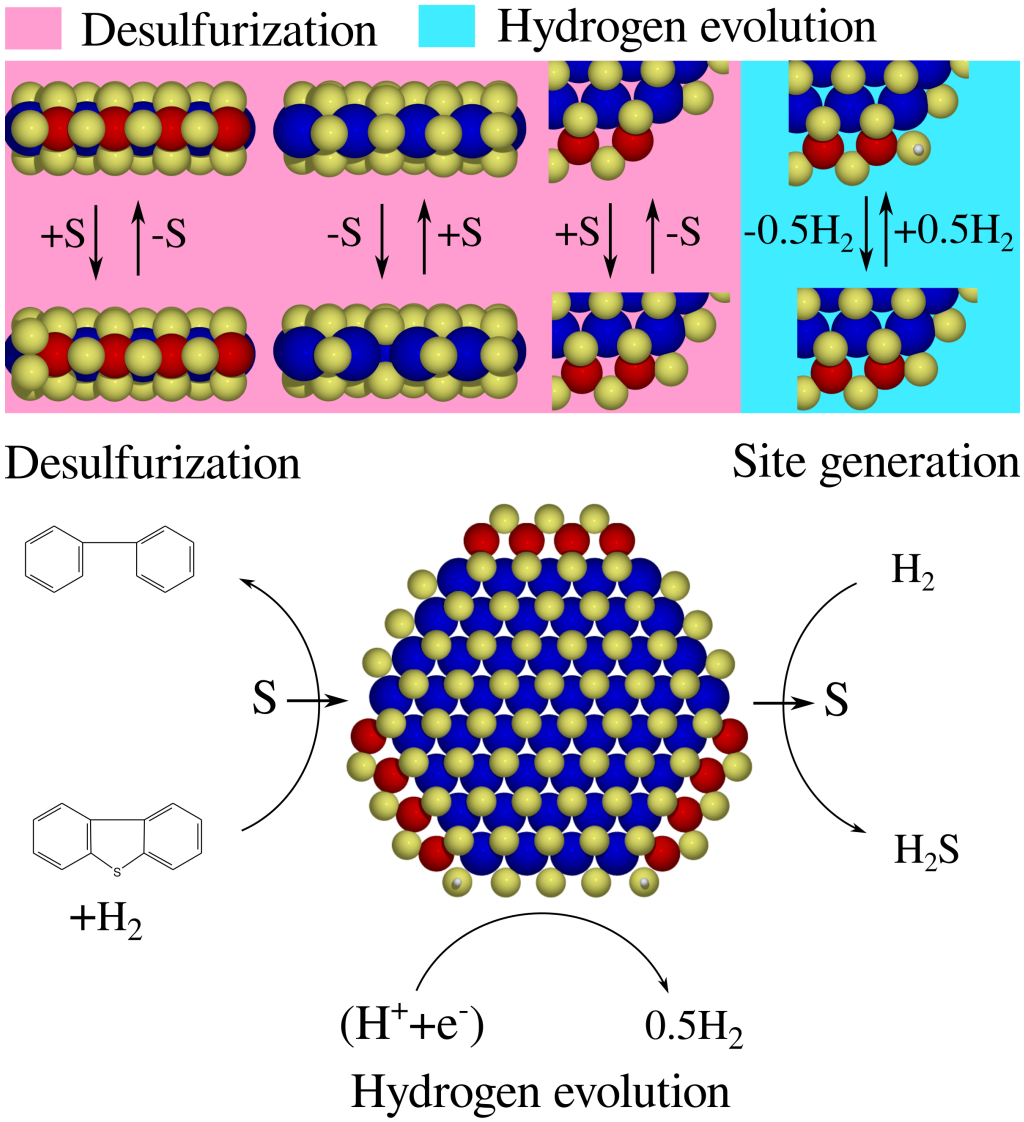

Figure 4.4: Illustration of the sulfur cycle during HDS. The active sties take sulfur atoms from sulfur containing molecules. Once the active sites are filled with sulfur atoms they are regenerated by releasing the additional sulfur atoms as H_2S. Once the sites have been regenerated the removal of sulfur can start over. The top part of the figure in pink shows the HDS cycles for the S-edge, M-edge and corner from left to right respectively. The blue zone shows hydrogen on the corner which is relevant for the HER. The red, blue, yellow and white spheres represent cobalt, molybdenum, sulfur and hydrogen atoms respectively.

We use DFT simulations and thermochemical data in order to model the structure of an ideal unsupported CoMoS particle under HER and HDS conditions. This is done by modeling the S-edge, M-edge, basal plane and corner of CoMoS separately and by cal-

culating a series of sulfur vacancy formation energies and hydrogen adsorption energies on the considered sites and by accounting for HER and HDS reaction conditions.

We determine that the S-edge and M-edge are terminated by sulfur monomers occupying bridge positions under both HER and HDS conditions. For the corner we find that it likely contains sulfur vacancies at HDS conditions and SH groups at HER conditions. These structures are shown in the top of figure 4.4. The intrinsic basal plane without sulfur add-atoms or vacancies was found to be the equilibrium structure under both HER and HDS conditions. For the S-edge it was found that the formation of single vacancies is unfavorable but the adsorption of additional sulfur atoms is possible as shown in figure 4.4. This indicates that the S-edge terminated by sulfur monomers can take in additional sulfur atoms from sulfur containing molecules i.e. it can desulfurize molecules containing sulfur. The additional sulfur is removed afterwards by releasing it as H_2S and returning to the equilibrium structure terminated by sulfur monomers once again. This idea is illustrated in figure 4.4 by going from the left to the right of the figure. At the M-edge it is not favorable to adsorb additional sulfur atoms but the formation of a single sulfur vacancy is possible as shown in figure 4.4. This means that at the M-edge a vacancy is generated first which is then filled by desulfurizing a sulfur containing molecule. This corresponds to going from the right to the left in figure 4.4. At corners, a vacancy that can take in sulfur atoms is present at equilibrium. The corners, similar to the S-edge, work in a way that corresponds to going from the left to the right of figure 4.4. The S-edge, M-edge and corner have one thing in common. Their equilibrium structures can either take in additional sulfur or create vacancies with small energy changes. This makes it possible for the structures to take in and release sulfur in cycles which is a fundamental requirement of HDS. The basal plane is inert as both adsorbing sulfur and creating sulfur vacancies is unfavorable.

When it comes to HER, we found that the most stable hydrogen adsorption sites are the corner sulfur atoms as shown in figure 4.4. Furthermore, the adsorption free energy of hydrogen at these sites is close to 0 eV under HER conditions. This indicates that corner sites might be more important than the edges when it comes to the HER.

4.5 Paper V: Modeling adsorption on CoMoS

In order to better understand how different sulfur containing molecules get desulfurized it necessary to study the way these molecules interact with the active sites of CoMoS [84, 86, 104, 147]. Additionally, the adsorption energies of various HDS intermediates such as hydrogenated molecules and species formed after breaking C-S bonds (thiolates) should also be considered in order to obtain a full picture [84].

We base our models on the sites established in paper IV by adsorbing various sulfur containing molecules and their possible hydrodesulfurization intermediates on them. The sites include the sulfur monomer terminated S-edge, single vacancy at the sulfur monomer terminated M-edge, single corner vacancy and basal plane. The studied molecules are methylthiol, thiophene, dibenzothiophene (DBT) and 4,6-DMDBT. The

studied intermediates include hydrogenation intermediates such as dihydro thiophene, tetrahydro thiophene, hexahydro DBT, hexahydro 4,6-DMDBT, dodecahydro DBT and dodecahydro 4,6-DMDBT, as well as intermediates resulting from the C-S bond breaking. It should be mentioned that the corner vacancies found in paper IV and used herein are not the same as the corner vacancies associated to the σ-mode in paper III. This is due to the different termination and position of sulfur atoms at the M-edge in the two studies. In STM studies the M-edge is found to be terminated by sulfur dimers sitting on top of the molybdenum atoms [91, 92, 99]. In paper IV but also in TEM studies [96, 97] the M-edge is found to be terminated by sulfur monomers in bridge position. The different observations could be caused by the different supports (gold in STM, carbon in TEM, no support in the present DFT studies) or by the different reaction conditions during the experiments. The σ-mode from paper III is associated to double vacancies at corners while herein it is associated to single vacancies. Single vacancies at corners only act as suitable adsorption sites if the M-edge is terminated by sulfur monomers in bridge position, otherwise double vacancies are required for chemisorption. The single corner vacancies studied herein are part of the equilibrium structure of CoMoS and are more stable than the double vacancies considered in paper III.

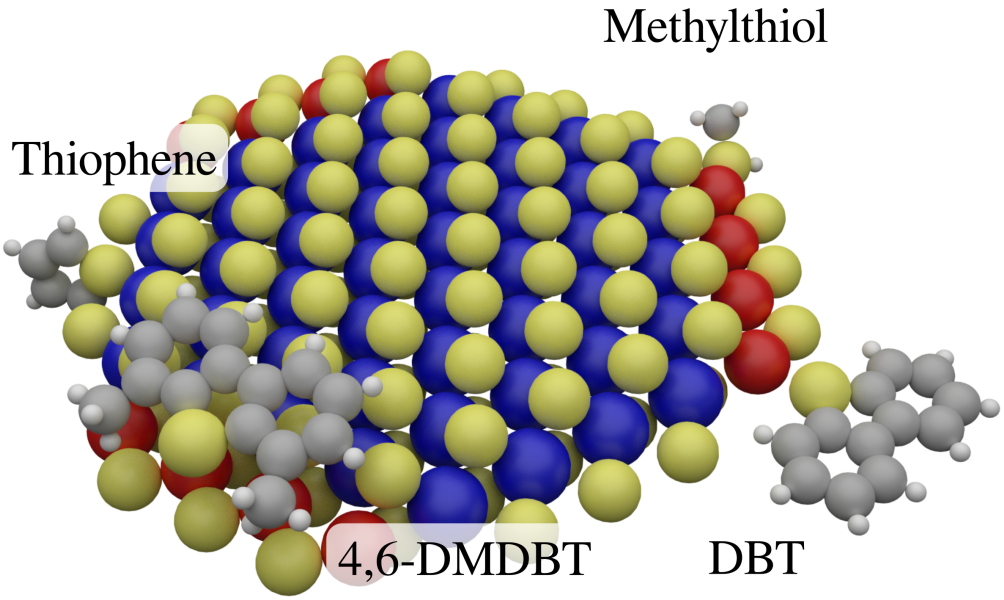

Figure 4.5: Illustration showing 4,6-DMDBT adsorbed in brim configuration on the S-edge, DBT and methylthiol adsorbed in edge configuration at corner vacancies, thiophene adsorbed in edge configuration at an M-edge vacancy by assuming a perpendicular position relative to the MoS_2 plane. The red, blue, yellow, gray and white spheres represent cobalt, molybdenum, sulfur, carbon and hydrogen atoms respectively.

We distinguish two different adsorption configurations, namely brim and edge adsorption. Brim adsorption corresponds to the π-mode reported in paper III for 4,6-DMDBT. It occurs when molecules interact with the brim of CoMoS by physisorbing

above the edges or corners of the particle. From figure 4.5 one can see an example of brim adsorption for 4,6-DMDBT. Edge adsorption occurs when the molecule approaches the particle from outside as can be seen from figure 4.5 for DBT, thiophene and methylthiol. Edge adsorption is also associated to corners, an example of this is the σ-mode of 4,6-DMDBT shown in paper III. As can be seen from figure 4.5, molecules adsorbing in edge position can either assume a planar orientation relative to the MoS_2 plane (like DBT in the figure) or a perpendicular orientation relative to the basal plane (like thiophene in the figure). We suggest that larger molecules such as 4,6-DMDBT and DBT might be prevented from assuming a perpendicular orientation as that would lead to them overlapping with the support or other MoS_2 layers in real supported or multilayer systems. Therefore, the perpendicular orientation at M-edge and corner vacancies might only be available to smaller molecules such as thiophene. Planar edge adsorption at M-edge vacancies was observed to be unfavorable for all molecules except methylthiol[1] due to steric effects. Planar edge adsorption at corner vacancies was observed to be just slightly less favorable than perpendicular adsorption. This indicates that corners can also chemisorb larger molecules such as DBT in planar orientation due to the more open structure of corner vacancies relative to M-edge vacancies.

Strong chemisorption between the sulfur atom of molecules and the active sites facilitates the process of breaking C-S bonds[2]. This indicates that molecules that adsorb strongly in edge configuration at M-edge and corner vacancies should get desulfurized directly, i.e. following the direct desulfurization pathway (DDS). On the other hand, molecules that prefer brim adsorption on the S-edge, where hydrogen has been made ready for hydrogenation by H_2 dissociation, should prefer the hydrogenation pathway (HYD). Furthermore, molecules which bind stronger as they get hydrogenated should also have a tendency of following the HYD pathway.

Smaller molecules such as methylthiol and thiophene were found to prefer adsorption at M-edge and corner vacancies indicating that they get desulfurized following DDS[3]. For thiophene it was also observed that it binds stronger the more hydrogenated it gets which points to the HYD pathway. Therefore, based on adsorption energies alone it is not clear which pathway should thiophene get desulfurized through. Earlier studies involving kinetic data suggest that it should follow the DDS pathway. Excluding the perpendicular orientations, no clear preference in adsorption sites was observed for DBT as they all have similar adsorption energies (within ≈ 0.2 eV). Contrary to thiophene, the adsorption energy of DBT on the S-edge brim does not change significantly as it gets hydrogenated which points to the DDS pathway. In the case of 4,6-DMDBT we show that it binds significantly stronger on the S-edge brim upon having one of its benzene rings hydrogenated to cyclohexane which points to HYD as the preferred HDS pathway. The low rate of 4,6-DMDBT desulfurization could be associated to it having to compete with nitrogen containing compounds for brim sites [104, 105, 147] and with other sulfur containing molecules for corner sites. Larger molecules such as DBT and 4,6-DMDBT

[1]For methylthiol we do not distinguish planar and perpendicular adsorption due to its geometry.

[2]Stronger adsorption of sulfur leads to lower activation energies for breaking carbon-sulfur bonds.

[3]Methylthiol can only get desulfurized thorugh DDS as it cannot be hydrogenated further.

were found to adsorb strongly on the basal plane which might lead to the wrong conclusion that the basal plane participates in HDS. By calculating the formation energies of thiolates formed after C-S or S-H bonds are broken we find that their formation on the basal plane is energetically unfavorable. This in return points to the correct conclusion of the basal plane being inert towards HDS.

Chapter 5

Included papers

Paper I **Towards electrification of chemical syntheses: electrocatalytic synthesis of dimethyl carbonate**
M. Šarić, B.J.V. Davies, M. Arenz, N.C. Schjødt, S. Dahl, P.G. Moses, J. Rossmeisl

Paper II **Relation between hydrogen evolution and hydrodesulfurization catalysis**
M. Šarić, P.G. Moses, J. Rossmeisl

Paper III **Atomic scale analysis of sterical effects in the adsorption of 4, 6-dimethyldibenzothiophene on a CoMoS hydrotreating catalyst**
S.S. Grønborg, M. Šarić, P.G. Moses, J. Rossmeisl, J.V. Lauritsen

Paper IV **Modeling the active sites of Co-promoted MoS_2 particles by DFT**
M. Šarić. J. Rossmeisl, P.G. Moses

Paper V **Modeling the adsorption of sulfur containing molecules on the Co-promoted MoS_2 catalyst by DFT**
M. Šarić, J. Rossmeisl, P.G. Moses

5.1 Paper I: Electrosynthesis of dimethyl carbonate

Towards electrification of chemical syntheses: electrocatalytic synthesis of dimethyl carbonate

M. Šarić, B.J.V. Davies, M. Arenz, N.C. Schjødt, S. Dahl, P.G. Moses, J. Rossmeisl

Submitted for publication

Towards electrification of chemical syntheses: electrocatalytic synthesis of dimethyl carbonate

Manuel Šarić[1], Bethan Jane Venceslau Davies[2], Niels Christian Schjødt[3], Søren Dahl[3], Poul Georg Moses[3], Matthias Arenz*[2,4], and Jan Rossmeisl†[2]

[1]Department of Physics, Technical University of Denmark, Denmark
[2]Department of Chemistry, University of Copenhagen, Denmark
[3]Haldor Topsøe A/S, Denmark
[4]Department of Chemistry and Biochemistry, University of Bern, Switzerland

December 9, 2016

Abstract

In the presented work, we demonstrate how the combination of density functional calculations and experiment can advance our understanding in the field of electrocatalytic production of chemicals; a research field that is expected to receive increasing attention as it can replace oil and gas by renewable alternatives. We form a set of criteria and requirements for the electrosynthesis reaction by calculating reaction energies of possible products and adsorption energies of possible intermediates on a series of metallic surfaces based on density functional theory. This set of criteria lead to the suggestion of suitable electrode materials for the reaction, namely noble metals. Gold was previously shown to be suitable as the electrode material, however, herein we conclude that copper should be more selective for dimethyl carbonate compared to the major co-product and also more energy efficient as it operates at a significantly lower potential than gold. The predictions of activity and selectivity are supported by experiments, where electrosynthesis tests confirm that copper is indeed active at a 1 V lower applied potential than gold and with an increased selectivity.

1 Introduction

Today most chemicals are derived from oil which also provides the necessary energy to drive reactions. Oil is a limited resource; at some point we will need to transform to a sustainable way of producing chemicals. Therefore, electrochemical and electrocatalytic production of chemicals receives increasing attention. The energy to drive the reaction can be obtained from renewable sources (e.g. wind or solar power). If abundant feedstocks are used, very attractive alternatives to standard processes seem possible. Prominent examples are water and carbon dioxide electrolysis to produce fuels. However, at such scale the technology is not yet mature enough to compete with fossil fuels and therefore relies on economical subsidies.

In the present work we focus on a different topic in the field electrocatalytic synthesis of chemicals, i.e. the electrocatalytic production of dimethyl carbonate (DMC). DMC is an environmentally benign and versatile chemical[1, 2] with potential to replace toxic compounds such as phosgene, currently used in various industrially important chemical processes. It meets the increasing demand in todays chemical industry for versatile reagents and solvents, which are non-toxic for the environment and can at the

*matthias.arenz@dcb.unibe.ch
†Jan.Rossmeisl@chem.ku.dk

same time replace traditional, often toxic and waste producing compounds. Thus, DMC constitutes an important example of a chemical, whose use adheres to the principles of green chemistry[3, 4, 5, 6, 7]. DMC is mostly used as a precursor in chemical synthesis although it can also be used as a solvent, electrolyte, fuel or fuel additive[1, 2, 8, 9, 10, 11, 12].

The chemical methods of producing DMC often involve toxic precursors or waste products and/or explosive mixtures of carbon monoxide and oxygen. Development of a new DMC production process in which toxic compounds and hazardous environments are avoided is desirable. Electrocatalysis offers an alternative, green synthesis method, for the production of chemicals without the use of chemical oxidants. The reaction energy can be controlled by the potential which means that energy rich, toxic and explosive reaction conditions can be avoided. An electrochemical method of synthesizing DMC was reported on gold by Funakawa et al[13, 14]:

$$2CH_3OH + CO \leftrightarrow CH_3OCOOCH_3 + H_2 \tag{1}$$

Additional electrochemical methods using transition metal complexes, metal-organic hybrids, $CuCl_2$ in gas phase and palladium based electrodes have also been reported by various authors[15, 16, 17, 18, 19, 20, 21, 22].

Herein we apply a combination of density functional theory (DFT), cyclic voltammetry and constant potential hold experiments to understand the fundamental requirements for the electrocatalysis of DMC and on this basis discover new efficient and selective catalysts.

2 Results and discussion

2.1 Surface species and products

The first step in a theoretical description of activity and selectivity of an electrocatalytic reaction on different metal surface is the identification of the reaction mechanism. Adsorption of methanol and carbon monoxide, as shown in figure 1a, are the first steps in the synthesis of DMC. Methanol can adsorb through oxygen as methoxy or through carbon as hydroxy methyl. The adsorption of methanol results in releasing a proton-electron pair making it a potential dependent step. After methanol is adsorbed, methoxy and hydroxy methyl can combine with adsorbed carbon monoxide to yield methyl formate and glycol aldehyde as intermediates respectively. These more complex intermediates can then react further either with the initial adsorbates or with themselves, resulting in a range of products as shown in figure 1b, with the corresponding reaction energies calculated by DFT shown in table 1 of the supplementary material.

It is clear that in order to produce DMC electrochemically the catalyst needs to bind methoxy and carbon monoxide and, at the same time, it needs to form DMC from the surface species selectively so that the redundant co-products (described in the supplementary material) are avoided. In order to perform a thermodynamic analysis and at the same time consider selectivity, all the surface species (carbon monoxide, methoxy, hydroxy methyl, methyl formate, glycol aldehyde) need to be taken in account, thus working with five parameters at once. Table 2 of the supplementary material contains the calculated formation energies of each intermediate for each surface considered in the present study.

It is possible to reduce the complexity of the analysis by using scaling relations between various surface species. The adsorption energies of the species that bind through carbon (carbon monoxide, hydroxy methyl, methyl formate and glycol aldehyde) will follow these scaling relations. This means that if a given surface binds carbon monoxide stronger it will also bind the rest of the species that bind through carbon stronger and vice versa. Figure 1 of the supplementary material shows the scaling relations of hydroxy methyl, methyl formate and glycol aldehyde with carbon monoxide. It is therefore possible to reduce the complexity of the analysis from five parameters to two parameters, the adsorption free energies of methoxy and carbon monoxide[23, 24, 25].

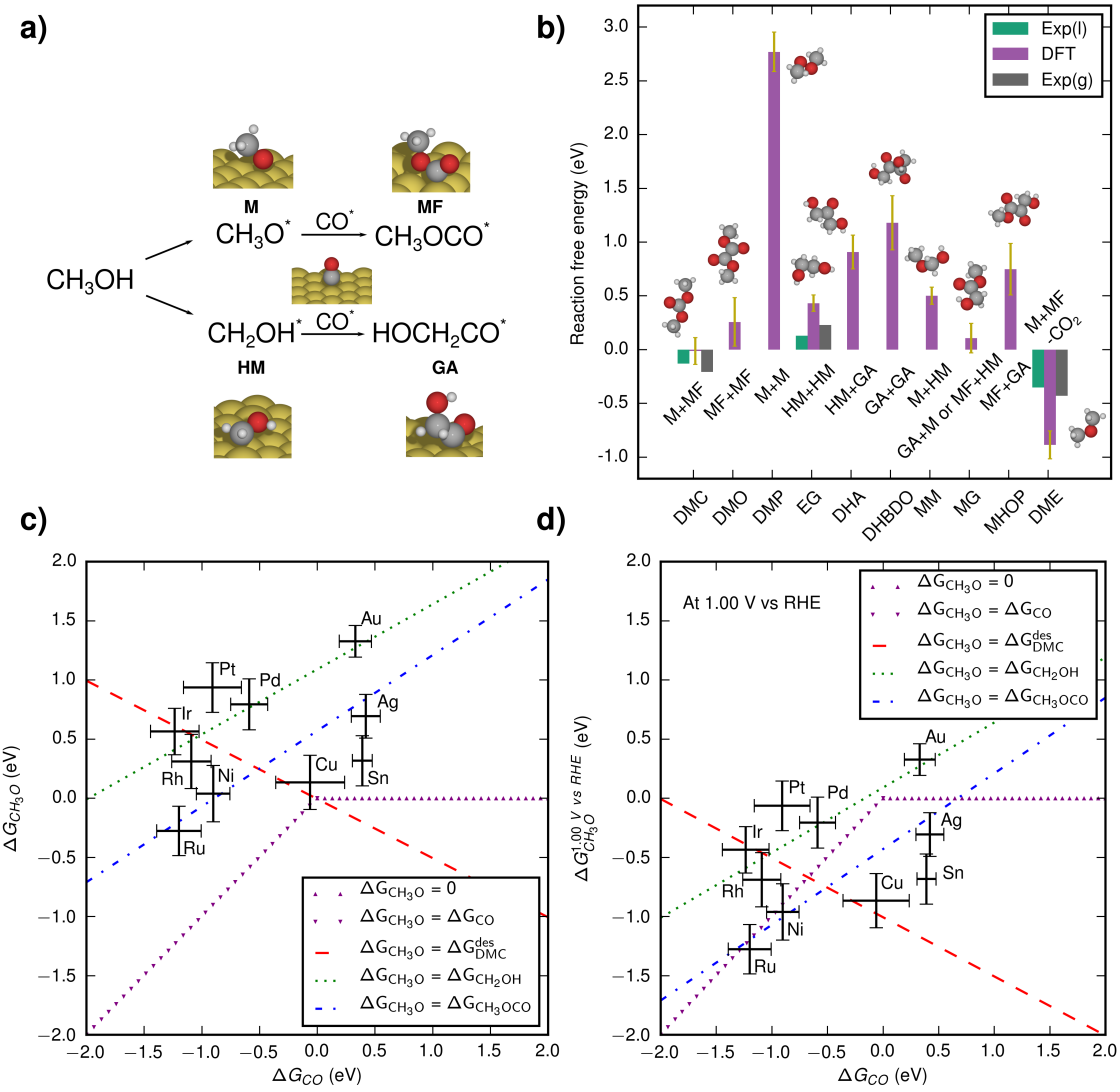

Figure 1: **a)** Proposed surface species during synthesis. Methoxy (M), hydroxy methyl (HM), carbon monoxide (CO), methyl formate (MF) and glycol aldehyde (GA). **b)** Calculated reaction free energies (experimental data for liquid and gas phase shown when available[26]) associated to specific combinations of surface species yielding dimethyl carbonate (DMC), dimethyl oxalate (DMO), dimethyl peroxide (DMP), ethylene glycol (EG), dihydroxy acetone (DHA), 1,4-dihydroxybutane-2,3-dione (DHBDO), methoxy methanol (MM), methyl glycolate (MG), methyl-3-hydroxy-2-oxopropanoate (MHOP) and dimethyl ether (DME). Error bars show one standard deviation of ensemble values calculated with the BEEF-vdW functional. **c)** Thermodynamic analysis classifying catalysts based on efficiency (vertical distance between points and purple triangles line determines required potential), surface poisoning (surfaces found at negative ΔG_{CO} and below the red dash line are poisoned by surface species) and selectivity (surfaces found above the blue dash-dot line have selectivity issues caused by DMO production and surfaces found above the green dotted line have selectivity issues caused by binding methanol through carbon). Error bars show one standard deviation of ensemble values calculated with the BEEF-vdW functional. **d)** Thermodynamic analysis at 1 V vs RHE; all the catalyst data points and the equilibrium (dashed red) and scaling relation (dotted green and dash-dot blue) lines move downwards for 1 eV.

2.2 Thermodynamic analysis

Using the adsorption free energies of carbon monoxide and methoxy as descriptors, we perform a thermodynamic analysis for the synthesis of DMC. Figure 1c shows the result of such a thermodynamic analysis. In the thermodynamic analysis we identify catalysts that satisfy a set of criteria for DMC production. Herein, these criteria can be stated as:

1) energy efficiency,

2) no surface poisoning,

3) selectivity towards DMC.

1) Energy efficiency assumes that the potential required to perform the synthesis is low. In figure 1c, the purple triangles line marks the points where the adsorption free energy of methoxy is 0 eV for positive carbon monoxide adsorption free energy and where the adsorption free energy of methoxy is equal to the adsorption free energy of carbon monoxide for negative carbon monoxide adsorption energies. Since the adsorption of methoxy includes a proton-electron pair as product, its reaction free energy can be tuned by applying a potential. Because of that, the vertical distance between the data point for a given catalyst and the purple triangles line defines the potential that needs to be applied in order to drive the electrochemical synthesis of DMC on that particular catalyst. Figure 1d shows how the situation changes when applying 1 V vs RHE. Based on this, it is possible to estimate that the potential required to produce DMC should be ≈ 1.3 V vs RHE on gold or ≈ 0.7 V vs RHE on silver. If the catalyst binds carbon monoxide too strongly its surface will be poisoned by it and there will be no free sites for methoxy binding. In such an event it is still possible to synthesize DMC but one needs to apply additional potential for replacing carbon monoxide with methoxy, which is why for negative carbon monoxide adsorption free energies the purple and orange triangles line is sloped. Another way of thinking about this is that carbon monoxide and methoxy should have similar surface coverage in order to produce DMC. Therefore, on platinum one needs to apply ≈ 1.8 V vs RHE and on copper ≈ 0.2 V vs RHE. This simple analysis indicates that switching from gold, used by Funakawa et al[13], to copper as the electrode material a decrease in the required potential by ≈ 1 V can be expected.

2) No surface poisoning requires that methoxy and carbon monoxide bind weakly enough so that it is possible to form DMC from the surface species. In order to talk about surface poisoning it is possible to define the equilibrium formation line of DMC with the two descriptors by using the following relation:

$$\Delta G_{ads}(CH_3O) = -\frac{1}{2}\Delta G_{ads}(CO) + \frac{1}{2}\Delta G_{DMC} = \Delta G^{des}_{DMC} \tag{2}$$

where ΔG_{DMC} and is the free energy of DMC formation and is described by equation 1. The red dashed line in figure 1c indicates where equilibrium is established for forming and desorbing DMC. In the zone above the red line the reaction for DMC formation and desorption will be shifted towards gas phase DMC while below it the reaction will be shifted towards the adsorbed species. The optimal catalyst will therefore be found above the red dash line, leading to the suggestion that noble metals and tin should be suitable catalysts.

3) Selectivity towards DMC means that the rest of the co-products are avoided. As a first step in analyzing the selectivity towards different molecules, it useful to consider the reaction free energies for different products. From figure 1b it can be seen that, excluding dimethyl ether (DME), DMC is thermodynamically the most stable product which makes the selectivity towards DMC greater. A possible issue with selectivity could arise if DME was formed instead of DMC as they follow a similar pathway and have the same energy requirements for binding methanol. The formation of DME requires a more involved rearrangement of the surface species as well as the cleavage of a C-O bond, indicating that the formation of DME could be limited by unfavorable kinetics.

The blue dash-dot line in figure 1c line is derived from the scaling relation between methyl formate and carbon monoxide and it represents the energy of methyl formate formation. If a surface data point is below the given line, forming methyl formate is less favorable than adsorbing methoxy and the distance between the line and the surface data point represents the energy required to form methyl formate from methoxy and carbon monoxide. If a surface is above the given line, forming methyl formate is more favorable than adsorbing M and the distance between the line and the surface data point represents the energy gained when forming methyl formate from methoxy and carbon monoxide. For example, copper lies below this line suggesting that it is not favorable to form methyl formate and that DMC is formed directly from two methoxy groups and a carbon monoxide on the surface. This can be seen in terms of simple free energy diagrams from figure 2 of the supplementary material. The unfavorable formation of methyl formate on copper suggests that DMC is produced selectively over DMO as the latter requires two methyl formate species to meet on the surface. Gold lies above the line which indicates that a smaller driving force is needed for methyl formate formation than for methoxy adsorption. As the potential required to bind methoxy is fairly high it is possible that methyl formate is made on the surface directly from methanol and carbon monoxide at potentials lower than what is required to adsorb methoxy. This suggests that, at lower potentials, gold will selectively produce DMO as the surface will be covered mainly by methyl formate. Furthermore, as the applied potential is increased, more methoxy species will populate the surface and the selectivity towards DMC should increase. This idea, further illustrated in figure 2 of the supplementary material, is confirmed by the experimental work performed herein and by a previous study from Funakawa at al[14].

The green dotted line in figure 1c is derived from the scaling relation between hydroxy methyl and carbon monoxide. It shows whether it is more favorable to bind methanol through carbon as hydroxy methyl or through oxygen as methoxy on a given surface. For the data points above the given line it is more favorable to bind through carbon while for the points below the line it is more favorable to bind through oxygen. This line indicates that gold, palladium, platinum and iridium could have further selectivity issues when trying to produce DMC as they rather bind methanol through carbon as hydroxy methyl which leads to a range of products discussed in the supplementary material. Furthermore, points that are found on or close to the green dotted line will show no preference in binding methanol through oxygen over binding methanol trough carbon. This means that the surface coverage of methoxy and hydroxy methyl will be comparable which in returns makes it possible to produce an even wider range of molecules further discussed in the supplementary material. These observations on selectivity are further discussed based on the free energy diagrams shown in figure 3 of the supplementary material.

Based on this simple thermodynamic analysis we identify noble metals and tin as promising catalyst. We predict that copper should operate at a significantly lower potential than gold ($\approx$ 1 V lower) and be more selective towards DMC compared to DMO. Furthermore, we provide an explanation to the effect of applied potential on the selectivity between DMC and DMO based on the formation energies of methoxy and methyl formate.

2.3 Electrochemical synthesis

For the experimental work, two electrochemical techniques were utilised. First, cyclic voltammetry (CV) tests were carried out in an inert (argon purged solution) and a reactive (carbon monoxide saturated) solution to investigate activity and potential window of interest. Secondly, constant potential hold tests (CPH) were performed to gain information on potential dependent selectivity. For the gold electrode, a clear change in the current-potential response was observed on switching from argon to a carbon monoxide saturated solution by an increase in current and change in CV shape, as shown in figure 2a. This observation has been previously reported for a gold wire working electrode[13]. Peaks Au-1 and Au-3 are assigned to gold oxide formation and reduction respectively. Peak Au-2 is assigned to methanol oxidation to dimethoxy methane and methyl formate based on previous work[13]. The Au-4 and Au-5 peaks occur

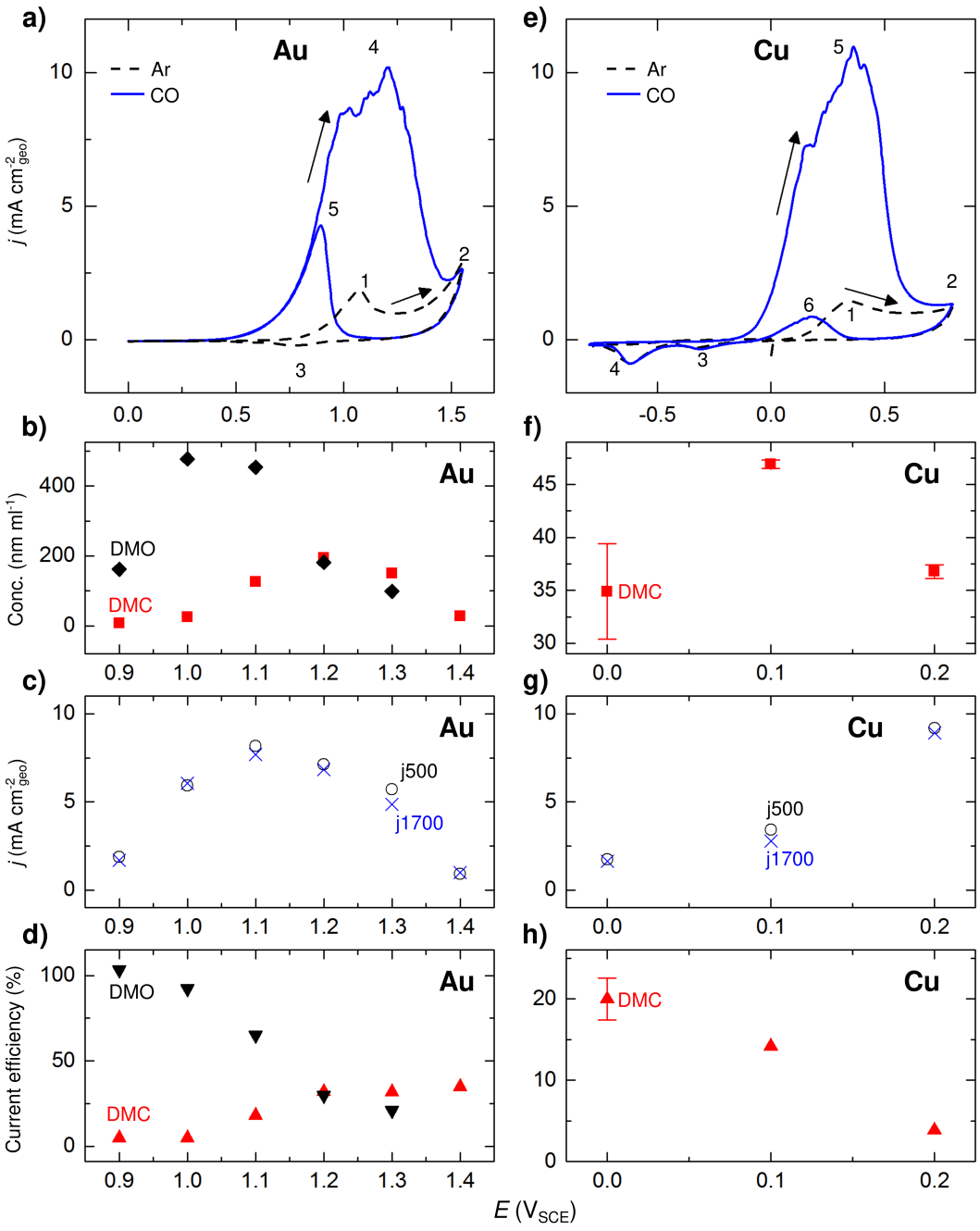

Figure 2: Typical cyclic voltammograms recorded with a gold wire (a) and a copper wire (e) working electrode in argon (dash/black) and carbon monoxide (solid/blue) saturated electrolyte solutions with a scan rate of 100 mV/s, where arrows indicate direction of scan. Constant potential hold results of current density reported early in the test at 500 s by j500 (circles) and towards the end at 1700 s by j1700 (crosses), for gold (c) and copper (g) during carbon monoxide bubbling of the electrolyte solution. Concentrations of products of interest produced, DMC (red squares) and DMO (black diamonds), by constant potential hold tests for gold (b) and copper (f) and the resulting current efficiency at each potential for gold (d) and copper (h) tests for DMC (red up-triangles) and DMO (black down-triangles). Electrolyte solution was 0.1 M $NaClO_4$/methanol.

as a result of carbon monoxide addition and are related to the formation of DMC and DMO, among other products. The other possible products made in this potential range are yet to be identified experimentally but have been suggested by theory. Multiple CV cycles in the shown range were performed to pass sufficient current for product detection and DMC (0.06 mol/ml) and DMO (0.23 mol/ml) were indeed detected after 100 cycles at 100 mV/s.

On the introduction of carbon monoxide to the system with a copper wire electrode, a current-potential response was recorded as shown in figure 2e, the carbon monoxide CV differs from the CV recorded with only argon present, indicating increased activity in the reactive (carbon monoxide) solution. A clear increase in current and CV shape is seen, with a peak current density value at 11 mA cm^{-2}_{geo}, similar to that of gold at 10 mA cm^{-2}_{geo}. This indicated that the combined rate of reactions on gold is similar to that on copper and that they have comparable activities in the reaction solution. Which products the reaction rates relate to however can be altogether different for each electrode, as we have described above. The oxidation peaks Cu-1 and Cu-2 and the two reduction peaks Cu-3 and Cu-4 have been assigned to redox reactions of copper. Peaks Cu-5 and Cu-6 are assigned to DMC and DMO formation, as well as other co-products, based on chemical analysis. The Cu-3 and Cu-4 reduction peaks are also observed in a carbon monoxide environment indicating that the oxidation and dissolution of the copper surface is not inhibited during the synthesis tests and that a proportion of the current and current efficiency is lost to this process. The CV tests show that copper is in fact electrochemically active in a lower potential region, as predicted by the DFT analysis. Multiple CVs were recorded and DMC (0.03 mol/ml) and DMO (negligible) was found in the electrolyte solution after 10 scans at 10 mV/s.

Constant potential hold tests were performed to disentangle the potential dependent processes as seen in figure 2. The potential regions chosen for each electrode were based on the activity seen in the CVs recorded in the reactive environment (carbon monoxide). The gold working electrode produced DMC and DMO in significant amounts at potentials lower than 1.4 V vs SCE (figure 2b). Above 1.4 V vs SCE, DMC and DMO production is negligible and is not shown. The total current efficiency lower than 100 % for all but 0.9 V vs SCE points to additional and undefined reactions occurring (figure 2d). In the region of 1.1-1.4 V vs SCE, DMC is produced with a CE ranging from 18-34 % which correlates with the Au-4 oxidation peak. DMO has a CE of 20-100 % in this range. At 1.4 V vs SCE the concentration of DMO was below the quantification threshold. Furthermore it can be seen that at 1.2 V vs SCE the selectivity of the process changes from favoring DMO to favoring DMC. This observation agrees with the results and suggestions from DFT where, at low potentials, the catalyst gets covered mostly by methyl formate thus leading mainly to DMO production, and as the potential increases, methoxy starts to adsorb on the surface allowing DMC to be produced.

In the potential range 0 to 0.2 V vs SCE tested for the copper electrode, DMC was produced (figure 2f), however, at lower concentrations then for the gold electrode. DMO production was zero or negligible at all potentials tested, as it was below the quantification threshold. CE ranges from ca. 4-20 %. Above 0.2 V vs SCE, DMC and DMO were not quantifiable but large current density is observed as shown in the CV in figure 2e, this is attributed to the oxidation and dissolution of copper, reducing the carbonylation of methanol and/or other product formation.

The change in current density with time is depicted in figure 2c for gold and 2g for copper by j500 and j1700. The current density recorded towards the end of each test (j1700) does not lie far from the current density recorded towards the beginning of each test (j500), signifying good stability in reaction over the 30 minutes of synthesis for gold and copper at the shown potentials.

Copper is selective towards DMC in the range tested, from 0 to 0.2 V vs SCE, with respect to DMO formation (figure 2h). This observed selectivity towards DMC on copper agrees with the theoretical framework set by the computational work. The copper electrode produces DMC with CE of 14 % at 1 V lower than gold at 1.1 V vs SCE and CE of 18 %. The current density and rate of formation were however larger by a factor of two on gold. There is room for optimising the copper electrode to improve the rate and stability of the electrode.

3 Conclusions

We have shown that selectivity and activity of the electrocatalytic formation of DMC can be understood by combining DFT simulations and experiments. By DFT simulations it was shown that it is possible to identify a good catalyst for DMC synthesis based on the adsorption energies of methoxy and carbon monoxide as well as the criteria that the optimal catalyst should be efficient, selective and avoid surface poisoning. The simulations indicate that it is possible to synthesise DMC on gold, silver, tin and copper with a decrease in the required potential of $\approx$1 V when going from gold to copper. Cyclic voltammetry and potential hold measurements confirm the trend predicted by simulations, showing that the copper catalysts performs well and at a lower potential than gold. Selectivity dependence on the applied potential when working with gold as well as selectivity towards DMC on copper was observed experimentally and was further explained by the simulations. Furthermore, based on DFT simulations, additional selectivity issues have been addressed and, at the current moment experimentally unidentified, likely products have been suggested. A significant finding has been presented with a lower potential requirement on copper compared to gold for DMC synthesis as well as the rationale for selectivity. By optimising the copper catalyst the electrochemical synthesis of DMC could become an attractive, environmentally friendly way to produce DMC. This provides hope that many chemical processes can be substituted with electrochemical catalytic reactions, which holds the promise to change the chemical industry towards a sustainable and green direction.

Acknowledgements

Funding: The authors acknowledge support from the Danish Council for Independent Research, the Innovation Fund Denmark and the Carlsberg Foundation.

References

[1] Tundo, P. et al. Synthetic pathways and processes in green chemistry. Introductory overview, *Pure Appl. Chem* **72**, 1207-1228 (2000).

[2] Tundo, P. & Selva, M. The chemistry of dimethyl carbonate, *Acc. Chem. Res.* **35**, 706-716 (2002).

[3] Anastas, P. T., & Warner, J. C. Principles of green chemistry, *Green chemistry: Theory and practice*, 29-56 (1998).

[4] Anastas, P. & Eghbali, N. Green Chemistry: Principles and Practice, *Chemical Society Reviews* **39**, 301-312, (2010).

[5] Sheldon, R. A. Green solvents for sustainable organic synthesis: state of the art, *Green Chemistry* **7**, 267-278 (2005).

[6] Clark, J. H. Green chemistry: challenges and opportunities, *Green Chemistry* **1**, 1-8 (1999).

[7] Siahrostami, S. et al. Enabling direct H_2O_2 production through rational electrocatalyst design, *Nature Materials* **12**, 1137-1143 (2013).

[8] Pacheco, M.A. & Christopher, L.M. Review of dimethyl carbonate (DMC) manufacture and its characteristics as a fuel additive, *Energy & Fuels* **11**, 2-29 (1997).

[9] Ono, Y. Catalysis in the production and reactions of dimethyl carbonate, an environmentally benign building block, *Applied Catalysis A: General* **155**, 133-166 (1997).

[10] Memoli, S., Selva, M. & Tundo, P. Dimethyl carbonate for eco-friendly methylation reactions, *Chemosphere* **43**, 115-121, (2001).

[11] Keller, N., Rebmann, G. & Keller, V. Catalysts, mechanisms and industrial processes for the dimethylcarbonate synthesis, *Journal of Molecular Catalysis A: Chemical* **317**, 1-18 (2010).

[12] Delledonne, D., Rivetti, F. & Romano, U. Developments in the production and application of dimethylcarbonate, *Applied Catalysis A: General* **221**, 241-251 (2001).

[13] Funakawa, A., Yamanaka, I. & Otsuka, K. Active control of methanol carbonylation selectivity over Au/carbon anode by electrochemical potential, *J. Phys. Chem. B* **109**, 9140-9147 (2005).

[14] Funakawa, A., Yamanaka, I., Takenaka, S., & Otsuka, K. Selectivity control of carbonylation of methanol to dimethyl oxalate and dimethyl carbonate over gold anode by electrochemical potential, *Journal of the American Chemical Society* **126**, 5346-5347 (2004).

[15] Galia, A., Filardo, G., Gambino, S., Mascolino, R., Rivetti, F., & Silvestri, G. Electrochemical activation of transition metal complexes for the carbonylation of methanol to dimethylcarbonate, *Electrochimica acta* **41**, 2893-2896 (1996).

[16] Jia, G. et al. Electrocatalytically Active MOF/Graphite Oxide Hybrid for Electrosynthesis of Dimethyl Carbonate, *Electrochimica Acta* **144**, 1-6 (2014).

[17] Yu, Y. et al. Electrosynthesis of dimethyl carbonate from methanol and carbon monoxide under mild conditions, *Industrial & Engineering Chemistry Research* **52**, 6901-6907 (2013.)

[18] Otsuka, K., Yagi, T., & Yamanaka, I. Electrolytic carbonylation of methanol over the CuCl2 anode in the gas phase, *Journal of The Electrochemical Society* **142**, 130-135 (1995).

[19] Drake, I. J., Fujdala, K. L., Bell, A. T., & Tilley, T. D. Dimethyl carbonate production via the oxidative carbonylation of methanol over Cu/SiO 2 catalysts prepared via molecular precursor grafting and chemical vapor deposition approaches, *Journal of Catalysis* **230**, 14-27 (2005).

[20] Yamanaka, I., Funakawa, A., & Otsuka, K. Selective Carbonylation of Methanol to Dimethyl Carbonate by Gas-Liquid-Solid-Phase Boundary Electrolysis, *Chemistry Letters* textbf4, 448-449 (2002).

[21] Funakawa, A., Yamanaka, I., & Otsuka, K. High Efficient Electrochemical Carbonylation of Methanol to Dimethyl Carbonate by Br2 Br Mediator System over Pd C Anode, *Journal of The Electrochemical Society* **153**, D68-D73 (2006).

[22] Yamanaka, I., Funakawa, A., & Otsuka, K. Electrocatalytic synthesis of DMC over the Pd/VGCF membrane anode by gasliquidsolid phase-boundary electrolysis, *Journal of Catalysis* **221**, 110-118 (2004).

[23] Ferrin, P. et al. Reactivity descriptors for direct methanol fuel cell anode catalysts, *Surface Science* **602** (2008). 3424-3431

[24] Rossmeisl, J. et al. Bifunctional anode catalysts for direct methanol fuel cells, *Energy & Environmental Science* **5** (2012). 8335-8342

[25] Nørskov, J. K. et al. Towards the computational design of solid catalysts, *Nature chemistry* **1**, (2009). 37-46

[26] Perry, R.H. & Green, D.W. *Perry's Chemical Engineers' Handbook* Appendix B - Physical Properties pp. 641-672 (McGraw-Hill, New York, 1984)

Towards electrification of chemical syntheses: electrochemical synthesis of dimethyl carbonate *supplemental material*

Manuel Šarić, Bethan Jane Venceslau Davies, Niels Christian Schjødt, Søren Dahl, Poul Georg Moses, Matthias Arenz and Jan Rossmeisl

December 9, 2016

Methodology

Density functional theory

The GPAW density functional theory code was employed in finite difference mode with a gridspacing of 0.18 Å in order to perform total energy and vibration frequency calculations[1, 2]. To describe the exchange and correlation the BEEF-vdW functional was used. The BEEF ensemble containing 2000 values was used to describe the computational uncertainty of the predicted values. Metal surfaces were modeled as periodic (3x3) fcc (111) slabs of four atomic layers. Inside the supercell the slabs were surrounded with 14 Å of vacuum in the z direction. The Brillouin zone was sampled with 4, 4, 1 k-points in the x, y and z directions respectively. During optimization the bottom two layers of the slab were fixed in bulk position using the calculated lattice constant. All structure consisting of slabs were relaxed until the largest interatomic force was smaller than or equal to 0.05 eV/Å. All the molecules were relaxed until the largest interatomic force was smaller than or equal to 0.01 eV/Å. The DFT electronic energies were corrected with zero-point energies and entropic contributions. Zero point energies and entropic contributions at room temperature were obtained by calculating vibration frequencies and employing the harmonic approximation for adsorbates and the ideal gas approximation for gas phase molecules as implemented in ASE/GPAW[3]. To treat the relation between the applied potential and the chemical potential of an proton-electron pair, the computational hydrogen electrode was employed, changing the proton-electron chemical potential by $-eU$[4].

$$\mu_{(H^+ + e^-)}(U) = \frac{1}{2}G_{H_2} - eU \tag{1}$$

thus being able to account for the effect of the applied potential on the energy of potential dependent steps. Adsorption and reaction energies as well as their uncertainties were calculated using methanol, carbon monoxide and the slab as references.

Experimental

The electrochemical tests were conducted in a custom made glass H-type cell, further illustrated in figure 4, based on the design of Funakawa et al[5]. The working and counter compartments were separated with a glass frit. A saturated calomel reference electrode (SCE) potential was placed in a separate compartment and connected to the working electrode compartment and close to the working electrode by the use of a Luggin capillary. The working electrode consisted either of a gold wire (Premion® 99.9985 % Alfa Aesar) or a copper wire (Puratonic® 99.9999 % Alfa Aesar) and was stabilized with a holder made of PFA tubing. Protruding wire from the holder resulted in geometric surface areas of 0.186 and 0.255 cm^2 respectively

for gold and copper. A nordic EC ECi-200 potentialstat/galvanostat was used to apply potential and record current. All measurements were performed at room temperature.

For the electrochemical tests the counter and working electrode compartments each contained 20 mL of electrolyte solution of 0.1 M $NaClO_4 \times H_2O$ dissolved in methanol (ultrapure, spectrophotometric grade 99.8 +% Alfa Aesar). The electrolyte solution in the counter compartment was purged with argon gas continuously. The electrolyte solution in the working compartment was initially purged with argon gas for 5-10 minutes to create an inert atmosphere. CO at atmospheric pressure was subsequently bubbled into the electrolyte to saturate the solution prior to the electrochemical synthesis tests. Constant potential hold tests were conducted each for 30 minutes. Between tests, all components of the cell were rinsed with ultrapure water then methanol.

For the product analysis a gas chromatograph with a flame ionization detector (FID) was used to detect DMC and DMO in the electrolyte solution samples. Calibration for identification and quantification was achieved by using reference samples of known concentration.

Current efficiency (CE) is calculated by the equation below for DMC and DMO respectively.

$$CE_{DMC} = \frac{2DMC[mol] \times F[Cmol^{-}1]}{coulomb[C]} \quad (2)$$

$$CE_{DMO} = \frac{2DMO[mol] \times F[Cmol^{-}1]}{coulomb[C]} \quad (3)$$

where F is Faraday's constant.

Co-products

DMC is not the only chemical that can be produced as it is formed when two methoxy species meet one carbon monoxide species, possibly with the intermediate step of forming a methyl formate species. If two methoxy species meet with two carbon monoxide species, in other words if two methyl formate species are allowed to meet, dimethyl oxalate (DMO) will be made instead. It is in principle also possible that dimethyl peroxide (DMP) will be formed if there is no carbon monoxide in the vicinity of methoxy. This scenario should only be possible on very noble surfaces operating at high potentials as the reaction free energy of DMP is fairly high. In the situation where the electrocatalyst surface binds methanol through the carbon atom (hydroxy methyl), rather than through the oxygen atoms (methoxy), a different range of molecules can be made. Ethylene glycol (EG) can be made equivalently to DMP, dihydroxy acetone (DHA) can be made equivalently to DMC and 1,4-dihydroxybutane-2,3-dione (DHBDO) can be made equivalently to DMO. An additional scenario is possible if the surface binds methoxy and hydroxy methyl with similar strength so that they can co-exist on the surface. Methoxy methanol (MM) can be made equivalently to EG and DMP, methyl glycolate (MG) can be made equivalently to DMC and DHA and methyl-3-hydroxy-2-oxopropanoate (MHOP) can be made equivalently to DMO and DHBDO. When binding methanol through oxygen, as methoxy, it is also possible that dimethyl ether (DME) is produced with the release of carbon dioxide.

Selectivity issues: binding methanol through oxygen or carbon

Figure 3 shows the free energy diagram of DMC and DHA synthesis over gold and copper with and without an applied potential. Again, it can be seen from figure 3 that it is possible to drive the reaction on gold by applying a potential of ≈1.3 V vs RHE thus bringing all the steps down by eU for each proton-electron pair exchanged. The relative energy between the chemical steps is potential independent and remains constant. On gold which binds carbon monoxide weakly there is an uphill step associated with binding carbon monoxide. If methyl formate is made directly without first having to adsorb methoxy and carbon monoxide the reaction could be driven at lower potentials producing DMO instead of DMC as was already discussed. For copper one can observe that after applying a potential of ≈0.2 V vs RHE there is an uphill

step associated with forming methyl formate. The formation of methyl formate is on copper either rate determining or it is possibly avoided by directly forming DMC from two methoxy species and a carbon monoxide as was already discussed. Figure 3 suggests that there will be no selectivity issues arising from binding methanol through carbon on the copper surface but on gold it will be possible to produce DHA and other products associated with binding methanol through carbon. Furthermore, the small difference in methoxy and hydroxy methyl adsortpion energies suggests that gold can, at sufficiently high potentials, yield all the products associated with binding methanol both through carbon and oxygen.

Supplemental tables and figures

Table 1: Reaction free energies calculated from DFT or from thermodynamic tables when available[6]. The experimental values were calculated both using free energies for liquid and gas phase.

Molecules	ΔG_{DFT} / eV	ΔG^{l}_{EXP} / eV	ΔG^{g}_{EXP} / eV
DMC	-0.01 ± 0.12	-0.13	-0.21
DMO	0.26 ± 0.23	NA	NA
DMP	2.77 ± 0.18	NA	NA
EG	0.43 ± 0.08	0.13	0.23
DHA	0.91 ± 0.16	NA	NA
DHBDO	1.18 ± 0.25	NA	NA
MM	0.50 ± 0.08	NA	NA
MG	0.11 ± 0.14	NA	NA
MHOP	0.75 ± 0.23	NA	NA
DME	-0.89 ± 0.13	-0.35	-0.43

Table 2: Adsorption free energies and standard deviation of the ensemble values for carbon monxide (CO), methoxy (M), hydroxy methyl (HM), methyl formate (MF) and glycol aldehyde (GA) on selected fcc (111) surfaces.

Surface	ΔG_{CO} / eV	ΔG_{M} / eV	ΔG_{HM} / eV	ΔG_{MF} / eV	ΔG_{GA} / eV
Ag	0.42 ± 0.13	0.69 ± 0.18	1.55 ± 0.20	0.93 ± 0.22	1.48 ± 0.24
Au	0.33 ± 0.14	1.33 ± 0.13	1.17 ± 0.23	0.84 ± 0.25	1.06 ± 0.26
Cu	-0.06 ± 0.30	0.13 ± 0.23	1.17 ± 0.27	0.43 ± 0.30	1.03 ± 0.33
Ir	-1.24 ± 0.21	0.56 ± 0.20	0.48 ± 0.16	-0.09 ± 0.24	0.05 ± 0.23
Ni	-0.90 ± 0.15	0.04 ± 0.24	0.61 ± 0.19	-0.06 ± 0.25	0.31 ± 0.24
Pd	-0.59 ± 0.16	0.79 ± 0.22	0.50 ± 0.20	0.07 ± 0.23	0.33 ± 0.24
Pt	-0.91 ± 0.25	0.94 ± 0.21	0.25 ± 0.19	-0.13 ± 0.22	0.14 ± 0.23
Rh	-1.09 ± 0.17	0.31 ± 0.23	0.52 ± 0.22	-0.06 ± 0.24	0.15 ± 0.24
Ru	-1.20 ± 0.19	-0.28 ± 0.21	0.73 ± 0.15	-0.19 ± 0.23	0.55 ± 0.21
Sn	0.39 ± 0.09	0.32 ± 0.21	1.23 ± 0.18	0.81 ± 0.22	1.36 ± 0.22

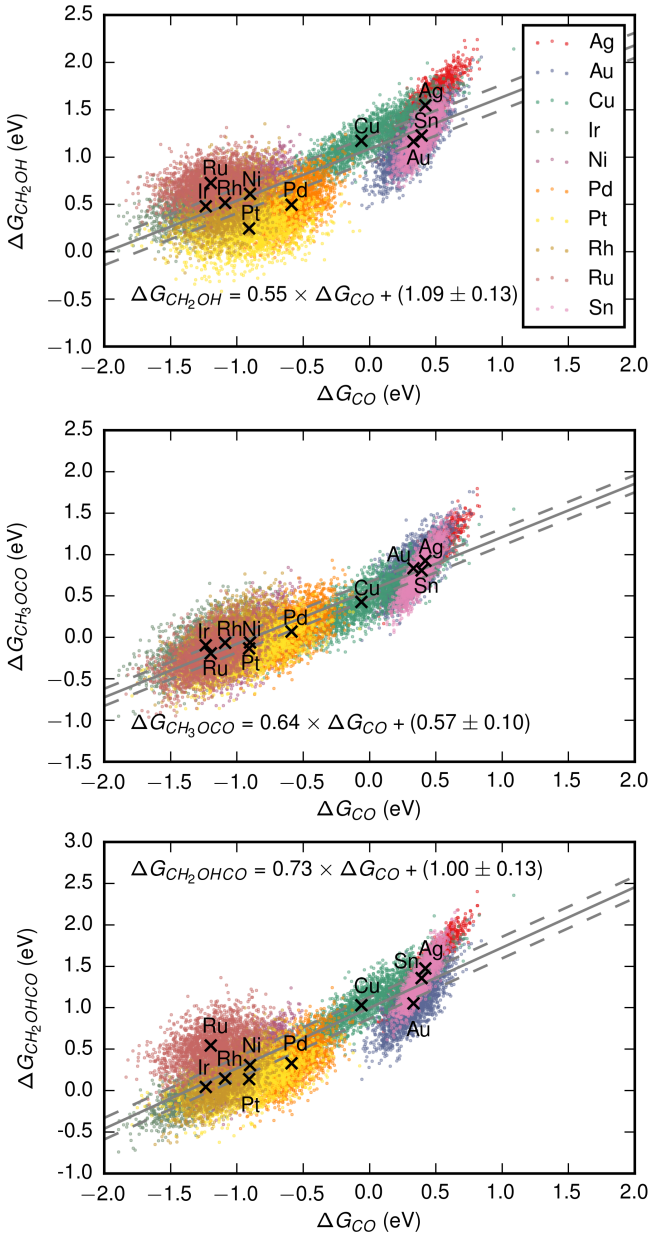

Figure 1: Scaling relations between carbon monoxide and reaction intermediates that bind on metals through a carbon atom. The colored scatter plots show the ensemble values for each metal.

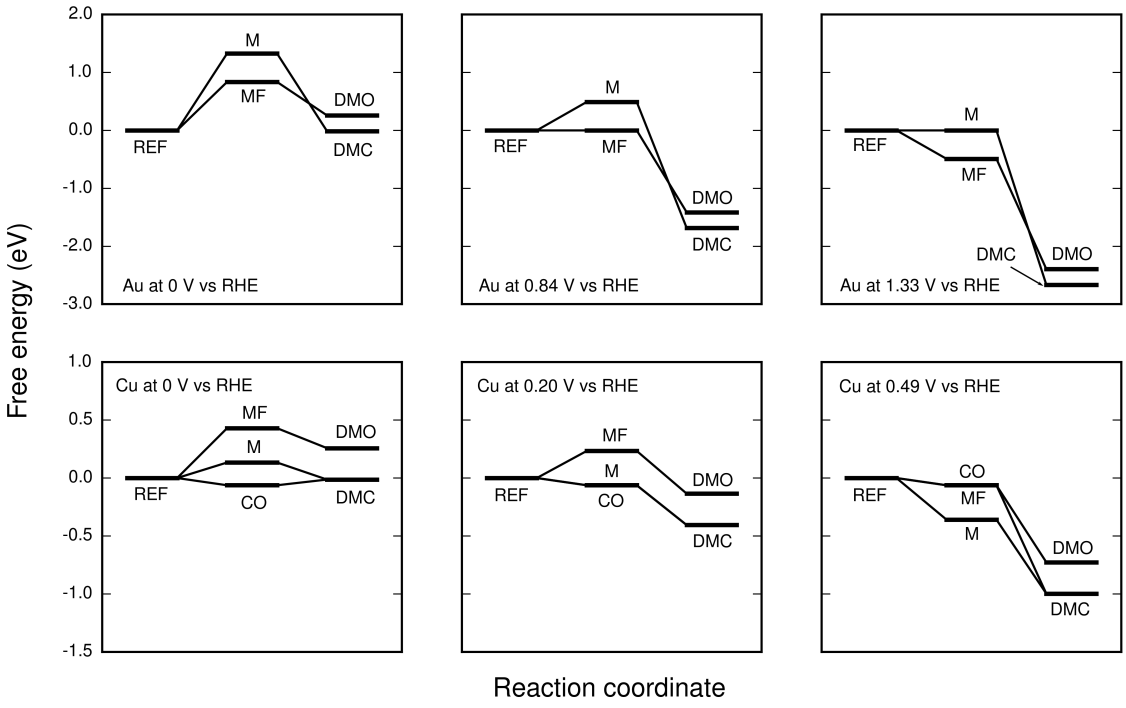

Figure 2: Free energy diagrams showing the selectivity dependence on potential for gold and copper.

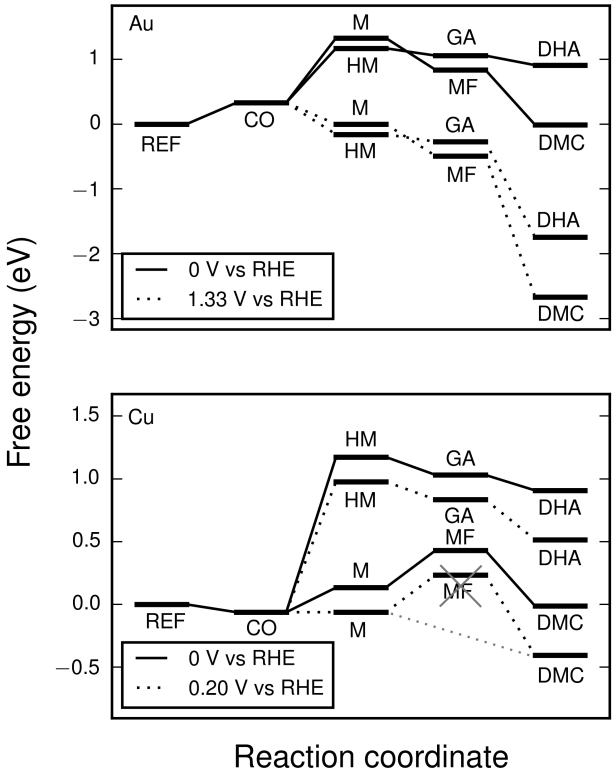

Figure 3: Free energy diagrams of DMC and DHA formation at 0 V and at 1.33 V on gold (top) and at 0 V and 0.20 V on copper (bottom) showing the affinity for binding methanol through carbon or oxygen.

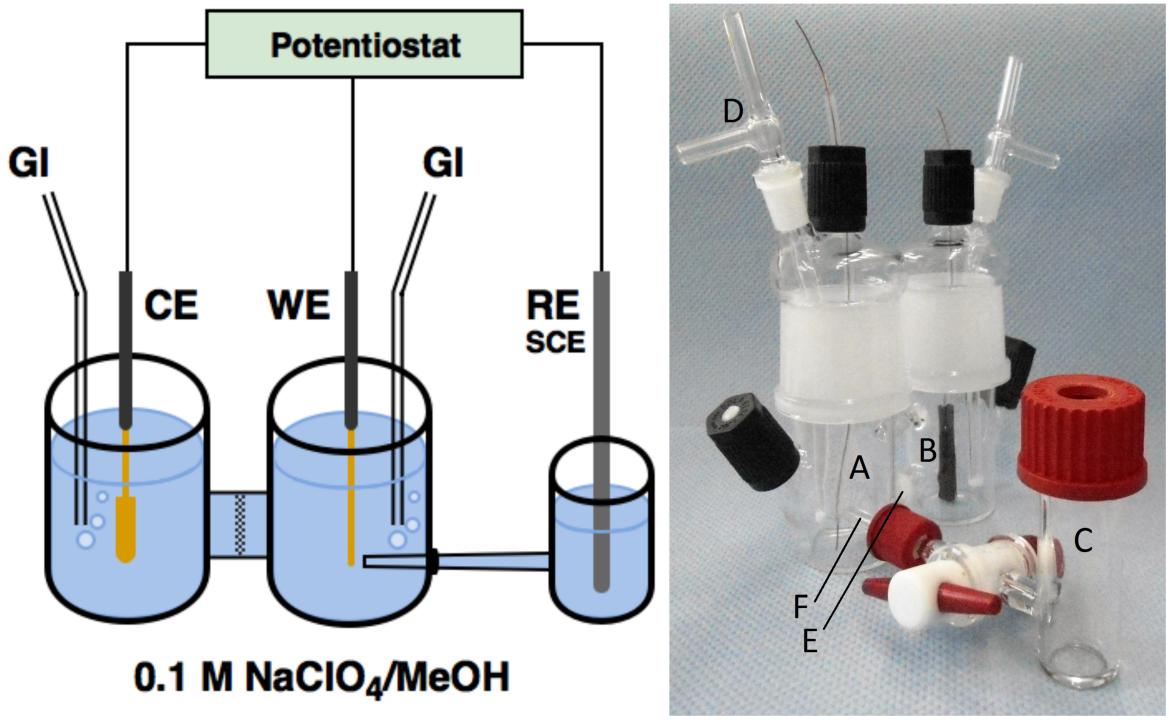

Figure 4: The schematic (left) of the H-cell used for synthesizing dimethyl carbonate. The working electrode (WE), counter electrode (CE), reference electrode (RE) and gas inlet (GI) are indicated. The electrolyte for each compartments was 0.1 M NaClO4/MeOH. The working compartment was separated from the counter compartment by a porous glass frit and a Luggin-like capillary tube was used to reduce the effect of electrolyte resistance between the working and reference electrode. Photo (right) of the H-cell used for synthesizing dimethyl carbonate, labelled with working electrode (A), counter electrode (B), reference electrode compartment (C), gas in/out (D), porous glass frit (E), Luggin capillary (F).

References

[1] Mortensen, J.J., Hansen, L.B. & Jacobsen, K.W. Real-space grid implementation of the projector augmented wave method *Physical Review B* **71**, 1-11 (2005).

[2] Enkovaara, J. et al. Electronic structure calculations with GPAW: a real-space implementation of the projector augmented-wave method *Journal of Physics: Condensed Matter* **22** 1-24 (2010).

[3] Atomic Simulation Environment - Thermochemistry,
https://wiki.fysik.dtu.dk/ase/ase/thermochemistry/thermochemistry.html,
Accessed on: 16.03.2016.

[4] Nørskov, J.K., Bligaard, T., Rossmeisl, J. & Christensen, C.H. Towards the computational design of solid catalysts, *Nature Chemistry* **1**, 37-46, (2009).

[5] Funakawa, A., Yamanaka, I. & Otsuka, K. Active control of methanol carbonylation selectivity over Au/carbon anode by electrochemical potential, *J. Phys. Chem. B* **109**, 9140-9147 (2005).

[6] Perry, R.H. & Green, D.W. *Perry's Chemical Engineers' Handbook* Appendix B - Physical Properties pp. 641-672 (McGraw-Hill, New York, 1984)

5.2 Paper II: Relation between HER and HDS

Relation between hydrogen evolution and hydrodesulfurization catalysis

M. Šarić, P.G. Moses, J. Rossmeisl

Published in ChemCatChem, 2016.

ChemPubSoc Europe

DOI: 10.1002/cctc.201601014

CHEMCATCHEM Communications

Relation between Hydrogen Evolution and Hydrodesulfurization Catalysis

Manuel Šarić,[b] Poul Georg Moses,[c] and Jan Rossmeisl*[a]

A relation between hydrogen evolution and hydrodesulfurization catalysis was found by density functional theory calculations. The hydrogen evolution reaction and the hydrogenation reaction in hydrodesulfurization share hydrogen as a surface intermediate and, thus, have a common elementary step, which indicates that the same catalyst should perform well for both hydrogen evolution and hydrogenation. If that catalyst also fulfills additional criteria for breaking carbon–sulfur bonds and releasing hydrogen sulfide, it will be a good hydrodesulfurization catalyst. The hydrogen evolution reaction is normally performed at room temperature and standard pressure, whereas the hydrodesulfurization reaction is driven by high temperature and pressure. Owing to the very different operating conditions, the adsorption free energy of hydrogen differs between hydrodesulfurization and the hydrogen evolution reaction, which makes the connection between the two less obvious.

In the search for non-noble catalysts that could replace platinum for the acidic hydrogen evolution reaction (HER), it is interesting to consider hydrodesulfurization (HDS)[1–12] catalysts, as they usually prove to be good HER catalysts. Various recent studies have drawn connections between the HER and HDS, and it has been reported that catalysts that are good for HDS are good candidates for the HER.[13–19] Even though the HER and HDS occur under very different conditions, they both involve hydrogen atoms adsorbed on the surface, as described by Figure 1, and this points to a fundamental connection in the way certain parts of these reactions operate at the atomic scale.

HDS reactions require hydrogenation steps in which hydrogen is transferred from the surface of the catalyst to the molecule being desulfurized.[2] These steps are part of a C–S cleavage reaction [Eq. (1)]

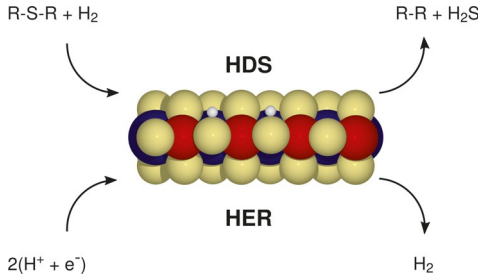

Figure 1. Sketch of the HER and HDS on the CoMoS catalysts pointing out that both processes involve surface hydrogen as an intermediate. The red, blue, yellow, and white spheres represent cobalt, molybdenum, sulfur, and hydrogen, respectively.

$$R{-}SH + H_2 \leftrightarrow R{-}H + H_2S \quad (1)$$

and a hydrogenation reaction [Eq. (2)] of unsaturated organic compounds

$$R{-}CH{=}CH{-}R + H_2 \leftrightarrow R{-}CH_2{-}CH_2{-}R \quad (2)$$

in which R is the main body of a hydrocarbon or aromatic molecule.

To perform hydrogenation reactions, it is necessary to split hydrogen molecules present in the gas phase through a reaction on the surface following the Langmuir–Hinshelwood mechanism [Eq. (3)]:

$$H_2 + 2^* \leftrightarrow 2H^* \quad (3)$$

in which * represents a site on the catalyst. This process is driven by the high chemical potential of hydrogen under HDS conditions. After the reaction, hydrogen atoms on the surface become available for hydrogenating molecules.

The necessity of having hydrogen on the surface available for hydrogenation links HDS to the HER, for which the Tafel reaction [Eq. (4)]:

$$2H^* \leftrightarrow H_2 + 2^* \quad (4)$$

along with the Volmer reaction [Eq. (5)]:

$$(H^+ + e^-) + ^* \leftrightarrow H^* \quad (5)$$

and the Heyrovsky reaction [Eq. (6)]:

$$H^* + (H^+ + e^-) \leftrightarrow H_2 + ^* \quad (6)$$

[a] Prof. J. Rossmeisl
Department of Chemistry
Copenhagen University
Universitetsparken 5, 2100 København Ø (Denmark)
E-mail: Jan.Rossmeisl@chem.ku.dk

[b] M. Šarić
Center for Atomic Scale Materials Design (CAMd)
Department of Physics
Technical University of Denmark
Fysikvej building 307, 2800 Kgs. Lyngby (Denmark)

[c] Dr. P. G. Moses
Haldor Topsøe A/S
Nymøllevej 55, 2800 Kgs. Lyngby (Denmark)

Supporting Information for this article can be found under http://dx.doi.org/10.1002/cctc.201601014.

make up the whole process.[20] Looking at the Tafel reaction [Eq. (4)] and the hydrogen splitting reaction in HDS [Eq. (3)] one can notice that they are the same elementary reaction only reversed, for which the reactants of one reaction are the products of the other reaction and vice versa. This points to a fundamental connection between the two processes.

The adsorption energies from Moses et al.[5] corrected to adsorption free energies to match the HER and HDS conditions are shown in Table 1.

Table 1. Adsorption energies of H and SH[5] and adsorption free energies under the HER (298.15 K and 0.1 MPa) and HDS (573 K and 3.8 MPa) conditions for H on transition-metal sulfide surfaces.

Surface	ΔE_{ads}(H) [eV]	ΔG_{ads}(H)$_{HER}$ [eV]	ΔG_{ads}(H)$_{HDS}$ [eV]	ΔE_{ads}(SH) [eV]
MoS_2 ($\bar{1}010$)	−0.42	−0.19	−0.11	−0.82
MoS_2 ($10\bar{1}0$)	−0.24	−0.01	0.07	0.48
CoMoS ($\bar{1}010$)	−0.19	0.04	0.12	0.26
$Co_{0.5}Mo_{0.5}S$ ($\bar{1}010$)	−0.32	−0.09	−0.01	−0.07
NiMoS ($\bar{1}010$)	−0.38	−0.15	−0.07	0.30
WS_2 ($\bar{1}010$)	−0.36	−0.13	−0.05	−1.04
WS_2 ($10\bar{1}0$)	−0.07	0.16	0.24	0.85
TaS_2 ($\bar{1}010$)	−0.29	−0.06	0.02	−0.35
TaS_2 ($10\bar{1}0$)	−0.31	−0.08	0.00	0.58
NbS_2 ($\bar{1}010$)	−0.43	−0.20	−0.12	−0.31
NbS_2 ($10\bar{1}0$)	−0.43	−0.20	−0.12	1.19
RuS_2 (111)	−0.56	−0.33	−0.25	0.42
RuS_2 (100)	0.78	1.01	1.09	−0.01
FeS (001)	0.25	0.48	0.56	−0.05

For the HER, the adsorption energy of hydrogen determines the driving force or overpotential needed to obtain a high current and, thus, the efficiency of the reaction. Because the HER involves only one surface intermediate, namely, hydrogen, the optimal catalyst has to have an adsorption free energy of zero towards hydrogen so that it does not bind hydrogen too weakly or too strongly, but just right. The Sabatier principle leads to a volcano plot for the HER with its maximum found at zero adsorption free energy of hydrogen.[21–23]

For HDS, it has been found that the adsorption energy of SH can be used as a descriptor, which suggests that the rate-determining step for HDS is normally related to sulfur chemistry. Scaling relations between the adsorption energy of SH and the barrier for carbon–sulfur bond cleavage as well as site regeneration have been established. From the scaling relations it was found that the maximum rate of the reaction occurs on materials that bind SH with an adsorption energy of approximately 0.1 eV.[5] Looking at the Sabatier plot from Moses et al.,[5] one can see that surfaces such as CoMoS ($\bar{1}010$), NiMoS ($\bar{1}010$), FeS (001), and RuS_2 (100) are closest to the adsorption energy of 0.1 eV towards SH and, as a consequence, are closest to the top of the volcano having the highest HDS rate. At the same time, by observing Figure 2 it can be seen that most sulfides that are usually considered when searching for better HDS catalysts have favorable binding of hydrogen for the HER. RuS_2 (100) is an outlier that does not have a favorable binding of hydrogen for the HER, which indicates that the HDS process

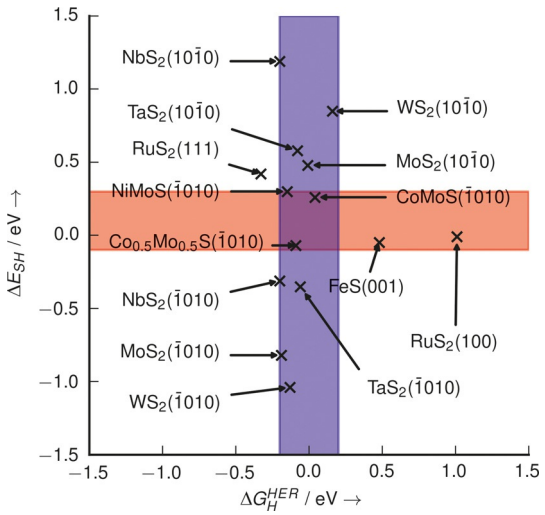

Figure 2. Relation between the descriptors for HDS and the HER for transition-metal sulfides. Good HDS catalysts will scatter around $\Delta E_{SH} = 0.1$ eV (red zone) and good HER catalysts around $\Delta G_H = 0$ eV (blue zone).

probably happens on the interface between RuS_2 (100) and RuS_2 (111). The same can be assumed for FeS (001).

From Figure 3 it can be seen that there can be an uphill step for splitting hydrogen and adsorbing it on the surface, but once the hydrogen is adsorbed the rest of the HDS process is thermodynamically downhill, which creates a driving force for desulfurization. One can also see that the energy required for hydrogen adsorption is higher under the HDS conditions than under the HER conditions. This is a result of the higher temperature needed for HDS relative to that of the HER conditions, which stabilizes the gas-phase hydrogen species more than the high pressure stabilizes the adsorbed hydrogen species. The presence of higher energy steps in binding hydrogen is not an issue owing to the higher temperature and the fact that gas-phase reactions have a much higher attempt frequency than electrochemical reactions.[22] As such, it is possible to have a higher energy step under the HDS conditions than under the HER conditions while still maintaining a high rate.

It is known that NiMoS (−1010) is used instead of CoMoS ($\bar{1}010$) if a high degree of hydrogenation is required.[24] Looking at the free-energy diagram in Figure 3, one can see that NiMoS ($\bar{1}010$) is not the best catalyst in terms of the HER and that CoMoS ($\bar{1}010$) will perform better. Consequently, the best HER catalyst will not at the same time be the best hydrogenation catalyst under HDS conditions because of the shift in the hydrogen adsorption energy.

With the present data it is not possible to quantify the optimal hydrogen adsorption free energy for HDS; however, it will have a value that enables the right trade-off between hydrogen dissociation and providing the driving force required for the hydrogenation steps, as shown in Figure 4. As long as the hydrogen binding energy is not so weak that splitting hydrogen becomes the rate-limiting step or so strong that hydrogenation becomes rate limiting, then the rate of the HDS process will be determined by the activation energy required to cleave the first carbon–sulfur bond.[5,6] Consequently, HDS catalysts

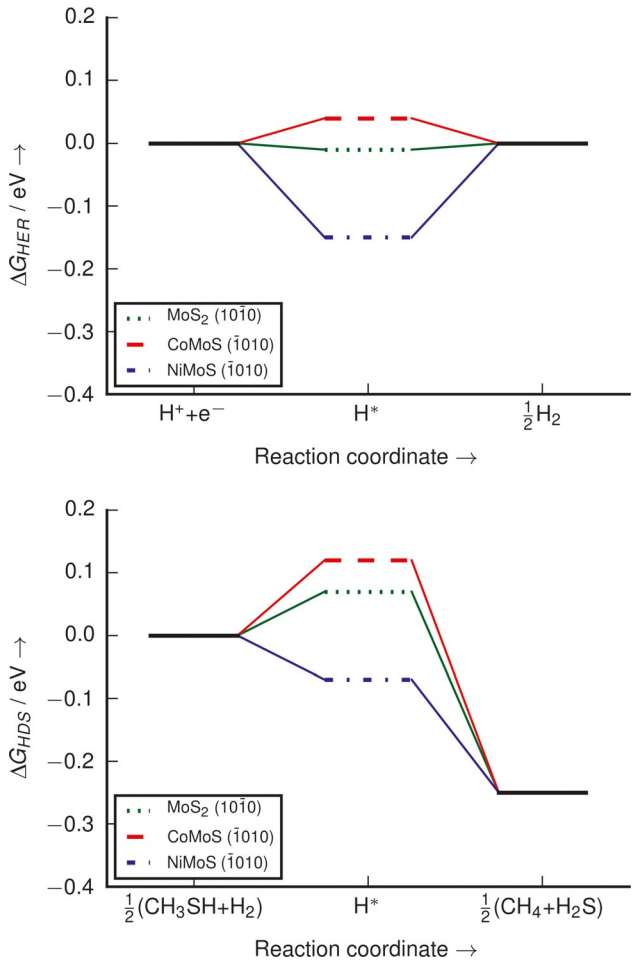

Figure 3. Free-energy diagrams showing the energetics of hydrogen adsorption under the context and conditions of the HER (top) and HDS (bottom) for three commonly used HDS catalysts.

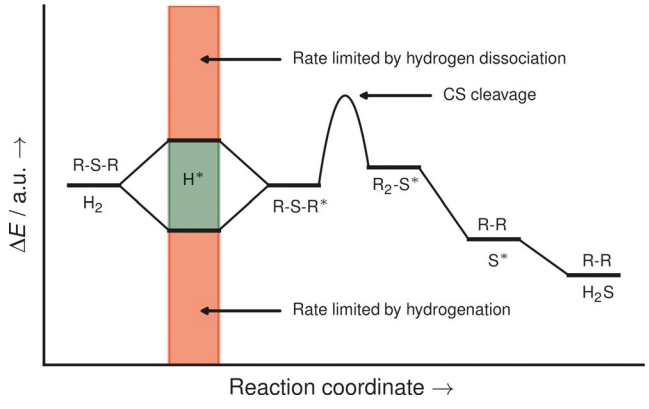

Figure 4. Sketch of a hypothetical energy diagram for HDS pointing out the right zone (green) for hydrogen adsorption.

will be materials that, besides binding SH with the right strength, have to have an adsorption free energy of hydrogen that falls in the right range.

By analyzing the present data and observations from various authors,[13–18] a correlation between hydrogenation and the HER can be observed, and it indicates that even though the conditions are very different for the HER and HDS, there are similar requirements for HDS and HER catalysts in terms of hydrogen binding. We conclude that the right hydrogen chemistry is a necessary but not sufficient requirement for a good HDS catalyst, which points to the importance of considering the adsorption free energy of hydrogen as a descriptor of HDS and at the same time explains the chemistry behind the observation that good HDS catalysts are good candidates for the HER.

Experimental Section

The density functional theory code GPAW[25,26] was employed to calculate the total energies and vibrational frequencies to get the reaction free energy of hydrodesulfurization of CH_3SH and CH_3SCH_3 and for applying thermodynamic corrections to the values from Moses et al.[5] Finite difference mode with a grid spacing of 0.18 Å with the RPBE exchange correlation functional was used. All the structures were optimized until the maximum force was less than or equal to 0.05 eV Å^{-1}. The free energies of molecules were calculated according to the following [Eq. (7)]:

$$G^{p,T}_{gas} = E + E_{ZP} + \Delta H^{0,T}_{gas} - TS^{T}_{gas} + k_B T \ln\left(\frac{p}{p^0}\right) \quad (7)$$

in which E is the electronic energy at 0 K, E_{ZP} is the zero-point contribution to the energy, $\Delta H^{0,T}_{gas}$ is the change in enthalpy on going from 0 K to higher temperatures, S^{T}_{gas} is the entropy term at a specific temperature, k_B is the Boltzmann constant, p is the partial pressure of the gas, and p° is the standard pressure. The enthalpy and entropy terms needed for calculating the free energies regarding H_2 and H_2S were obtained from thermodynamic tables.[27,28] The enthalpy and entropy terms for CH_3SH and CH_3SCH_3 were not available in standard thermochemical tables and were thus obtained from the calculated vibrational frequencies and the ideal gas approximation as implemented in ASE/GPAW.[29] The free energy of adsorbed species was calculated as [Eq. (8)]:

$$G^{T}_{ads} = E + E_{ZP} + \Delta U^{0,T}_{vib} - TS^{T}_{vib} \quad (8)$$

in which $\Delta U^{0,T}_{vib}$ is the change in internal energy of an adsorbate on going from 0 K to a specific temperature and S^{T}_{vib} is the entropy of an adsorbate at a specific temperature. The zero-point energy, the change in internal energy on going from 0 K to HER and HDS conditions, and the entropy term under HER and HDS conditions for hydrogen adsorbed on CoMoS ($\bar{1}010$) were obtained by calculating the vibrational frequencies by using the stripe model from Moses et al.[5] with a Brillouin zone sampling of 4×1×1 k-points and by employing the harmonic approximation [Eqs. (9)–(11)]:

$$E_{ZP} = \frac{1}{2}\sum_i h\nu_i \quad (9)$$

$$TS^{T}_{vib} = \sum_i \frac{h\nu_i}{e^{h\nu_i/k_BT} - 1} - k_B T \sum_i \ln\left(1 - e^{-h\nu_i/k_BT}\right) \quad (10)$$

$$\Delta U^{0,T}_{vib} = \sum_i \frac{h\nu_i}{e^{h\nu_i/k_BT} - 1} \quad (11)$$

in which ν_i are the vibrational frequencies calculated from GPAW and h is the Planck constant. It was assumed that the corrections obtained for hydrogen on CoMoS ($\bar{1}010$) could be applied to the rest of the sulfides from Moses et al.[5] The reaction free energies of desulfurization of CH_3SH and CH_3SCH_3 normalized to the same amount of hydrogen were calculated according to the following equations [Eqs. (12) and (13)]:

$$CH_3SH + H_2 \leftrightarrow CH_4 + H_2S \quad (12)$$

$$^1/_2\, CH_3SCH_3 + H_2 \leftrightarrow CH_4 + {}^1/_2\, H_2S \quad (13)$$

HER conditions were taken as 298.15 K and 0.1 MPa of hydrogen. HDS conditions were taken from Moses et al.[5] as 573 K and partial pressures of 3.8 and 0.013 MPa for H_2 and H_2S, respectively. The partial pressures of the carbon-containing molecules were assumed to be 0.1 MPa. The reaction free energies were found to have similar values of approximately −0.5 eV. Calculating the free energies of H_2 and H_2S by using the ideal gas approximation as was done for CH_3SH and CH_3SCH_3 yielded results that differed only by 0.02 eV, which confirmed the obtained thermodynamic corrections.

Acknowledgements

This work was supported by the Danish Council for Independent Research and the Carlsberg Foundation.

Keywords: density functional calculations · heterogeneous catalysis · hydrodesulfurization · hydrogen · sulfur

[1] I. Babich, J. Moulijn, *Fuel* **2003**, *82*, 607.
[2] G. Schuit, B. Gates, *AIChE J.* **1973**, *19*, 417.
[3] J. Lauritsen, M. Nyberg, J. K. Nørskov, B. Clausen, H. Topsøe, E. Lægsgaard, F. Besenbacher, *J. Catal.* **2004**, *224*, 94.
[4] P. G. Moses, B. Hinnemann, H. Topsøe, J. K. Nørskov, *J. Catal.* **2009**, *268*, 201.
[5] P. G. Moses, L. C. Grabow, E. M. Fernandez, B. Hinnemann, H. Topsøe, K. G. Knudsen, J. K. Nørskov, *Catal. Lett.* **2014**, *144*, 1425.
[6] P. G. Moses, B. Hinnemann, H. Topsøe, J. K. Nørskov, *J. Catal.* **2007**, *248*, 188.
[7] B. Hinnemann, P. G. Moses, J. K. Nørskov, *J. Phys. Condens. Matter* **2008**, *20*, 064236.
[8] J. V. Lauritsen, R. T. Vang, F. Besenbacher, *Catal. Today* **2006**, *111*, 34.
[9] J. V. Lauritsen, J. Kibsgaard, G. H. Olesen, P. G. Moses, B. Hinnemann, S. Helveg, J. K. Nørskov, B. S. Clausen, H. Topsøe, E. Lægsgaard, *J. Catal.* **2007**, *249*, 220.
[10] J. Lauritsen, S. Helveg, E. Lægsgaard, I. Stensgaard, B. Clausen, H. Topsøe, F. Besenbacher, *J. Catal.* **2001**, *197*, 1.
[11] Á. Logadóttir, P. G. Moses, B. Hinnemann, N.-Y. Topsøe, K. G. Knudsen, H. Topsøe, J. K. Nørskov, *Catal. Today* **2006**, *111*, 44.
[12] R. Prins, M. Egorova, A. Röthlisberger, Y. Zhao, N. Sivasankar, P. Kukula, *Catal. Today* **2006**, *111*, 84.
[13] C. G. Morales-Guio, L.-A. Stern, X. Hu, *Chem. Soc. Rev.* **2014**, *43*, 6555.
[14] E. J. Popczun, J. R. McKone, C. G. Read, A. J. Biacchi, A. M. Wiltrout, N. S. Lewis, R. E. Schaak, *J. Am. Chem. Soc.* **2013**, *135*, 9267.
[15] M. H. Hansen, L.-A. Stern, L. Feng, J. Rossmeisl, X. Hu, *Phys. Chem. Chem. Phys.* **2015**, *17*, 10823.
[16] J. Kibsgaard, Z. Chen, B. N. Reinecke, T. F. Jaramillo, *Nat. Mater.* **2012**, *11*, 963.
[17] T. F. Jaramillo, K. P. Jørgensen, J. Bonde, J. H. Nielsen, S. Horch, I. Chorkendorff, *Science* **2007**, *317*, 100.
[18] D. Merki, X. Hu, *Energy Environ. Sci.* **2011**, *4*, 3878.
[19] H. Li, C. Tsai, A. L. Koh, L. Cai, A. W. Contryman, A. H. Fragapane, J. Zhao, H. S. Han, H. C. Manoharan, F. Abild-Pedersen, J. K. Nørskov, X. Zheng, *Nat. Mater.* **2016**, *15*, 48.
[20] E. Skúlason, G. S. Karlberg, J. Rossmeisl, T. Bligaard, J. Greeley, H. Jónsson, J. K. Nørskov, *Phys. Chem. Chem. Phys.* **2007**, *9*, 3241.
[21] B. Hinnemann, P. G. Moses, J. Bonde, K. P. Jørgensen, J. H. Nielsen, S. Horch, I. Chorkendorff, J. K. Nørskov, *J. Am. Chem. Soc.* **2005**, *127*, 5308.
[22] J. K. Nørskov, T. Bligaard, A. Logadottir, J. Kitchin, J. Chen, S. Pandelov, U. Stimming, *J. Electrochem. Soc.* **2005**, *152*, J23.
[23] R. Parsons, *Trans. Faraday Soc.* **1958**, *54*, 1053.
[24] P. Torres-Mancera, J. Ramírez, R. Cuevas, A. Gutiérrez-Alejandre, F. Murrieta, R. Luna, *Catal. Today* **2005**, *107*, 551.
[25] J. J. Mortensen, L. B. Hansen, K. W. Jacobsen, *Phys. Rev. B* **2005**, *71*, 035109.
[26] J. Enkovaara, C. Rostgaard, J. J. Mortensen, J. Chen, M. Dułak, L. Ferrighi, J. Gavnholt, C. Glinsvad, V. Haikola, H. Hansen, *J. Phys. Condens. Matter* **2010**, *22*, 253202.
[27] NIST, *Vol. 2016*, http://kinetics.nist.gov/janaf/html/H-050.html, p. H2 thermochemical table.
[28] NIST, *Vol. 2016*, http://kinetics.nist.gov/janaf/html/H-080.html, p. H2S thermochemical table.
[29] ASE, *Vol. 2016*, https://wiki.fysik.dtu.dk/ase/ase/thermochemistry/thermochemistry.html, p. ASE thermochemistry.

Received: August 16, 2016
Published online on October 4, 2016

5.3 Paper III: Sterical effects in adsorbing 4,6-DMDBT on CoMoS

Atomic scale analysis of sterical effects in the adsorption of 4, 6-dimethyldibenzothiophene on a CoMoS hydrotreating catalyst

S.S. Grønborg, M. Šarić, P.G. Moses, J. Rossmeisl, J.V. Lauritsen

Published in Journal of Catalysis, 2016.

Journal of Catalysis 344 (2016) 121–128

Contents lists available at ScienceDirect

Journal of Catalysis

journal homepage: www.elsevier.com/locate/jcat

Atomic scale analysis of sterical effects in the adsorption of 4,6-dimethyldibenzothiophene on a CoMoS hydrotreating catalyst

Signe S. Grønborg [a], Manuel Šarić [b], Poul G. Moses [d], Jan Rossmeisl [c], Jeppe V. Lauritsen [a,*]

[a] Interdisciplinary Nanoscience Center (iNANO), Aarhus University, Denmark
[b] Center for Atomic-scale Materials Design, Department of Physics, Technical University of Denmark, Denmark
[c] Department of Chemistry, Copenhagen University, Denmark
[d] Haldor Topsøe A/S, Kgs. Lyngby, Denmark

ARTICLE INFO

Article history:
Received 4 July 2016
Revised 30 August 2016
Accepted 3 September 2016

Keywords:
Scanning tunneling microscopy
Density functional theory
CoMoS
Hydrotreating
Hydrodesulfurization
Ultra-low sulfur diesel
Sterical hindrance

ABSTRACT

The low catalytic hydrodesulfurization (HDS) activity toward sterically hindered sulfur-containing molecules is a main industrial challenge in order to obtain ultra-low sulfur diesel. In this study we report a combined Scanning Tunneling Microscopy (STM) and Density Functional Theory (DFT) investigation of the adsorption of the sterically hindered sulfur-containing molecule 4,6-dimethyldibenzothiophene (4,6-DMDBT) onto a hydrotreating model catalyst for the Co promoted MoS_2 (CoMoS) phase. The molecular adsorption occurs exclusively on the Co-promoted S-edge, most predominantly in a precursor-like diffusive physisorption referred to as delocalized π-mode. 4,6-DMDBT adsorption directly in a S-edge sulfur vacancy is observed exclusively in S-edge corner vacancies in an adsorption configuration reflecting a σ-coordination. STM movies reveal dynamic conversion between the σ-mode and an on-top π-adsorption providing a link between different adsorption sites and hence between the hydrogenation and direct desulfurization pathways in HDS. The low overall direct desulfurization activity of 4,6-DMDBT and related molecules is consistent with the low occurrence of S-vacancies on CoMoS S-edges predicted under HDS conditions in this study.

1. Introduction

In hydrodesulfurization (HDS) catalysis, a major challenge is the removal of sulfur from sterically hindered sulfur-containing molecules containing sulfur in a position spatially shielded by the remaining functional groups of the molecule [1]. Improvement on this matter is of key importance to meet with new legislation demanding still lower sulfur content for transportation fuels [2–4] and the catalysis industry is hence compelled to find novel methods to increase the catalytic reactivity toward the refractory sulfur, mainly locked up in sterically hindered molecules.

This category of molecules includes alkyl-substituted dibenzothiophenes (DBT) among which the hardest to desulfurize are those having the alkyl placed in the 4th and/or 6th position of the molecule [5] such as 4-methyldibenzothiophene (4-MDBT) and 4,6-dimethyldibenzothiophene (4,6-DMDBT), respectively. These molecules are especially challenging as the position of the methyl groups causes the sulfur atom to be spatially unavailable for adsorption [6,5]. Such components (4-DMDBT, 4,6-DMDBT and related molecules) are responsible for the majority of the residual sulfur content in the refined crude oil and hence generate a lower bar for the sulfur content in the treated oil. In order to increase the catalytic activity a deeper fundamental understanding of the molecular interaction between this category of molecules and the catalyst is needed.

Cobalt promoted single-layer MoS_2 (CoMoS) is the active phase of the MoS_2-based industrial HDS catalyst. The CoMoS structure has been revealed in detail in previous atom-resolved microscopy and theory studies to reflect predominantly hexagonal MoS_2-like nanoparticles terminated by two different edge types called Mo-edge and S-edge. The structural effect of the cobalt was concluded to be related to a selective substitution of Mo atoms along the S-edge [7–12]. In the literature there is broad consensus that the desulfurization activity of the CoMoS catalyst proceeds through two different pathways: the direct desulfurization (DDS) and the hydrogenation (HYD) pathway [13–16]. In the DDS pathway the sulfur atom is directly cleaved from the molecule upon hydrogenolysis of the C—S bonds, whereas in the HYD pathway the hydrogenation of the aromatic ring happens prior to desulfurization [14,17,18]. Studies have suggested that DDS and HYD occur at different active sites [19] and it has further been proposed that a

* Corresponding author.
E-mail address: jvang@inano.au.dk (J.V. Lauritsen).

http://dx.doi.org/10.1016/j.jcat.2016.09.004
0021-9517/

diffusion step may be necessary for the HYD pathway [20–22]. The sulfur extrusion involved in both the DDS pathway and as the final step in the HYD pathway is believed to happen through molecular interaction with coordinative unsaturated sites (CUS) on the cluster edge, such as sulfur vacancies. There exists, however, some debate in the literature about the nature of such CUS and their role in the DDS and HYD pathway. Furthermore are S—H groups on the cluster edge speculated to be involved in both pathways as the source of H.

The sterically hindered sulfur containing molecules such as alkyl substituted DBTs (e.g. 4-MDBT and 4,6-DMDBT) are primarily desulfurized through the HYD pathway and generally have a very low DDS reactivity. The HYD pathway has the advantage that bonding flexibility is added by hydrogenating the benzene rings of the DBTs which distorts the planar structure of the molecule, allowing additional available adsorption-configurations onto sulfur vacancies which are generally believed to be unavailable for direct adsorption of the intact alkyl-substituted DBTs. Several adsorption geometries on MoS_2 have been considered for the HYD active sites including multiple vacancies and perimeter sites. It has been proposed that the first hydrogenation step in the reaction for sterically hindered molecules in the HYD pathway occurs in a planar configuration in which the molecule is adsorbed onto the cluster interacting through the conjugated π-system of the molecules [23]. Studies have proposed the active site for the HYD pathway to be the perimeter sites along the cluster edges, denoted the cluster brim. The conclusion was based on STM studies which first showed that the MoS_2 edges express a modified electronic structure visible as a bright brim in STM images [24], together with the finding that the small π-conjugated molecules, such as thiophene and pyridine preferentially interact with the brim of unpromoted MoS_2 nanoclusters [22,20,25].

Relative to the unpromoted MoS_2 nanoclusters, molecular adsorption is less studied on CoMoS due to the more complex morphology of the system arising from an additional element, Co, and the presence of two, instead of one, edge types in the CoMoS structure [26,7] (further discussed in Section 3.1). Previously DBT, 4-MDBT and 4,6-DMDBT adsorption on unpromoted MoS_2 has been studied; however, for CoMoS only DBT adsorption was reported until now [27].

Here we combine Scanning Tunneling Microscopy (STM) imaging and Density Functional Theory (DFT) calculations to study the adsorption of 4,6-DMDBT on a well-characterized CoMoS model system [10,7]. We activate the CoMoS phase by exposing the sample to atomic hydrogen to introduce S—H groups and sulfur vacancies to the cluster edges and then investigate the available adsorption modes. The most predominant 4,6-DMDBT adsorption mode appears on top of the cluster brim and we exclusively see this interaction on the Co-promoted S-edge on the CoMoS nanocluster as a diffusive π-bonded species. This configuration is considered to be a possible precursor state for HYD reaction as the mobility of the molecule indicates that it can scavenge multiple H atoms adsorbed on the edge sulfurs under HDS conditions. Static chemisorption of 4,6-DMDBT is observed in the experiment exclusively in corner S-vacancies in a σ-bonded adsorption, which is considered a precursor state to direct sulfur extrusion. Interestingly it was observed in a STM movie that the σ-adsorbed 4,6-DMDBT could reversibly transform into a static π-mode adsorption revealing strong evidence for a direct link between the adsorption on brim and sulfur vacancies. To explore the possible extent of the static chemisorption of 4,6-DMDBT in a corner vacancy, under catalytic relevant conditions, the vacancy formation energies were calculated for HDS conditions. The calculations however, predict a very low concentration of corner vacancies in CoMoS under HDS conditions and hence explain the low DDS activity for 4,6-DMDBT in the industrial catalyst and, thus, confirm the preference for this molecule to react through the HYD pathway.

2. Experimental

2.1. Scanning tunneling microscopy

The experiment is carried out in a homebuilt, standard ultra-high vacuum (UHV) chamber equipped with a homebuilt Aarhus type STM. The synthesis is made on a Au(1 1 1) single crystal cleaned using sputtering and anneal cycles. The CoMoS nanoclusters were synthesized by e-beam evaporation of Mo and Co in an H_2S atmosphere as reported in [10,7]. H_2S was dosed into the chamber through a doser tube providing a controlled leak from a high pressure reservoir. This resulted in a local H_2S pressure at approximately 10^{-6} mbar at the sample surface. Simultaneously, Mo was evaporated onto the surface at a deposition rate of approximately 0.02 monolayer (ML) per minute to reach a 0.1 ML coverage. In the last part of the deposition Co was co-deposited to reach a Co coverage of 0.02 ML. Next the sample was annealed at 673 K for 10 min, still in the H_2S atmosphere resulting in the CoMoS nanoparticles. The CoMoS is subsequently activated through exposure to atomic hydrogen to introduce vacancies and possibly SH-groups on the cluster edges [27]. Atomic hydrogen is used here as in previous studies, since molecular hydrogen at vacuum compatible pressures was not sufficiently reactive to create vacancies. The activation procedure was carried out by backfilling the chamber to 8×10^{-8} mbar with molecular hydrogen and crack the hydrogen using an Oxford Applied Research TC-50 thermal gas cracker while keeping the sample at room temperature (RT). Subsequently the activated sample was flashed to 500 K.

Prior to the 4,6-DMDBT dosing the activated CoMoS/Au(1 1 1) sample was cooled in the STM body to approximately 190 K. 4,6-DMDBT was heated to 60 °C in a vacuum glass tube, to increase the vapor pressure, and dosed through a leak valve onto the sample at a chamber pressure of 2×10^{-9} mbar for 2 min. The sample is transferred to the STM and investigated at both low temperatures (190 K) and again when the sample has reached RT. The cooling of the sample proved to be essential for the adsorption process; however once adsorbed, the molecules are still observed as the sample reached RT. In the full monolayer limit the molecules tend to pack in a ordered structure on the gold whereas lower coverages resulted in layer of mobile molecules partly fixed around the cluster perimeter.

2.2. Density functional theory

DFT calculations [28,29] were carried out using the DFT package GPAW, ASE [30–32] with the BEEF-vdW exchange-correlation functional using a real-space grid with a spacing of 0.18 Å. In order to computationally study different adsorption sites on the Co-promoted S-edge nanoparticle two different models were constructed representing the Co-promoted S-edges and the corners of the nanocluster. All the models were constructed using the calculated lattice constant of monolayer MoS_2, $a = 3.173$ Å, which agrees well with the experimental obtained value as well as other theoretical work [33]. The 4,6-DMDBT adsorption on gold was studied using a Au slab model with the calculated fcc lattice constant, $a = 4.215$ Å, which agrees with experiments and other theoretical values [34,35]. The S-edge has been modeled with 6×4 stripes periodic in the x-direction. The Mo atoms on the S-edge are replaced by Co atoms as observed in MoS_2 nanoparticles promoted with Co [36,7]. The Co promoted S-edge is terminated in S monomers (50% sulfur coverage) as shown in previous studies [7]. Corners were modeled as a stepped stripe with four Co atoms

on the S-edge side and two Mo atoms on the Mo-edge side of the corner. The stripes are separated by 18 Å in the *z*-direction and 12 Å in the y-direction to avoid interactions between stripes. The gold fcc surface was modeled as a $4 \times 4 \times 4$ slab with the bottom two layers fixed in the bulk atomic positions and with 20 Å of vacuum in the *z* direction. The surface models are shown in Supplemental information. The Brillouin zone was sampled employing the Monkhorst-Pack scheme [24] with a *k*-point grid of $(1 \times 1 \times 1)$ for the edge and corner models and $(2 \times 2 \times 1)$ for the gold surface. A Fermi temperature of $k_BT = 0.1$ eV is used and all energies are extrapolated to zero electronic temperature. The quasi-Newton minimization scheme was employed, relaxing the ionic degrees of freedom until the maximum force was smaller than 0.05 eV $Å^{-1}$. In the surface optimizations all the atoms were allowed to relax. In the adsorption optimizations on the edge the last two rows of Mo and S were fixed at the positions they relaxed to without an adsorbate, while in the case of the corner all atoms were allowed to relax. 4,6-DMDBT was centered and optimized in a non-periodic cell with 10 Å of vacuum in all directions. The Nudged Elastic Band (NEB) method was used to calculate activation energies of interest. The adsorption energies were calculated using Eq. (1).

$$\Delta E_{ads} = E_{adsorbate+surface} - E_{adsorbate} - E_{surface} \quad (1)$$

where $E_{adsorbate+surface}$ is the total energy of the system with the molecule adsorbed on the surface, $E_{adsorbate}$ is the total energy of the isolated molecule, $E_{surface}$ is the total energy of the surface. All the energies are given at 0 K and do not include vibrational ground state energies.

The method for obtaining vacancy formation energies is described in the Supplemental information.

3. Results and discussion

3.1. Synthesis and activation procedure

The CoMoS nanoclusters in the model system are oriented with their MoS_2 (0001) basal plane parallel to the gold substrate and appear in hexagonal shapes as seen in Fig. 1a and b. The two different edge terminations, which result from the characteristic hexagonal shape, were previously determined to be the $(10\bar{1}0)$ termination, exposing the so called Mo-edge, and the $(\bar{1}010)$ termination exposing the S-edge (Fig. 1a) according to the CoMoS structure in Refs. [7,10]. The Co promoter atoms are substituted on the outer Mo positions only along the S-edge [8,10,37,38] and this edge is hence referred to as the Co-promoted S-edge. Under synthesis conditions applied in this experiment, the Mo-edge contains a 100% S-coverage reflected by a termination by S-dimers whereas the Co-promoted S-edge is 50% covered and terminated by sulfur monomers in bridging positions (Fig. 1a) [7].

The CoMoS edge structures can be atom-resolved in STM images. Fig. 1b illustrates an atomically resolved STM image of a pristine CoMoS nanocluster with these edge terminations. As previously concluded from a comparison of experiment and STM simulations, the outer S-monomers on the Co promoted S-edge are imaged in registry with the basal plane S-lattice of the cluster [7] whereas the outer S-dimers on the Mo-edge are imaged in a shifted registry with the basal plane S-lattice in STM imaging [24] as illustrated by the dots in Fig. 1b. Theoretical studies have concluded that the same 50% coverage on Co-promoted S-edge is present under HDS conditions [39,40] whereas the sulfur coverage on the Mo-edge is reduced toward a 50% S coverage [41–43]. We note that along both edges of the nanoclusters the bright brim of higher apparent height in the STM image is present adjacent to the outermost row of atoms. The brim reflects an electronic modification to the edge structure due to one-dimensional electronic edge states to which STM imaging is sensitive [24]. Recent studies have also shown a modified optical activity of the MoS_2 edges which is another reflection of the electronic structure changes [44].

In our experiment the CoMoS nanoclusters are activated by exposing the sample to atomic hydrogen as described in Section 2.1. In the STM images, vacancies can now be seen as missing protrusions along the edge (indicated by arrows in Fig. 1c) which appear in the majority of the clusters after exposure to atomic hydrogen under the experimental conditions. The formation of vacancies appears as a statistical process and hence the distribution ranges from zero vacancies to multiple like the one shown in Fig. 1c. The vacancies are observed to appear on both edge-types (Mo-edge and S-edge) on corner sites as well as centrally in the edge on the hydrogen activated CoMoS.

Possible preferences for the position of the S-vacancy formation observed in the experiment are important in the analysis of 4,6-DMDBT-vacancy interaction since this distribution will be reflected in the adsorption location of 4,6-DMDBT. A statistical analysis of the experimental images shows that the ratio between vacancies placed in corners and centrally in the edge appears to be 5:3 in favor of the corner position in the experiment (based on 39 observed edge vacancies distributed over 30 CoMoS nanoclusters). Formation of an under-coordinated Co atom at the outer corner is always exothermic and we therefore refer to this site and an "intrinsic vacancy" (Fig. 2a). Reduction of the CoMoS structure however can lead to the formation of actual S-vacancies in the edges (Fig. 2b–d). A vacancy at the corner of the S-edge has a formation energy of $\Delta E = 1.67$ eV (Fig. 2b), slightly larger but still comparable to the formation of a single vacancy in a center position on the S-edge which has a formation energy of $\Delta E = 1.49$ eV (Fig. 2c). Creating another vacancy next to an existing one on the center position of the edges (Fig. 2d) has a higher formation energy than the formation of two isolated vacancies. It is not surprising that theory finds the central vacancy to be more favorable than the corner vacancy, as the Co atom in the CoMoS corner is already partly under-coordinated and hence creating a vacancy here will result in an even more under-coordinated Co atom compared to the under-coordination of the Co-atoms resulting from a central edge vacancy. The same argument applies to why it is much less favorable to create two neighboring central vacancies compared to two isolated ones. We speculate that the reason for the apparent higher stability on corner vacancies in the experiment may be a result of the lack of Au-support and S—H groups in the DFT calculations.

To study preferences in S-vacancy formation in the CoMoS S-edge for different sulfiding and sulfo-reductive conditions, a phase diagram (Fig. 2e) is constructed based on the DFT calculations for the experimental synthesis conditions available in our STM studies [45] as well as realistic HDS conditions. The details of the calculation of the phase diagram describing the different temperatures present for HDS and experimental synthesis are given in the Supplemental material. The equilibrium lines of the phase diagram in Fig. 2e) reveal the stable state of the edge S-coverage under a given set of chemical potentials of H_2S and H_2, varied through changes in partial pressure of H_2S and H_2 gas. All conditions can be represented by a point in the phase diagram, and if a given point lies below a certain equilibrium line, the change in free energy for the formation of a given structure is positive, and hence, its formation is unfavorable. However, if the point is above the equilibrium line, the structure described by this equilibrium line has negative formation energy and the formation will hence be favorable. From this we can see how both industrial HDS conditions as well as the experimental conditions available (not considering the atomic hydrogen later introduced) will result in the structure shaded in blue in Fig. 2e and shown in Fig. 2f as a ball model. The phase diagram confirms that the most strongly under-coordinated S-atom

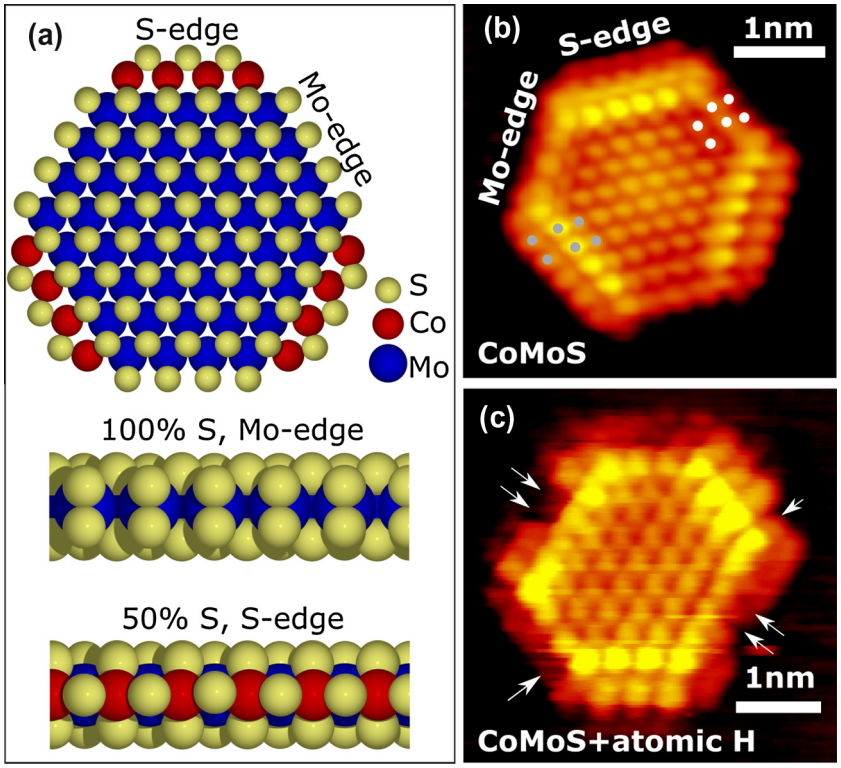

Fig. 1. (a) CoMoS ball model shown from above (top), from the side contemplating at the Mo-edge (middle) and the S-edge (bottom). (b) STM image of CoMoS nanocluster on Au(1 1 1) (tunneling parameters I_t = 0.930 nA, V_t = −0.625 V, T = 300 K). White circles illustrate how the outer S-atoms of the Mo-edge are imaged out of registry with the basal plane S-atoms whereas the gray circles emphasize how the outer S-atoms of the S-edge are imaged in registry however shifted slightly outward. (c) CoMoS nanocluster exposed to atomic hydrogen. Introduced vacancies are indicated by the arrows in the figure. (I_t = 0.280 nA, V_t = −0.537 V, T = 300 K).

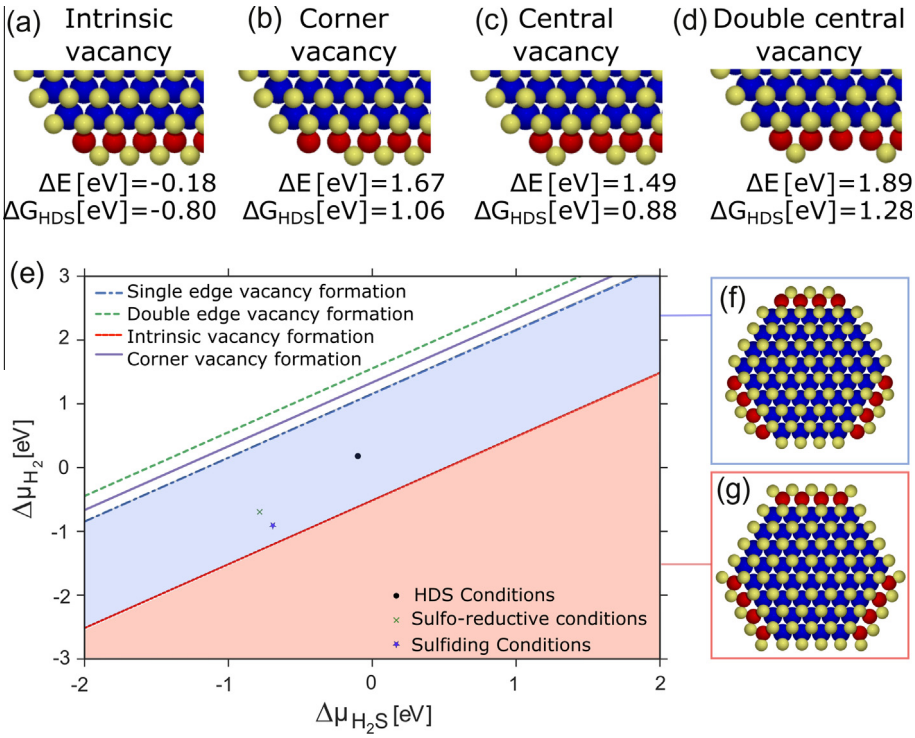

Fig. 2. (a–d) Ball model and formation energies (ΔE and Gibbs free energies calculated for HDS conditions) of the different types of vacancies observed on the Co-promoted S-edge. For double-vacancy in (d) the formation energy is given as the formation to remove the second S-atom after the first is removed. (e) Adaptation of the phase diagrams for vacancy formation at HDS conditions (T = 573 K, $p(H_2)$ = 38 atm, $p(H_2S)$ = 0.13 atm) and sulfiding (sulfur rich conditions T = 723 K, $p = 2 \times 10^{-9}$ bar, $p(H_2S)/p(H_2)$ = 500) and sulfo-reductive (sulfur poor T = 723 K, $p = 2 \times 10^{-9}$ bar, $p(H_2S)/p(H_2)$ = 0:07) STM conditions (conditions adapted from [45]). (f) The equilibrium state for the conditions highlighted in blue in figure (e) including the conditions present for HDS conditions, experimental sulfiding and sulfo-reductive conditions. (g) The equilibrium state of the CoMoS nanoparticles under the conditions highlighted in red in figure (e).

(the intrinsic vacancy in Fig. 2a) is absent under both the experimental conditions and the HDS conditions. Thus the corner Co-atom at the intrinsic vacancy site is coordinated to three sulfur atoms rather than four and hence formally missing a S-atom (Fig. 1b).

Further reduction to the structures in Fig. 2b, c and d is not predicted to be favorable for CoMoS, neither in the real catalyst nor in the model catalyst under the given conditions [45]. When comparing to the experiment under reducing conditions it is important to consider that the phase diagram (Fig. 2e) is constructed for equilibrium with the gas phase, while in the experimental conditions the activity of hydrogen is achieved through the cracking of H_2 into atomic hydrogen. Atomic hydrogen is very reactive and hence serves to obtain model conditions for the hydrogen activity at the elevated pressures present in the real catalyst. Due to the poorly defined chemical potential of the atomic hydrogen in the experiment it was not possible to fix an accurate point for the experiment in the phase diagram. However, the presence of S-vacancies in the STM images clearly proves that the reactivity of the atomic hydrogen is sufficiently efficient for vacancy formation reflecting the situations in Fig. 2b and c. This makes it possible to probe their affinity for adsorption in Section 3.2. It is, however, noted that the location of the HDS point in the phase diagram suggests that edge and corner vacancies in Fig. 2b and c are not equilibrium structures even under HDS conditions. Hence, statistically they are only present in quite low numbers in the catalyst when operating at HDS conditions.

3.2. 4,6-DMDBT adsorption

To investigate the adsorption of 4,6-DMDBT, the molecule is dosed onto the hydrogen activated CoMoS nanoclusters at low temperature (Fig. 1c). At a coverage of slightly below 1 ML of 4,6-DMDBT the molecules pack in an ordered self-assembled monolayer (SAM) (previously also reported by Tuxen et al. [27]) on the Au(111) support (Fig. 3a). No such SAM appears on the basal plane of the CoMoS nanoclusters. The periodicity of the SAM is in good agreement with that reported in [27] and in qualitative agreement with the dimensions of the spatial extension of the molecule (Fig. 3b) calculated based purely on bond lengths and geometry showing that the molecule adsorbs in an intact configuration. Our DFT results show that the adsorption on the Au (111) surface is a pure van der Waals binding as expected. The model of 4,6-DMDBT adsorption on Au(111) (Fig. 3c) is used to generate the corresponding STM simulation of 4,6-DMDBT on Au (111) (Fig. 3d) showing excellent agreement with the experimental obtained STM images of the molecular appearance on the surface (Fig. 3a). The shape of the individual molecules further confirms that the molecules are deposited as intact 4,6 DMDBT. Importantly, the position of the S-atom is easily deduced from STM images as the S-atom appears much brighter in STM than the remaining molecule (Fig. 3a and d).

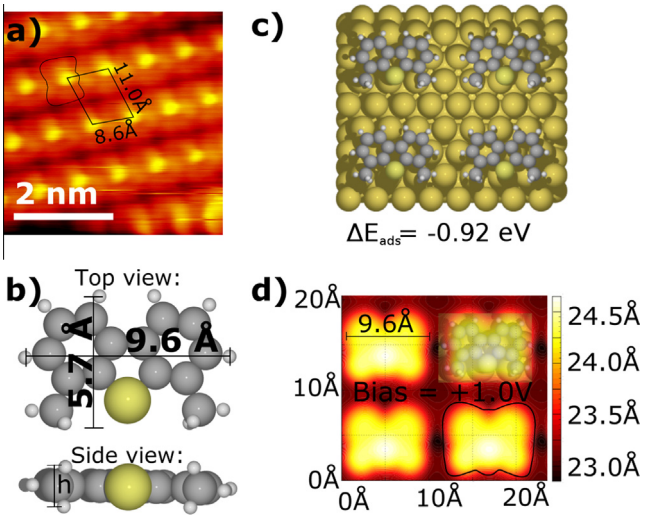

Fig. 3. (a) Packing of 4,6-DMDBT on a clean area of Au(111) in a CoMoS/Au(111) synthesis. The superimposed unit cell shows the unit cell dimensions of the SAM are in great agreement with the dimensions reported in Ref. [27] (I_t = 0.5 nA, V_t = −1.1 V, T = 190 K). (b) The molecular dimensions of a 4,6-DMDBT molecule based on center positions of the individual atoms. These will be referred to as the long and the short axis of the molecule whereas h indicates the height of the planar molecule. (c) DFT calculation of 4,6-DMDBT on Au(111) including the calculated adsorption energy. (d) Simulated STM image of 4,6-DMDBT on Au(111) at V_t = 1.0 V.

Upon dosage of 4,6-DMDBT overall three different adsorption modes were observed and will in the following discussion be referred to as delocalized π-mode, localized π-mode and σ-mode.

3.2.1. Delocalized π-adsorption

The most predominant adsorption mode observed in our experiments is the delocalized π-mode, which appears in the STM images of CoMoS on one or more S-edges which appear broader and brighter compared with the unreacted S-edges (see the two bright S-edge of the encircled clusters in Fig. 4a and a close-up in Fig. 4b). This adsorbate-related signature is observed only for the brim region of the S-edge, leading to the conclusion that the molecule has a preference for interacting with the S-edge under the conditions of our experiment.

The line scans along the adsorbate-related signature reveal no apparent structural information of single adsorbates and the edge perimeter appears planar and homogeneous (line scan in Fig. 4c). Compared with the well-resolved appearance of the molecules in the SAM, this diffuse appearance already suggests that the adsorption on CoMoS does not reflect static molecular adsorption. To identify the adsorbate further, the dimensions (height and width) of all observed cases were measured. Heights measured using STM are not of pure topological nature but consist of a convolution of topography and electronic effects and one should bear this in mind when considering heights determined using STM. The relative height differences were determined relative to the basal plane, the opposite edge (Mo-edge), and same edge type (bare S-edge) within the same cluster (Fig. 4d and e). The height distribution was fitted to a Gaussian distribution, revealing that the apparent height difference between the adsorbate-related signature on the brim and the basal plane was 0.94 Å (B). The molecular signature protrudes 0.62 Å (A) above the level of the Mo-edge and 0.36 Å (C) above the clean S-edge brim (data summarized in Table 1 including its standard deviation). The latter value is hence considered the apparent height of the delocalized molecule itself (“h” Fig. 3b) as it appears in STM.

The width is estimated by qualitative extrapolation of the curvature of the peak to basal plane level on both sides (Fig. 4e, arrow D). The width was measured for each observation and plotted in a histogram and fitted to a Gaussian distribution. From this the width was determined to be 7.17 Å ± 0.74 Å and therefore fits better with the short dimension of the molecule observed as 8.6 Å in for the SAM of 4,6-DMDBT on Au(111) (Fig. 3a). When considering possible tip convolution effect of STM, the molecule is most likely adsorbed on the cluster with the longest molecular axis parallel to the cluster edge as depicted in Fig. 4f).

The apparent dimension of the adsorbate related signature is consistent with a planar adoption of 4,6-DMDBT on the brim region of the cluster, i.e. similar to the π-mode adsorption mode on unpromoted MoS_2 [27] which arises from bonding of the aromatic π-system to the edge region. However, the unresolved structural information along the brim is not consistent with a static

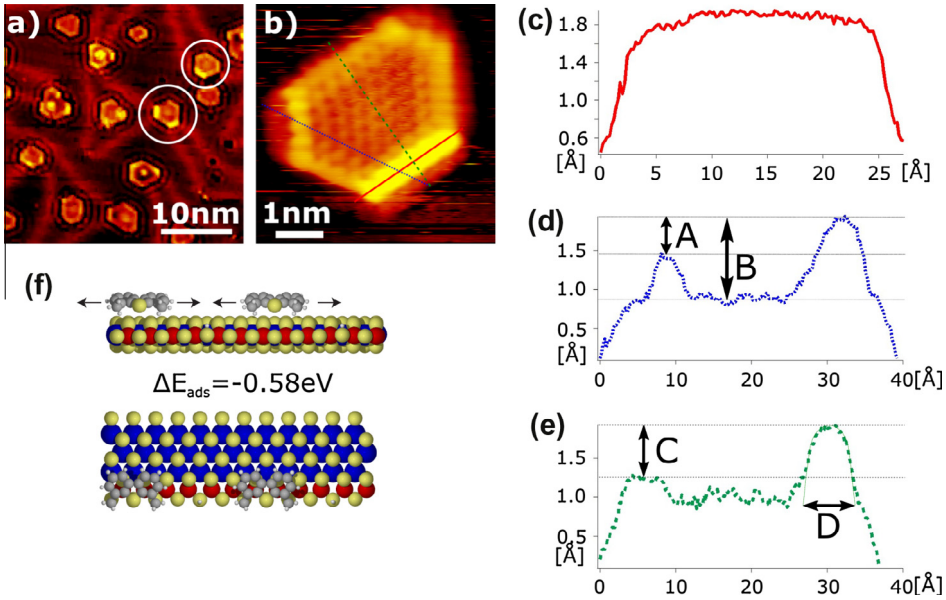

Fig. 4. (a) Overview image showing a typical appearance of the activated CoMoS after exposure to 4,6-DMDBT. Two clusters containing delocalized π-modes are highlighted by the white circles. (RT, I_t = 0.58 nA, V_t = −0.8 V) (b) CoMoS nanocluster exposed to 4,6-DMDBT. Imaged at 170 K (I_t = 1.0 nA V_t = −0.8 V). The broad, bright brim on the lower S-edge appears as a result of the dosed molecule. (c–e) Line scans indicated in figure (b) (color and pattern coded). (c) Shows low corrugation along the lower the S-edge (delocalized π-mode). (d) Shows the height of the delocalized π-mode relative to A: the Mo-edge, B: the basal plane and (e) C: relative to the pristine Co-promoted S-edge. D shows the estimated width of the molecule by extrapolating the curvature of the line scan peak. (f) DFT results of π-mode on a Co promoted S-edge containing SH-groups.

Table 1
Height of the delocalized π-mode edges compared to basal plane, Mo edge and bare S-edges within the same cluster based on the peak and width of a Gaussian fit of the observations. The letters (A), (B) and (C) refer to the arrows in Fig. 4d and e.

Height relative to	Height (Å)
Basal plane (B)	0.94 ± 0.30
Other edge type (C)	0.62 ± 0.23
Same edge type (A)	0.36 ± 0.13

adsorption configuration. It has previously been reported how diffuse structural information in STM images can arise from a diffusing physisorbed state functioning as a precursor to chemical bond formation [46]. Similarly we suggest here that the lack of structural information along the S-edge brims is caused by the 4,6-DMDBT molecule in a diffuse physisorbed mode in which the molecule is free to move along the brim of the cluster at a higher rate than the STM scan rate. Consequently the STM is imaging a superposition of the molecular position in the duration of the scan. 4,6-DMDBT is adsorbed through its conjugated π-system onto the cluster S-edge brim (Fig. 4f) and is free to diffuse along the metallic edge state as a consequence of the electronic homogeneity along the edge. This mode is referred to as the delocalized π-mode.

DFT calculations implementing the Nudged-Elastic-Band (NEB) model reveal that whereas 4,6-DMDBT adsorption is relative strong on the S-edge (ΔE_{ads} = −0.58 eV including van der Waals bonding), the diffusion barrier along the edge is less than 0.1 eV which is low enough to make diffusion along the S-edge possible, consistent with a delocalized π-mode (indicated with arrows in Fig. 4f). Even though the relevant adsorption in the DDS process is a chemisorption of the reactive species, the delocalized π-mode, having no chemisorption character of its own may, however, play an important role as a precursor state to bond-formation in the catalyst under reaction conditions.

3.2.2. σ- and localized π-adsorption

A completely different and stronger interaction appears at the corners of the hydrogen activated CoMoS nanoclusters. In the σ-mode (bottom of Fig. 5a) the molecule interacts through the S-atom of the molecule with a corner S-vacancy of the CoMoS in a configuration similar to those reported for DBT on CoMoS [27]. The molecule appears as a heart shaped protrusion attached, through its bright S-atom, to the corner of the CoMoS nanocluster (Fig. 5a). The fact that 4,6-DMDBT is actually capable of adsorbing in the σ-configuration is surprising as it was often predicted to be a strongly inhibited configuration due sterical hindrance. The S-atom of the 4,6-DMDBT, which appears bright in the STM image, takes up the space otherwise occupied by a S-atom in the pristine CoMoS and it is hence concluded that the molecular S-atom is chemisorbed in a corner S-vacancy in the CoMoS nanocluster. The position of the vacancy in this adsorption configuration is restricted to the corner position as the methyl groups of the molecules sterically prevent the adsorption to occur for central edge vacancies. Hence a S-vacancy in the corner position of the CoMoS nanocluster is of key importance for the existence of this adsorption, and is observed exclusively at corner sites.

To demonstrate the necessity of the corner S-vacancy, the adsorption energies of a molecule at the corner site with and without a corner S-vacancy were calculated utilizing DFT (Fig. 5e and f). The adsorption energy was determined to ΔE_{ads} = −0.89 eV for a cluster containing a corner vacancy whereas it is only −0.10 eV in a corner site containing only the intrinsic vacancy. It is hence conclude that the strong σ-adsorption of 4,6-DMDBT is in fact possible and that the corner S-vacancy is necessary for σ-adsorption to occur, as it provides the space for this adsorption configuration. As shown in Fig. 5e the sterical hinderance provided by the methyl groups of 4,6-DMDBT prevents it from binding in the absence of a corner vacancy, all in agreement with the experimental findings that the σ-mode is observed only in the presence of a corner vacancy. As expected no σ-adsorption was observed in STM in the central edge vacancies as a consequence of the sterically hinderance of 4,6-DMDBT in this specific configuration (Fig. 5g). Perpendicular adsorption into the defect sites was excluded since such configurations would result in an overlap of the molecule and gold support, but it may be possible for unsupported CoMoS.

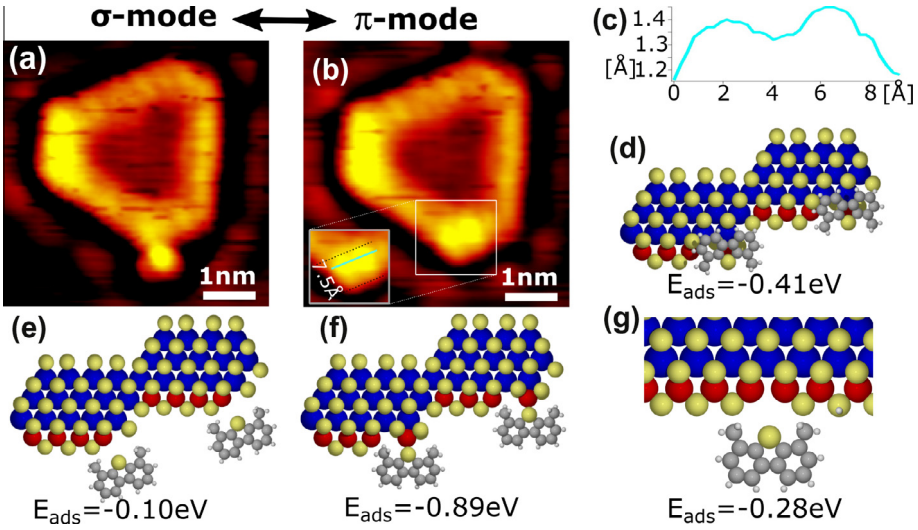

Fig. 5. (a) STM image of 4,6-DMDBT adsorbed in σ-adsorption. (b) Localized π-adsorption appearing as a result of a molecular flipping from the σ-mode shown in (a). Both images are a 70×70 Å^2 STM image taken at $I_t = 0.93$ nA, $V_t = -1.16$ V at room temperature. (c) Line scan along the cyan line shown in the inset of figure (b) revealing structural information present in the localized π-mode. (d) DFT calculations for 4,6-DMDBT adsorbed on top of a corner S-vacancy in π-mode. (e) DFT result for a molecule adsorbed at corner-site without a corner vacancy. (f) DFT result for a molecule adsorbed in σ-mode at a corner site with one corner vacancy. (g) Ball model showing how the σ-mode is sterically impossible to occur in central corner vacancies.

A highly interesting observation was made regarding the dynamics of the 4,6-DMDBT adsorbed in σ-mode in a corner S-vacancy. A reversible flipping of the intact 4,6-DMDBT molecule between the σ-mode and the π-like adsorption occurs during STM scans at room temperature (Fig. 5a and b, see Supplemental material for STM movie). This π-mode is different from the delocalized π-mode as it appears static and with two distinguishable protrusions which only take up part of the cluster brim (line scan along the blue line in the insert in Fig. 5b shown in Fig. 5c. We refer to this as the localized π-mode, due to its apparent stationary character on the brim. The width of the molecular signature in the STM for the localized π-mode (see insert in Fig. 5b) measured perpendicular to the cluster edge is 7.5 Å and hence comparable to the delocalized π-mode (7.17 Å $\pm$ 0.74 Å). This leads us to conclude that the localized π-mode also represents a planar adsorption of the molecule with the long molecular axis placed parallel to the cluster edge, but now in an immobile strongly adsorbed state (Fig. 5d).

The calculated adsorption energy of 4,6-DMDBT on an edge vacancy in a π-like configuration was calculated using DFT and found to be $\Delta E_{ads} = -0.41$ eV (Fig. 5d), revealing that the adsorption mode is stable, however less than the σ-mode). When counting the number of frames containing each adsorption mode (counting those frames containing a transformation as both adsorption modes) in the obtained STM movie (see Supplemental material) it is found that the ratio is ~4:3 in favor of the σ-mode in agreement with the prediction that the σ-mode is in fact the most stable. The observation of the transformation between the two adsorption modes reveals that the two predominant absorption modes are indeed linked. It is possible that the rate of the observed flipping may be influenced by the STM-tip, but this has no influence on the conclusions just made: if the molecule is able to alternate between the two adsorption modes in the same adsorption site this specific adsorption site must accommodate conditions allowing both the σ- and the localized π-modes. Hence must the localized π-mode be a consequence of an underlying S-vacancy, just like the σ-mode was concluded to be.

This link is particularly interesting in light of a two-site model [19,15,5] on CoMoS catalysts for the HYD and DDS reactions, respectively. While the 4,6 DMDBT adsorbs as a diffusive species on the brim sites of CoMoS, the molecule can be hydrogenated by reacting with S-H groups found on the S-edge under HDS conditions [21,47,48] and thus follow the HYD route. However, once the 4,6 DMDBT molecule diffuses and encounters a corner vacancy the molecule can first enter the localized π-mode, after which the molecule can transfer into the observed σ-mode. The latter configuration reflects a strong adsorption and can be considered to be an important intermediate step to the DDS route leading to the complete sulfur extrusion. The proposed mechanism and link between π-mode and σ-mode on CoMoS S-edge is in fact very consistent with the reaction rates and selectivity of the CoMoS catalysts, where the HYD route is strongly favored and the DDS route is heavily suppressed for 4,6-DMDBT. To understand this we draw the attention to the phase diagram (Fig. 2e) in which we see that under HDS conditions the equilibrium phase contains no corner vacancies. In view of the observations above, the rate of the DDS for 4,6 DMDBT should be determined by the formation rate of the only sites which allows for chemisorption, the corner vacancies, which is statistically very low and possibly even less predominant than in our experiment where highly reactive hydrogen radicals are required to form such sites. Instead the HYD route is favored since the brim sites are not sterically hindered and adsorption requires no prior formation of vacancies. Such a model also supports the fact that HDS selectivity and reactivity are widely different for different groups of molecules [49], as smaller molecules and less sterically restriced molecules might react also with the more predominant active edge-sites and thus follow the DDS reaction pathway through those. On the other hand, larger organosulfur molecules in the DBT group are more likely to interact strongly with the brim region due to large van der Waals forces [50]. Finally, we note that diffusion onto the unpromoted Mo-edge was not observed in our experiments, but it is possible that elevated temperature may facilitate this transfer and open up for sulfur extrusion pathway on the Mo-edge as proposed in [21].

4. Conclusion

In this study we have reported an insight into the nature of the interaction between the bulky S-containing molecule 4,6-DMDBT and the CoMoS model catalyst. Through STM imaging of a well-defined UHV model system we find that the most predominant

observation is a smeared out adsorption exclusively found on the S-edge of the CoMoS nanocluster addressed to a diffusive physisorption on the nanocluster which has the proposed function of a precursor-like state of the molecule prior to chemisorption under real catalytic conditions.

The low activity of the DDS pathway for 4,6-DMDBT in the industrial catalyst can be well understood from this study. It was found that the only option for direct chemisorption on the CoMoS nanocluster of the intact molecule is through a vacancy in the corner position of the S-edge in a peripheral σ-adsorption. However DFT shows that this vacancy formation is unfavorable under HDS conditions and must hence be present only at a very limited frequency explaining the low catalytic activity.

In addition it is found that the σ-adsorption reversibly can transform into a π-like adsorption observed through STM movies. This surprising dynamic behavior is highly interesting as it reveals the possibility to alternate between the two configurations and hence to alternate between the two proposed active sites of the different reaction pathways (on-top brim π-adsorption and the peripheral σ-chemisorption in cluster corner). In this way both hydrogenation and direct desulfurization may happen in the same adsorption process but in different configurations at the same adsorption site.

Acknowledgment

We gratefully acknowledge financial support from the Innovation Fund Denmark (CAT-C), the Danish Research Council - Technology and Production (HYDECAT) and Haldor Topsøe A/S.

Appendix A. Supplementary material

Supplementary data associated with this article can be found, in the online version, at http://dx.doi.org/10.1016/j.jcat.2016.09.004.

References

[1] C. Song, X. Ma, Appl. Catal., Bl 41 (12) (2003) 207–238 (3rd International Conference on Environmental Catalysis).
[2] C. Song, Catal. Today 86 (1) (2003) 211–263.
[3] M. Breysse, G. Djega-Mariadassou, S. Pessayre, C. Geantet, M. Vrinat, G. Pérot, M. Lemaire, Catal. Today 84 (3) (2003) 129–138.
[4] I. Mochida, K. Sakanishi, X. Ma, S. Nagao, T. Isoda, Catal. Today 29 (14) (1996) 185–189 (Second Japan-EC Joint Workshop on the Frontiers of Catalytic Science and Technology for Energy, Environment and Risk Prevention).
[5] B. Gates, H. Topsøe, Polyhedron 16 (18) (1997) 3213–3217.
[6] K.G. Knudsen, B.H. Cooper, H. Topsøe, Appl. Catal., A 189 (2) (1999) 205–215.
[7] J.V. Lauritsen, J. Kibsgaard, G.H. Olesen, P.G. Moses, B. Hinnemann, S. Helveg, J. K. Nørskov, B.S. Clausen, H. Topsøe, E. Lægsgaard, F. Besenbacher, J. Catal. 249 (2) (2007) 220–233.
[8] Y. Zhu, Q.M. Ramasse, M. Brorson, P.G. Moses, L.P. Hansen, C.F. Kisielowski, S. Helveg, Angew. Chem., Int. Ed. 53 (40) (2014) 10723–10727.
[9] N.-Y. Topsøe, H. Topsøe, J. Catal. 84 (2) (1983) 386–401.
[10] J. Lauritsen, S. Helveg, E. Lægsgaard, I. Stensgaard, B. Clausen, H. Topsøe, F. Besenbacher, J. Catal. 197 (1) (2001) 1–5.
[11] H. Topsøe, B.S. Clausen, R. Candia, C. Wivel, S.M. ørup, J. Catal. 68 (2) (1981) 433–452.
[12] C. Wivel, B.S. Clausen, R. Candia, S.M. ørup, H. Topsøe, J. Catal. 87 (2) (1984) 497–513.
[13] M. Egorova, R. Prins, J. Catal. 241 (1) (2006) 162–172.
[14] X. Li, A. Wang, M. Egorova, R. Prins, J. Catal. 250 (2) (2007) 283–293.
[15] M. Egorova, R. Prins, J. Catal. 225 (2) (2004) 417–427.
[16] F. Bataille, J.-L. Lemberton, P. Michaud, G. Pérot, M. Vrinat, M. Lemaire, E. Schulz, M. Breysse, S. Kasztelan, J. Catal. 191 (2) (2000) 409–422.
[17] D.D. Whitehurst, T. Isoda, I. Mochida, Present state of the art and future challenges in the hydrodesulfurization of polyaromatic sulfur compounds, Advances in Catalysis, vol. 42, Academic Press, 1998, pp. 345–471.
[18] M. Breysse, G. Djega-Mariadassou, S. Pessayre, C. Geantet, M. Vrinat, G. Prot, M. Lemaire, Catal. Today 84 (34) (2003) 129–138 (Catalysis for the Environment and New Energy Sources).
[19] M. Daage, R. Chianelli, J. Catal. 149 (2) (1994) 414–427.
[20] P.G. Moses, B. Hinnemann, H. Topsøe, J.K. Nørskov, J. Catal. 248 (2) (2007) 188–203.
[21] P.G. Moses, B. Hinnemann, H. Topsøe, J.K. Nørskov, J. Catal. 268 (2) (2009) 201–208.
[22] J. Lauritsen, M. Nyberg, J. Nørskov, B. Clausen, H. Topsøe, E. Lægsgaard, F. Besenbacher, J. Catal. 224 (1) (2004) 94–106.
[23] T. Kabe, A. Ishihara, Q. Zhang, Appl. Catal., A 97 (1) (1993) L1–L9.
[24] M.V. Bollinger, J.V. Lauritsen, K.W. Jacobsen, J.K. Nørskov, S. Helveg, F. Besenbacher, Phys. Rev. Lett. 87 (19) (2001) 196803.
[25] B. Temel, A.K. Tuxen, J. Kibsgaard, N.-Y. Topsøe, B. Hinnemann, K.G. Knudsen, H. Topsøe, J.V. Lauritsen, F. Besenbacher, J. Catal. 271 (2) (2010) 280–289.
[26] S. Helveg, J.V. Lauritsen, E. Lægsgaard, I. Stensgaard, J.K. Nørskov, B.S. Clausen, H. Topsøe, F. Besenbacher, Phys. Rev. Lett. 84 (2000) 951–954, Jan.
[27] A.K. Tuxen, H.G. Füchtbauer, B. Temel, B. Hinnemann, H. Topsøe, K.G. Knudsen, F. Besenbacher, J.V. Lauritsen, J. Catal. 295 (0) (2012) 146–154.
[28] P. Hohenberg, W. Kohn, Phys. Rev. B 136 (3B) (1964) B864.
[29] W. Kohn, L.J. Sham, Phys. Rev. B 140 (4A) (1965) A1133.
[30] S.R. Bahn, K.W. Jacobsen, Comput. Sci. Eng. 4 (3) (2002) 56–66.
[31] J.J. Mortensen, L.B. Hansen, K.W. Jacobsen, Phys. Rev. B B 71 (3) (2005) 035109.
[32] J. Enkovaara, C. Rostgaard, J.J. Mortensen, J. Chen, M. Duak, L. Ferrighi, J. Gavnholt, C. Glinsvad, V. Haikola, H.A. Hansen, H.H. Kristoffersen, M. Kuisma, A.H. Larsen, L. Lehtovaara, M. Ljungberg, O. Lopez-Acevedo, P.G. Moses, J. Ojanen, T. Olsen, V. Petzold, N.A. Romero, J. Stausholm-Møller, M. Strange, G.A. Tritsaris, M. Vanin, M. Walter, B. Hammer, H. Hkkinen, G.K.H. Madsen, R.M. Nieminen, J.K. Nørskov, M. Puska, T.T. Rantala, J. Schiøtz, K.S. Thygesen, K.W. Jacobsen, J. Phys.: Condens. Matter 22 (25) (2010) 253202.
[33] Á. Logadóttir, P.G. Moses, B. Hinnemann, N.-Y. Topsøe, K.G. Knudsen, H. Topsøe, J.K. Nørskov, Catal. Today 111 (1) (2006) 44–51.
[34] J.K. Mavrikakis, M. Norskov, Abstr. Pap. Am. Chem. S 219 (2000) U521.
[35] Landolt-Bornstein, Structure Data of Elements and Intermetallic Phases, vol. 3b, Springer, Berlin, 1971.
[36] F. Besenbacher, M. Brorson, B. Clausen, S. Helveg, B. Hinnemann, J. Kibsgaard, J. V. Lauritsen, P.G. Moses, J.K. Nørskov, H. Topsøe, Catal. Today 130 (1) (2008) 86–96.
[37] P. Raybaud, J. Hafner, G. Kresse, S. Kasztelan, H. Toulhoat, J. Catal. 190 (1) (2000) 128–143.
[38] H. Schweiger, P. Raybaud, H. Toulhoat, J. Catal. 212 (1) (2002) 33–38.
[39] P.G. Moses, B. Hinnemann, H. Topsøe, J.K. Nørskov, J. Catal. 268 (2) (2009) 201–208.
[40] L.S. Byskov, J.K. Nørskov, B.S. Clausen, H. Topsøe, Catal. Lett. 64 (2) (2000) 95–99.
[41] H. Schweiger, P. Raybaud, G. Kresse, H. Toulhoat, J. Catal. 207 (1) (2002) 76–87.
[42] P. Raybaud, J. Hafner, G. Kresse, S. Kasztelan, H. Toulhoat, J. Catal. 189 (1) (2000) 129–146.
[43] L.S. Byskov, J.K. Nørskov, B.S. Clausen, H. Topsøee, J. Catal. 187 (1) (1999) 109–122.
[44] X. Yin, Z. Ye, D.A. Chenet, Y. Ye, K. O'Brien, J.C. Hone, X. Zhang, Science 344 (6183) (2014) 488–490.
[45] J.V. Lauritsen, M.V. Bollinger, E. Lægsgaard, K.W. Jacobsen, J.K. Nørskov, B. Clausen, H. Topsøe, F. Besenbacher, J. Catal. 221 (2) (2004) 510–522.
[46] D.E. Brown, D.J. Moffatt, R.A. Wolkow, Science 279 (5350) (1998) 542–544.
[47] P.-Y. Prodhomme, P. Raybaud, H. Toulhoat, J. Catal. 280 (2) (2011) 178–195.
[48] M. Sun, A.E. Nelson, J. Adjaye, J. Catal. 233 (2) (2005) 411–421.
[49] J. Lauritsen, F. Besenbacher, J. Catal. 328 (2015) 49–58 (Special Issue: The Impact of Haldor Topsøe on Catalysis).
[50] S. Rangarajan, M. Mavrikakis, ACS Catal. 6 (5) (2016) 2904–2917.

Supplemental material: Atomic scale analysis of sterical effects in the adsorption of 4,6-dimethyldibenzothiophene on a CoMoS hydrotreating catalyst

Signe S. Grønborg[1], Manuel Šarić[2,3,4], Poul G. Moses[4], Jan Rossmeisl[3], and Jeppe V. Lauritsen[1,*]

[1]Interdisciplinary Nanoscience Center (iNANO), Aarhus University, Denmark
[2]Department of Physics, Technical University of Denmark, Denmark
[3]Department of Chemistry, Copenhagen University, Denmark
[4]Haldor Topsøe A/S, Kgs. Lyngby, Denmark
[*]Corresponding author: jvang@inano.au.dk

DFT model surfaces

Figure 1 shows the model surfaces used for to perform the calculations. The stripes and the corner model were repeated in the x direction once to point out the periodicity of the structure. The MoS_2 basal plane and Au surface model were not repeated, they are both periodic in the x and y directions.

Vacancy formation

Vacancy formation in CoMoS particles can be described with the following relation:

$$\mathrm{CoMoS} + \mathrm{H_2} \leftrightarrow \mathrm{CoMo} + \mathrm{H_2S} \tag{1}$$

where CoMoS represents the particle before the removal of one sulfur atom and CoMo after the removal (not to be confused with a fully metallic Co-Mo phase. CoMo should be read as the CoMoS phase with one missing S-atom), thus forming a vacancy. Considering equation 1 one can write out the expression for the free energy of vacancy formation.

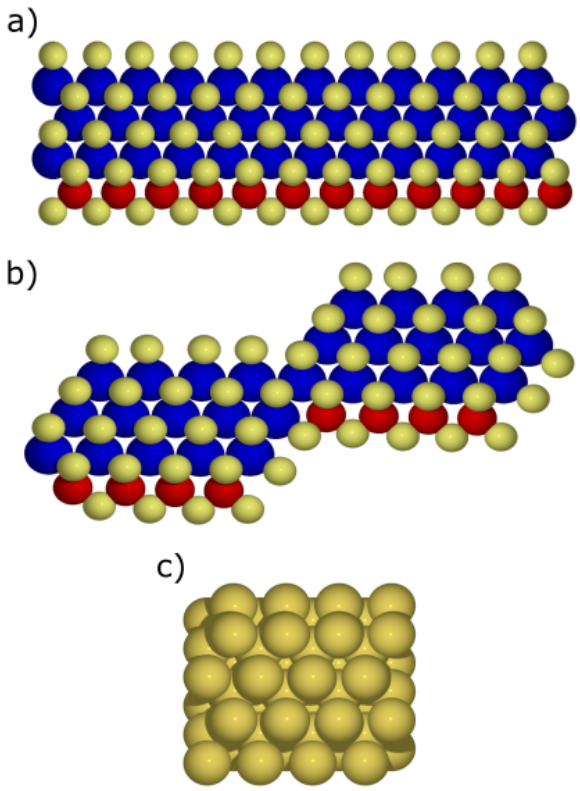

Figure 1: Model surfaces used in the DFT calculations seen from top. a) S-edge b) Corner c) Au surface. (a) and (b) are repeated once in the x direction

$$\begin{aligned}\Delta G =& E(H_2S) + E_{ZP}(H_2S) + \Delta H^{0,T}(H_2S) - TS^T(H_2S) + k_B T \ln\frac{p(H_2S)}{p^\circ} \\ &+ E(CoMo) - [E(H_2) + E_{ZP}(H_2) + \Delta H^{0,T}(H_2) - TS^T(H_2) \\ &+ k_B T \ln\frac{p(H_2)}{p^\circ} + E(CoMoS)]\end{aligned} \tag{2}$$

which can, by grouping related terms, be written as:

$$\Delta G = \Delta E + \Delta E_{ZP} + \Delta(\Delta H^{0,T}) - T\Delta S^T + \Delta\mu(H_2S) - \Delta\mu(H_2) \tag{3}$$

By setting ΔG to 0, a linear relation between the two chemical potentials is obtained. These are equilibrium lines whose positions depends on the temperature, but the relative position of the lines is

independent of the temperature.

$$\Delta\mu(\mathrm{H_2}) = \Delta\mu(\mathrm{H_2S}) + (\Delta\mathrm{E} + \Delta\mathrm{E_{ZP}} + \Delta(\Delta\mathrm{H^{0,T}}) - \mathrm{T}\Delta\mathrm{S^T}) \tag{4}$$

The value for ΔE can be obtained from DFT calculations (differential energies), $\Delta\mathrm{E_{ZP}}$ can be obtained by performing vibrational analysis with DFT and applying the harmonic approximation, $E_{ZP} = \frac{1}{2}\sum_i h\nu_i$, $\Delta(\Delta\mathrm{H^{0,T}})$ and $\mathrm{T}\Delta\mathrm{S^T}$ can be obtained from thermodynamic tables[1, 2].

Table 1: Data calculated from DFT

Vacancy	ΔE [eV]
Single edge	1.49
Double edge	1.89
Outer sulfur vacancy	-0.18
Corner vacancy	1.67

Table 2: Free energy corrections to the DFT data

Correction	H_2S	H_2
$\mathrm{E_{ZP}}$ [eV]	0.437	0.336
$\Delta\mathrm{H^{0,T}_{573K}}$ [eV]	2.066×10^{-1}	1.709×10^{-1}
$\Delta\mathrm{H^{0,T}_{723K}}$ [eV]	2.684×10^{-1}	2.116×10^{-1}
$\mathrm{S^T_{573K}}$ [eVK^{-1}]	2.375×10^{-3}	1.551×10^{-3}
$\mathrm{S^T_{723K}}$ [eVK^{-1}]	2.472×10^{-3}	1.622×10^{-3}

By plotting the chemical potentials against each other i.e. the equilibrium lines, one obtains the phase diagram for vacancy formation. One phase diagram representing HDS conditions[3] (T=573 K, p(H_2)=38 atm, p(H_2S)=0.13 atm) and the other STM[4] "sulfiding" (T=723 K, p=2×10^{-9} bar,

$\frac{p(H_2S)}{p(H_2)} = 500$) and "sulfo-reductive" (T=723 K, p=2×10^{-9} bar, $\frac{p(H_2S)}{p(H_2)} = 0.07$) conditions.

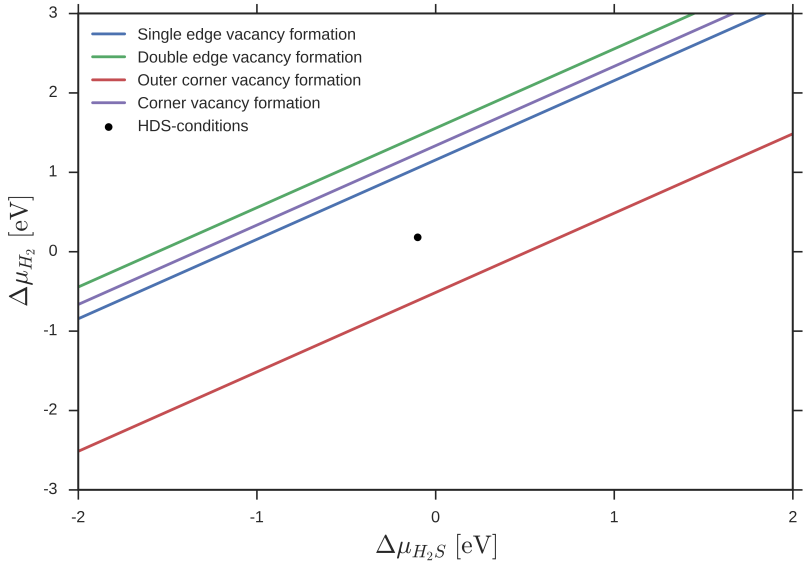

Figure 2: Phase diagram of vacancy formation under HDS conditions

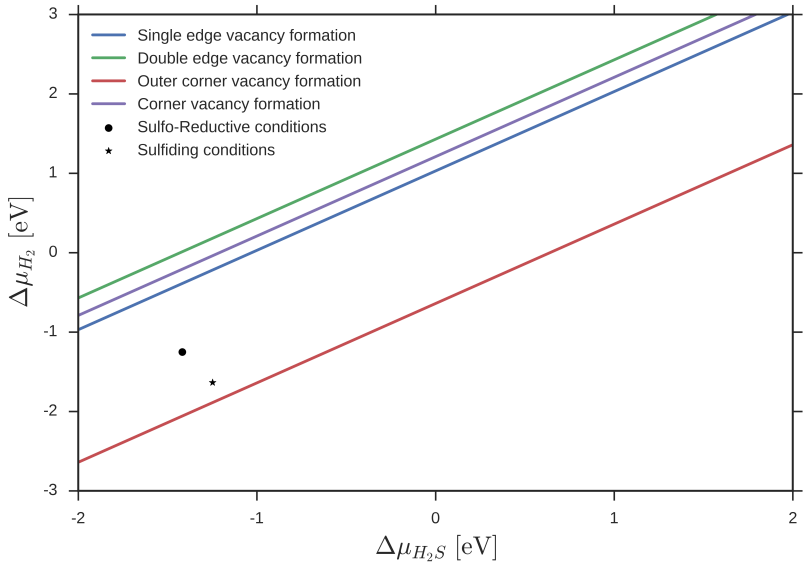

Figure 3: Phase diagram of vacancy formation under STM "sulfiding" and STM "sulfo-reductive" conditions

By observing the equilibrium lines in figures 2 and 3 one can find out which type of defects i.e. vacancies are present in the particles at specific partial pressures of H_2 and H_2S. If the conditions are below the observed equilibrium line the change in free energy for making that vacancy is positive, thus the process is unfavorable. If the conditions are above the observed equilibrium line the change in free energy is negative and the process is favorable. E.g. in figure 1 the conditions fall below the lines for making corner and any edge vacancies which means that the vacancies aren't present. At the same time the conditions fall above the line for removing the under-coordinated sulfur at the corner positions which means that this sulfur is not present at HDS conditions. Each phase diagram corresponds to a specific temperature since, as was already mentioned, the position of the lines depends on the temperature and they shift upwards or downwards when the temperature is changed. The figure used in the main body of the paper is qualitatively adapted to contain all the important information in one plot.

References

[1] `http://kinetics.nist.gov/janaf/html/H-050.html`.

Accessed: 2015-12-22.

[2] `http://kinetics.nist.gov/janaf/html/H-080.html`.

Accessed: 2015-12-22.

[3] P. G. Moses, L. C. Grabow, E. M. Fernandez, B. Hinnemann, H. Topsøe, K. G. Knudsen, and J. K. Nørskov. *Catal. Lett.*, 144(8):1425–1432, 2014.

[4] J. V. Lauritsen, M. V. Bollinger, E. Lægsgaard, K. W. Jacobsen, J. K. Nørskov, B. S. Clausen, H. Topsøe, and F. Besenbacher. *J. Catal.*, 221(2):510–522, 2004.

5.4 Paper IV: Modeling the active sites of CoMoS

Modeling the active sites of Co-promoted MoS_2 particles by DFT

M. Šarić. J. Rossmeisl, P.G. Moses

Published in PCCP, 2016.

PCCP

PAPER

View Article Online
View Journal

Cite this: DOI: 10.1039/c6cp06881b

Modeling the active sites of Co-promoted MoS_2 particles by DFT

Manuel Šarić,[a] Jan Rossmeisl[b] and Poul Georg Moses*[c]

Received 7th October 2016,
Accepted 8th December 2016

DOI: 10.1039/c6cp06881b

www.rsc.org/pccp

The atomic-scale structure of the Co-promoted MoS_2 catalyst (CoMoS), used for hydrodesulfurization and as a potential replacement for platinum in the acidic hydrogen evolution reaction has been analyzed by modeling its sites using density functional theory and applying thermochemical corrections to account for different reaction conditions. The equilibrium structures of the edges, basal plane and corners have been found and used to obtain a picture of an ideal CoMoS nanoparticle under hydrodesulfurization and hydrogen evolution reaction conditions. Under hydrodesulfurization conditions small energy differences between structures having an additional or missing sulfur atom relative to the equilibrium structures have been observed for the edges and corners explaining their activity towards hydrodesulfurization at the atomic scale. The lack of these small energy differences at the basal plane explains why it is inert towards hydrodesulfurization. The adsorption free energy of hydrogen was calculated and used as a descriptor for qualifying each site in the context of hydrogen evolution, finding that the corner site should perform better than the edges.

1 Introduction

An important part of today's chemical industry is making existing technologies cleaner and friendlier for our environment. A part of such an effort is removing or preventing the formation of pollutants such as CO_2, SO_2 and NO_x gasses that are products of fossil fuel combustion, a process that we will still depend on in the years to come.

SO_2 which is produced from combustion engines of motorized vehicles, various power plants and factories causes the formation of acid rain. Acid rain harms green areas such as forests and decreases the pH level of soil and water but it also damages urban areas by increasing the rate at which man-made structures corrode.[1] High levels of SO_2 also decrease the quality of air and cause the formation of small particles which act as pulmonary irritants.[2] Due to this, there are various regulations that prevent the use of fuels that have more sulfur content than just a few ppm, causing the need for improved catalytic technologies in hydrotreating processes.[3,4]

The hydrodesulfurization (HDS) process is performed in refineries to decrease the sulfur content before fuels can be used in our everyday life. In HDS, hydrogen gas at a high partial pressure is introduced together with oil in a reactor that contains a catalytic bed. Oil among other organic molecules, contains molecules with sulfur such as mercaptans, thiophenes, benzothiophenes, substituted benzothiophenes, *etc.*, which are harder and harder to desulfurize.[4–6]

The HDS reaction can be described by a simple equation:

$$\mathrm{R{-}SH + H_2 \rightleftharpoons R{-}H + H_2S} \quad (1)$$

where R is the main body of an organic molecule. Although the total reaction can be described by a simple enough equation, the complete HDS mechanism is very complex and its complexity increases as the molecule that is being desulfurized becomes structurally more complex.[7–10]

A different way of reducing emissions is based on trying to replace fossil fuels by an environment-friendly fuel. Hydrogen can be used as a fuel in fuel cells, giving water as a waste product which makes it a sustainable energy carrier.

$$\text{Anode:}\quad 2H_2 \leftrightarrow 4(H^+ + e^-) \quad (2)$$

$$\text{Cathode:}\quad O_2 + 4(H^+ + e^-) \leftrightarrow 2H_2O \quad (3)$$

$$\text{Total:}\quad 2H_2 + O_2 \leftrightarrow 2H_2O \quad (4)$$

Hydrogen can be made by steam reforming, which does not solve the problem of CO_2 emissions and it can also be made by water splitting, *i.e.* water electrolysis where water is turned into oxygen and hydrogen electrochemically.

$$\text{Anode:}\quad 2H_2O \leftrightarrow O_2 + 4(H^+ + e^-) \quad (5)$$

$$\text{Cathode:}\quad 4(H^+ + e^-) \leftrightarrow 2H_2 \quad (6)$$

$$\text{Total:}\quad 2H_2O \leftrightarrow 2H_2 + O_2 \quad (7)$$

[a] Center for Atomic Scale Materials Design (CAMd), Department of Physics, Technical University of Denmark, Fysikvej building 307, 2800 Kgs. Lyngby, Denmark. E-mail: msaric@fysik.dtu.dk
[b] Department of Chemistry, Copenhagen University, Universitetsparken 5, 2100 København Ø, Denmark. E-mail: Jan.Rossmeisl@chem.ku.dk
[c] Haldor Topsøe A/S, Nymøllevej 55, 2800 Kgs. Lyngby, Denmark. E-mail: pogm@topsoe.dk

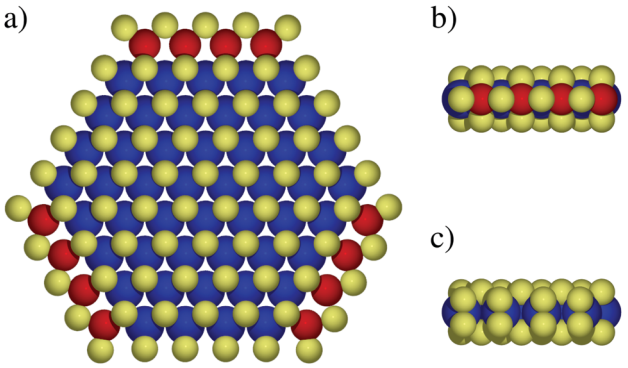

Fig. 1 Model of an ideal CoMoS particle as reported in the literature: (a) the particle as seen from above, (b) side view of the S-edge and (c) side view of the M-edge; the red, blue and yellow spheres represent cobalt, molybdenum and sulfur, respectively.

The issue in the electrochemical production of hydrogen as well as the conversion of hydrogen back to water in a fuel cell is that noble metal catalysts are required to make the process viable.[11,12]

It has been shown in various studies that transition metal sulfides which are in general used for hydrodesulfurization usually perform well in the hydrogen evolution reaction (HER) due to the link between hydrogenation and the HER, thus, making Co-promoted MoS_2 (CoMoS) a possible replacement for platinum.[13–19]

HDS catalysts have been a subject of intense research in the past decade and today's state-of-the-art catalysts are CoMoS and NiMoS based. The structure of CoMoS has also been investigated[20–26] and is shown in Fig. 1.

It can be seen from Fig. 1 that the CoMoS particle is hexagonal compared to the triangular MoS_2 particles.[23,26–28] Studies have pointed that the S-edge is terminated by sulfur monomers occupying bridge positions between two cobalt atoms. For the M-edge it was shown in STM and DFT studies that it is terminated by sulfur dimers occupying top positions on molybdenum atoms,[20–25] although a sulfur monomer termination was reported for hexagonal MoS_2 particles.[29] In TEM studies, the Mo atoms occupy bridge positions similar to the S-edge.[26,27] Furthermore, it is suggested that the under-coordinated sulfur atoms found at the corners of Fig. 1(a) are lost to H_2S in the gas phase due to the hydrogenating environment.[25,26]

The edges of the CoMoS particle, similarly to MoS_2 particles, have a metallic character and have been shown to be active towards HDS and the HER, while the basal plane appears to be inert.[13,19,30–32] It is also speculated that defects and corners play an important part in the desulfurization mechanisms and that a better catalyst will have a higher ratio of corners or defects relative to the surface area.[33]

Although previous studies provided valuable insight into the structure of CoMoS such as its hexagonal shape, edge structure, hydrogen coverages and possible active sites, the corner structure of CoMoS and its role in HDS are still not clear. Most of these studies are often not performed under the same conditions that occur in HER and HDS systems which could affect the catalyst's surface structure. Furthermore, the computational work based on density functional theory that was performed for constructing phase diagrams[21,34–36] employed the PW91 functional[37] which systematically overestimates binding energies.

In the present study, we use DFT applying a modern functional, namely BEEF-vdW,[38] and apply thermochemical corrections to provide further insight into the atomic scale structure of CoMoS under HER and HDS reaction conditions as well as the connection between structure and activity.

2 Materials and methods

The GPAW density functional theory code was used in finite difference mode with a spacing of 0.18 Å in order to perform total energy and vibrational frequency calculations.[39,40] The BEEF-vdW functional was used to treat the exchange and correlation.[38] The CoMoS particle edges at different sulfur terminations were modeled with 4×4 stripes periodic in the x direction and separated by vacuum in the y and z directions. The corners of the CoMoS particle were modeled with a stepped stripe continuous in the x direction separated by vacuum in the y and z directions. The model exposes 3 Co and 2 Mo atoms of the S and M edges, respectively. The surface models of the edges and corners are shown in Fig. 2. The Brillouin zone was sampled using 2, 1, 1 k-points in the x, y and z directions, respectively. The basal plane was modeled with a 4×4 2D sheet periodic in the x and y directions, separated by vacuum in the z direction, using 2, 2, 1 k-points to sample the Brillouin zone in the x, y and z directions, respectively. All the structures were optimized until the maximum force was lower than 0.05 eV $Å^{-1}$.

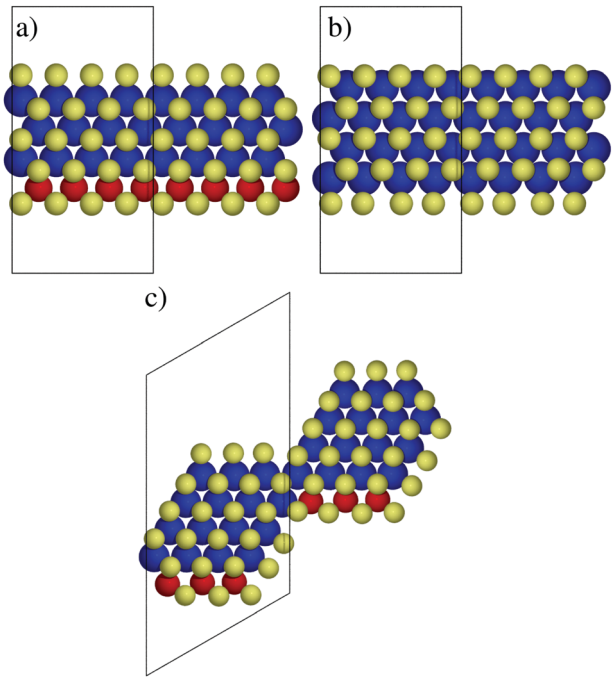

Fig. 2 Supercells of the S-edge (a), M-edge (b) and corner (c).

The free energies of H_2 and H_2S were calculated according to the following equation:

$$G^{p,T}_{\text{gas}} = E + E_{\text{ZP}} + \Delta H^{0,T}_{\text{gas}} - TS^{T}_{\text{gas}} + k_{\text{B}}T\ln\frac{p}{p^{\circ}} \quad (8)$$

where E is the electronic energy at 0 K, E_{ZP} is the zero point contribution to the energy, $\Delta H^{0,T}_{\text{gas}}$ the change in enthalpy when going from 0 K to higher temperatures, S^{T}_{gas} the entropy term at a specific temperature, k_{B} the Boltzmann constant, p the partial pressure of the gas and p° the standard pressure.[41] The zero point energy, enthalpy and entropy terms needed for calculating the free energies regarding H_2 and H_2S have been obtained by calculating the vibrational frequencies and employing the ideal gas approximation as implemented in ASE/GPAW.[42] Alternatively, the enthalpy and entropy corrections can be obtained from standard thermochemical tables.[43,44] Using one method or the other does not affect the obtained results in any significant way.

The free energy of adsorbed hydrogen was calculated according to:

$$G^{T}_{\text{ads}} = E + E_{\text{ZP}} + \Delta U^{0,T}_{\text{vib}} - TS^{T}_{\text{vib}} \quad (9)$$

where $\Delta U^{0,T}_{\text{vib}}$ is the change in internal energy when going from 0 K to higher temperatures and S^{T}_{vib} the entropy term at a specific temperature. The zero-point energy, change in internal energy when going form 0 K to a temperature T and the entropy term at temperature T were calculated for hydrogen adsorbed at the S-edge by ASE/GPAW's thermochemistry class implementing the harmonic approximation:[42]

$$E_{\text{ZP}} = \frac{1}{2}\sum_i h\nu_i \quad (10)$$

$$TS^{T}_{\text{vib}} = \sum_i \frac{h\nu_i}{e^{h\nu_i/k_{\text{B}}T} - 1} - k_{\text{B}}T\sum_i \ln\left(1 - e^{-h\nu_i/k_{\text{B}}T}\right) \quad (11)$$

$$\Delta U^{0,T}_{\text{vib}} = \sum_i \frac{h\nu_i}{e^{h\nu_i/k_{\text{B}}T} - 1} \quad (12)$$

It was assumed that the contributions calculated for hydrogen adsorbed on the S-edge can be used for all the remaining sites. The HDS conditions were taken from ref. 45 as 573 K, 38 atm of H_2 and 0.13 atm of H_2S. For HER conditions, the pressures of H_2 and H_2S were taken as 1 bar and 10^{-6} bar, respectively, and the temperature was taken as 298.15 K.[46]

The structure of CoMoS in terms of sulfur termination was characterized using the sulfur saturated edges and corners terminated by sulfur dimers as a reference and by calculating the energy of vacancy formation according to the following equation:

$$Co_xMo_yS_z + nH_2 \rightleftharpoons Co_xMo_yS_{z-n} + nH_2S \quad (13)$$

x, y and z represent the number of cobalt, molybdenum and sulfur atoms in the supercell, respectively, and n represents the number of vacancies formed.

For the basal plane the tendency to form a vacancy or adsorb an additional sulfur add-atom was calculated using the pristine basal plane as a reference.

The adsorption energy of hydrogen was calculated according to the following reaction:

$$\frac{1}{2}H_2 + * \leftrightarrow H^* \quad (14)$$

where * represents a site on the surface.

To estimate the computational uncertainties of the performed calculation the BEEF ensemble was used. The BEEF ensemble was obtained after performing total energy calculations using the BEEF-vdW functional with no significant increase in computational time. The obtained BEEF ensemble for each system was a distribution of 2000 energies. These 2000 energies were used to obtain lists of 2000 values for the sulfur vacancy formation and hydrogen adsorption energies. The uncertainty was calculated as the standard deviation of the ensemble of 2000 values of energy differences (hydrogen adsorption or sulfur vacancy formation).

The uncertainty of hydrogen adsorption energies, σ_{H}, was calculated as:

$$\sigma_{\text{H}} = \left[\frac{1}{1999}\sum_{i=1}^{2000}\left(E_i(H^*) - E_i(*) - \frac{1}{2}E_i(H_2)\right)^2\right]^{\frac{1}{2}} \quad (15)$$

where $E_i(H^*)$, $E_i(*)$ and $E_i(H_2)$ are the i-th members in the ensembles of adsorbed hydrogen, the surface and hydrogen gas, respectively.

The uncertainty of sulfur vacancy formation, σ_{S}, was calculated as:

$$\sigma_{\text{S}} = \left[\frac{1}{1999}\sum_{i=1}^{2000}\left(E_i\left(Co_xMo_yS_{z-n}\right) + nE_i(H_2S) - E_i\left(Co_xMo_yS_z\right) - nE_i(H_2)\right)^2\right]^{\frac{1}{2}} \quad (16)$$

where $E_i(Co_xMo_yS_{z-n})$, $E_i(H_2S)$, $E_i(Co_xMo_yS_z)$ and $E_i(H_2)$ are the i-th members in the ensembles of CoMoS with n vacancies, H_2S gas, CoMoS with no vacancies and H_2 gas, respectively.

3 Results and discussion

3.1 Equilibrium structure of CoMoS

In order to obtain the equilibrium structures of the S-edge, M-edge, corners and basal plane under various conditions defined by temperature and chemical potentials of H_2 and H_2S the vacancy formation energy and sulfur adsorption energy were calculated. Fig. 3 shows the differential energy diagrams at 0 K (electronic energy only) and the differential free energy diagrams under HER and HDS conditions for each site. The differential diagram represents the energy difference (gain if negative or loss if positive) for removing each subsequent sulfur atom. The uncertainty of the calculation is displayed as an error bar on the 0 K curve only, although the same uncertainty is also associated with the free energies.

From Fig. 3(a) one can see that at 0 K it is favorable to remove the first two sulfur atoms from the 8/4 structure (saturated with sulfur dimers). The equilibrium S-edge will have a 6/4 ratio of edge

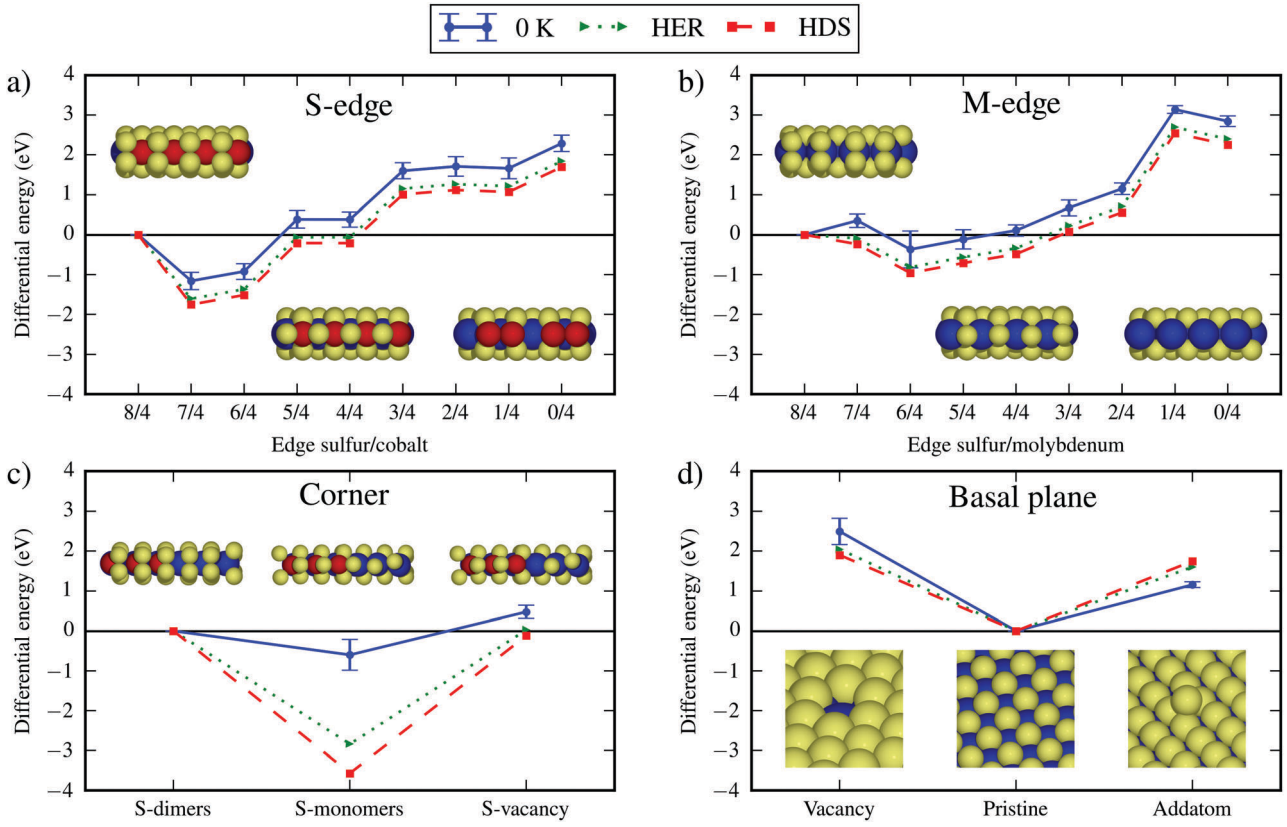

Fig. 3 Differential energy diagrams for the formation of vacancies at the S-edge (a), M-edge (b) and corner (c) as well as the formation of a vacancy and the adsorption of a sulfur atom at the basal plane (d).

sulfur to cobalt, *i.e.* it will have a sulfur coverage of 75%, assuming that the 8/4 sulfur to cobalt ratio is 100% coverage. Correcting the 0 K energy for HER and HDS conditions it can be seen that the energy diagram changes significantly due to the temperature and the high ratio of partial pressure of hydrogen to partial pressure of hydrogen sulfide and thus it becomes easier to form vacancies. There is therefore a gain in energy for removing 4 sulfur atoms from the 8/4 structure which means that the equilibrium structure of the S-edge under both HER and HDS conditions is terminated by sulfur monomers (4/4), *i.e.* 50% sulfur termination, an observation which is in agreement with earlier studies.[23,25,45]

It can be observed from Fig. 3(b) that there is an uphill step for removing the first sulfur atom from the M-edge at 0 K which could explain why it is usually the 100% covered M-edge that is seen in STM experiments.[22,23,25] Removing the subsequent sulfur atoms is favorable and the equilibrium structure under HER and HDS conditions is the 4/4 structure, *i.e.* the structure with a 50% coverage of sulfur or monomer termination. An additional observation from the calculations for the M-edge is that the sulfur atoms switch from sitting on top of the Mo atoms to the bridge position between two Mo atoms when reaching a ratio of 6/4 and below. This position of the sulfur atoms at the M-edge is in agreement with the TEM work.[26–28] The difference in sulfur atom position between STM and TEM observations could be due to the different support materials used in the experiments or due to the different operating conditions. For the S-edge the sulfur atoms prefer the bridge site for all sulfur terminations. This change in position will have an impact on the structure of corners since the corner sulfur from the previous picture of the particle, shown in Fig. 1 and 4(a), which is coordinated only to cobalt will now be coordinated to both cobalt and molybdenum sitting in between them as shown in Fig. 4(b). Furthermore, one could ask how plausible it is to turn this kind of sulfur sitting where cobalt meets molybdenum into a vacancy thus forming the structure shown in Fig. 4(c), namely a corner vacancy.

In Fig. 3(c) one can see that it is, as expected from the data for the S and M edges, favorable to go from a corner surrounded by sulfur dimers to a corner surrounded by sulfur monomers (difference of 5 sulfur atoms). Furthermore, one can observe that at 0 K it is not favorable to make a vacancy at the corners. The vacancy formation is slightly uphill under HER conditions, 0.03 eV, which is shadowed by the uncertainty of the calculation, 0.17 eV (one standard deviation). Due to the uncertainty it is not possible to claim with certainty that a vacancy will not be formed under HER conditions. One should also consider that the corner filled by a sulfur atom could be stabilized by forming an SH group though hydrogen adsorption, this is addressed in the next subsection. HDS conditions allow a vacancy to be formed, −0.12 eV, although this observation is again shadowed by the uncertainty of the calculation, 0.17 eV, and one cannot

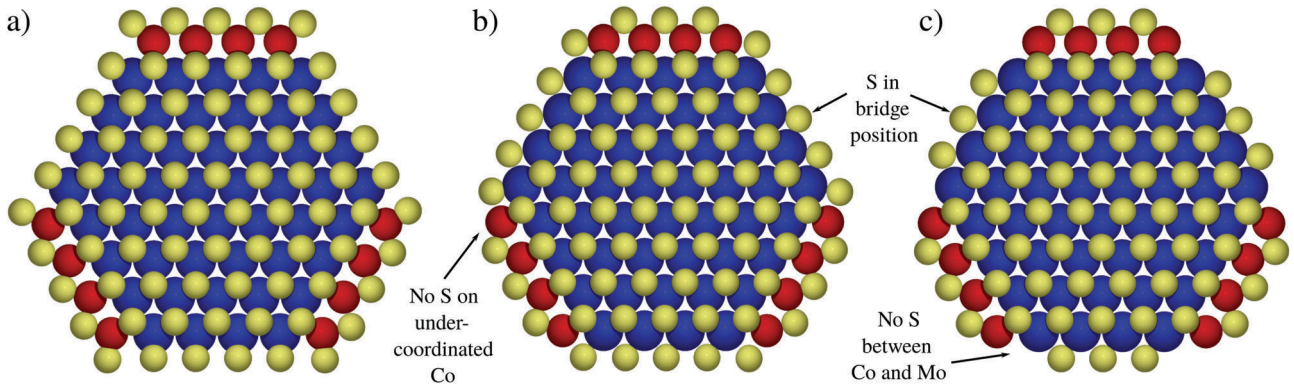

Fig. 4 Different corner structures: (a) corner filled with sulfur as seen in various studies (b) sulfur atoms at the M-edge shifted to the bridge position leaving more space at the corner (c) a corner vacancy formed by losing the sulfur sitting where cobalt and molybdenum meet; the red, blue and yellow spheres represent cobalt, molybdenum and sulfur, respectively.

say with complete certainty that the vacancy is the equilibrium structure. Even if the formation of a vacancy is slightly uphill this state will be populated significantly due to the high temperature under HDS conditions. For the sake of further discussion, it is assumed that the equilibrium structure under HER conditions is the corner saturated by sulfur monomers as shown in Fig. 4(b) and under HDS conditions the corner with a vacancy where the cobalt and molybdenum atoms meet as shown in Fig. 4(c).

From Fig. 3(d) it can be seen that, under all conditions, it is neither favorable to introduce vacancies at the basal plane or to adsorb additional sulfur atoms. The pristine basal plane is thus the structure that will be found under both HER and HDS conditions.

3.2 Activity towards HDS

An important property of the S-edge regarding sulfur chemistry and the activity towards HDS is illustrated in Fig. 3(a). There is a small energy difference of 0.21 eV between the equilibrium structure (4/4) and the structure that has one sulfur atom more (5/4). This observation indicates that it is possible to bind an additional sulfur atom on the equilibrium edge which is crucial for binding molecules or intermediates that contain sulfur and for creating a driving force for desulfurization. After the sulfur containing molecule has been desulfurized it is favorable to form the equilibrium structure (4/4) once again by releasing hydrogen sulfide in the gas phase and in that way completing a HDS cycle. This property of the S-edge explains the activity towards HDS at the atomic level and is further illustrated in Fig. 5.

When it comes to the M-edge it can be seen from Fig. 3(b) that it is not favorable to bind an additional sulfur atom onto the equilibrium structure, 0.71 eV. It is on the other hand possible to make a vacancy in the equilibrium structure since the energy associated with going from the 4/4 to the 3/4 structure is quite small, *i.e.* 0.08 eV. Once a vacancy is made it is possible to bind a sulfur containing species in it and desulfurize it, thus, forming the 4/4 structure once again. So in the case of the M-edge, it is first necessary to create a sulfur vacancy (3/4 structure)

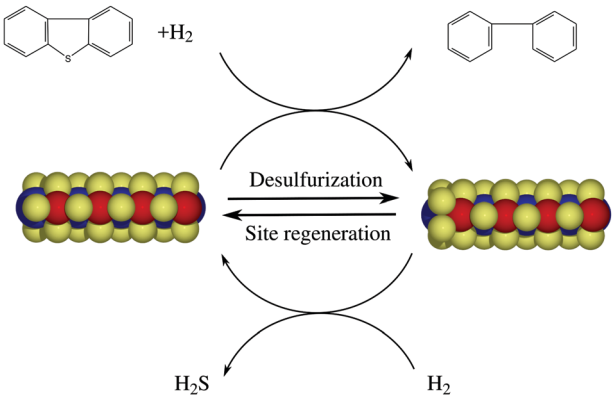

Fig. 5 Sketch explaining the activity of the S-edge towards hydrodesulfurization; the red, blue and yellow spheres represent cobalt, molybdenum and sulfur, respectively.

which will then act as the active site for desulfurization. This mechanism is further illustrated by Fig. 6.

The equilibrium structure of the CoMoS particle will have a vacancy at the corner which will be able to adsorb surface containing species in it. Once the given species is adsorbed it will

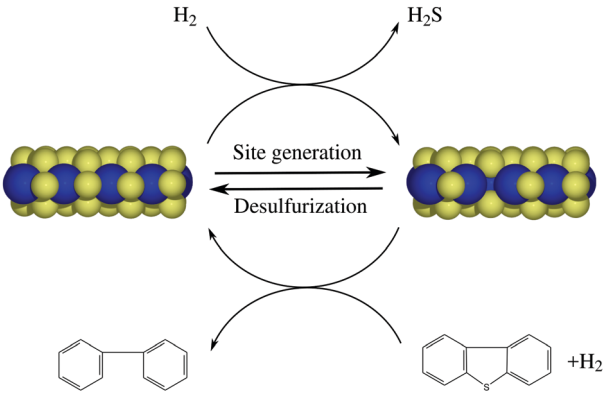

Fig. 6 Sketch explaining the activity of the M-edge towards hydrodesulfurization; the blue and yellow spheres represent molybdenum and sulfur respectively.

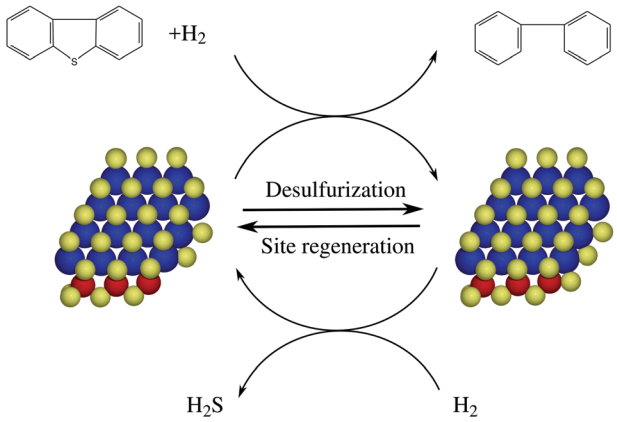

Fig. 7 Sketch explaining the activity of the corner towards hydrodesulfurization; the blue and yellow spheres represent molybdenum and sulfur, respectively.

get desulfurized, filling the vacancy with a sulfur atom. The vacancy will then be formed once again by releasing H_2S in the gas phase, thus enabling the HDS cycle to start again. The mechanism is shown in Fig. 7.

The corner and S-edge behave in a similar way since the equilibrium structure is the active site, while the M-edge needs to become active by first forming a vacant site. Fig. 3(a–c) suggest that for the S-edge, M-edge and corner, respectively, there has to be a structure whose differential energy is close to 0 eV for the site to be active towards HDS.

In the case of the basal plane which is illustrated in Fig. 3(d) one can see that there is no structure for which the differential energy is close to 0 eV. Both making a vacancy and adsorbing a sulfur atom are very unfavorable which in return means that the basal plane will be inert towards HDS. Several studies have investigated the possibility of creating active sties on the basal either by creating extended defects[47] or by applying strain to MoS_2.[48] The application of strain has been particularly successful in activating the basal plane towards HER[48] which also indicates that it should benefit hydrogenation during HDS.[17] The formation of extended vacancies was shown to lead to a stabilization of $\approx$0.4 eV per sulfur atom over forming single sulfur vacancies.[47] Although more stable compared to single vacancies, extended vacancies yield endergonic H_2S formation (greater than $\approx$1.5 eV) under HDS and HER conditions which makes them unfavorable under both contexts.

The M-edge vacancy binds sulfur stronger than the S-edge which could indicate that the barriers for cleaving carbon–sulfur bonds are small and the rate of desulfurization is limited by either vacancy generation or hydrogen chemistry.[45,49] On the S-edge, where the adsorption energy of sulfur is weaker compared to the M-edge, it was shown that the highest activation energy and the rate determining step are related to C–S bond cleavage.[7] It is also plausible that the explanation regarding the small activation energy for C–S cleavage at the M-edge only holds for molecules where the sulfur atom is easily accessible. These are molecules such as thiols or perhaps some mercaptans which are able to chemisorb in the vacancy only through the sulfur atom. Such molecules will desulfurize through the so-called direct desulfurization pathway using the least amount of hydrogen possible to complete a HDS cycle.[7,8] For more complex molecules such as benzothiophenes and substituted benzothiophenes where the sulfur atom is hidden between benzene rings and substituents, the vacancy is inaccessible to the sulfur atom. This means that hydrogen chemistry and the hydrogenation pathway will play an important role in the desulfurization process *i.e.* additional hydrogen will be used to turn the molecule into a hydrogenated intermediate that is easier to desulfurize.[7,8] This should only be possible on vacancy free sites where hydrogen is available for hydrogenation, namely the S-edge. Another plausible explanation is that larger molecules get desulfurized directly at the corner vacancy which, compared to the M-edge vacancy, has more space available for binding benzothiophenes and similar molecules.

3.3 Activity towards HER and hydrogenation

It was shown that the adsorption free energy of hydrogen can be used as a descriptor for HER[13] and that the optimal HER catalyst will bind hydrogen with an adsorption free energy of 0 eV.[50] Regardless of the mechanism the HER has only one surface intermediate, adsorbed hydrogen, thus the optimal binding is 0 eV. Fig. 8 shows the differential energy diagram of hydrogen adsorption for the 50% terminated S and M edges under 0 K, HER and HDS conditions. It can be seen in Fig. 8 that hydrogen binding is weaker under HDS than under HER conditions.

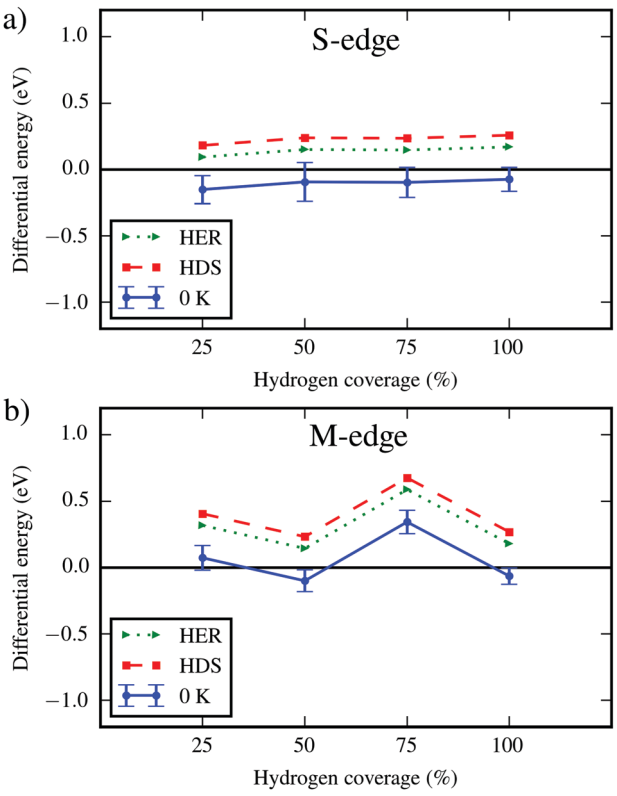

Fig. 8 Differential energy diagram of hydrogen adsorption at the S-edge (a) and M-edge (b) under 0 K, HER and HDS conditions.

This is due to the high temperature under HDS conditions which stabilizes gas phase H_2 more than the high pressure which stabilizes the surface hydrogen. Based on the optimal adsorption free energy of hydrogen of 0 eV[13,50] and the results obtained one can conclude that the S-edge will be a better site for HER since the adsorption free energy of hydrogen is closer to 0 eV. This observation is somewhat different from other studies which predicted a stronger binding of hydrogen on MoS_2 (no cobalt), *i.e.* the M-edge.[13]

It is evident that the surface coverage will be lower than 25% for HER and even lower under HDS conditions for both edges, furthermore there will be a higher hydrogen coverage on the S-edge than on the M-edge since the adsorption of hydrogen is more favorable there. This indicates that the hydrogenation pathway of HDS in which the sulfur containing species get pre-hydrogenated to some extent will be more pronounced at the S-edge.

When it comes to the CoMoS corner it was suggested that there is a vacancy under HDS conditions and that the formation of a vacancy is less likely under HER conditions. The adsorption energies and free energies under relevant conditions are shown in Fig. 9. The free energy of hydrogen adsorption at the corner, −0.12 eV, under HER conditions is favorable. This confirms the previous assumption that the corner under HER conditions does not have a vacancy but SH groups. The adsorption free energy of hydrogen at the S-edge, 0.09, is closer to 0 eV than at the corner, −0.12 eV, and one can at first conclude that the S-edge should be slightly better under HER conditions than the corner sites, however due the uncertainty of the calculations one cannot claim which site is better. Hydrogen binds on the corner sites rather than at the edge; furthermore as seen from Fig. 8, the adsorption at the S-edge becomes weaker if there is already some hydrogen adsorbed in the vicinity. Hydrogen adsorbed at the corner can thus destabilize hydrogen bound at the S-edge which indicates that the corner sites might actually be the active sites for hydrogen evolution.

It can be seen that under HDS conditions the adsorption energy at the corner site prior to the formation of a vacancy is slightly negative, but not enough to prevent the predicted HDS vacancy. From the adsorption energies related to the sulfur vacancy it is clear that, once the vacancy is formed, the corner becomes unfavorable for hydrogen adsorption and no hydrogenation occurs at that point. Hydrogenation could although occur at the corner if the vacancy formation is limited by kinetics, indicating that the corner is either an important sulfur adsorption (cleaving C–S bonds) site or hydrogen adsorption (hydrogen dissociation and hydrogenation) site. Perhaps there is a synergy between them.

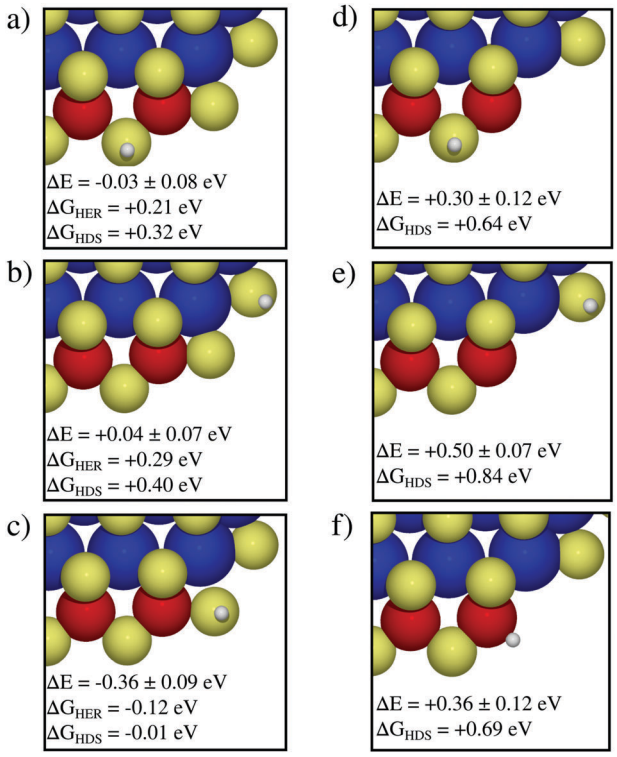

Fig. 9 Hydrogen adsorption energies and free energies under HER or HDS conditions on the: (a) S-edge side of the filled corner, (b) M-edge side of the filled corner, (c) filled corner, (d) S-edge side of the corner vacancy, (e) M-edge side of the corner vacancy, and (f) corner vacancy.

4 Conclusion

The equilibrium structure of the S-edge, M-edge, corner and basal plane of an ideal CoMoS particle under HER and HDS conditions has been shown. The activity of the edges and the corner towards HDS has been explained through the small free energy required to bind sulfur or form a vacancy, while the basal plane was shown to be inert. The entire length of the S-edge is active for HDS, while at the M-edge and corner only the vacancies are active. It was speculated that the S-edge and perhaps corner play an important role in the hydrogenation pathway through hydrogen chemistry and that the M-edge is active towards simple molecules where sulfur is spatially available, while the corner could also be active towards more complex molecules. For the HER it was shown that the S-edge is more active than the M-edge, additionally it was argued that the corner is the most important site for HER since it is best at adsorbing hydrogen and has an adsorption free energy of hydrogen close to 0 eV. In the end, we conclude that both for HER and HDS the particle should be small in order to reduce the area of the inert basal plane and to have many defect (corner) sites which will be active for HER and for HDS either through cleaving C–S bonds or hydrogenating molecules.

Acknowledgements

Funding: This work was supported by the Danish Council for Independent Research (grant HYDECAT, DFF-1335-00016) and the Carlsberg Foundation (grant CF15-0165).

References

1 G. E. Likens, C. T. Driscoll and D. C. Buso, *Science*, 1996, **272**, 244.
2 M. Andreae and D. Rosenfeld, *Earth-Sci. Rev.*, 2008, **89**, 13–41.

3 M. Greenstone, *Journal of environmental economics and management*, 2004, **47**, 585–611.
4 C. Song, *Catal. Today*, 2003, **86**, 211–263.
5 I. Babich and J. Moulijn, *Fuel*, 2003, **82**, 607–631.
6 G. Schuit and B. Gates, *AIChE J.*, 1973, **19**, 417–438.
7 P. G. Moses, B. Hinnemann, H. Topsøe and J. K. Nørskov, *J. Catal.*, 2007, **248**, 188–203.
8 R. Prins, M. Egorova, A. Röthlisberger, Y. Zhao, N. Sivasankar and P. Kukula, *Catal. Today*, 2006, **111**, 84–93.
9 S. Humbert, G. Izzet and P. Raybaud, *J. Catal.*, 2016, **333**, 78–93.
10 J.-F. Paul, S. Cristol and E. Payen, *Catal. Today*, 2008, **130**, 139–148.
11 E. Skúlason, G. S. Karlberg, J. Rossmeisl, T. Bligaard, J. Greeley, H. Jónsson and J. K. Nørskov, *Phys. Chem. Chem. Phys.*, 2007, **9**, 3241–3250.
12 J. K. Nørskov, T. Bligaard, A. Logadottir, J. Kitchin, J. Chen, S. Pandelov and U. Stimming, *J. Electrochem. Soc.*, 2005, **152**, J23–J26.
13 B. Hinnemann, P. G. Moses, J. Bonde, K. P. Jørgensen, J. H. Nielsen, S. Horch, I. Chorkendorff and J. K. Nørskov, *J. Am. Chem. Soc.*, 2005, **127**, 5308–5309.
14 C. G. Morales-Guio, L.-A. Stern and X. Hu, *Chem. Soc. Rev.*, 2014, **43**, 6555–6569.
15 E. J. Popczun, J. R. McKone, C. G. Read, A. J. Biacchi, A. M. Wiltrout, N. S. Lewis and R. E. Schaak, *J. Am. Chem. Soc.*, 2013, **135**, 9267–9270.
16 M. H. Hansen, L.-A. Stern, L. Feng, J. Rossmeisl and X. Hu, *Phys. Chem. Chem. Phys.*, 2015, **17**, 10823–10829.
17 M. Šarić, P. G. Moses and J. Rossmeisl, *ChemCatChem*, 2016, **8**, 3334–3337.
18 J. Bonde, P. G. Moses, T. F. Jaramillo, J. K. Norskov and I. Chorkendorff, *Faraday Discuss.*, 2009, **140**, 219–231.
19 T. F. Jaramillo, K. P. Jorgensen, J. Bonde, J. H. Nielsen, S. Horch and I. Chorkendorff, *Science*, 2007, **317**, 100–102.
20 P. G. Moses, B. Hinnemann, H. Topsøe and J. K. Nørskov, *J. Catal.*, 2009, **268**, 201–208.
21 P. Raybaud, J. Hafner, G. Kresse, S. Kasztelan and H. Toulhoat, *J. Catal.*, 2000, **190**, 128–143.
22 J. V. Lauritsen, J. Kibsgaard, G. H. Olesen, P. G. Moses, B. Hinnemann, S. Helveg, J. K. Nørskov, B. S. Clausen, H. Topsøe and E. Lægsgaard, *et al.*, *J. Catal.*, 2007, **249**, 220–233.
23 F. Besenbacher, M. Brorson, B. Clausen, S. Helveg, B. Hinnemann, J. Kibsgaard, J. V. Lauritsen, P. G. Moses, J. K. Nørskov and H. Topsøe, *Catal. Today*, 2008, **130**, 86–96.
24 B. Hinnemann, P. G. Moses and J. K. Nørskov, *J. Phys.: Condens. Matter*, 2008, **20**, 064236.
25 S. S. Grønborg, M. Šarić, P. G. Moses, J. Rossmeisl and J. V. Lauritsen, *J. Catal.*, 2016, **344**, 121–128.
26 Y. Zhu, Q. M. Ramasse, M. Brorson, P. G. Moses, L. P. Hansen, C. F. Kisielowski and S. Helveg, *Angew. Chem., Int. Ed.*, 2014, **53**, 10723–10727.
27 L. P. Hansen, Q. M. Ramasse, C. Kisielowski, M. Brorson, E. Johnson, H. Topsøe and S. Helveg, *Angew. Chem., Int. Ed.*, 2011, **50**, 10153–10156.
28 C. Kisielowski, Q. Ramasse, L. Hansen, M. Brorson, A. Carlsson, A. Molenbroek, H. Topsøe and S. Helveg, *Angew. Chem., Int. Ed.*, 2010, **49**, 2708–2710.
29 J. Lauritsen, M. Bollinger, E. Lægsgaard, K. Jacobsen, J. Nørskov, B. Clausen, H. Topsøe and F. Besenbacher, *J. Catal.*, 2004, **221**, 510–522.
30 M. Bollinger, J. Lauritsen, K. W. Jacobsen, J. K. Nørskov, S. Helveg and F. Besenbacher, *Phys. Rev. Lett.*, 2001, **87**, 196803.
31 D. Merki and X. Hu, *Energy Environ. Sci.*, 2011, **4**, 3878–3888.
32 L. Byskov, J. Norskov, B. Clausen and H. Topsoe, *Catal. Lett.*, 2000, **64**, 95–99.
33 E. Hensen, P. Kooyman, Y. Van der Meer, A. Van der Kraan, V. De Beer, J. Van Veen and R. Van Santen, *J. Catal.*, 2001, **199**, 224–235.
34 M. Bollinger, K. W. Jacobsen and J. K. Nørskov, *Phys. Rev. B: Condens. Matter Mater. Phys.*, 2003, **67**, 085410.
35 H. Schweiger, P. Raybaud, G. Kresse and H. Toulhoat, *J. Catal.*, 2002, **207**, 76–87.
36 P.-Y. Prodhomme, P. Raybaud and H. Toulhoat, *J. Catal.*, 2011, **280**, 178–195.
37 J. P. Perdew, J. Chevary, S. Vosko, K. A. Jackson, M. R. Pederson, D. Singh and C. Fiolhais, *Phys. Rev. B: Condens. Matter Mater. Phys.*, 1992, **46**, 6671.
38 J. Wellendorff, K. T. Lundgaard, A. Møgelhøj, V. Petzold, D. D. Landis, J. K. Nørskov, T. Bligaard and K. W. Jacobsen, *Phys. Rev. B: Condens. Matter Mater. Phys.*, 2012, **85**, 235149.
39 J. J. Mortensen, L. B. Hansen and K. W. Jacobsen, *Phys. Rev. B: Condens. Matter Mater. Phys.*, 2005, **71**, 035109.
40 J. Enkovaara, C. Rostgaard, J. J. Mortensen, J. Chen, M. Dułak, L. Ferrighi, J. Gavnholt, C. Glinsvad, V. Haikola and H. Hansen, *et al.*, *J. Phys.: Condens. Matter*, 2010, **22**, 253202.
41 J. Kleis, G. Jones, F. Abild-Pedersen, V. Tripkovic, T. Bligaard and J. Rossmeisl, *J. Electrochem. Soc.*, 2009, **156**, B1447–B1456.
42 ASE, *Atomic simulation environment thermochemistry class*, Accessed April 28, 2016.
43 NIST, *H_2 thermochemical table*, Accessed April 28, 2016.
44 NIST, *H_2S thermochemical table*, Accessed April 28, 2016.
45 P. G. Moses, L. C. Grabow, E. M. Fernandez, B. Hinnemann, H. Topsøe, K. G. Knudsen and J. K. Nørskov, *Catal. Lett.*, 2014, **144**, 1425–1432.
46 H. G. S. Casalongue, J. D. Benck, C. Tsai, R. K. Karlsson, S. Kaya, M. L. Ng, L. G. Pettersson, F. Abild-Pedersen, J. Nørskov and H. Ogasawara, *et al.*, *J. Phys. Chem. C*, 2014, **118**, 29252–29259.
47 D. Le, T. B. Rawal and T. S. Rahman, *J. Phys. Chem. C*, 2014, **118**, 5346–5351.
48 H. Li, C. Tsai, A. L. Koh, L. Cai, A. W. Contryman, A. H. Fragapane, J. Zhao, H. S. Han, H. C. Manoharan and F. Abild-Pedersen, *et al.*, *Nat. Mater.*, 2016, **15**, 48–53.
49 E. M. Fernandez, P. G. Moses, A. Toftelund, H. A. Hansen, J. I. Martinez, F. Abild-Pedersen, J. Kleis, B. Hinnemann, J. Rossmeisl, T. Bligaard and J. K. Norskov, *Angew. Chem., Int. Ed.*, 2008, **47**, 4683–4686.
50 R. Parsons, *Trans. Faraday Soc.*, 1958, **54**, 1053–1063.

5.5 Paper V: Modeling adsorption on CoMoS

Modeling adsorption of sulfur containing molecules on the Co-promoted MoS_2 catalyst by DFT

M. Šarić. J. Rossmeisl, P.G. Moses

Submitted for publication, 2016.

Modeling the adsorption of sulfur containing molecules and their hydrodesulfurization intermediates on the Co-promoted MoS_2 catalyst by DFT

Manuel Šarić

Center for Atomic Scale Materials Design (CAMd), Department of Physics, Technical University of Denmark, Fysikvej building 311, 2800 Kgs. Lyngby, Denmark

Jan Rossmeisl

Department of Chemistry, Copenhagen University, Universitetsparken 5, 2100 København Ø, Denmark

Poul Georg Moses

Haldor Topsøe A/S, Nymøllevej 55, 2800 Kgs. Lyngby, Denmark

Abstract

Achieving ultra-deep hydrodesulfurization means enabling removal of the last fractions of sulfur, contained in refractory molecules, from oil. Improving the state-of-the-art Co-promoted MoS_2 (CoMoS) catalyst or the development of novel catalysts is crucial for this. Improving CoMoS requires more insight in the way sulfur containing molecules interact with it. Herein, we model the adsorption of sulfur containing molecules on the S-edge, M-edge, corner and basal plane of CoMoS using density functional theory. The obtained adsorption configurations and energies point to a preference towards physisorption at the S-edge and chemisorption in vacancies at the M-edge and corner. Smaller molecules, such as thiophene and methylthiol, were found to prefer vacancies when adsorbing while larger, sterically hindered molecules as 4,6-dimethyldibenzothiophene prefer physisorption on the brim of the edges or the basal plane through van der Waals interactions. Hydrogenation generally increases adsorption strengths with smaller molecules and dibenzothiophene showing a larger increase for M-edge and corner chemisorption and 4,6-dimethyldibenzothiophene showing a larger increase on the S-edge brim, possibly explaining why 4,6-dimethyldibenzothiophene does not get desulfurized directly but follows a hydrogenation route. Thiolate formation energies were also calculated for the different molecules and used to predict which sites are most likely to be involved in breaking carbon-sulfur bonds. The thiolate formation energies show the inert nature of the basal plane towards breaking carbon-sulufr and sulfur-hydrogen bonds.

Keywords: hydrodesulfurization, hydrogenation, catalysis, methylthiol, thiophene, dibenzothiophene, 4,6-dimethyldibenzothiophene, cobalt, promoted, molybdenum, sulfide, CoMoS, adsorption, DFT, vdW, physisorption, chemisorption

1. Introduction

Hydrodesulfurization (HDS) is performed in refineries in order to reduce sulfur contents of oil prior to its distribution[1, 2, 3]. Reducing sulfur contents of oil decreases SO_2 emissions upon combustion. SO_2 emissions are associated with the formation of acid rain and decreasing air quality, due to this there are regulations that limit SO_2 emissions and sulfur contents of fuels. These regulations are getting stricter with time, causing a need for new of further improvement of current state-of-the-art HDS catalysts[4, 5, 6].

The cobalt promoted MoS_2 hydrodesulfurization catalyst (CoMoS) has been the topic of many studies in the past decade. These studies have uncovered several structural aspects such as hexagonal particle shape, position of cobalt promoters, edge and corner sulfur coverage, metallic character of edges, sulfur vacancy formation energies[7, 8, 9, 10, 11, 12, 13, 14, 15, 16, 17, 18, 19, 20]. Furthermore, a number of studies address adsorption of various sulfur and nitrogen containing molecules representing oil feeds in HDS. These studies gave insight on how different molecules interact with CoMoS, addressing issues of surface poisoning as well as suggesting mechanism and reaction pathways that these molecules follow during HDS[21, 22, 23, 10, 24, 25, 26, 27, 28].

HDS can be described with the following equation:

$$R - SH + H_2 \leftrightarrow R - H + H_2S \quad (1)$$

Here, R represents the main body of an organic molecule[1, 2, 3]. Although equation 1 seems very simple, the mechanism of HDS can get very involved and its complexity increases with the complexity of the molecule that is being desulfurized. Two pathways for hydrodesulfurization have been

Email addresses: msaric@fysik.dtu.dk (Manuel Šarić), Jan.Rossmeisl@chem.ku.dk (Jan Rossmeisl), pogm@topsoe.dk (Poul Georg Moses)

Abbreviations: HDS, hydrodesulfurization; CoMoS, Co-promoted MoS_2; DFT, density functional theory; DDS, direct desulfurization; HYD, hydrogenation; DBT, dibenzothiophene; 4,6-DMDBT, 4,6-dimethyldibenzothiophene

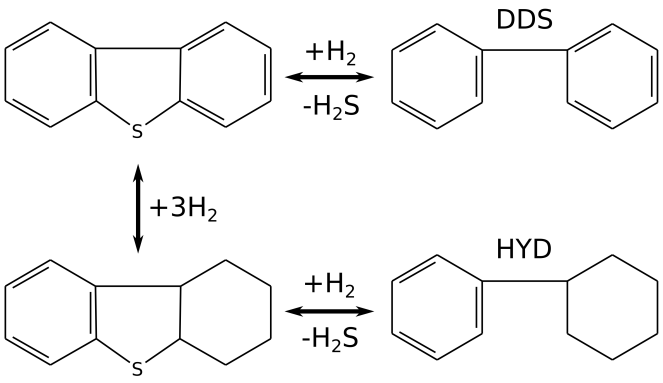

Figure 1: Scheme showing the difference between the DDS and HYD pathways using DBT as example. Adopted from Prins et al[22].

identified and reported in the literature, the direct desulfurization (DDS) and hydrogenation (HYD) pathways[21, 22, 12]. In DDS, the molecule is desulfurized directly, using the least amount of hydrogen necessary to break the carbon-sulfur (C-S) bonds. In HYD, a series of hydrogenation steps precedes the C-S bonds cleavage. These hydrogenation steps saturate organic molecules with hydrogen turning π-bonds to σ-bonds which is speculated to increase the "flexibility" of some organic molecules, particularly those containing benzene rings, which in return allows them to adsorb stronger at the active sites. The difference between DDS and HYD is further illustrated in figure 1.

Although many studies were performed on the adsorption of various molecules on CoMoS, most studies address structure and adsorption separately. Information on the fundamental connection between atomic scale structure and adsorption configurations is lacking. Furthermore, most studies address adsorption of non-hydrogenated molecular species on the edges of CoMoS exclusively, neglecting the role of corner sites. Additionally, in order to describe adsorption of larger molecules computationally, inclusion of van der Waals (vdW) interactions is needed. This was made possible by the recent development of various exchange-correlation functionals that include long range vdW interactions[29, 30]. In the present work we model the adsorption of sulfur containing molecular species and their HDS intermediates on CoMoS. Furthermore, we base our model systems on previous work performed with density functional theory (DFT) in which the equilibrium atomic scale structure and active sites of an ideal CoMoS particle at HDS conditions were determined[31]. This approach makes it possible to identify the role that each active site has in HDS, determining if some sites are active only towards particular molecular species and argue whether a specific molecular specie can get desulfurized directly through the DDS mechanism or if it needs to go through a series of hydrogenation steps prior to the removal of sulfur. Another benefit of basing the present adsorption models on established structures is ensuring that all the sites are treated in a systematic and rational way without speculating whether a certain type of defect or sulfur vacancy is present at a given site under HDS conditions.

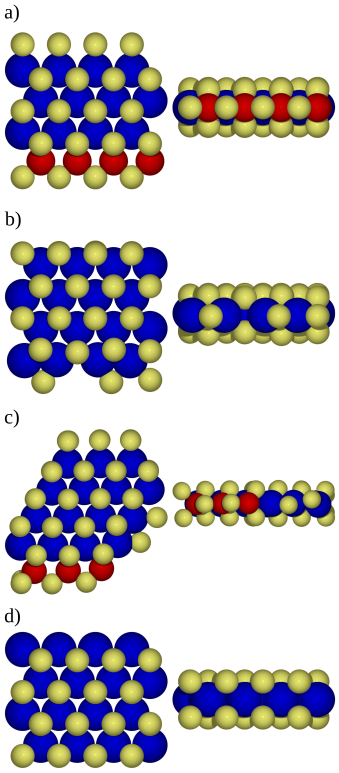

Figure 2: S-edge stripe model seen from above and the side (a), M-edge stripe model seen from above and the side (b), corner stripe model seen from above and the side (c), basal plane model seen from above and the side (d). The red, blue and yellow spheres represent cobalt, molybdenum and sulfur atoms respectively.

2. Materials and methods

Total energy calculations were performed using the DFT code GPAW employing grid mode with a spacing of 0.18 Å[32, 33]. To treat exchange and correlation and to get an ensemble of 2000 energies used for uncertainty estimation the BEEF-vdW functional was used[29, 30]. The systems representing various molecules adsorbed on the sites of CoMoS were modeled by taking the surface structures from our previous study[31], where the active and inert sites of CoMoS releavant for HDS conditions were identified, and relaxing various molecules on them. In previous work[31] the active S-edge is a 4x4 stripe terminated by sulfur monomers periodic in the x direction separated by 13 Å of vacuum in the y and 15 Å in the z direction. The M-edge is modeled similarly, with the difference that it is terminated by sulfur monomers having single sulfur vacancies. The corner is modeled as a stepped stripe continuous in the x direction and, similarly to the edges, separated in the y and z direction and it exposes 3 Co atoms at the S-edge side and 2 Mo atoms at the M-edge side. The basal plane is modeled as a 4x4 sheet periodic in the x and y directions separated by 15 Å of vacuum in the z direction and is considered inert. The surface models are shown in figure 2. The Brillouin zone of the edges and corner models were sampled with 2, 1,

1 k-points in the x, y and z directions respectively, while the basal plane was sampled with 2, 2, 1 k-points. The same sampling was kept for the adsorption systems in the present work. All the molecules were modeled as single molecules centered in a box with sufficient empty space added in the x, y and z directions respectively. All the structures were optimized until the maximum force was lower than 0.05 eV/Å.

The adsorption energy of the considered molecular species was calculated as follows:

$$\Delta E_{ads} = E_{surf+mol} - E_{mol} - E_{surf} \quad (2)$$

where $E_{surf+mol}$ is the electronic energy of the molecule adsorbed on a specific site, E_{mol} is the electronic energy of the molecule and E_{surf} is the electronic energy of the site without a molecule adsorbed on it.

Thiolate formation energies were calculated on each site as follows for methylthiolate:

$$\Delta E_{thiolate} = E_{surf+thiolate} + \frac{1}{2}E_{H_2} - E_{mol} - E_{surf} \quad (3)$$

while for the rest of the thiolates the calculations were performed as:

$$\Delta E_{thiolate} = E_{surf+thiolate} - E_{mol} - \frac{1}{2}E_{H_2} - E_{surf} \quad (4)$$

where $E_{surf+thiolate}$ is the electronic energy of the thiolate adsorbed on a specific site, E_{H_2} is the electronic energy of a hydrogen molecule, E_{mol} is the electronic energy of the intact molecule and E_{surf} is the electronic energy of the site without the thiolate adsorbed on it. The formation of a thiolate from methylthiol is associated to breaking the sulfur-hydrogen (S-H) bond by the removal of a hydrogen atom from the initial molecule. For the rest of the molecules, thiolate formation is associated to breaking the C-S bond by the addition of a hydrogen atom to the molecule. This is the reason behind the difference between equations 3 and 4.

3. Results and discussion

3.1. Brim and edge configurations

Figure 3 shows a model of CoMoS with molecules adsorbed in different configurations. We distinguish between brim and edge adsorption configurations similar to Rangarajan and Mavrikakis in their recent computational adsorption study for sulfur and nitrogen containing molecules on the S-edge of CoMoS[28]. Visualization of all the computed adsorption configurations can be found in the supplementary material. It can be seen that brim adsorption occurs when a molecule adsorbs above an edge. Similar adsorption configurations can also be achieved with a molecule adsorbing above a corner site or on top of the basal plane. Such brim interaction was observed for 4,6-dimethyldibenzothiophene (4,6-DMDBT) in a recent scanning tunneling microscopy (STM) and DFT study by Grønborg et al and is called delocalized π-mode[27]. The name π-mode for brim adsorption reflects that the π system of the molecule interacts with the particle and the term delocalized addresses the observation that the molecule appears as a bright protrusion on the entire length of the S-edge, interpreted as the molecule being free to diffuse along the edge. The same study identified brim adsorption on the corner and named it localized π-mode since the studied molecule, namely 4,6-DMDBT, appeared as being restricted to the corner position. As was addressed in the studies by Grønborg et al and Rangarajan and Mavrikakis, the nature of brim adsorption or π-configurations is of a physisorbed nature[27, 28]. Calculating the adsorption energies of such configurations without including vdW interactions yields significantly weaker binding, often close to 0 eV.

Figure 4 shows the adsorption energies of all the considered molecules at the S-edge of CoMoS in brim and edge configurations. It can be seen that all the molecules prefer adsorbing at the S-edge in brim configuration since such a configuration maximizes the vdW interactions between the molecule and surface. From the error bars shown, it can be seen that the adsorption energies relative to gas phase molecules are not very well defined. Furthermore, it can be seen that the differences in adsorption energies (shown in green) are better defined, having smaller uncertainties. Therefore, instead of focusing on individual adsorption energies we focus on differences between adsorption energies of various molecules as those are better defined.

From figure 3 one can also see two different instances of edge adsorption configurations. Edge configurations occur through chemisorption at sulfur vacancies that form at the M-edge or corner. For edge adsorption we distinguish perpendicular adsorption relative to the MoS_2 plane (shown for the M-edge in figure 3) and planar adsorption relative to the MoS_2 plane (shown for the corner in figure 3). A similar perpendicular edge configuration was presented by Rangarajan and Mavrikakis for the S-edge[28]. In the present study, vacancies are only considered for the M-edge and corner as it was shown in our previous study[31] that a vacancy at HDS conditions is achievable at the M-edge and corner, while vacancy formation at the S-edge is energetically unfavorable.

Figure 5 shows the adsorption energies of all the considered molecules at the M-edge vacancy, in brim and edge configurations. With the exception of 4,6-DMDBT, for which the uncertainty prevents us to predict whether it prefers the chemisorbed edge or physisorbed brim mode, all the molecules prefer the chemisorbed edge mode. In order for the molecules to chemisorb at the edge vacancy they need to assume a configuration perpendicular to the basal plane of MoS_2, with the exception of methylthiol for which we do not distinguish perpendicular and planar configurations due to its geometry. It is possible that such a perpendicular configuration is not achievable for larger molecules (DBT and 4,6-DMDBT series) in real systems since the benzene rings could overlap with the support material or other MoS_2 slabs for multilayer structures.

Figure 6 shows the adsorption energies of all the considered molecules at the corner vacancy, in brim and edge configurations. Compared to the M-edge, the difference in adsorption energies between the perpendicular and planar edge configurations at the corner is much smaller (order of 1 eV for M-edge and 0.1 eV for corner). In case that perpendicular modes for

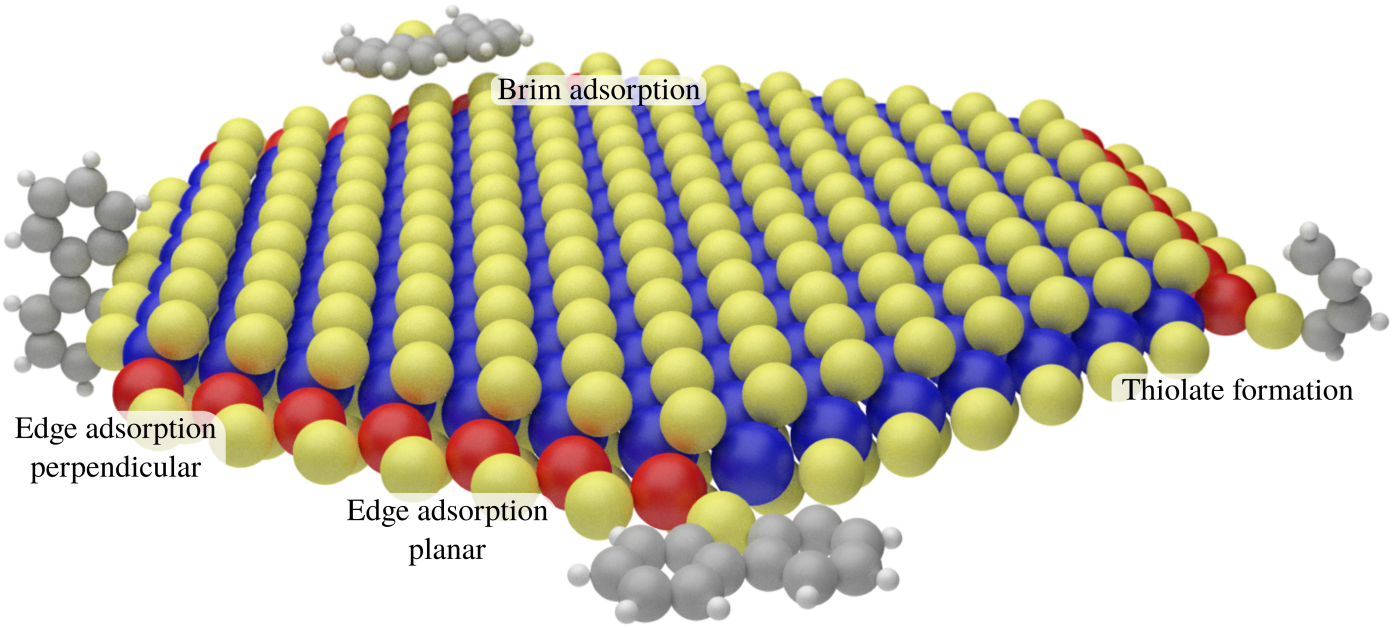

Figure 3: Model of an ideal CoMoS particle showing the differences between brim and edge adsorption, perpendicular and planar edge adsorption as well as showing thiolate formation. The red, blue, yellow, gray and white spheres represent cobalt, molybdenum, sulfur, carbon and hydrogen atoms respectively.

larger molecules are not available due to the support material, it is still possible for the molecules to chemisorb at the corner. Similar to the M-edge, it is more favorable for the molecules to chemisorb at the corner edge then to physisorb on the brim with the exception of 4,6-DMDBT for which the edge and brim configurations seem equally likely as the adsorption energies are similar (difference within 0.1 eV). A corner adsorption mode similar to those presented here was observed by Grønborg et al for 4,6-DMDBT, but it was associated to a double corner vacancy, where as herein we focus on a single corner vacancy which is more stable than the double corner vacancies. The mode was named σ-mode in order to reflect strong chemisorption between the corner site and the sulfur atom of 4,6-DMDBT. Additionally, the study from Grønborg et al also captures a dynamic switching between corner edge and corner brim configurations, i.e. switching between σ-mode and π-mode for 4,6-DMDBT[27]. This agrees well with the present result which shows that brim and edge configurations have comparable energies for 4,6-DMDBT.

3.2. Preferred adsorption site and hydrogenation

The strong chemisorption between the sulfur atom of a molecule and the M-edge or corner vacancy facilitates the process of breaking C-S bonds[24]. Therefore, we assume that a strong chemisorption between the sulfur atom in the molecule and the active site is needed for molecules to get desulfurized directly (DDS). This in return means that molecules preferring adsorption in edge configurations at M-edge or corner vacancies will tend to follow the DDS path. At the same time, molecules that prefer adsorption in brim configurations at the S-edge, where hydrogen atoms are available for hydrogenation, and molecules that show an increase in adsorption energy when being hydrogenated should prefer the HYD pathway as it leads to stronger interactions with the active sites.

Figure 7 shows the adsorption energies of all the considered molecules in the most favorable configuration on the S-edge (brim), M-edge (perpendicular), corner (perpendicular) and basal plane. Visualization of the molecules adsorbed on each site are found in the supplementary material. It can be seen that for the smaller molecules (methylthiol and thiophene series) the preferred adsorption sites are the M-edge vacancy and corner vacancy. This indicates that methylthiol and thiophene get desulfurized on defect sites with vacancies where the metal atom is undercoordinated, thus, allowing the molecule to chemisorb. In the hydrogenation series for thiophene it can be seen that the adsorption energy increases (more negative) when the aromatic molecule is hydrogenated. The increase in adsorption energy (towards negative values) is more pronounced for the chemisorption modes on sites with vacancies (M-edge, corner) than on vacancy free sites (S-edge, basal plane). The preference towards undercoordinated sites of thiophene indicates that it gets desulfurized through the DDS pathway. At the same time, the fact that the adsorption energy of thiophene gets greater with further hydrogenation indicates that it should prefer the HYD pathway. Therefore, it is not possible to conclude which pathway thiophene follows based only on adsorption energies. An earlier study from Moses et al. which includes transition state data for thiophene indicates that thiophene follows the DDS route[21]. For DBT it is not clear what the preferred adsorption site is since the adsorption energies on different sites are similar (difference within 0.2 eV). It can be seen in the hydrogenation series of DBT that further hydrogenation makes adsorption stronger at the M-edge and slightly stronger on the corner. Adsorption gets slightly weaker at the basal plane and stays constant on the S-edge.

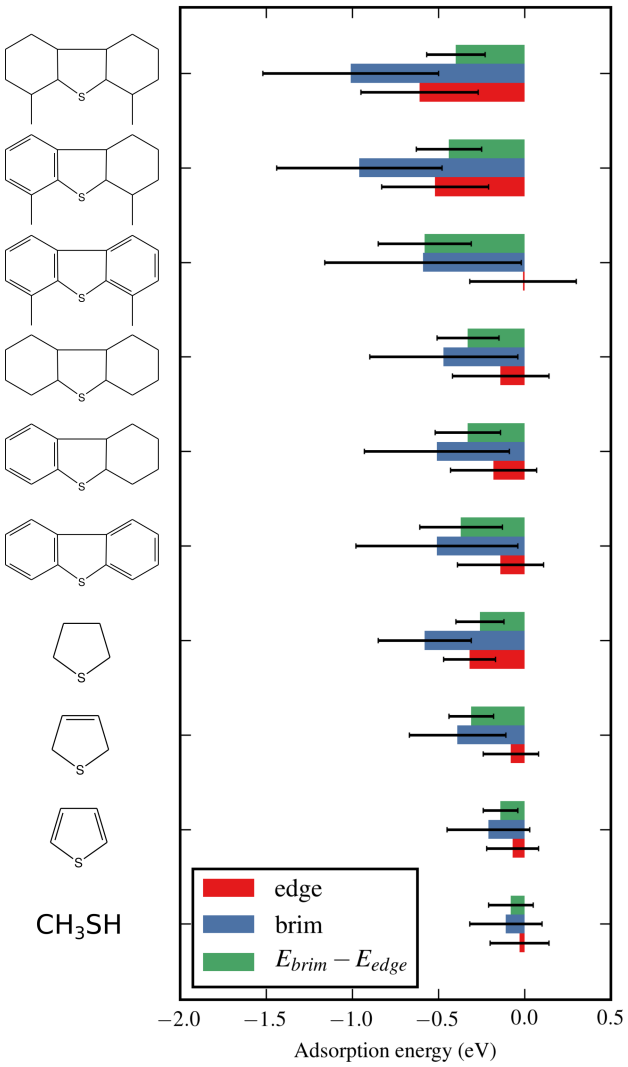

Figure 4: Adsorption energies of sulfur containing molecules on the S-edge of CoMoS in brim and edge configurations as well as the energy difference between brim and edge configurations. Error bars show one standard deviation of the ensemble values.

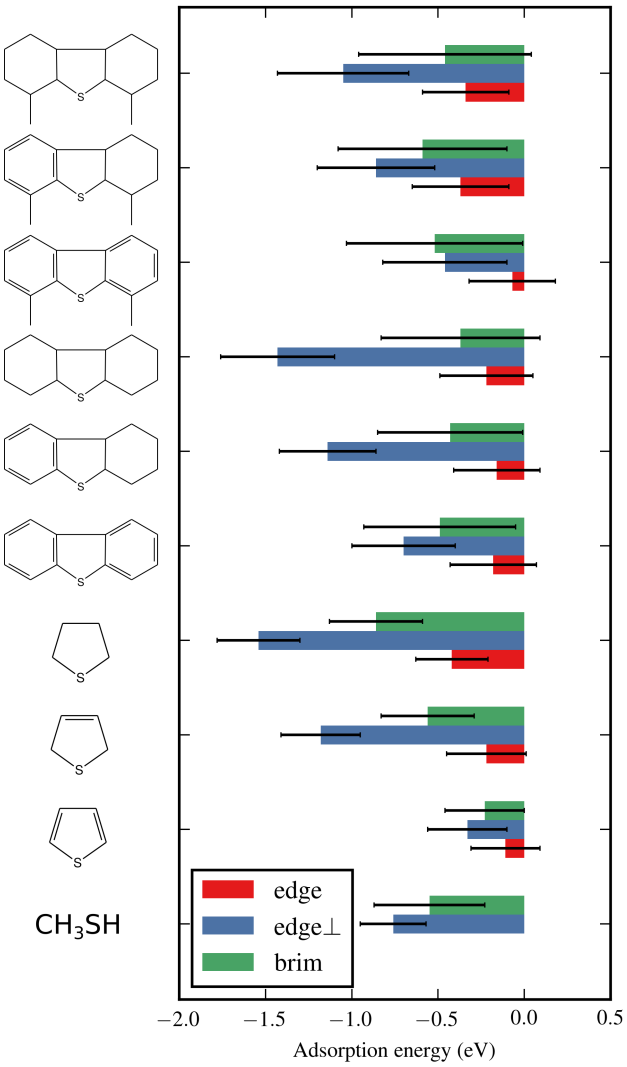

Figure 5: Adsorption energies of sulfur containing molecules on the M-edge of CoMoS in brim and edge configurations. Error bars show one standard deviation of the ensemble values.

Once again it is not possible to claim which route DBT follows based only on the adsorption energies, although the observation that adsorption energy at the S-edge does not increase with hydrogenation points to DDS. Looking at 4,6-DMDBT it can be seen that it actually prefers the basal plane and S-edge over the defect sites. Furthermore, it can be seen that hydrogenation of 4,6-DMDBT leads to stronger adsorption on the S-edge, weaker adsorption on the basal plane and some fluctuating changes for defect sites. Hydrogenating one of the benzene rings of 4,6-DMDBT leads to a clear preference towards the S-edge, indicating that 4,6-DMDBT gets desulfurized at the S-edge following the HYD route. In the study of Rangarajan and Mavrikakis it was shown that nitrogen containing compounds rather adsorb in brim than edge configurations, which is contrary to sulfur containing compounds that generally prefer edge configurations[28]. In real HDS systems with both sulfur and nitrogen containing molecules, 4,6-DMDBT has to compete with nitrogen containing compounds to adsorb on the S-edge brim, therefore, decreasing the rate at which 4,6-DMDBT gets desulfurized. A combination of the steric hinderance towards chemisorption at corners caused by methyl groups and brim poisoning by nitrogen compounds could explain why it is generally very difficult to desulfurize 4,6-DMDBT.

3.3. Thiolate formation

From figure 8 it can be seen, especially for larger molecules (DBT, 4,6-DMDBT), that there is a strong interaction with the basal plane. While it was determined by previous studies that the basal plane is inert towards HDS, the results for the basal plane in figure 7 can be misleading by indicating that the basal plane participates in HDS because it potentially acts as the preferred adsorption site. We suggest that in order to get a better description of which site participates in the sulfur chemistry of

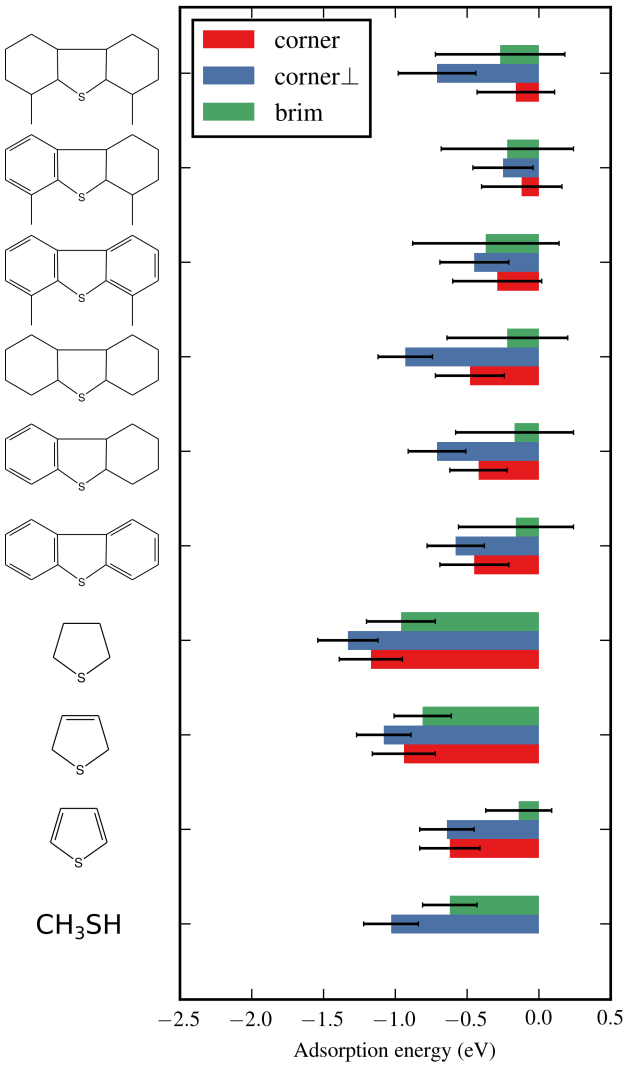

Figure 6: Adsorption energies of sulfur containing molecules on the corner of CoMoS in brim and edge configurations. Error bars show one standard deviation of the ensemble values.

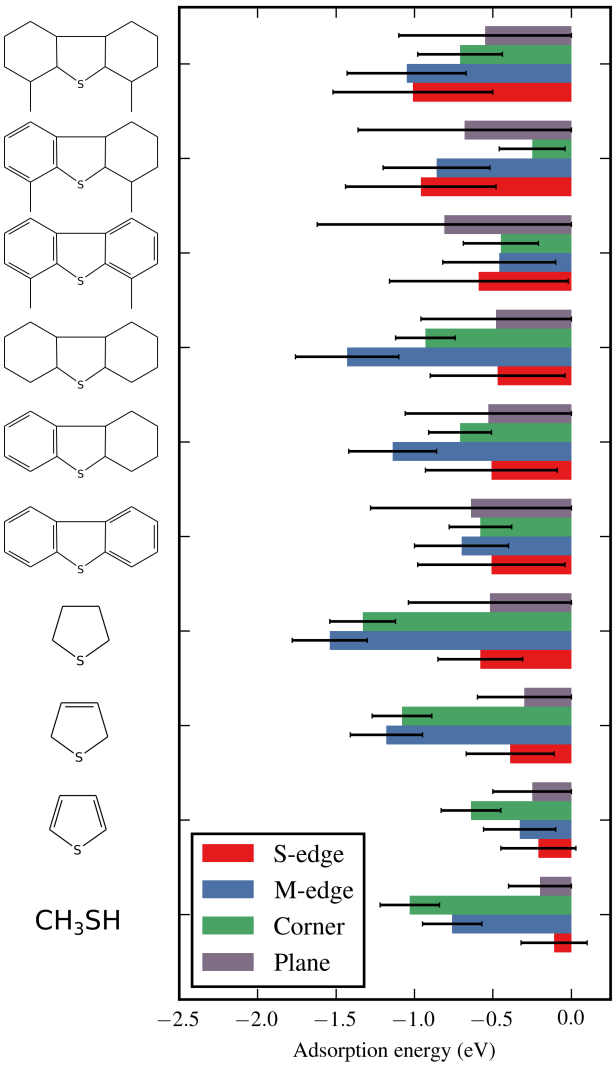

Figure 7: Adsorption energies of sulfur containing molecules in the most favorable adsorption configurations of the S-edge (brim), M-edge (perpendicular), corner (perpendicular) and basal plane. Error bars show one standard deviation of the ensemble values.

HDS, i.e. which sites participate in cleaving C-S bonds of the initial molecules, it is necessary to consider thiolates and their formation energies. A thiolate is formed after the C-S bond breaks as shown to the right of figure 3 for thiophene. This is illustrated by the following reaction:

$$C_4H_4S + \frac{1}{2}H_2 + * \leftrightarrow C_4H_5S^* \tag{5}$$

Figure 8 shows thiolate formation energies for each molecular species in the energetically most favorable configurations. For the S-edge, M-edge and corner trends similar to those of the intact molecules can be seen. For the basal plane it can be seen that the formation of thiolates is unfavorable. This indicates that the basal plane is inert towards hydrodesulfurization since there is no driving force towards thiolate formation, i.e. no C-S bonds can be cleaved there. It should be noted that the thiolate formation energy for methylthiol does not describe the energetics of C-S scission as its C-S bond stays intact. It describes the driving force for cleaving the S-H bond, therefore, it can be seen that there is no driving force for cleaving S-H bonds on the basal plane either.

4. Conclusion

It was shown that sulfur containing species prefer to interact with the brim of the S-edge. For the M-edge and corner it was shown that strong chemisorption can be achieved by interaction with vacancies in edge configuration. On the M-edge, molecules consisting of aromatic ring and cyclic structures need to assume a perpendicular orientation relative to the basal plane in order to achieve negative chemisorption energies. Perpendicular M-edge adsorption was speculated to be limited

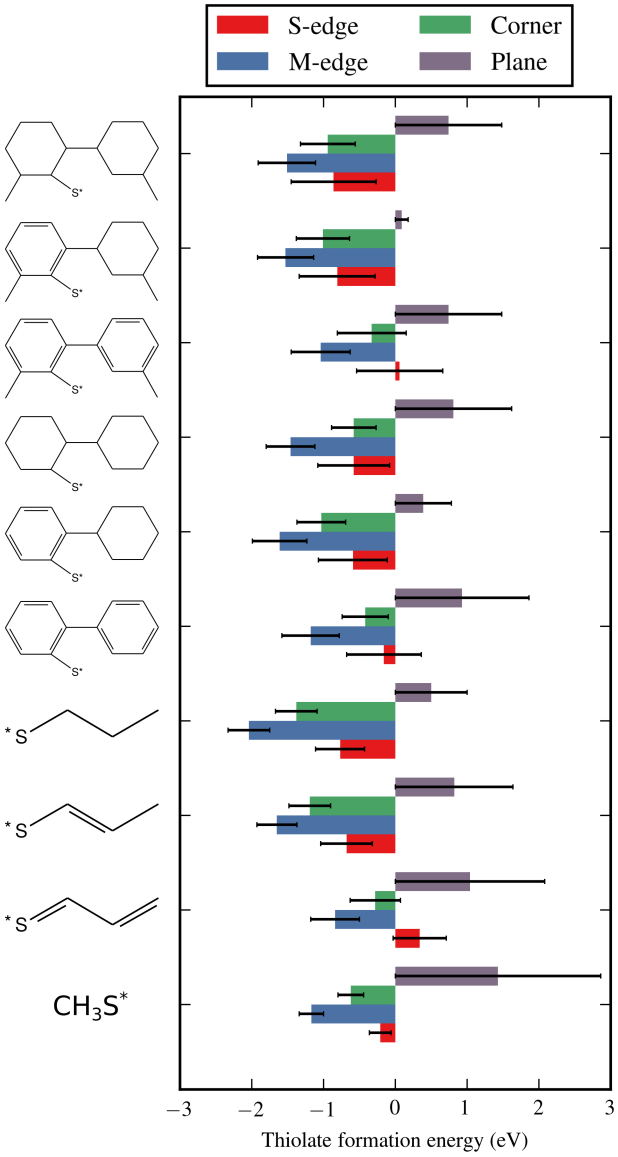

Figure 8: Thiolate formation energies of sulfur containing molecules in the most favorable adsorption configurations of the S-edge (brim), M-edge (perpendicular), corner (perpendicular) and basal plane. Error bars show one standard deviation of the ensemble values.

for most molecules expect the smallest ones (methylthiol, thiophene), due to overlap of benzene rings of large molecules (DBT, 4,6-DMDBT) with the support material or other MoS_2 clusters in multilayer systems. For the corner it was shown that, although interacting slightly weaker, most molecules can also chemisorb by assuming a planar configuration, thus, limiting steric hindrance due to multilayer MoS_2 stacks or the support. Hydrogenation of thiophene and DBT lead to stronger interaction with defects and vacancies while hydrogenation of 4,6-DMDBT yielded strong interactions with the S-edge brim, possibly explaining why it follows the hydrogenation route instead of direct desulfurization. In order to get a better description of processes involving cleaving of C-S and S-H bonds, it was shown that thiolate formation energies should be considered as well. By using thiolate formation energies as the descriptor of the role of each site, similar trends to those of using intact molecules were achieved, with the additional prediction of the inert nature of the basal plane. In conclusion, based on the present analysis of adsorption energies, we conclude that smaller molecules such as methylthiol and thiophene and possibly larger molecules without substituents such as DBT get desulfurized at the corner and M-edge by interacting with vacancies, while larger molecules with substituents that sterically hinder chemisorption get desulfurized by getting hydrogenated at the S-edge.

Acknowledgements

Funding: This work was supported by the Danish Council for Independent Research (grant HYDECAT, DFF-1335-00016) and the Carlsberg Foundation (grant CF15-0165).

References

[1] C. Song, An overview of new approaches to deep desulfurization for ultra-clean gasoline, diesel fuel and jet fuel, Catalysis today 86 (2003) 211–263.

[2] I. Babich, J. Moulijn, Science and technology of novel processes for deep desulfurization of oil refinery streams: a review, Fuel 82 (2003) 607–631.

[3] G. Schuit, B. Gates, Chemistry and engineering of catalytic hydrodesulfurization, AIChE Journal 19 (1973) 417–438.

[4] G. E. Likens, C. T. Driscoll, D. C. Buso, Long-term effects of acid rain: response and recovery of a forest ecosystem, Science 272 (1996) 244.

[5] M. Andreae, D. Rosenfeld, Aerosol–cloud–precipitation interactions. Part 1. The nature and sources of cloud-active aerosols, Earth-Science Reviews 89 (2008) 13–41.

[6] M. Greenstone, Did the Clean Air Act cause the remarkable decline in sulfur dioxide concentrations?, Journal of environmental economics and management 47 (2004) 585–611.

[7] P. Raybaud, J. Hafner, G. Kresse, S. Kasztelan, H. Toulhoat, Structure, energetics, and electronic properties of the surface of a promoted MoS_2 catalyst: an ab initio local density functional study, Journal of Catalysis 190 (2000) 128–143.

[8] J. V. Lauritsen, J. Kibsgaard, G. H. Olesen, P. G. Moses, B. Hinnemann, S. Helveg, J. K. Nørskov, B. S. Clausen, H. Topsøe, E. Lægsgaard, et al., Location and coordination of promoter atoms in Co-and Ni-promoted MoS_2-based hydrotreating catalysts, Journal of Catalysis 249 (2007) 220–233.

[9] F. Besenbacher, M. Brorson, B. Clausen, S. Helveg, B. Hinnemann, J. Kibsgaard, J. V. Lauritsen, P. G. Moses, J. K. Nørskov, H. Topsøe, Recent STM, DFT and HAADF-STEM studies of sulfide-based hydrotreating catalysts: Insight into mechanistic, structural and particle size effects, Catalysis Today 130 (2008) 86–96.

[10] B. Hinnemann, P. G. Moses, J. K. Nørskov, Recent density functional studies of hydrodesulfurization catalysts: insight into structure and mechanism, Journal of Physics: Condensed Matter 20 (2008) 064236.

[11] M. Bollinger, J. Lauritsen, K. W. Jacobsen, J. K. Nørskov, S. Helveg, F. Besenbacher, One-dimensional metallic edge states in MoS_2, Physical Review Letters 87 (2001) 196803.

[12] J.-F. Paul, S. Cristol, E. Payen, Computational studies of (mixed) sulfide hydrotreating catalysts, Catalysis Today 130 (2008) 139 – 148.

[13] Y. Zhu, Q. M. Ramasse, M. Brorson, P. G. Moses, L. P. Hansen, C. F. Kisielowski, S. Helveg, Visualizing the stoichiometry of industrial-style co-mo-s catalysts with single-atom sensitivity, Angewandte Chemie International Edition 53 (2014) 10723–10727.

[14] L. P. Hansen, Q. M. Ramasse, C. Kisielowski, M. Brorson, E. Johnson, H. Topse, S. Helveg, Atomic-scale edge structures on industrial-style MoS_2 nanocatalysts, Angewandte Chemie International Edition 50 (2011) 10153–10156.

[15] C. Kisielowski, Q. Ramasse, L. Hansen, M. Brorson, A. Carlsson, A. Molenbroek, H. Topse, S. Helveg, Imaging MoS_2 nanocatalysts with single-atom sensitivity, Angewandte Chemie International Edition 49 (2010) 2708–2710.

[16] L. Byskov, J. Norskov, B. Clausen, H. Topsoe, Edge termination of MoS_2 and CoMoS catalyst particles, Catalysis Letters 64 (2000) 95–99.

[17] M. Bollinger, K. W. Jacobsen, J. K. Nørskov, Atomic and electronic structure of MoS_2 nanoparticles, Physical Review B 67 (2003) 085410.

[18] H. Schweiger, P. Raybaud, G. Kresse, H. Toulhoat, Shape and edge sites modifications of MoS_2 catalytic nanoparticles induced by working conditions: A theoretical study, Journal of Catalysis 207 (2002) 76 – 87.

[19] P.-Y. Prodhomme, P. Raybaud, H. Toulhoat, Free-energy profiles along reduction pathways of MoS_2 M-edge and S-edge by dihydrogen: a first-principles study, Journal of catalysis 280 (2011) 178–195.

[20] J. Lauritsen, M. Bollinger, E. Lgsgaard, K. Jacobsen, J. Nrskov, B. Clausen, H. Topse, F. Besenbacher, Atomic-scale insight into structure and morphology changes of MoS_2 nanoclusters in hydrotreating catalysts, Journal of Catalysis 221 (2004) 510 – 522.

[21] P. G. Moses, B. Hinnemann, H. Topsøe, J. K. Nørskov, The hydrogenation and direct desulfurization reaction pathway in thiophene hydrodesulfurization over MoS_2 catalysts at realistic conditions: a density functional study, Journal of Catalysis 248 (2007) 188–203.

[22] R. Prins, M. Egorova, A. Röthlisberger, Y. Zhao, N. Sivasankar, P. Kukula, Mechanisms of hydrodesulfurization and hydrodenitrogenation, Catalysis Today 111 (2006) 84–93.

[23] P. G. Moses, B. Hinnemann, H. Topsøe, J. K. Nørskov, The effect of Co-promotion on MoS_2 catalysts for hydrodesulfurization of thiophene: a density functional study, Journal of Catalysis 268 (2009) 201–208.

[24] P. G. Moses, L. C. Grabow, E. M. Fernandez, B. Hinnemann, H. Topsøe, K. G. Knudsen, J. K. Nørskov, Trends in hydrodesulfurization catalysis based on realistic surface models, Catalysis Letters 144 (2014) 1425–1432.

[25] S. Humbert, G. Izzet, P. Raybaud, Competitive adsorption of nitrogen and sulphur compounds on a multisite model of NiMoS catalyst: A theoretical study, Journal of Catalysis 333 (2016) 78 – 93.

[26] M. Šarić, P. G. Moses, J. Rossmeisl, Relation between hydrogen evolution and hydrodesulfurization catalysis, ChemCatChem 8 (2016) 3334–3337.

[27] S. S. Grønborg, M. Šarić, P. G. Moses, J. Rossmeisl, J. V. Lauritsen, Atomic scale analysis of sterical effects in the adsorption of 4, 6-dimethyldibenzothiophene on a CoMoS hydrotreating catalyst, Journal of Catalysis 344 (2016) 121–128.

[28] S. Rangarajan, M. Mavrikakis, DFT insights into the competitive adsorption of sulfur-and nitrogen-containing compounds and hydrocarbons on Co-promoted molybdenum sulfide catalysts, ACS Catalysis 6 (2016) 2904–2917.

[29] J. Wellendorff, K. T. Lundgaard, A. Møgelhøj, V. Petzold, D. D. Landis, J. K. Nørskov, T. Bligaard, K. W. Jacobsen, Density functionals for surface science: Exchange-correlation model development with Bayesian error estimation, Physical Review B 85 (2012) 235149.

[30] A. Tkatchenko, M. Scheffler, Accurate molecular van der Waals interactions from ground-state electron density and free-atom reference data, Physical review letters 102 (2009) 073005.

[31] M. Šarić, J. Rossmeisl, P. G. Moses, Modeling the active sites of Co-promoted MoS_2 particles by DFT, Physical Chemistry Chemical Physics (2016).

[32] J. J. Mortensen, L. B. Hansen, K. W. Jacobsen, Real-space grid implementation of the projector augmented wave method, Physical Review B 71 (2005) 035109.

[33] J. Enkovaara, C. Rostgaard, J. J. Mortensen, J. Chen, M. Dułak, L. Ferrighi, J. Gavnholt, C. Glinsvad, V. Haikola, H. Hansen, et al., Electronic structure calculations with GPAW: a real-space implementation of the projector augmented-wave method, Journal of Physics: Condensed Matter 22 (2010) 253202.

Modeling the adsorption of sulfur containing molecules and their hydrodesulfurization intermediates on the Co-promoted MoS_2 catalyst by DFT: Supplemental material

M. Šarić, J. Rossmeisl, P.G. Moses

The following figures show rendered images of all the adsorption modes calculated under this study as seen from above and the side. The red, blue, yellow, gray and white spheres represent cobalt, molybdenum, sulfur, carbon and hydrogen atoms respectively.

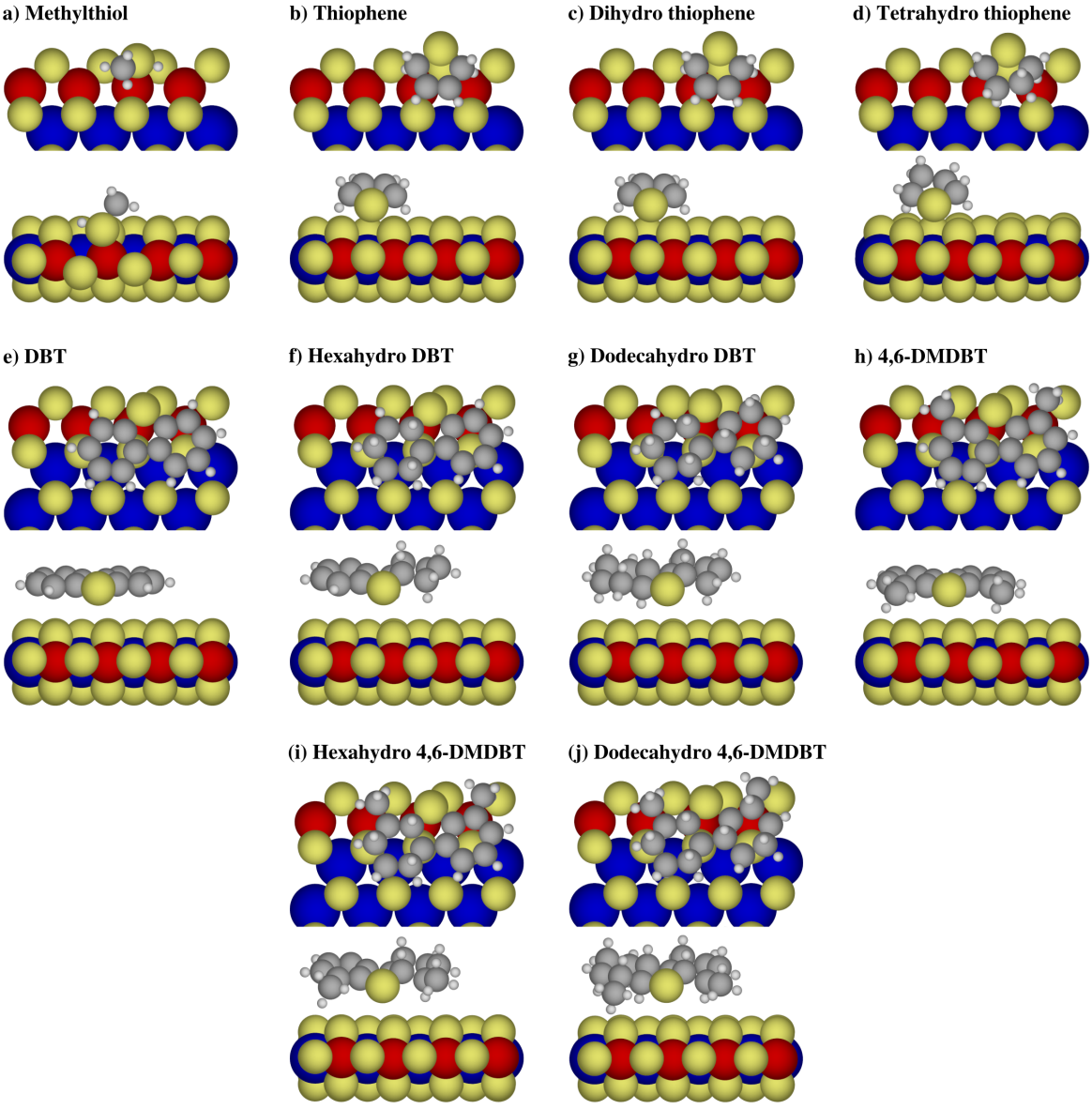

Figure 1: Adsorption configurations of the studied molecules at the S-edge in brim position.

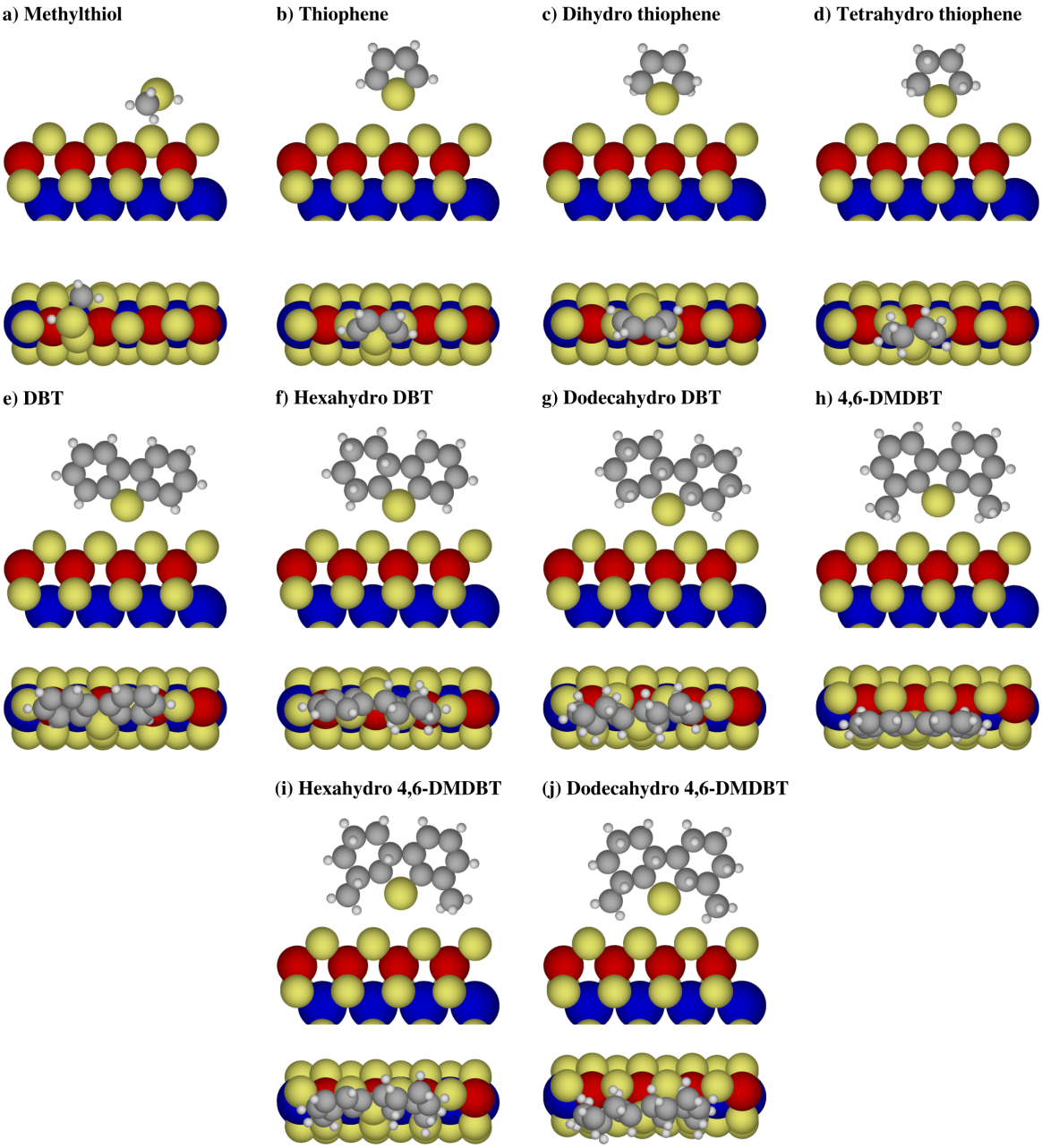

Figure 2: Adsorption configurations of the studied molecules at the S-edge in edge position.

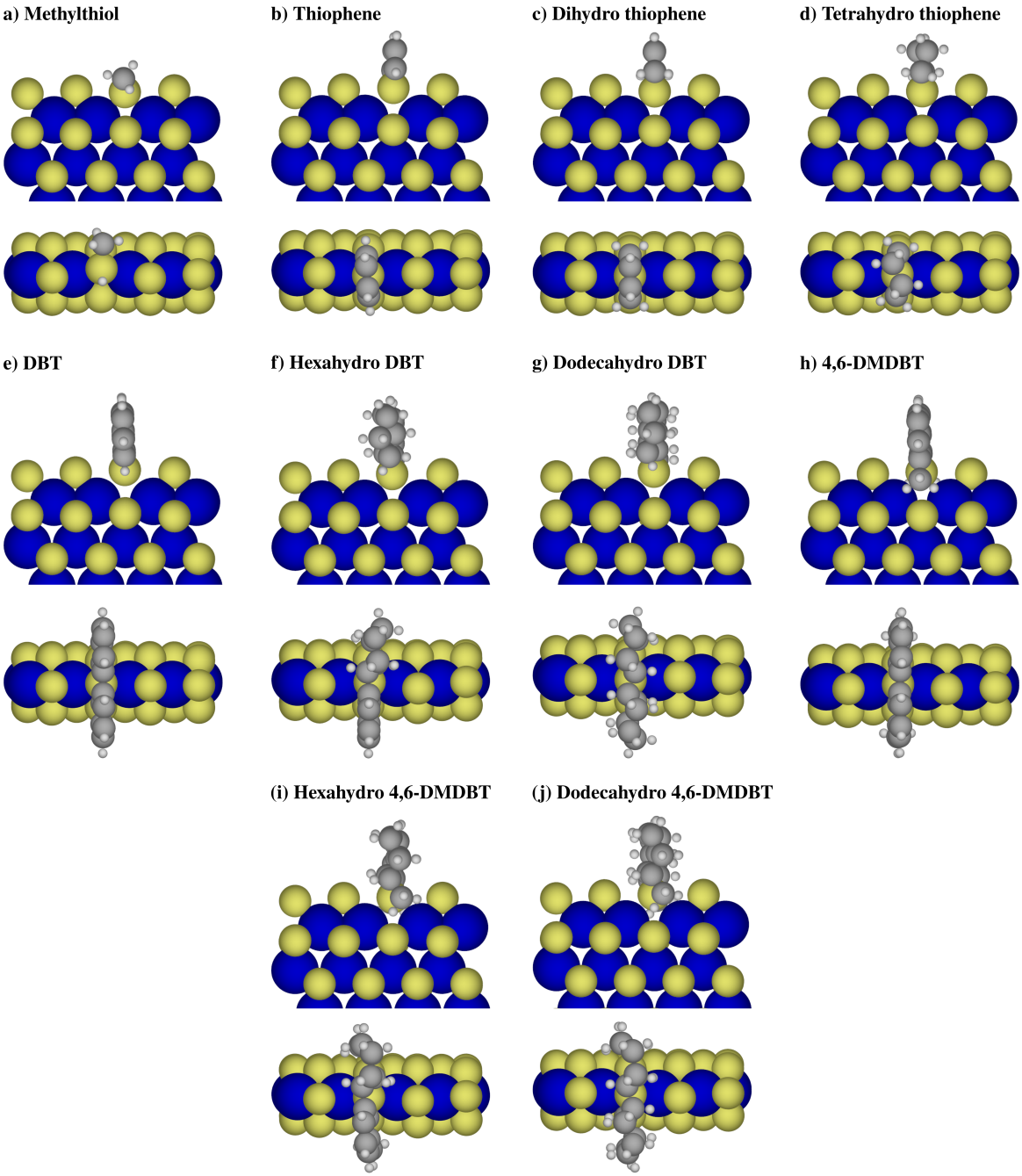

Figure 3: Adsorption configurations of the studied molecules at an M-edge vacancy in edge position, perpendicular to the MoS_2 plane.

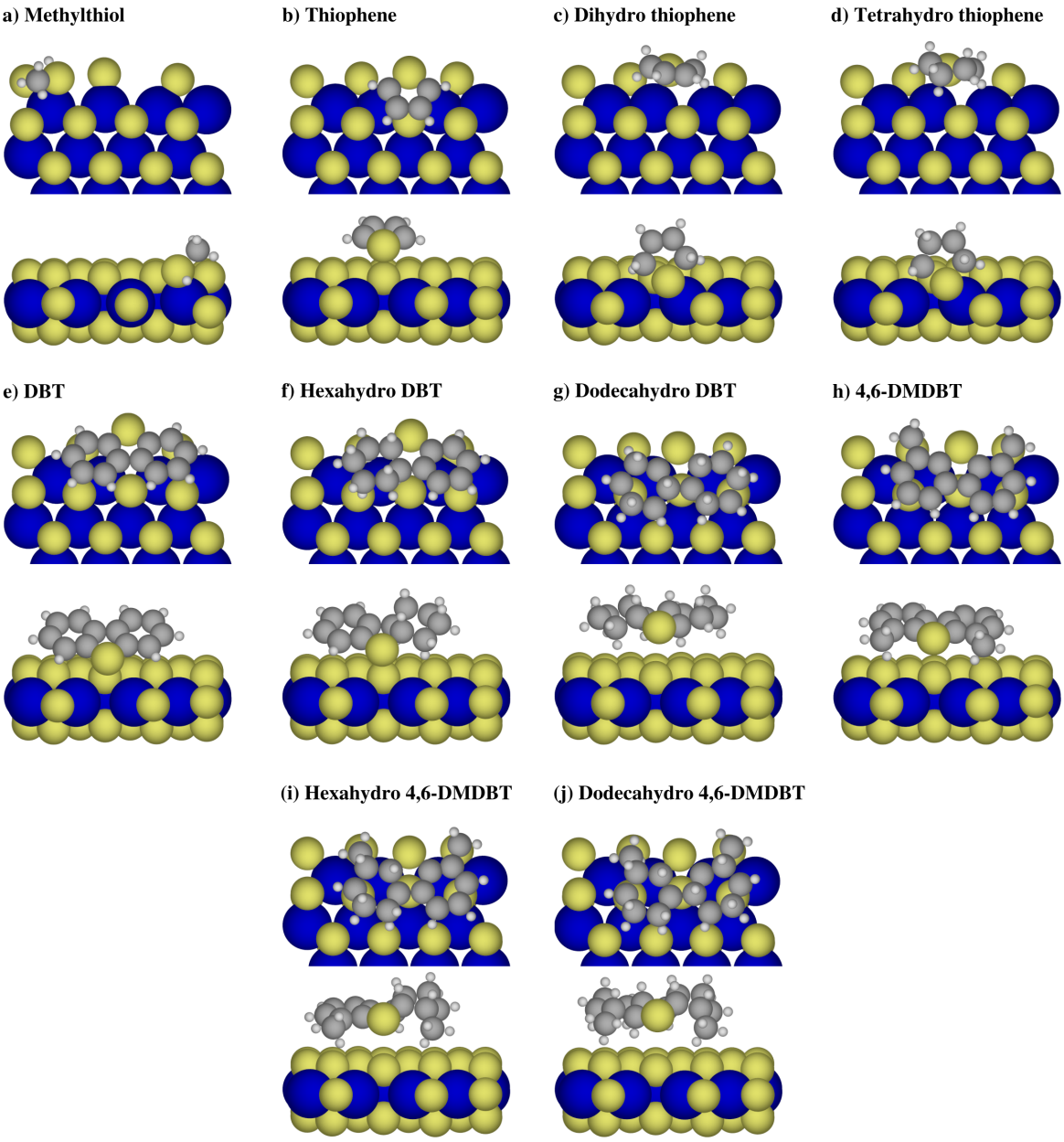

Figure 4: Adsorption configurations of the studied molecules at the M-edge in brim position.

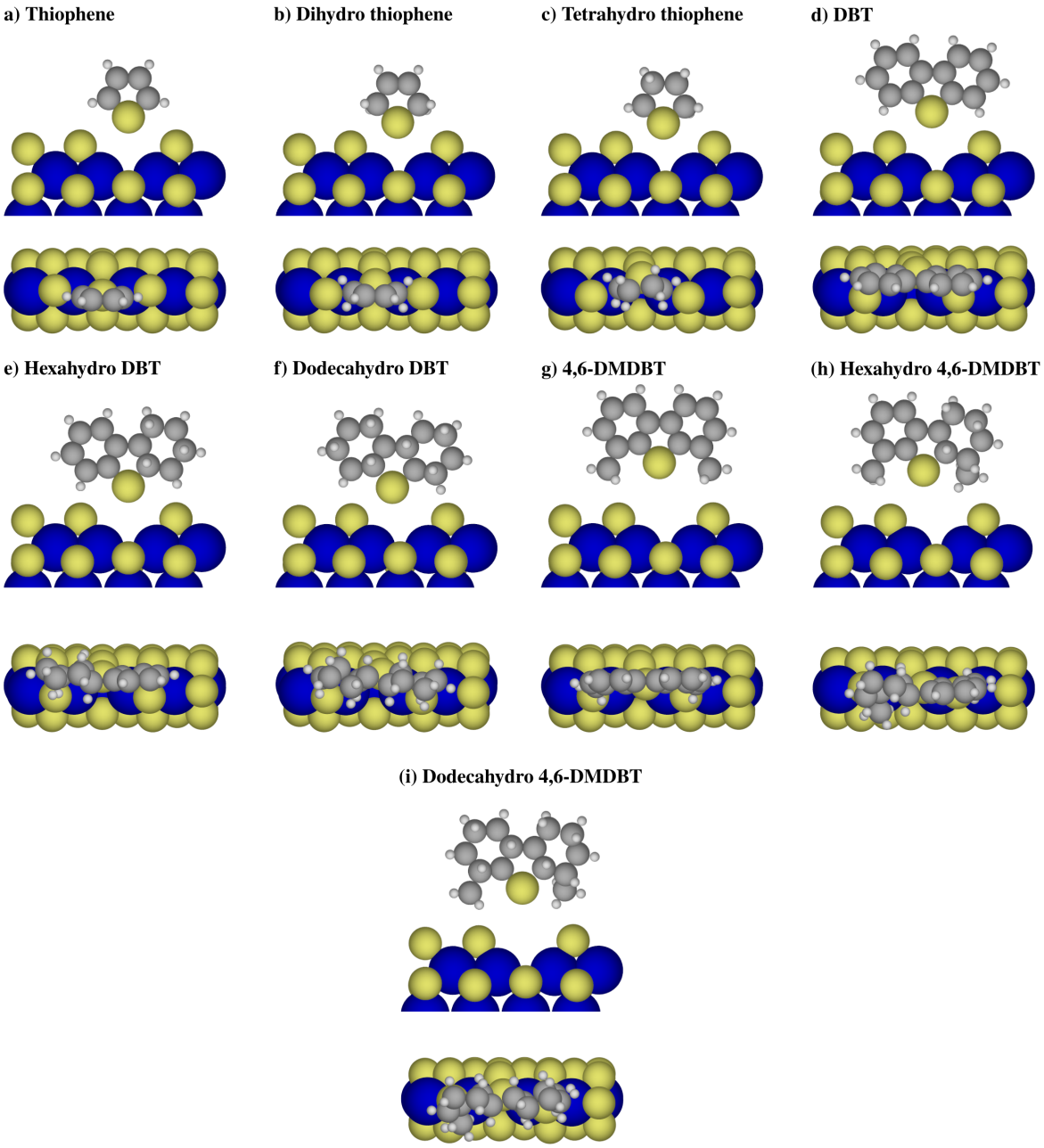

Figure 5: Adsorption configurations of the studied molecules at the M-edge in edge position, aligned with the MoS_2 plane.

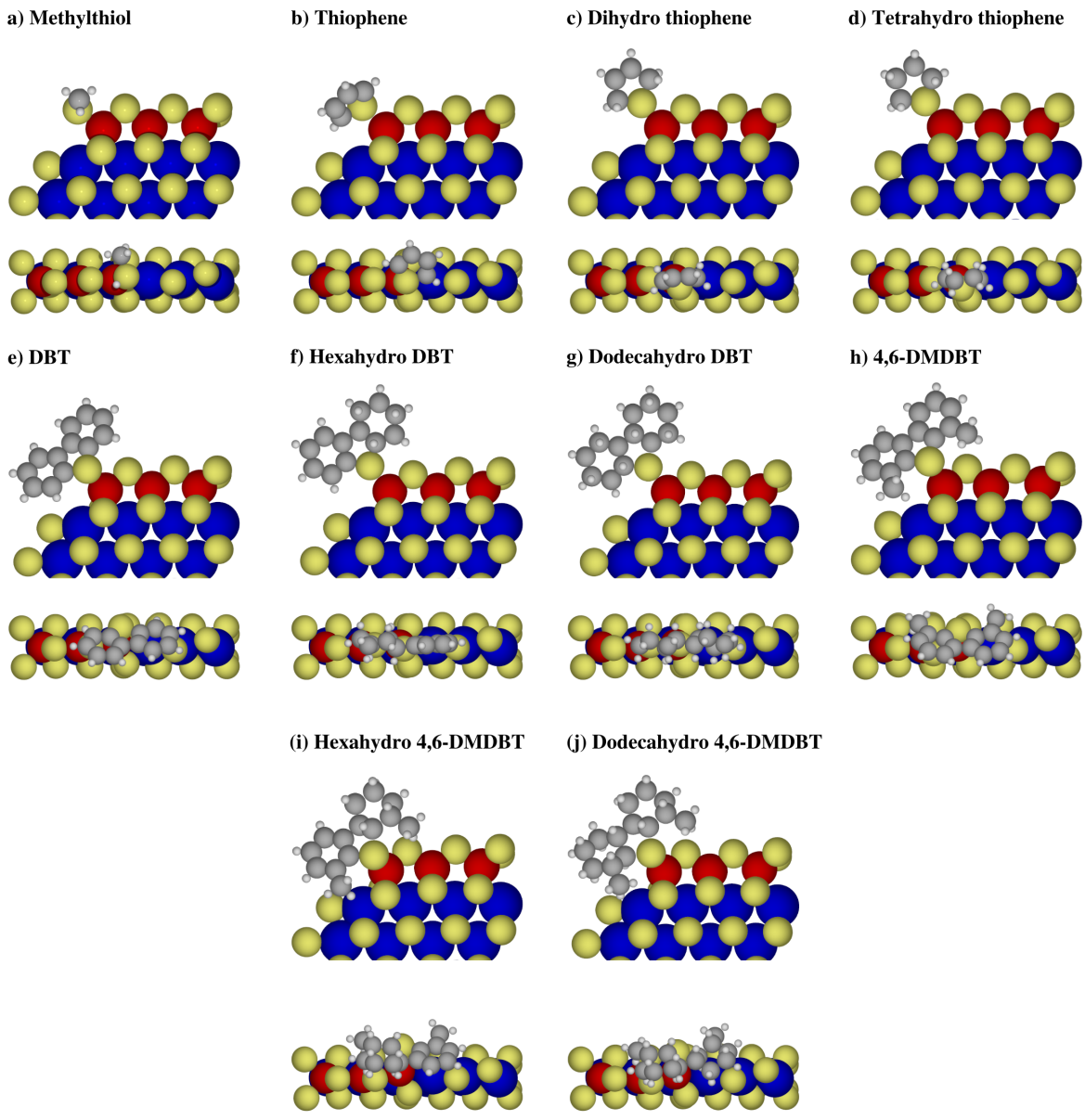

Figure 6: Adsorption configurations of the studied molecules at a corner vacancy, aligned with the MoS_2 plane.

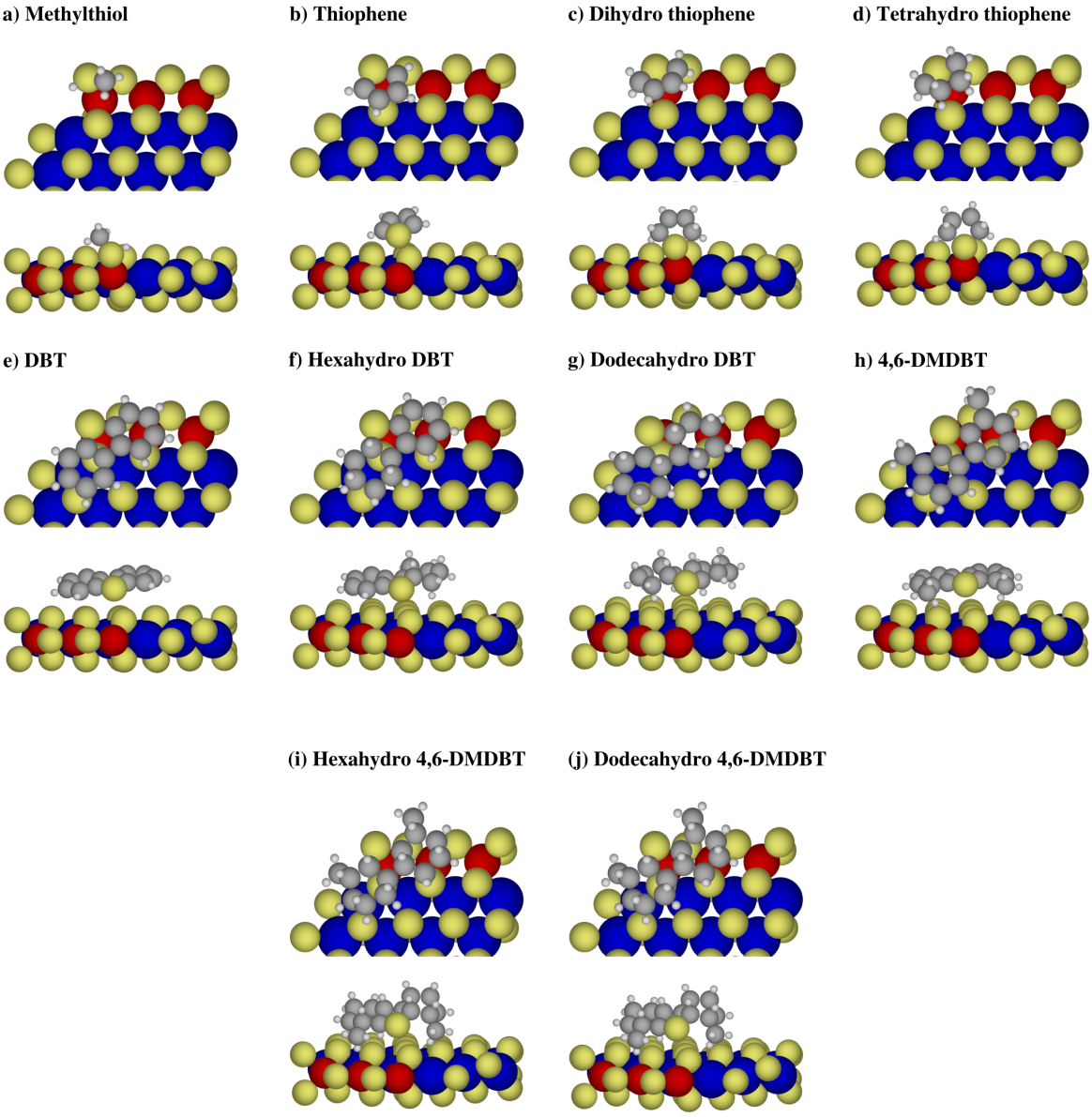

Figure 7: Adsorption configurations of the studied molecules at the corner in brim position.

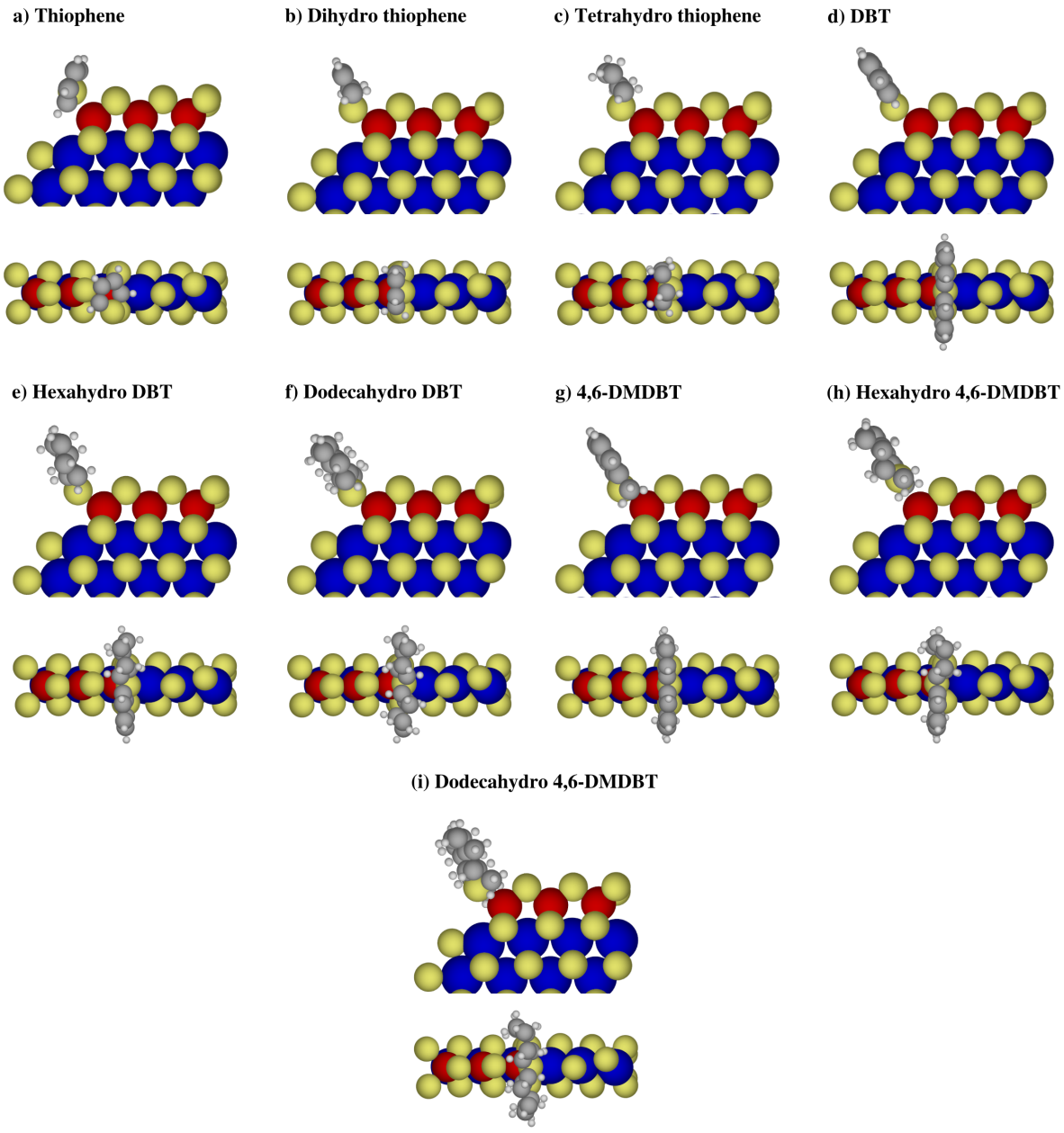

Figure 8: Adsorption configurations of the studied molecules at a corner vacancy, perpendicular to the MoS_2 plane.

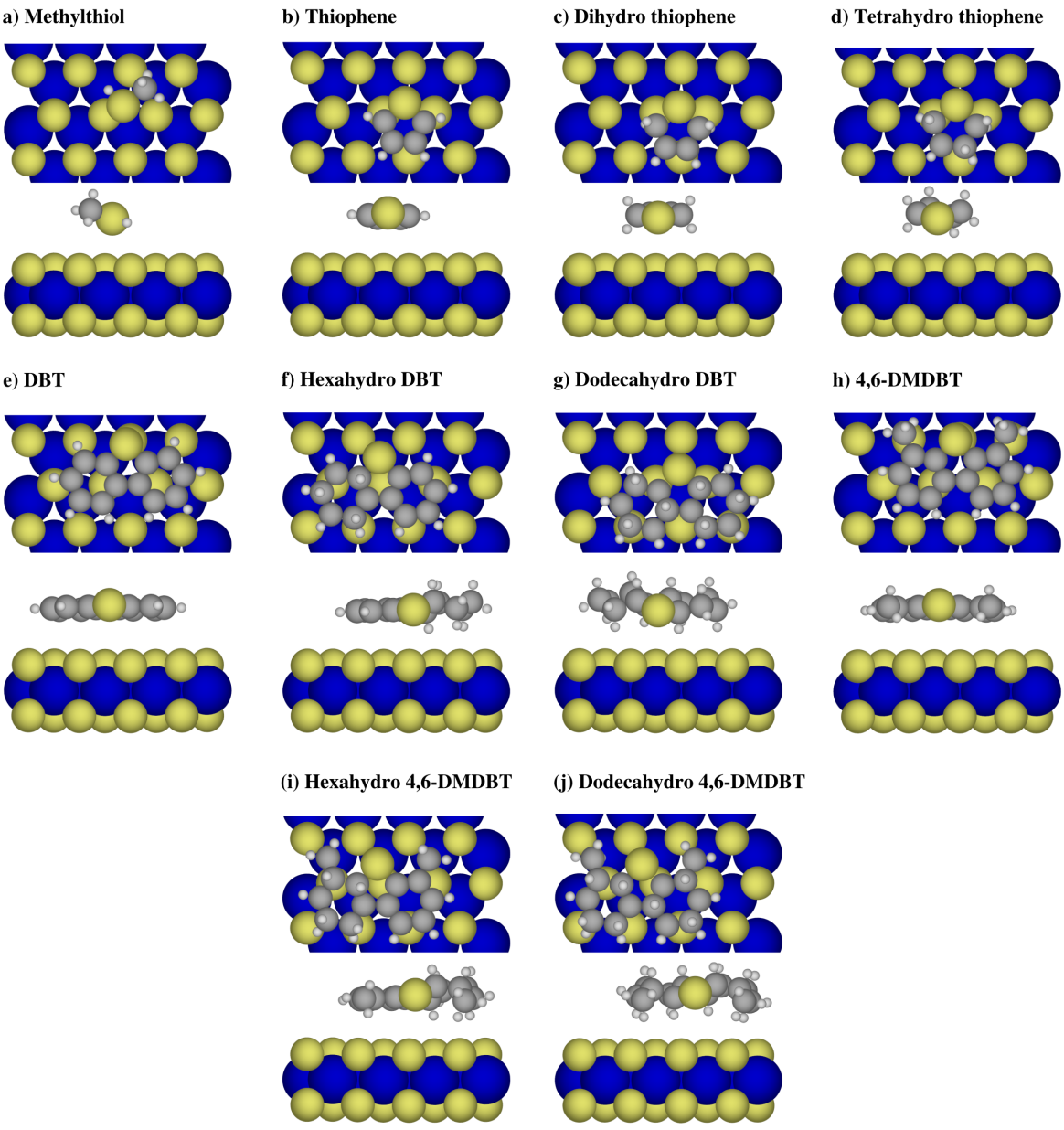

Figure 9: Adsorption configurations of the studied molecules on the basal plane.

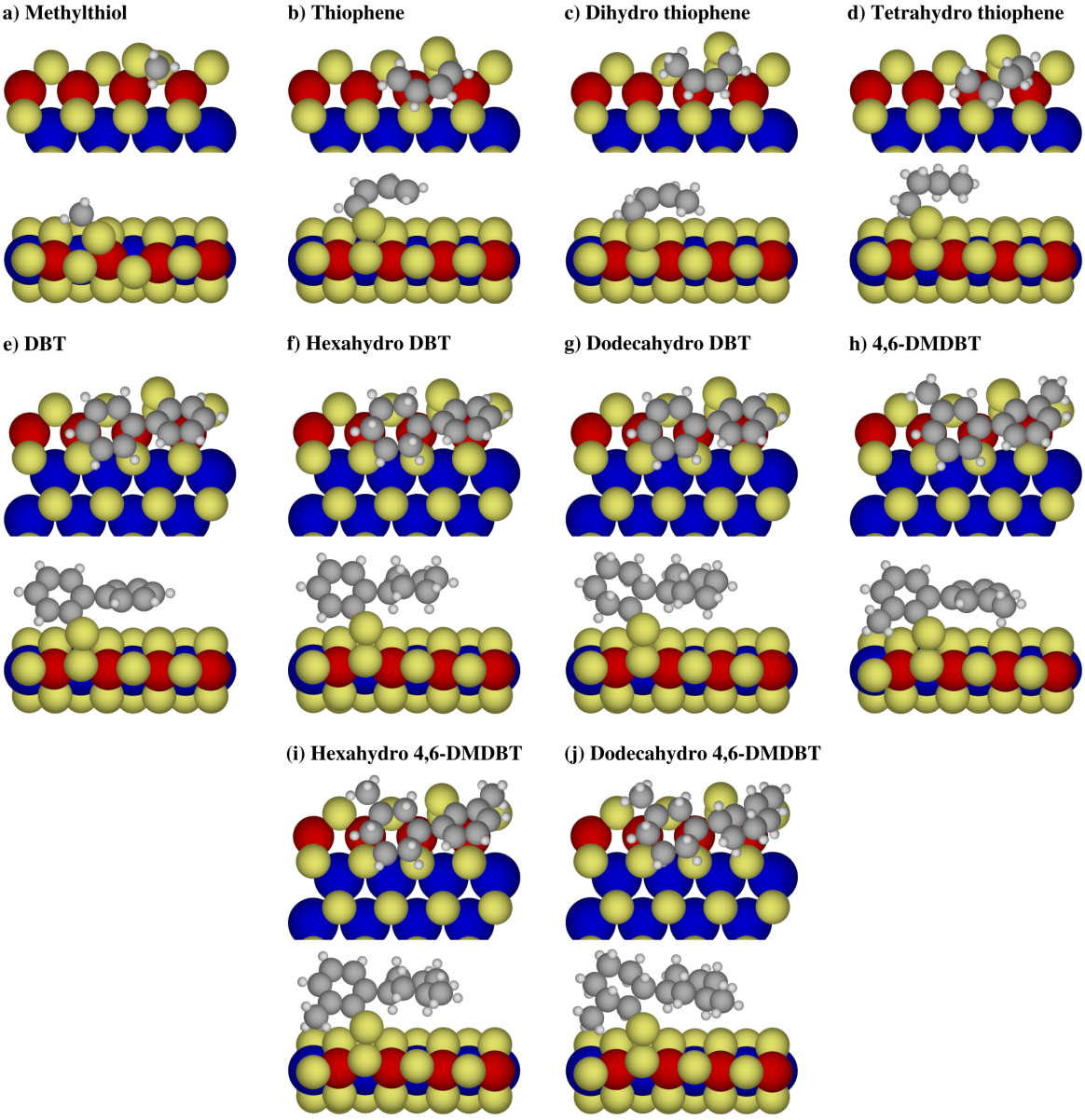

Figure 10: Adsorption configurations of the studied molecules in thiolate form at the S-edge in brim position.

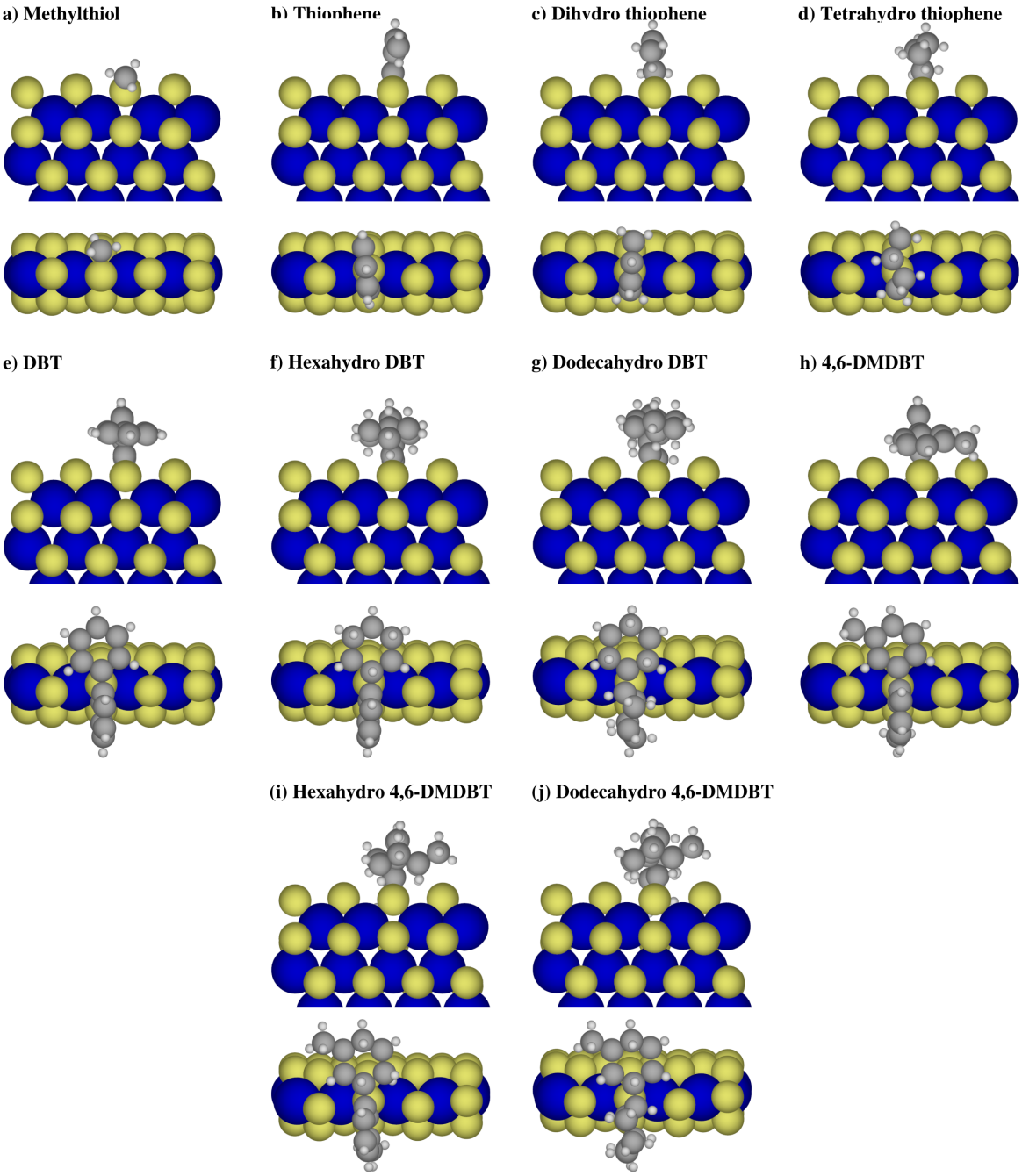

Figure 11: Adsorption configurations of the studied molecules in thiolate form at the M-edge in edge position perpendicular to the MoS_2 plane.

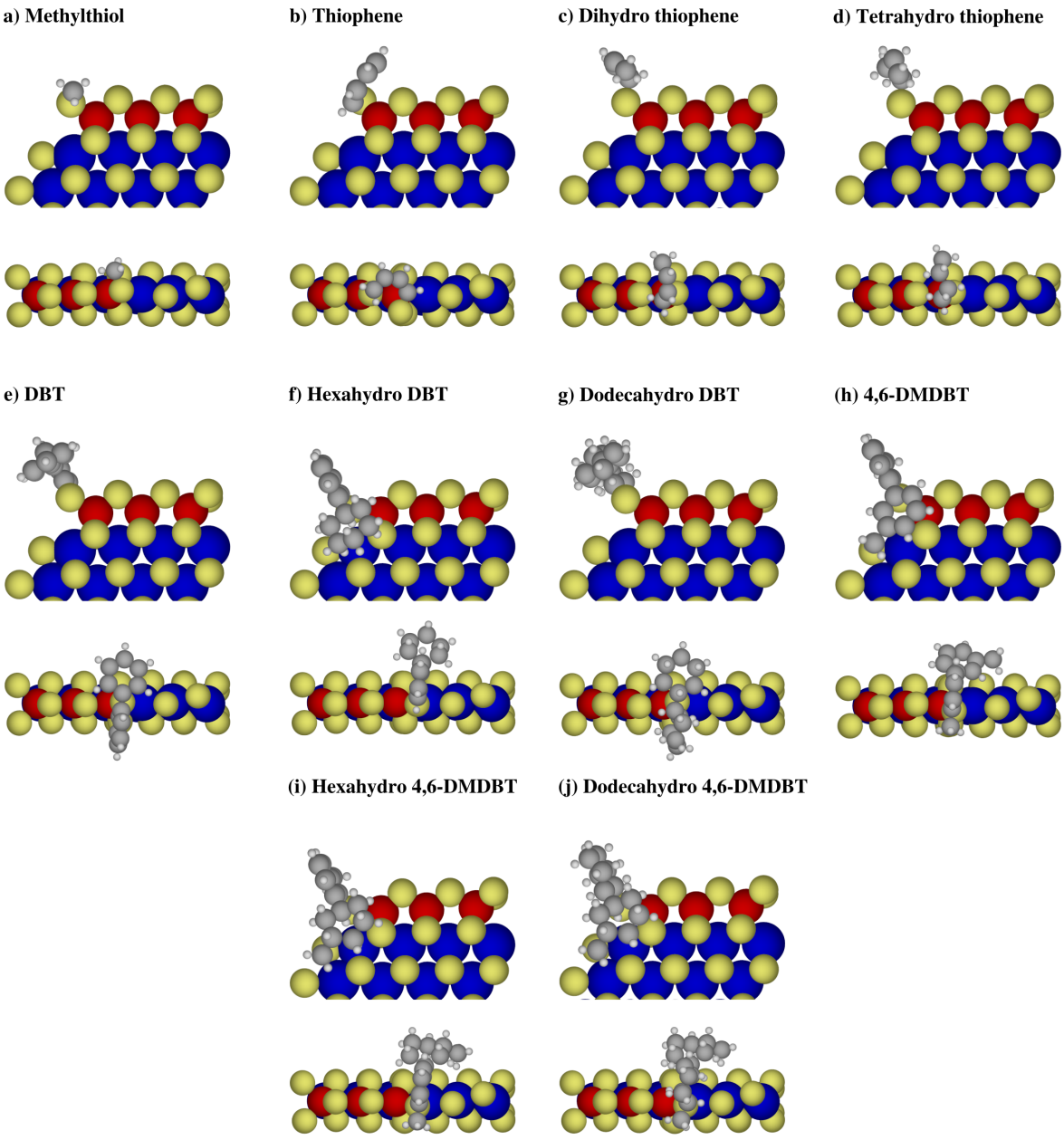

Figure 12: Adsorption configurations of the studied molecules in thiolate form at the corner in edge position perpendicular to the MoS_2 plane.

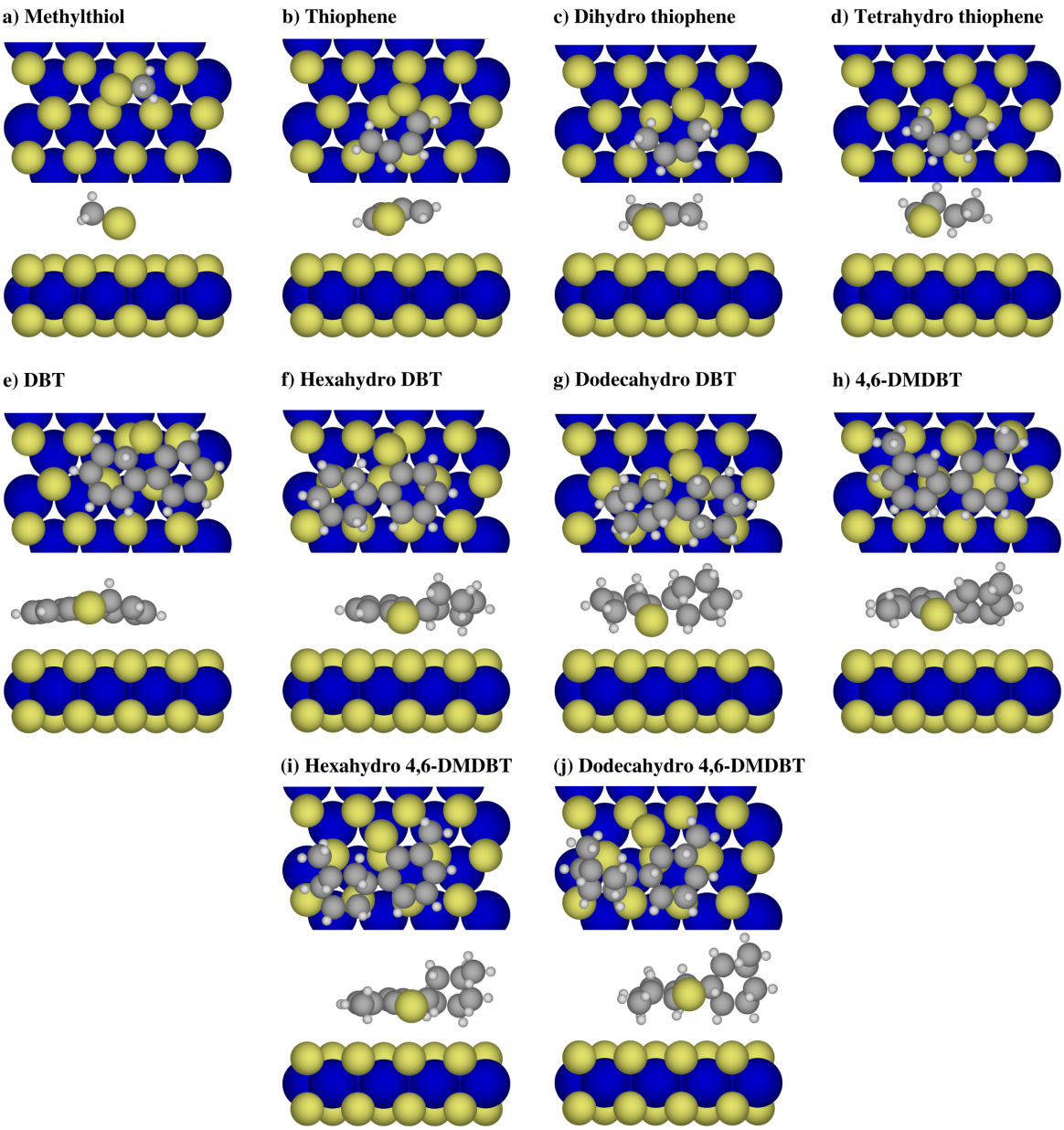

Figure 13: Adsorption configurations of the studied molecules in thiolate form at the basal plane.

Chapter 6

Additional results

6.1 Kinetics of thiophene desulfurization

In order to get more insight into the HDS activity of the edges and corners of CoMoS particles, a simple kinetic model for the direct desulfurization of thiophene was constructed. The following mechanism was considered on the S-edge, M-edge vacancy and corner vacancy models:

$$\text{I}: \quad C_4H_4S + * \leftrightarrow C_4H_4S^* \tag{6.1}$$

$$\text{II}: \quad C_4H_4S^* + \frac{1}{2}H_2 \leftrightarrow C_4H_5S^* \tag{6.2}$$

$$\text{III}: \quad C_4H_5S^* + \frac{1}{2}H_2 \leftrightarrow C_4H_6 + S^* \tag{6.3}$$

$$\text{IV}: \quad S^* + H_2 \leftrightarrow H_2S + * \tag{6.4}$$

where C_4H_4S is a thiophene molecule.

Figure 6.1 shows a potential energy diagram and free energy diagram at 600 K, 0.1 bar of H_2S and 40 bar of H_2 for the desulfurization of thiophene on the S-edge, M-edge vacancy and corner vacancy model. In reaction I, thiophene adsorbs on the active site. In reaction II, the first C-S bond of thiophene gets cleaved and a thiolate is formed. In reaction III, the second C-S bond of thiophene gets cleaved and butadiene is released while a sulfur atoms remains adsorbed. In reaction IV, the additional sulfur atom is removed from the surface. The free energy diagram was constructed by correcting H_2 and H_2S with zero point energy, thermal contributions and pressures and using non-corrected DFT 0 K energies for the rest of the molecules, adsorbates and surfaces. One can see from the energy diagrams that the reaction is thermodynamically favorable with a barrier related to the C-S bond being broken (TS). The removal of sulfur is not favorable at 0 K but it becomes so when going to HDS conditions.

It was suggested in previous studies that the most difficult step to carry out for the desulfurization of thiophene is breaking the C-S bond [84, 142]. This is also seen from the barriers (TS) in the energy diagrams in figure 6.1. Therefore we assume that the rate determining step is reaction II (6.2). We also assume steady reaction conditions

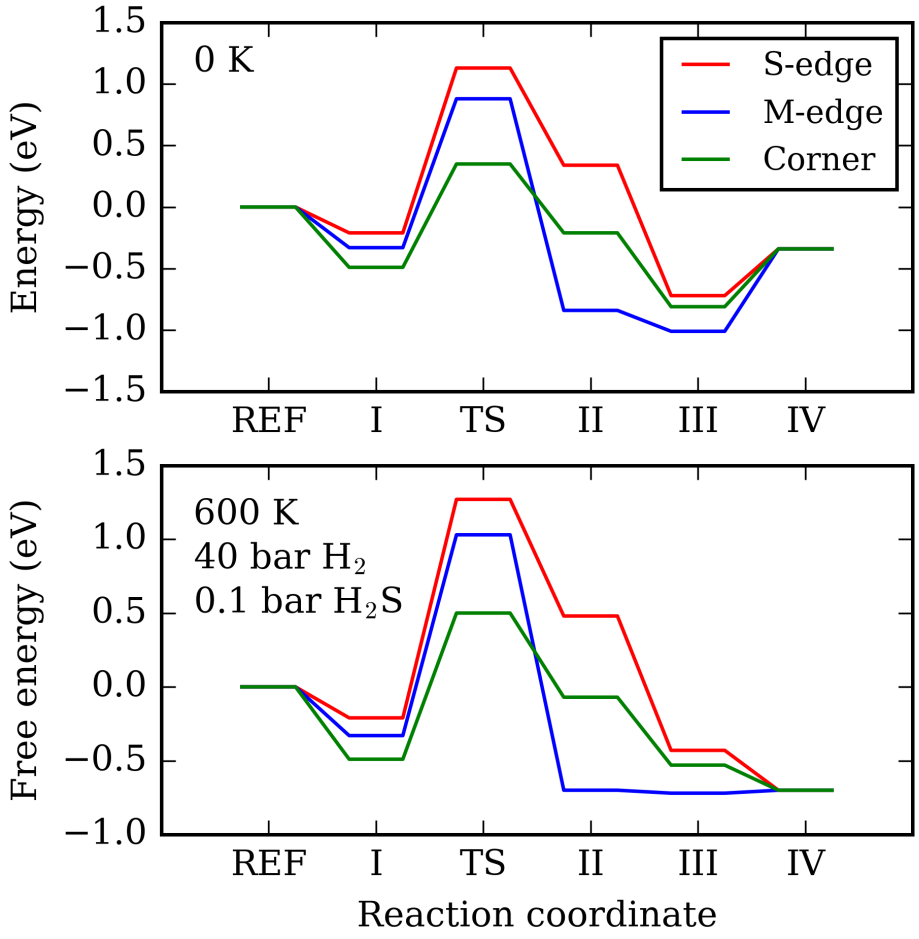

Figure 6.1: Energy (top) and free energy (bottom) diagram of the direct desulfurization of thiophene on the S-edge (red), M-edge vacancy (blue) and corner vacancy (green) models of an ideal CoMoS particle.

which means that the temperature and pressures are constant throughout the reactor and steady state which assumes that the coverage of surface species is time independent. Furthermore we assume that the partial pressures of thiophene and butadiene are 1 bar. From these assumptions the following steady state coverages are obtained:

$$\theta_* = \left[1 + K_1 + \frac{p_{H_2S}}{p_{H_2} K_4} + \frac{p_{H_2S}}{p_{H_2}^{3/2} K_3 K_4}\right]^{-1} \tag{6.5}$$

$$\theta_{C_4H_4S} = K_1 \theta_* \tag{6.6}$$

$$\theta_S = \frac{p_{H_2S}}{p_{H_2} K_4} \theta_* \tag{6.7}$$

$$\theta_{C_4H_5S} = \frac{p_{H_2S}}{p_{H_2}^{3/2} K_3 K_4} \theta_* \tag{6.8}$$

The expression for the turnover frequency (rate) obtained from the microkinetic model is:

$$\mathrm{TOF} = \mathrm{A} e^{\frac{-\mathrm{E_a}}{\mathrm{k_B T}}} \theta_{\mathrm{C_4H_4S}} \mathrm{p}_{\mathrm{H_2}}^{1/2} \left(1 - \frac{\mathrm{p_{H_2S}}}{\mathrm{p}_{\mathrm{H_2}}^2} \mathrm{K}^{-1}\right) \tag{6.9}$$

where K is the equilibrium constant of the overall reaction which corresponds to the product of the equilibrium constants of the elementary reactions, $K = K_1 K_2 K_3 K_4$. For the prefactor, A, a value of 10^{13} site^{-1} s^{-1} was used [53].

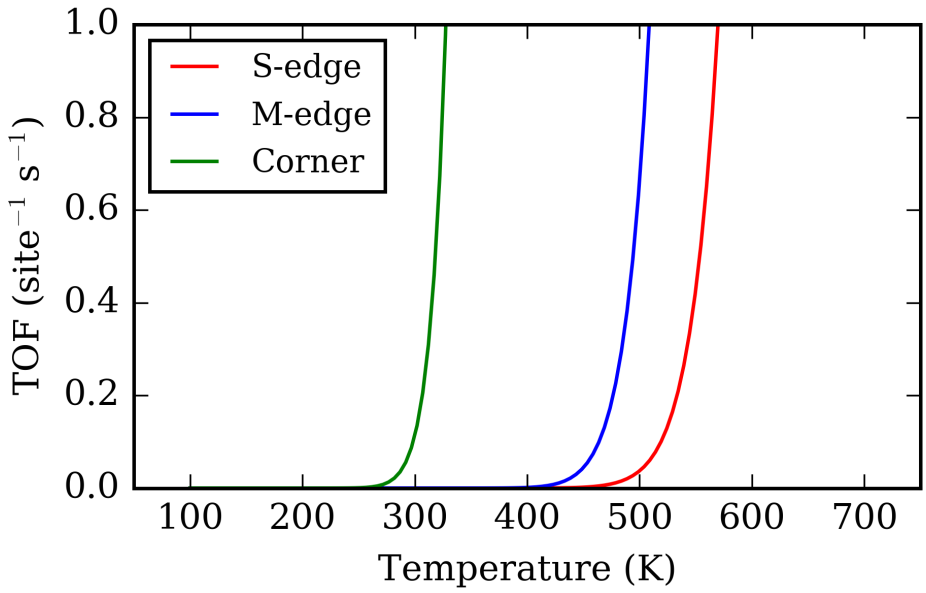

Figure 6.2: Turnover frequency dependence on temperature from the microkinetic model for the direct desulfurization of thiophene on the S-edge (red), M-edge (blue) and corner (red) of CoMoS.

Figure 6.2 shows how the computed turnover frequency depends on temperature. From figure 6.2 one can see that the turnover frequency is higher on the M-edge than the S-edge. To obtain a significant turnover frequency (≈ 1 site^{-1} s^{-1}), a temperature of ≈ 550 K is required on the S-edge and ≈ 475 K at the M-edge, although it is possible that the rate on the M-edge becomes limited by the generation of vacancies at lower temperatures. A temperature between 500 K and 600 K corresponds to the industrially used temperatures and confirms the simple model on the edges. It can be seen that the activity is much higher at the corner sites compared to the edges. The model predicts that the corners are active enough to perform desulfurization at significantly lower temperatures (≈ 300 K) than used industrially. The high predicted activity of the corners suggests that the model is not representative for the catalysis on corner sites. Breaking the C-S

bonds on the corners might be easy enough so that there is a different process that is rate determining. A possible candidate for the alternative rate determining step might be the dissociation of H_2. We have calculated the activation energy of H_2 dissociation on the S-edge since it is the most likely site for H_2 dissociation as it is free of vacancies under HDS conditions. The hydrogen dissociation on the S-edge was found to occur between a S-Co bond with an activation energy of ≈ 1 eV with a subsequent diffusion step that has a small activation energy ≈ 0.5 eV. This is more favorable than the dissociation between a S-S bond directly with an activation energy of ≈ 1.4 eV. The activation energy of ≈ 1 eV is higher than the activation energy for cleaving the C-S bonds on the corners (≈ 0.8 eV). This indicates that the turnover frequency on the corners will not be as high as predicted from the simple microkinetic model which does not include hydrogen dissociation and adsorption energies. This idea should be tested further by constructing a more complicated microkinetic model including hydrogen adsorption and dissociation energies.

A microkinetic model of thiophene direct desulfurization was shown. It predicts reasonable rates at high temperatures on the edges, with a slightly higher rate on the M-edge. The corners were predicted to be active at significantly lower temperatures than used in industrial HDS. It was suggested that the reason behind this is the wrong rate determining step used in the model for corner desulfurization. The possible rate determining step for corner desulfurization could be hydrogen dissociation. This is further supported by the activation energy of ≈ 1 eV for hydrogen dissociation which is higher than the corner C-S scission activation energy of ≈ 0.8 eV. Regardless of the model seemingly failing for corner sites, possibly due to not including the correct hydrogen chemistry, it was shown that the process of removing sulfur is much more favorable on the corners compared to the edges.

6.2 Kinetics of dibenzothiophene desulfurization

A similar microkinetic model as the one shown for thiophene was constructed for dibenzothiophene (DBT). The mechanism was assumed to be the following:

$$\text{I}: \quad C_{12}H_8S + * \leftrightarrow C_{12}H_8S^* \tag{6.10}$$

$$\text{II}: \quad C_{12}H_{12}S^* + \frac{1}{2}H_2 \leftrightarrow C_{12}H_9S^* \tag{6.11}$$

$$\text{III}: \quad C_{12}H_9S^* + \frac{1}{2}H_2 \leftrightarrow C_{12}H_{10} + S^* \tag{6.12}$$

$$\text{IV}: \quad S^* + H_2 \leftrightarrow H_2S + * \tag{6.13}$$

where $C_{12}H_8S$ is a DBT molecule.

Energy and free energy diagrams for the process are shown in figure 6.3 In reaction I, DBT adsorbs on the active site. In reaction II, the first C-S bond of DBT gets cleaved and a thiolate is formed. In reaction III, the second C-S bond of DBT gets cleaved and biphenyl is released while a sulfur atom remains adsorbed. In reaction IV, the additional sulfur atom is removed from the surface.

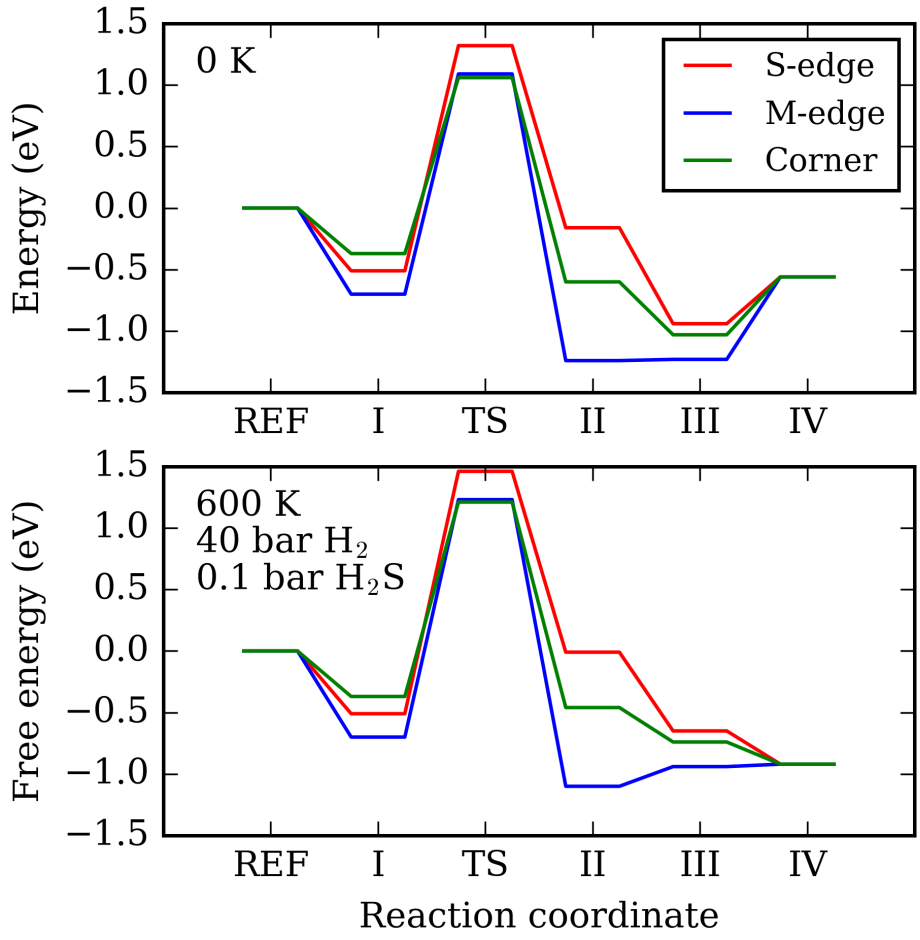

Figure 6.3: Energy (top) and free energy (bottom) diagram of the direct desulfurization of DBT on the S-edge (red), M-edge vacancy (blue) and corner vacancy (green) models of an ideal CoMoS particle.

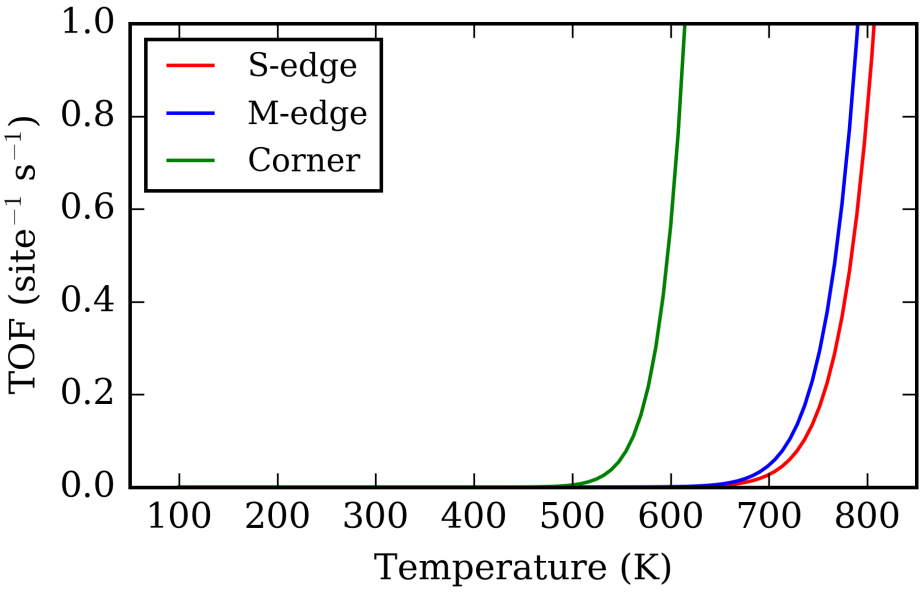

Figure 6.4: Turnover frequency dependence on temperature from the microkinetic model for the direct desulfurization of DBT on the S-edge (red), M-edge (blue) and corner (red) of CoMoS.

By assuming that the partial pressures of DBT and biphenyl are 1 bar, steady reaction conditions, steady state and that reaction II (6.11) is rate determining, the following coverages are obtained:

$$\theta_* = \left[1 + K_1 + \frac{p_{H_2S}}{p_{H_2}K_4} + \frac{p_{H_2S}}{p_{H_2}^{3/2}K_3K_4}\right]^{-1} \tag{6.14}$$

$$\theta_{C_{12}H_8S} = K_1\theta_*\theta_S = \frac{p_{H_2S}}{p_{H_2}K_4}\theta_* \tag{6.15}$$

$$\theta_{C_{12}H_9S} = \frac{p_{H_2S}}{p_{H_2}^{3/2}K_3K_4}\theta_* \tag{6.16}$$

The turnover frequency from the microkinetic model is:

$$\mathrm{TOF} = \mathrm{A}e^{\frac{-\mathrm{E_a}}{\mathrm{k_B T}}}\theta_{\mathrm{C_{12}H_8S}}\mathrm{p}_{\mathrm{H_2}}^{1/2}\left(1 - \frac{\mathrm{p_{H_2S}}}{\mathrm{p}_{\mathrm{H_2}}^2}\mathrm{K}^{-1}\right) \tag{6.17}$$

Figure 6.4 shows the turnover frequency of the direct desulfurization of DBT on the S-edge, M-edge vacancy and corner vacancy as a function of temperature. It can be seen that a reasonable turnover frequency (1 site^{-1} s^{-1}) is obtained on the corners at $\approx$ 600 K while the edges require higher temperatures $\approx$ 750 K. The temperature at which the corner sites achieve reasonable turnover frequencies matches temperatures applied industrially. This observation suggests that the removal of sulfur from DBT occurs at corner sites of CoMoS particles.

Chapter 7

Conclusion and perspective

In the presented work, a theoretical approach in studying the electrochemical production of dimethyl carbonate and hydrodesulfurization on the Co-promoted MoS_2 catalyst was demonstrated. Density functional theory calculations using the GPAW code were performed to calculate energies and concepts from thermodynamics were applied to analyze trends in various catalytic descriptors.

7.1 Dimethyl carbonate

It was shown that dimethyl carbonate can be produced electrochemically on noble metals. The efficiency of the process was found to be determined by the adsorption free energies of methoxy and carbon monoxide, with higher adsorption energies of methoxy (weaker binding) and lower adsorption free energies of carbon monoxide (stronger binding) leading to an increase in required potential. More importantly, the analysis led to the experimentally confirmed prediction that using a copper catalyst instead of a gold catalyst results with ≈ 1 V lower required potential. The selectivity between dimethyl carbonate and dimethyl oxalate was analyzed in terms of the adsorption free energies of methoxy and methyl formate. Catalysts that rather adsorb methoxy, such as copper, are selective towards dimethyl carbonate at lower potentials while catalysts that rather adsorb methyl formate, such as gold, are selective towards dimethyl oxalate at lower potentials. The prediction that copper is selective towards dimethyl carbonate at lower potentials while gold is selective towards dimethyl oxalate and requires a higher potential for dimethyl carbonate production was found to be in excellent agreement with experiments. The electrochemical path and the copper catalyst could act as a foundation in creating an efficient and selective green process for the production of dimethyl carbonate.

Future work on the electrochemical synthesis of dimethyl carbonate should be led by experiment and supported by theory with the goal of improving the promising copper catalyst. Furthermore, different morphologies of the catalyst should be tested as well as different electrochemical cell designs. This should be done with the goal of slowly

upscaling the process to an industrially competent one. My future personal work[1] will focus on identifying other similar reactions that could be performed electrochemically as well as further supporting the experimental effort in the studies on dimethyl carbonate.

7.2 Hydrodesulfurization

It was shown that hydrodesulfurization is a very complex reaction involving various types of sulfur containing molecules and an interplay between sulfur and hydrogen chemistry. The hydrogen evolution reaction was discussed together with hydrodesulfurization as it was found that hydrodesulfurization catalysts have to satisfy similar requirements towards adsorbing hydrogen as hydrogen evolution catalysts, thus, making hydrodesulfurization catalysts good candidates when looking for cheaper and more abundant alternatives to platinum for the hydrogen evolution reaction. The Co-promoted MoS_2 state-of-the-art hydrodesulfurization catalyst was modeled and the equilibrium structures of its edges, corners and basal plane were determined. The edges were found to be terminated by sulfur monomers sitting in bridge positions while the corners were found to have a sulfur vacancy where a cobalt and molybdenum atom meet. The active sites were determined based on the energies required to adsorb additional sulfur or create sulfur vacancies in the equilibrium structures. For the S-edge and corner vacancies it was found that they can adsorb additional sulfur, in that way desulfurizing molecules. On the other hand, for the M-edge it was found that it can easily form single vacancies which can act as adsorption sites where molecules get desulfurized. In this way, the edges and corners were determined as active while the basal plane was confirmed as inert. It was also suggested that corners might play the role of the active sites for the hydrogen evolution reaction as they act as the most favorable hydrogen adsorption sites with and adsorption free energy of hydrogen close to 0 eV at hydrogen evolution reaction conditions. Additionally, the adsorption of various sulfur containing species on the determined active sites has been modeled. It was found that smaller molecules such as thiophene and methylthiol have a preference for adsorbing at vacancies. Further analysis of kinetics confirmed the suggestion that thiophene prefers to get desulfurized at vacancies but can also get desulfurized at the S-edge by interacting with the brim. Dibenzothiophene and 4,6-dimethyldibenzothiophene were found to interact similarly with the vacancies and in brim configuration (vdW interactions) as well as interacting strongly with the basal plane. We have suggested that the adsorption of larger molecules such as dibenzothiophene and 4,6-dimethyldibenzothiophene in vacancies, with an orientation perpendicular relative to the basal plane is prevented in real systems due to possible overlapping with the support or other MoS_2 structures. Calculations of thiolate (molecules after carbon-sulfur or carbon-hydrogen bonds are broken) formation energies on the Co-promoted MoS_2 enabled the prediction of the inert nature of the basal plane towards breaking carbon-sulfur and carbon-hydrogen bonds. Further analysis of kinetics showed that dibenzothiophene gets desulfurized at corner vacancies. Scanning tunneling microscopy showed that it is

[1] At the University of Copenhagen, Department of Chemistry.

possible for molecules to actively switch between various configuration modes which suggests that it is possible for different stages of hydrodesulfurization to occur on different sites. It was found that hydrogenating molecules leads to stronger adsorption on the edges and corners, except in the case of dibenzothiophene on the S-edge. It was suggested that molecules able to adsorb at vacancies get desulfurized directly while molecules preferring brim adsorption, and that adsorb significantly stronger when hydrogenated, prefer the hydrogenation pathway. If put in simple words, the presented work suggests that the role of the S-edge is to dissociate and adsorb hydrogen and get hydrogen atoms ready for hydrogenation while the vacancies play a role in breaking carbon-sulfur bonds.

Due to the complexity of hydrodesulfurization, future work should focus on methods that allow sampling of all the possible configurations and pathways that might occur in the desulfurization of different molecules on different sites. This should be done in a way that makes it possible to screen for new catalysts or catalyst morphologies instead of just focusing on understanding the reaction on a single catalyst. Further elementary insight in the mechanism behind the desulfurization of complex and difficult to desulfurize molecules such as 4,6-dimethyldibenzothiophene is also needed. Better and more transparent integration of computational, experimental but also industrial results and observations can also lead to better understanding and possible improvements in hydrodesulfurzation catalysis. Although it has been studied for decades, hydrodesulfurization catalysis remains full of exciting chemistry waiting to be discovered.

Bibliography

[1] I. C. Prentice, G. Farquhar, M. Fasham, M. Goulden, M. Heimann, V. Jaramillo, H. Kheshgi, C. Le Quéré, R. J. B. Scholes, D. W. Wallace *et al.*, *The carbon cycle and atmospheric carbon dioxide*, Cambridge University Press, 2001.

[2] P. Falkowski, R. Scholes, E. Boyle, J. Canadell, D. Canfield, J. Elser, N. Gruber, K. Hibbard, P. Högberg, S. Linder *et al.*, *Science*, 2000, **290**, 291–296.

[3] A. McGuire, S. Sitch, J. Clein, R. Dargaville, G. Esser, J. Foley, M. Heimann, F. Joos, J. Kaplan, D. Kicklighter *et al.*, *Global Biogeochemical Cycles*, 2001, **15**, 183–206.

[4] L. Hughes, *Trends in Ecology & Evolution*, 2000, **15**, 56–61.

[5] J.-P. Gattuso, M. Frankignoulle and R. Wollast, *Annual Review of Ecology and Systematics*, 1998, 405–434.

[6] S. Smith and J. Hollibaugh, *Reviews of Geophysics*, 1993, **31**, 75–89.

[7] E. A. Davidson and I. A. Janssens, *Nature*, 2006, **440**, 165–173.

[8] J. Le Mer and P. Roger, *European Journal of Soil Biology*, 2001, **37**, 25–50.

[9] A. D. McGuire, L. G. Anderson, T. R. Christensen, S. Dallimore, L. Guo, D. J. Hayes, M. Heimann, T. D. Lorenson, R. W. Macdonald and N. Roulet, *Ecological Monographs*, 2009, **79**, 523–555.

[10] D. J. Wuebbles and K. Hayhoe, *Earth-Science Reviews*, 2002, **57**, 177–210.

[11] B. M. Vinther, S. L. Buchardt, H. B. Clausen, D. Dahl-Jensen, S. J. Johnsen, D. Fisher, R. Koerner, D. Raynaud, V. Lipenkov, K. Andersen *et al.*, *Nature*, 2009, **461**, 385–388.

[12] S. C. Raper and R. J. Braithwaite, *Nature*, 2006, **439**, 311–313.

[13] S. C. Raper and R. J. Braithwaite, *Geophysical Research Letters*, 2005, **32**, year.

[14] N. Kato and H. Akimoto, *Atmospheric Environment. Part A. General Topics*, 1992, **26**, 2997–3017.

[15] H. Akimoto and H. Narita, *Atmospheric Environment*, 1994, **28**, 213–225.

[16] E. Croiset and K. Thambimuthu, *Fuel*, 2001, **80**, 2117–2121.

[17] G. E. Likens, C. T. Driscoll and D. C. Buso, *Science*, 1996, **272**, 244.

[18] M. Andreae and D. Rosenfeld, *Earth-Science Reviews*, 2008, **89**, 13–41.

[19] E. Boeker and R. van Grondelle, *Environmental Physics: Sustainable Energy and Climate Change*, Wiley, 2011.

[20] M. Z. Jacobson, *Energy & Environmental Science*, 2009, **2**, 148–173.

[21] A. Goetzberger, C. Hebling and H.-W. Schock, *Materials Science and Engineering: R: Reports*, 2003, **40**, 1–46.

[22] M. Grätzel, *Journal of Photochemistry and Photobiology C: Photochemistry Reviews*, 2003, **4**, 145–153.

[23] G. Li, R. Zhu and Y. Yang, *Nature Photonics*, 2012, **6**, 153–161.

[24] A. Shah, P. Torres, R. Tscharner, N. Wyrsch and H. Keppner, *Science*, 1999, **285**, 692–698.

[25] M. Grätzel, *Accounts of Chemical Research*, 2009, **42**, 1788–1798.

[26] G. J. Herbert, S. Iniyan, E. Sreevalsan and S. Rajapandian, *Renewable and Sustainable Energy Reviews*, 2007, **11**, 1117–1145.

[27] Z. Chen, J. M. Guerrero and F. Blaabjerg, *IEEE Transactions on Power Electronics*, 2009, **24**, 1859–1875.

[28] J.-M. Tarascon and M. Armand, *Nature*, 2001, **414**, 359–367.

[29] J. B. Goodenough and Y. Kim, *Chemistry of Materials*, 2009, **22**, 587–603.

[30] B. Dunn, H. Kamath and J.-M. Tarascon, *Science*, 2011, **334**, 928–935.

[31] B. Scrosati and J. Garche, *Journal of Power Sources*, 2010, **195**, 2419–2430.

[32] V. Etacheri, R. Marom, R. Elazari, G. Salitra and D. Aurbach, *Energy & Environmental Science*, 2011, **4**, 3243–3262.

[33] J. A. Turner, *Science*, 2004, **305**, 972–974.

[34] G. W. Crabtree, M. S. Dresselhaus and M. V. Buchanan, *Physics Today*, 2004, **57**, 39–44.

[35] S. Dunn, *International Journal of Hydrogen Energy*, 2002, **27**, 235–264.

[36] M. K. Debe, *Nature*, 2012, **486**, 43–51.

[37] A. S. Arico, P. Bruce, B. Scrosati, J.-M. Tarascon and W. Van Schalkwijk, *Nature Materials*, 2005, **4**, 366–377.

[38] B. C. Steele and A. Heinzel, *Nature*, 2001, **414**, 345–352.

[39] M. Winter and R. J. Brodd, *Chemical Reviews*, 2004, **104**, 4245–4270.

[40] K. Zeng and D. Zhang, *Progress in Energy and Combustion Science*, 2010, **36**, 307–326.

[41] M. Carmo, D. L. Fritz, J. Mergel and D. Stolten, *International Journal of Hydrogen Energy*, 2013, **38**, 4901–4934.

[42] P. C. Vesborg, B. Seger and I. Chorkendorff, *The Journal of Physical Chemistry Letters*, 2015, **6**, 951–957.

[43] M. G. Walter, E. L. Warren, J. R. McKone, S. W. Boettcher, Q. Mi, E. A. Santori and N. S. Lewis, *Chemical Reviews*, 2010, **110**, 6446–6473.

[44] P. C. Vesborg and T. F. Jaramillo, *RSC Advances*, 2012, **2**, 7933–7947.

[45] S. Choi, J. H. Drese and C. W. Jones, *ChemSusChem*, 2009, **2**, 796–854.

[46] Q. Wang, J. Luo, Z. Zhong and A. Borgna, *Energy & Environmental Science*, 2011, **4**, 42–55.

[47] E. E. Benson, C. P. Kubiak, A. J. Sathrum and J. M. Smieja, *Chemical Society Reviews*, 2009, **38**, 89–99.

[48] W. Wang, S. Wang, X. Ma and J. Gong, *Chemical Society Reviews*, 2011, **40**, 3703–3727.

[49] R. Gold, E. Bloom, F. Clinard Jr, D. Smith, R. Stevenson and W. Wolfer, *Fusion Science and Technology*, 1981, **1**, 169–237.

[50] A. Ulbricht, J. Duchateau, W. Fietz, D. Ciazynski, H. Fillunger, S. Fink, R. Heller, R. Maix, S. Nicollet, S. Raff *et al.*, *Fusion Engineering and Design*, 2005, **73**, 189–327.

[51] I. Babich and J. Moulijn, *Fuel*, 2003, **82**, 607–631.

[52] G. Schuit and B. Gates, *AIChE Journal*, 1973, **19**, 417–438.

[53] I. Chorkendorff and J. W. Niemantsverdriet, *Concepts of Modern Catalysis and Kinetics*, Wiley-VCH, 2007.

[54] P. T. Anastas and M. M. Kirchhoff, *Accounts of Chemical Research*, 2002, **35**, 686–694.

[55] R. A. Sheldon, *Green Chemistry*, 2005, **7**, 267–278.

[56] P. Anastas and N. Eghbali, *Chemical Society Reviews*, 2010, **39**, 301–312.

[57] J. H. Clark, *Green Chemistry*, 1999, **1**, 1–8.

[58] Jens K. Nørskov and Felix Studt and Frank Abild-Pedersen and Thomas Bligaard, *Fundamental Concepts in Heterogeneous Catalysis*, Wiley, 2014.

[59] Atkins, *Atkins Physical Chemistry 9th edition*, WH Freman,2010, 2010.

[60] L. Pauling, *General Chemistry*, Dover, 2013.

[61] J. J. Mortensen, L. B. Hansen and K. W. Jacobsen, *Physical Review B*, 2005, **71**, 035109.

[62] J. Enkovaara, C. Rostgaard, J. J. Mortensen, J. Chen, M. Dułak, L. Ferrighi, J. Gavnholt, C. Glinsvad, V. Haikola, H. Hansen *et al.*, *Journal of Physics: Condensed Matter*, 2010, **22**, 253202.

[63] P. Tundo and M. Selva, *Accounts of Chemical Research*, 2002, **35**, 706–716.

[64] P. Tundo, P. Anastas, D. S. Black, J. Breen, T. J. Collins, S. Memoli, J. Miyamoto, M. Polyakoff and W. Tumas, *Pure and Applied Chemistry*, 2000, **72**, 1207–1228.

[65] D. Delledonne, F. Rivetti and U. Romano, *Applied Catalysis A: General*, 2001, **221**, 241–251.

[66] M. A. Pacheco and C. L. Marshall, *Energy & Fuels*, 1997, **11**, 2–29.

[67] Y. Ono, *Applied Catalysis A: General*, 1997, **155**, 133–166.

[68] S. Memoli, M. Selva and P. Tundo, *Chemosphere*, 2001, **43**, 115–121.

[69] I. Omae, *Catalysis Today*, 2006, **115**, 33–52.

[70] Z.-H. Fu and Y. Ono, *Journal of Molecular Catalysis A: Chemical*, 1997, **118**, 293–299.

[71] J. Gong, X. Ma and S. Wang, *Applied Catalysis A: General*, 2007, **316**, 1–21.

[72] N. Keller, G. Rebmann and V. Keller, *Journal of Molecular Catalysis A: Chemical*, 2010, **317**, 1–18.

[73] A. Funakawa, I. Yamanaka and K. Otsuka, *The Journal of Physical Chemistry B*, 2005, **109**, 9140–9147.

[74] A. Funakawa, I. Yamanaka, S. Takenaka and K. Otsuka, *Journal of the American Chemical Society*, 2004, **126**, 5346–5347.

[75] I. J. Drake, K. L. Fujdala, A. T. Bell and T. D. Tilley, *Journal of Catalysis*, 2005, **230**, 14–27.

[76] I. Yamanaka, A. Funakawa and K. Otsuka, *Chemistry Letters*, 2002, 448–449.

[77] A. Funakawa, I. Yamanaka and K. Otsuka, *Journal of The Electrochemical Society*, 2006, **153**, D68–D73.

[78] I. Yamanaka, A. Funakawa and K. Otsuka, *Journal of Catalysis*, 2004, **221**, 110–118.

[79] A. Galia, G. Filardo, S. Gambino, R. Mascolino, F. Rivetti and G. Silvestri, *Electrochimica Acta*, 1996, **41**, 2893–2896.

[80] G. Jia, W. Zhang, Z. Jin, W. An, Y. Gao, X. Zhang and J. Liu, *Electrochimica Acta*, 2014, **144**, 1–6.

[81] Y. Yu, X. Liu, W. Zhang, Y. Zhang, L. Li, Z. Cao, Z. Guo, H. Wang, G. Jia, Y. Pan *et al.*, *Industrial & Engineering Chemistry Research*, 2013, **52**, 6901–6907.

[82] K. Otsuka, T. Yagi and I. Yamanaka, *Journal of The Electrochemical Society*, 1995, **142**, 130–135.

[83] C. Song, *Catalysis Today*, 2003, **86**, 211–263.

[84] P. G. Moses, B. Hinnemann, H. Topsøe and J. K. Nørskov, *Journal of Catalysis*, 2007, **248**, 188–203.

[85] R. Prins, M. Egorova, A. Röthlisberger, Y. Zhao, N. Sivasankar and P. Kukula, *Catalysis Today*, 2006, **111**, 84–93.

[86] J.-F. Paul, S. Cristol and E. Payen, *Catalysis Today*, 2008, **130**, 139 – 148.

[87] J. Lauritsen, M. Nyberg, J. K. Nørskov, B. Clausen, H. Topsøe, E. Lægsgaard and F. Besenbacher, *Journal of Catalysis*, 2004, **224**, 94–106.

[88] P. G. Moses, B. Hinnemann, H. Topsøe and J. K. Nørskov, *Journal of Catalysis*, 2009, **268**, 201–208.

[89] B. Hinnemann, P. G. Moses and J. K. Nørskov, *Journal of Physics: Condensed Matter*, 2008, **20**, 064236.

[90] J. V. Lauritsen, R. T. Vang and F. Besenbacher, *Catalysis Today*, 2006, **111**, 34–43.

[91] J. V. Lauritsen, J. Kibsgaard, G. H. Olesen, P. G. Moses, B. Hinnemann, S. Helveg, J. K. Nørskov, B. S. Clausen, H. Topsøe, E. Lægsgaard *et al.*, *Journal of Catalysis*, 2007, **249**, 220–233.

[92] J. Lauritsen, S. Helveg, E. Lægsgaard, I. Stensgaard, B. Clausen, H. Topsøe and F. Besenbacher, *Journal of Catalysis*, 2001, **197**, 1–5.

[93] L. Byskov, J. Nørskov, B. Clausen and H. Topsøe, *Catalysis Letters*, 2000, **64**, 95–99.

[94] E. Hensen, P. Kooyman, Y. Van der Meer, A. Van der Kraan, V. De Beer, J. Van Veen and R. Van Santen, *Journal of Catalysis*, 2001, **199**, 224–235.

[95] C. Kisielowski, Q. Ramasse, L. Hansen, M. Brorson, A. Carlsson, A. Molenbroek, H. Topse and S. Helveg, *Angewandte Chemie International Edition*, 2010, **49**, 2708–2710.

[96] Y. Zhu, Q. M. Ramasse, M. Brorson, P. G. Moses, L. P. Hansen, C. F. Kisielowski and S. Helveg, *Angewandte Chemie International Edition*, 2014, **53**, 10723–10727.

[97] L. P. Hansen, Q. M. Ramasse, C. Kisielowski, M. Brorson, E. Johnson, H. Topse and S. Helveg, *Angewandte Chemie International Edition*, 2011, **50**, 10153–10156.

[98] P. Raybaud, J. Hafner, G. Kresse, S. Kasztelan and H. Toulhoat, *Journal of Catalysis*, 2000, **190**, 128–143.

[99] F. Besenbacher, M. Brorson, B. Clausen, S. Helveg, B. Hinnemann, J. Kibsgaard, J. V. Lauritsen, P. G. Moses, J. K. Nørskov and H. Topsøe, *Catalysis Today*, 2008, **130**, 86–96.

[100] H. Schweiger, P. Raybaud, G. Kresse and H. Toulhoat, *Journal of Catalysis*, 2002, **207**, 76 – 87.

[101] J. Lauritsen, M. Bollinger, E. Lægsgaard, K. Jacobsen, J. Nørskov, B. Clausen, H. Topsøe and F. Besenbacher, *Journal of Catalysis*, 2004, **221**, 510 – 522.

[102] M. Bollinger, J. Lauritsen, K. W. Jacobsen, J. K. Nørskov, S. Helveg and F. Besenbacher, *Physical Review Letters*, 2001, **87**, 196803.

[103] M. Bollinger, K. W. Jacobsen and J. K. Nørskov, *Physical Review B*, 2003, **67**, 085410.

[104] S. Rangarajan and M. Mavrikakis, *ACS Catalysis*, 2016, **6**, 2904–2917.

[105] Á. Logadóttir, P. G. Moses, B. Hinnemann, N.-Y. Topsøe, K. G. Knudsen, H. Topsøe and J. K. Nørskov, *Catalysis Today*, 2006, **111**, 44–51.

[106] P.-Y. Prodhomme, P. Raybaud and H. Toulhoat, *Journal of Catalysis*, 2011, **280**, 178–195.

[107] R. Parsons, *Transactions of the Faraday Society*, 1958, **54**, 1053–1063.

[108] E. Skúlason, G. S. Karlberg, J. Rossmeisl, T. Bligaard, J. Greeley, H. Jónsson and J. K. Nørskov, *Physical Chemistry Chemical Physics*, 2007, **9**, 3241–3250.

[109] J. K. Nørskov, T. Bligaard, A. Logadottir, J. Kitchin, J. Chen, S. Pandelov and U. Stimming, *Journal of The Electrochemical Society*, 2005, **152**, J23–J26.

[110] R. J. Kriek, J. Rossmeisl, S. Siahrostami and M. E. Björketun, *Physical Chemistry Chemical Physics*, 2014, **16**, 9572–9579.

[111] B. Hinnemann, P. G. Moses, J. Bonde, K. P. Jørgensen, J. H. Nielsen, S. Horch, I. Chorkendorff and J. K. Nørskov, *Journal of the American Chemical Society*, 2005, **127**, 5308–5309.

[112] D. Merki and X. Hu, *Energy & Environmental Science*, 2011, **4**, 3878–3888.

[113] C. G. Morales-Guio, L.-A. Stern and X. Hu, *Chemical Society Reviews*, 2014, **43**, 6555–6569.

[114] E. J. Popczun, J. R. McKone, C. G. Read, A. J. Biacchi, A. M. Wiltrout, N. S. Lewis and R. E. Schaak, *Journal of the American Chemical Society*, 2013, **135**, 9267–9270.

[115] M. H. Hansen, L.-A. Stern, L. Feng, J. Rossmeisl and X. Hu, *Physical Chemistry Chemical Physics*, 2015, **17**, 10823–10829.

[116] J. Bonde, P. G. Moses, T. F. Jaramillo, J. K. Norskov and I. Chorkendorff, *Faraday Discuss.*, 2009, **140**, 219–231.

[117] T. F. Jaramillo, K. P. Jorgensen, J. Bonde, J. H. Nielsen, S. Horch and I. Chorkendorff, *Science*, 2007, **317**, 100–102.

[118] C. J. Cramer, *Essentials of Computational Chemistry: Theories and Models*, Wiley, 2004.

[119] D. Sholl and J. A. Steckel, *Density Functional Theory: A Practical Introduction*, Wiley-Interscience, 2011.

[120] J. Kohanoff, *Electronic Structure Calculations for Solids and Molecules: Theory and Computational Methods*, Cambridge University Press, 2006.

[121] D. J. Griffiths, *Introduction to Quantum Mechanics*, Cambridge University Press, 2016.

[122] P. Hohenberg and W. Kohn, *Physical Review*, 1964, **136**, B864.

[123] W. Kohn and L. J. Sham, *Physical Review*, 1965, **140**, A1133.

[124] B. Hammer, L. B. Hansen and J. K. Nørskov, *Physical Review B*, 1999, **59**, 7413.

[125] J. Wellendorff, K. T. Lundgaard, A. Møgelhøj, V. Petzold, D. D. Landis, J. K. Nørskov, T. Bligaard and K. W. Jacobsen, *Physical Review B*, 2012, **85**, 235149.

[126] M. Dion, H. Rydberg, E. Schröder, D. C. Langreth and B. I. Lundqvist, *Physical Review Letters*, 2004, **92**, 246401.

[127] K. Lee, É. D. Murray, L. Kong, B. I. Lundqvist and D. C. Langreth, *Physical Review B*, 2010, **82**, 081101.

[128] A. Tkatchenko and M. Scheffler, *Physical Review Letters*, 2009, **102**, 073005.

[129] G. Mills, W. Jacobsen *et al.*, 1998.

[130] G. Henkelman and H. Jónsson, *The Journal of Chemical Physics*, 2000, **113**, 9978–9985.

[131] G. Henkelman, B. P. Uberuaga and H. Jónsson, *The Journal of Chemical Physics*, 2000, **113**, 9901–9904.

[132] NIST, *NIST-JANAF thermochemical table*, Accessed 2016.

[133] D. W. P. Robert H. Green, *Perry's Chemical Engineers' Handbook*, McGraw-Hill Professional, 1998.

[134] ASE, *Atomic simulation environment thermochemistry class*, Accessed 2016.

[135] J. Kleis, G. Jones, F. Abild-Pedersen, V. Tripkovic, T. Bligaard and J. Rossmeisl, *Journal of The Electrochemical Society*, 2009, **156**, B1447–B1456.

[136] F. Calle-Vallejo, J. Martinez, J. M. García-Lastra, J. Rossmeisl and M. Koper, *Physical Review Letters*, 2012, **108**, 116103.

[137] E. M. Fernandez, P. G. Moses, A. Toftelund, H. A. Hansen, J. I. Martinez, F. Abild-Pedersen, J. Kleis, B. Hinnemann, J. Rossmeisl, T. Bligaard and J. K. Nørskov, *Angewandte Chemie International Edition*, 2008, **47**, 4683–4686.

[138] K. Honkala, A. Hellman, I. Remediakis, A. Logadottir, A. Carlsson, S. Dahl, C. H. Christensen and J. K. Nørskov, *Science*, 2005, **307**, 555–558.

[139] J. K. Nørskov, J. Rossmeisl, A. Logadottir, L. Lindqvist, J. R. Kitchin, T. Bligaard and H. Jonsson, *The Journal of Physical Chemistry B*, 2004, **108**, 17886–17892.

[140] M. Busch, N. B. Halck, U. I. Kramm, S. Siahrostami, P. Krtil and J. Rossmeisl, *Nano Energy*, 2016.

[141] A. Logadottir, T. H. Rod, J. K. Nørskov, B. Hammer, S. Dahl and C. Jacobsen, *Journal of Catalysis*, 2001, **197**, 229–231.

[142] P. G. Moses, L. C. Grabow, E. M. Fernandez, B. Hinnemann, H. Topsøe, K. G. Knudsen and J. K. Nørskov, *Catalysis Letters*, 2014, **144**, 1425–1432.

[143] S. Dahl, A. Logadottir, C. J. Jacobsen and J. K. Nørskov, *Applied Catalysis A: General*, 2001, **222**, 19–29.

[144] J. K. Nørskov, T. Bligaard, J. Rossmeisl and C. H. Christensen, *Nature Chemistry*, 2009, **1**, 37–46.

[145] J. Rossmeisl, P. Ferrin, G. A. Tritsaris, A. U. Nilekar, S. Koh, S. E. Bae, S. R. Brankovic, P. Strasser and M. Mavrikakis, *Energy & Environmental Science*, 2012, **5**, 8335–8342.

[146] P. Ferrin, A. U. Nilekar, J. Greeley, M. Mavrikakis and J. Rossmeisl, *Surface Science*, 2008, **602**, 3424–3431.

[147] S. Humbert, G. Izzet and P. Raybaud, *Journal of Catalysis*, 2016, **333**, 78 – 93.